UNIVERSITY OF SOUTHAMPTON

FACULTY OF ENGINEERING AND PHYSICAL SCIENCES
OPTOELECTRONICS RESEARCH CENTRE

Tapered silicon core fibres for supercontinuum generation

by

JOSEPH CAMPLING

Thesis for the degree of Doctor of Philosophy

November 4, 2021

UNIVERSITY OF SOUTHAMPTON

ABSTRACT

FACULTY OF PHYSICAL SCIENCES AND ENGINEERING
OPTOELECTRONICS RESEARCH CENTRE

Thesis for the degree of DOCTOR OF PHILOSOPHY

TAPERED SILICON CORE FIBRES FOR SUPERCONTINUUM GENERATION

by
Joseph CAMPLING

A series of silicon-core fibre tapers are designed that allow for longitudinal variation of their nonlinear and dispersion parameters with length. A supercontinuum (SC) is generated in the waist region of the taper due to the increased nonlinearity there. The long-wavelength edge of the SC is then boosted by up-tapering to a specific core diameter which is chosen to optimise the phase-matching conditions for four-wave mixing. This means that the bulk of the initially-generated SC can be used as pump sources for transferring power to the long-wavelength edge. Each design targets a specific wavelength range with a 0.25 μm bandwidth.

The design work is driven by simulations of mid-infrared laser pulse propagation through the fibres, which work by solving the generalised nonlinear Schrödinger equation (GNLSE). This incorporates numerous nonlinear effects in silicon affecting SC generation, including two-photon absorption (TPA), three-photon absorption and free-carrier effects. The wavelength-dependence of linear loss and the effective area of the fundamental mode is incorporated into the GNLSE, which is extended to also incorporate the wavelength-dependence of TPA.

The possibility of using these taper design principles is also explored for silicon-on-insulator waveguides.

Contents

List of Figures

List of Tables

List of Abbreviations

3PA	**3 P**hoton **A**bsorption
DW	**D**ispersive **W**ave
FCA	**F**ree **C**arrier **A**bsorption
FWM	**F**our **W**ave **M**ixing
GNLSE	**G**eneralised **N**onlinear **S**chrödinger **Equation**
GVD	**G**roup **V**elocity **D**ispersion
HPCVD	**H**igh **P**ressure **C**hemical **V**apour **D**eposition
MCD	**M**olten **C**ore **D**rawing
MI	**M**odulation **I**nstability
SC	**S**uper**c**ontinuum
SMF	**S**ingle **M**ode **F**ibre
SOI	**S**ilicon **O**n **I**insulator
SPM	**S**elf **P**hase **M**odulation
TOD	**T**hird **O**rder **Dispersion**
TPA	**T**wo **P**hoton **A**bsorption
XPM	**X** (Cross) **P**hase **M**odulation
ZDW	**Z**ero **D**ispersion **W**avelength

Declaration of Authorship

I, Joseph CAMPLING, declare that this thesis entitled, “Tapered silicon core fibres for supercontinuum generation” and the work presented in it are my own and has been generated by me as the result of my own research work.

I confirm that:

1. This work was done wholly or mainly while in candidature for a research degree at this University.
2. Where any part of this thesis has previously been submitted for a degree or any other qualification at this University or any other institution, this has been clearly stated.
3. Where I have consulted the published work of others, this is always clearly attributed.
4. Where I have quoted from the work of others, the source is always given. With the exception of such quotations, this thesis is entirely my own work.
5. I have acknowledged all main sources of help.
6. Where the thesis is based on work done by myself jointly with others, I have made clear exactly what was done by others and what I have contributed myself.
7. Parts of this work have been published as journal and conference contributions listed in the List of Publications.

Signature: ....

Date: ....

Acknowledgements

I would like to thank my supervisors, Anna Peacock and Peter Horak for their guidance and patience; Haonan Ren, Antoine Runge and Dong Wu for fruitful collaboration; and my colleagues John Begleris, Stuart MacFarquhar, Ozan Aktas, Mathias Weisen and Alan Gray for useful advice. Finally, I am eternally grateful to my wife Katie for all her support and encouragement.

Dedicated to my Grandad

Chapter 1

Introduction

A supercontinuum (SC) is a broadband source of coherent light that has many practical applications in sensing, spectroscopy and microscopy. The mid-infrared (mid-IR) region is particularly useful as it can be used to study biological molecules as well as accurately measure greenhouse gas emissions. For SC generation in the mid-IR, silicon is a promising material due to its high nonlinearity and broad transparency window. It is also versatile as it can be drawn as a fibre or etched as a ridge waveguide onto CMOS-compatible chips.

The purpose of this work is to find a way to extend the long-wavelength edge of a SC. The emphasis, however, is not merely on the points at which the SC drops below a certain threshold relative to the pump wavelength (such as -30 dB, a commonly used metric) which define its width. The work focusses rather on the average power (or spectral density) available in the long-wavelength portion of the SC. As such, the SC studied here could have practical applications in spectroscopy, for which a minimum average power is required.

To this end, I have designed a series of silicon-core fibres that are tapered longitudinally, thus varying their dispersion parameters with length. This allows a SC to be generated in the waist region of the taper due to the increased nonlinearity there. The long-wavelength edge is then boosted by up-tapering to a specific core diameter which is chosen to optimise the phase-matching conditions for four-wave mixing (FWM). This means that the bulk of the initially-generated SC can be used as pump sources for transferring power to the long-wavelength edge. Each design targets a specific wavelength range with a 0.25 µm bandwidth.

In order to carry out this design work, which is entirely simulation-based at this juncture, I first study the generalised nonlinear Schrödinger equation (GNLSE), which incorporates numerous nonlinear effects in silicon affecting SC generation, including two-photon absorption (TPA), three-photon absorption (3PA) and free-carrier effects. I develop code to solve the equation and compare simulation results produced by it with a number of experimentally measured spectra to ensure the simulations are in good agreement. I incorporate the wavelength-dependence of linear loss and the effective area of the fundamental mode into the GNLSE. Furthermore, I extend the GNLSE to incorporate the wavelength-dependence of TPA, as this has an impact on the SC produced with the taper designs which are pumped near the edge of the TPA band.

The design work starts with a simple two-fibre model, where a pump and seed are used to generate a third wavelength using degenerate-FWM in the first fibre. The three wavelengths are then sent into a second fibre in order to generate a fourth (target) wavelength. The core diameter of the output fibre is such that the input wavelengths are phase-matched with the target in a non-degenerate FWM process.

This principle is essentially extended with the full fibre taper designs, in which the output facet core diameter allows for many such phase-matched processes to occur across the whole input spectrum, with targets contained in a limited wavelength range at the edge of the SC.

Finally, the possibility of using these taper design principles is explored for silicon-on-insulator (SOI) waveguides, which offer some promise but are found to be less effective than the fibre designs for the pump and target wavelengths studied in this work.

Nonetheless, these design principles are shown to be sound and tapered silicon-core fibres have the potential to significantly enhance the power available for mid-IR spectroscopy.

1.1 Supercontinuum generation in the mid-infrared

The infrared (IR) is an important domain in terms of sensing applications because many energy transitions of molecules involve the absorption and emission of IR photons. It can be used for studying ultrafast hydrogen-bond dynamics in water [1], detecting trace gases [2] or even for monitoring volcanoes [3].

It is divided up in different ways by different authors, into bands such as the near-infrared (NIR) [4], the mid-infrared (mid-IR) [5] and the far-infrared (FIR). Sometimes the term short-wavelength infrared (SWIR) is used to cover the region between the NIR and mid-IR [6]. For the purposes of this study, I will define the NIR as 0.65 - 1.7 µm, the SWIR as 1.7 - 3.5 µm and the mid-IR as 3.5 - 10 µm. The spectral bandwidths studied in this report range from $\sim 1.4 - 5.5$ µm, thus covering the SWIR and significant portions of the NIR and the mid-IR.

When information about the optical response of a sample over a range of wavelengths is required, as in the case of fluorescence or absorption spectroscopy, it is necessary to have a coherent broadband source of light [7]. In this process, the light is passed through a sample and the output measured to resolve fluorescence or absorption lines across a wide spectrum, thus providing information about chemicals and/or biological processes present. A supercontinuum (SC), which simply means a continuum of frequencies over a wide ('super') range, is just such a source. SC generation has a range of additional applications: low-coherence interferometry [8], optical coherence tomography [9], gas sensing (as mentioned) and confocal microscopy [10].

An SC is generated by pumping an optical fibre or waveguide with short laser pulses (generally < 1 ps). A combination of the material nonlinearity and dispersion then broadens the spectrum of the input light. A strong nonlinear interaction is important for modifying the phase of the electric field component of the light in order to change the spectrum. Equally crucial is the dispersion profile which determines how wavelengths can be converted to different ones through a process of phase-matching.

Optical fibres have been used for a long time for SC generation. The problem traditionally has been that silica fibres have a very low material nonlinearity [11] and a small index contrast between the core and cladding, which means that light cannot be confined well in structures smaller than a few microns. As the nonlinearity achievable is inversely proportional to the area of a waveguide, very high peak powers (> 10 kW) have to be used to generate the nonlinear effects necessary for producing an SC. This means that such setups are not very portable or compact, and thus not suitable for use outside dedicated laboratories. In response to this problem, photonic crystal fibres (PCFs) have been developed which still use silica, but the structure is such that air-holes confine the light more strongly, increasing the strength of the nonlinear response. PCFs have improved the efficiency of SC generation, but this is still limited to the NIR or telecoms region by the transparency window of silica. Fibres and waveguides have also been developed using different glasses such as chalcogenide, bismuth and tellurite [11]. These materials have a higher intrinsic nonlinear coefficient, so do not require microstructuring, and a higher refractive index than silica allowing for a higher index contrast which means the laser light can be trapped in a smaller core. These effects combine to increase the nonlinearity affecting the propagating light, and mean that lower peak powers, and thus more compact lasers, can be used to generate an SC. Furthermore, their transparency extends to longer wavelengths, allowing more versatility. However, these materials are not entirely stable due to photo-darkening effects, and are difficult to handle [12].

Concomitant to this has been research into waveguides using semiconductors such as germanium and silicon [5]. There is a great deal of interest in the latter for several reasons. Firstly, it has a very high nonlinearity allowing for lower power lasers to be used for SC generation. Secondly, it is transparent from the NIR to the mid-IR (and thus allows for an octave-spanning SC across the SWIR range). Thirdly, a great deal of progress has been made in reducing the propagation losses. Finally, the standardised fabrication process for silicon chips means that there is a great desire to combine optical processing with electronic processing on the same monolithic chip.

While there is much focus on silicon chips, this material can be also used to produce silica-clad fibres, one of the advantages of which is that they can be integrated with 'standard' silica single-mode fibres (SMFs). In addition to SC generation, the nonlinearity of silicon can be used for wavelength-conversion based information processing, which can be built into existing fibre networks, allowing for such processing to be done 'en route' [13]. In terms of sensing and spectroscopy, silicon fibres can be incorporated into compact devices or connected externally to them without the need to write waveguides on a chip, which can require multiple etching and bonding steps if different materials are combined. Furthermore, and post-processing those materials can be difficult if not impossible without ruining other aspects of the chip. Silicon fibres do not suffer from this problem, and thus they offer much more versatility in terms of post-processing.

In terms of SC generation, with which this study is concerned, silicon fibres offer the possibility of portable spectroscopy-based technology that links in naturally with standard fibres, covering the near-to-mid infrared region. The large core sizes relative to typical ridge waveguides allows for higher input pulse powers to be used, allowing for higher average output powers which are crucial for spectroscopy. The circular geometry and smoother surfaces of silicon-core fibres, due to the flow of the silica cladding around the core during fabrication, mean that the loss is lower as well, potentially allowing for longer lengths which utilise the nonlinearity further.

1.2 Motivation

Although some success has been had with SC generation in silicon (eg [9, 14, 15, 16, 17]), there are limitations such as multi-photon absorption (arising from the excitation of electrons into the conduction band) [18] and free-carrier absorption (additional absorption by the released electrons) [19]. These processes require further study, particularly in terms of how they vary with frequency, in order to better model and potentially design new silicon fibres.

Part of this design work includes exploring the possibilities offered by tapered fibres, which can be fabricated using established techniques. The immediate advantage of these is that it is easier to free-space couple light into them as they have an input diameter comparable to standard fibres (so no lossy elements such as coupling lenses are introduced). In the smallest diameter section (the waist) the nonlinearity is highest, so the most spectral broadening occurs, but tight modal confinement means the modal field spreads into the silica cladding, which strongly absorbs wavelengths longer than 3.5 µm. However, the waist can be reduced in length while still keeping the overall fibre long enough to be manageable. The SC can be generated in the waist and then the up-tapered section allows the light to exit the fibre before cladding-induced losses have accumulated.

Beyond the immediate practicality of having a waist which is narrow and of short length, a further advantage of a taper is that its dispersion profile can be tailored with length so as to open up new phase-matching conditions as the light propagates, thus inducing additional spectral broadening. The goal of this PhD is to design tapered fibres that effectively exploit this phase-matching in order to generate more average power in the long wavelength edge of a mid-IR SC. This could have practical uses for mid-IR spectroscopy.

1.3 Simulating SC generation

One of the main methods for numerically studying nonlinear effects and the resulting evolution of pulses in both the time and frequency domains is the generalised nonlinear Schrödinger equation (GNLSE) [20]. This is because it is not only straightforward to understand conceptually but also solve numerically using the well-established split-step Fourier method (SSFM) [21], as described in Chapter 2. It has been used successfully to recreate the measured spectra of pulses in SMFs and PCFs, including the case where pulses are short and the spectra very broad, which occurs during supercontinuum (SC) generation [7]. In this case, accurate modelling requires the frequency-dependence of all of the parameters to be taken into account, including the nonlinear term which has been achieved for glass fibres. However, because semiconductor fibres and waveguides affect light via additional nonlinearities (multi-photon and free carrier absorption), it is necessary to include extra frequency-dependent terms. One such term, accounting for the frequency-dependence of two-photon absorption (TPA), is studied in Chapter 5.

1.4 The structure of the thesis

Chapter 2 introduces the background theory pertaining to the types of silicon used in silicon-core fibres, confinement of the modes and dispersion characteristics of a fibre, and the GNLSE itself. The fundamentals of nonlinear effects are then introduced.

Chapter 3 studies these nonlinear effects in more detail, with simulations to illustrate them individually and in combination. This will help to understand supercontinuum generation in silicon-core fibres better.

Chapter 4 tests the code by comparing simulations with measured spectra from experiments with silicon-core fibres (including a tapered one) and a silicon-on-insulator (SOI) ridge waveguide.

In Chapter 5 the GNLSE is modified by making the nonlinear loss terms (TPA and 3PA) fully wavelength-dependent. The effects of the wavelength-dependence of the linear loss and effective area of the fundamental mode are also considered.

The final three chapters comprise design work of silicon fibre and ridge systems that can extend the spectral reach of wavelength-conversion and SC generation.

Chapter 6 looks at connecting two fibres together with different diameters in order to convert two pumps to a longer wavelength than would be achievable with only one fibre.

In Chapter 7, this principle is extended to a full taper-shape and applied to SC generation, where the aim is to boost the long-wavelength side of the SC for use in spectroscopy of greenhouse gases.

Chapter 8 then applies these design principles to a ridge platform to demonstrate that they are also applicable in different waveguide geometries.

Finally, Chapter 9 summarises and concludes.

Chapter 2

Background

In this Chapter I introduce the theory necessary to understand nonlinear optics in silicon-core fibres. This will include the optical properties of silicon, the structure of silicon-core fibres and the equations governing the confinement of optical modes and the propagation of pulses through these fibres. Finally I will look at some of the main nonlinear processes, self-phase-modulation (SPM) and four wave mixing (FWM) and the consequences of these, such as higher-order solitons and soliton fission that play a key role in supercontinuum generation.

2.1 Useful equations

The following equations will be used several times in this chapter, so it is useful to define them here:

The Fourier transform is defined as follows:

$$\tilde{\mathbf{E}}(\mathbf{r}, \omega) = \int_{-\infty}^{\infty} \mathbf{E}(\mathbf{r}, t) \exp(\mathrm{i}\omega t) \mathrm{d}t \tag{2.1}$$

Correspondingly, the inverse Fourier transform is:

$$\tilde{\mathbf{E}}(\mathbf{r}, \omega) = \frac{1}{2\pi} \int_{-\infty}^{\infty} \tilde{\mathbf{E}}(\mathbf{r}, \omega) \exp(-\mathrm{i}\omega t) \mathrm{d}\omega \tag{2.2}$$

There is also the Fourier transform property which follows from these definitions:

$$\frac{\partial \tilde{\mathbf{E}}(\mathbf{r}, \omega)}{\partial t} = -\mathrm{i}\omega \tilde{\mathbf{E}}(\mathbf{r}, \omega) \tag{2.3}$$

Finally, there is the convolution theorem which means time-delays can be dealt with in the frequency domain:

$$\begin{aligned} \text{Given } h(t) &= (f * g)(t) = \int_{-\infty}^{\infty} f(t') g(t - t') dt' \\ \text{then } \tilde{h}(\omega) &= \tilde{f}(\omega) \cdot \tilde{g}(\omega) \end{aligned} \tag{2.4}$$

2.2 Optical properties of silicon

Silicon has a transpacency window from 1.1 - 8.5 µm [16]. It is a semiconductor, and has a bandgap of E_g = 1.13eV, which corresponds to light of a wavelength 1.1 µm. This means that it has extremely high absorption at shorter wavelengths than this (and hence does not transmit) because it only requires a single photon to excite an electron in the valence band enough to jump into the conduction band. The absorption is reduced at longer wavelengths, but a pair of photons can still be simultaneously absorbed in a process called two-photon absorption (TPA). In this case, if a photon of energy $E_g/2 < h\nu < E_g$ (where h is the Planck constant and ν is the frequency) is absorbed by an electron in the valence band of the material, exciting it into a virtual (forbidden) state, and a second photon is absorbed rapidly enough that has enough energy to excite the electron above the bandgap, that electron can jump into the conduction band. There is a caveat, in that silicon is an indirect bandgap material [22], which means there is a difference in momentum between the bands, and so vibrational states of the material (phonons) are required to assist in the process. This means that photon absorption processes have a lower probability than in a direct bandgap material, but nonetheless they still occur and can have a dramatic effect on SC generation, as will be demonstrated. The TPA process is illustrated in Fig. 2.1 which also shows the recombination of the released free electron (carrier) back into the valence band by emission of a single photon.

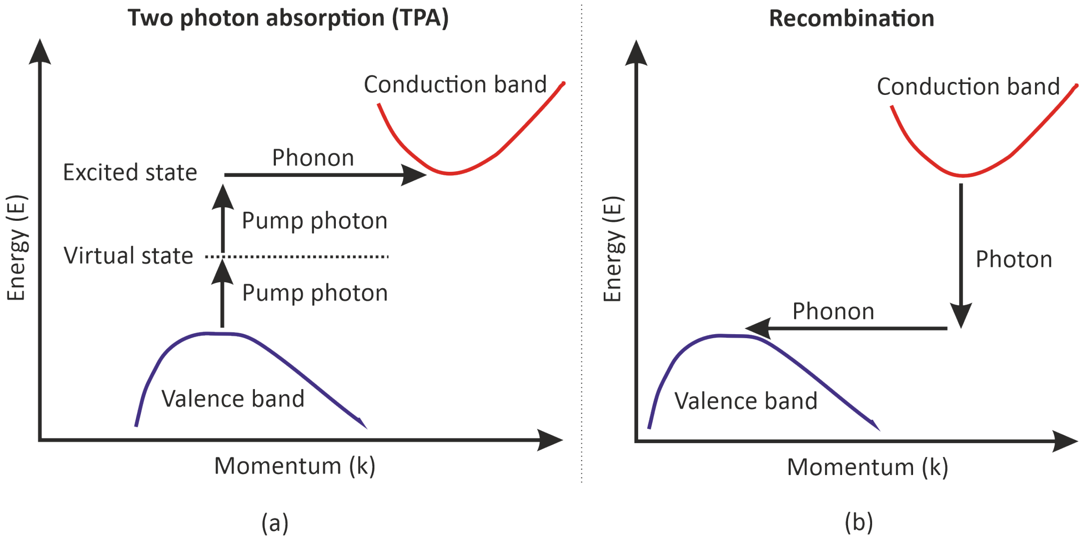

(a) (b)

FIGURE 2.1: Energy diagram for TPA in silicon. (a) Absorption of two photons by an electron, assisted by a phonon. The electron becomes a free carrier. (b) Recombination of free carrier by emitting a single photon, also assisted by a phonon.

At longer wavelengths (i.e. lower frequencies), there are even higher orders of multi-photon absorption, such as 3-photon absorption (3PA) which is also considered in this study. The electrons released into the conduction band by this process are called free carriers, which also act as an additional source of absorption, free carrier absorption (FCA).

Silicon has a crystalline form (single crystal, c-Si, or polycrystalline, p-Si) or an amorphous form (a-Si) [23], and both types are looked at in this study. Table 2.1 shows the optical properties of a-Si:H (hydrogenated amorphous silicon) and p-Si fibres at 1.55 µm.

Optical parameter	**p-Si**	**a-Si:H**
n2 ($\times 10^{-13}$cm^2/W)	0.4 – 0.6	1.5 – 1.85
β_{TPA} (cm/GW)	0.7 – 1	0.5 – 0.8
Loss (dB/cm)	1.6 – 3	0.9 – 3.5

TABLE 2.1: Optical properties of silicon-core fibres at 1.55 µm (taken from [24]).

Most of the silicon-core fibres studied in this thesis are p-Si, but the more it is reheated and tapered, the more the grains melt and recrystallise in a form approaching c-Si. The optical properties of c-Si are essentially the same as for p-Si, but the loss is slightly lower because the grains grow larger and so there are fewer grain boundaries to cause scattering.

Crystalline silicon generally has lower losses than amorphous silicon but the latter can be hydrogenated (a-Si:H) to remove dangling bonds and thus reduce optical absorption [23]. Furthermore, it has higher nonlinearity (2-5 times higher than c-Si) and lower TPA [14] which makes it very useful for nonlinear optics and particularly SC generation (as demonstrated in [14] and [17]). For fibres or waveguides longer than a cm, however, crystalline silicon is more versatile than amorphous because it is more stable and it can be post-processed (i.e. melted and re-crystallised). Amorphous cannot, as such heating and cooling of the material would cause crystals to form, such that it loses its amorphous form. Furthermore, crystalline silicon has lower losses ([24]). These advantages of crystalline silicon make it a good material for fabricating fibre tapers (see Section 2.3.3).

2.3 Silicon-core fibres

2.3.1 Fabrication

Silicon core fibres can be fabricated in one of two ways: high pressure chemical vapour deposition (HPCVD) or the molten core drawing (MCD) method.

In HPCVD, layers of silicon are deposited inside a silica capillary [25]. A mixture of silane and helium is forced through this capillary at a high pressure (of $\sim$ 35 MPa) and a temperature of 400 – 500°C. The material is deposited in an amorphous state and thus bonds smoothly to the silica walls, which means the roughness at the interface is as low as the silica walls, which are very smooth. The fibre can then be used with the silicon left in its amorphous state (a-Si). If hydrogen is added to the original deposition mixture, it saturates the dangling bonds in the silicon, producing hydrogenated amorphous silicon (a-Si:H) which has a reduced optical loss. Alternatively, it can be subsequently annealed at a much higher temperature of 1325°C in order to produce a p-Si core.

The MCD method [26] is essentially the process used to draw SMFs and thus is much more versatile than CVD, which can be very slow, limiting the reasonably obtainable lengths. In the MCD method, a rod of the core material (in this case silicon) is sleeved inside a silica cladding tube, which is coated with a thin layer of calcium oxide (CaO). The complete structure is then fed into a drawing tower at a temperature of 1950 °C, melting core and cladding, and the resulting fibre is then drawn down from the tower at a rate of 2.7 m/min [27]. The CaO interface layer prevents oxygen transfer from the silica to the silicon and reduces the stress between these materials during the process of heating them to such high temperatures, following

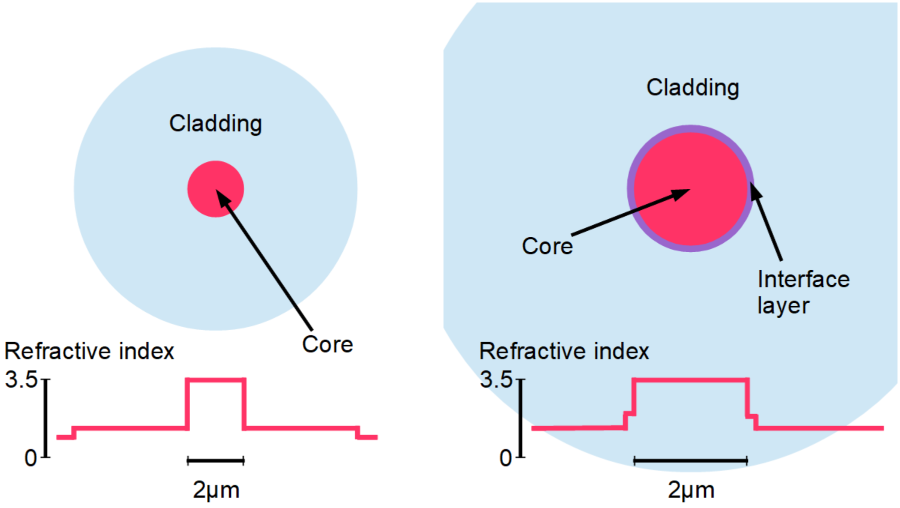

(a)

(b)

FIGURE 2.2: (a) Refractive index profile of a step index silicon-core fibre fabricated with the HPCVD method. The core has diameter 2 µm and the cladding 10 µm. Note that the refractive index outside the cladding is that of air (1). (b) Profile of a silicon-core fibre fabricated with the MCD method, which includes a CaO interface layer between core and cladding.

which the core crystallises upon cooling [28]. The resulting fibre is very thick (with core diameters of 60 – 120 µm) and so is characterised as 'cane'. It can then subsequently be tapered down to a usable core size of 1 – 3 µm by heating it and pulling it.

2.3.2 Fibre structure

In this study, I investigate Si-core fibres fabricated via the two different methods, a-Si:H as produced by HPCVD, and p-Si, as produced by MCD, which approaches c-Si when it is heated again in order to taper the core longitudinally and subsequently recrystallises.

Figure 2.2 shows the refractive index profile of the two types of fibre: (a) shows a fibre fabricated using HPCVD, such that there is no gap between core and cladding. (b) shows a fibre fabricated using MCD, with the CaO interface layer between the core and cladding. This interface layer has a composition of roughly 50% CaO and 50% SiO_2, and thus its refractive index depends on both. For the purposes of this chapter I talk about calculating the propagation constant for the simple step-index case only (ignoring the CaO layer), but for my simulations of p-Si and c-Si fibres I use a finite-difference model (in Comsol, a commercially-available package) to do this calculation which takes the interface layer into account.

Due to the refractive index change between core and cladding, light is guided in the same way as standard fibres, i.e. by total internal reflection.

2.3.3 Tapering

The design work carried out in this thesis is based on the principle that silicon core fibres, like other types of fibre, can be tapered. This can be for the purposes of decreasing the core diameter to create tighter mode confinement and thus higher nonlinearity, changing the mode size to couple to a different fibre or waveguide, or for controlling the dispersion parameters along the length. This latter purpose will be the main focus of this thesis, as the tapered fibre and waveguide designs studied in later chapters are designed to access different phase-matching conditions as the light propagates through them.

Silicon core fibres can be tapered by feeding them through a fusion splicer, as shown in Fig. 2.3, which heats the silicon to above its melting point of 1410°C [29]. This does not melt the silica cladding, but it does soften it, and the fibre can then be pulled at a rate of $\sim 100\,\mu\mathrm{m}$ / s. The exact rate can be varied to produce different waist sizes and taper transition lengths as required.

The silicon crystallises as it cools, forming larger grain sizes such that it approaches c-Si. As mentioned previously, in-diffusion of oxygen from the silica cladding to the silicon core is prevented by the CaO interface layer, which also acts to reduce tensile stress between the two materials during drawing and subsequent tapering processes as they have different melting points [30].

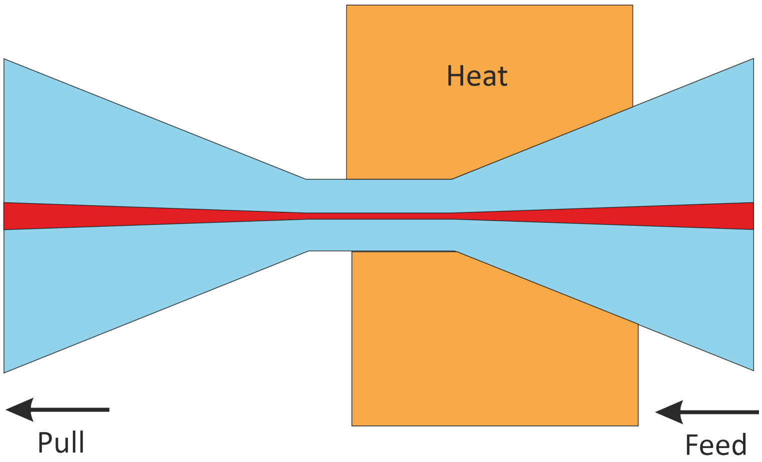

FIGURE 2.3: Tapering of a silicon core fibre by feeding it into a heated zone it and then pulling it through.

2.3.4 Ridge Waveguides

The majority of this thesis is concerned with silicon-core fibres, but ridge waveguides are also considered as a point of comparison. These are silicon on insulator (SOI) waveguides, which have a rectangular structure as shown in Fig. 2.4.

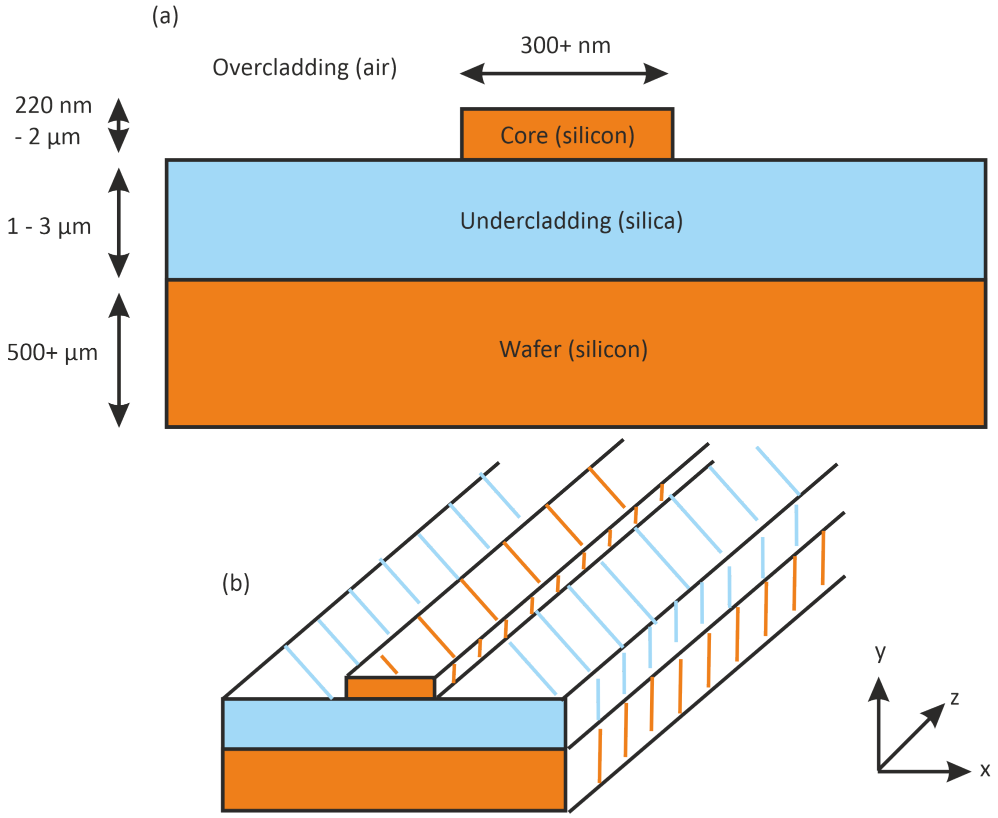

FIGURE 2.4: Structure of SOI ridge waveguides. (a) Cross section. (b) Three-dimensional view.

As shown in Fig. 2.4, the thickness of typical SOI waveguide cores is 220 nm. These are designed for telecoms wavelengths (∼ 1.55 µm) rather than longer wavelengths in the mid-IR. However, the thickness can be increased up to 2 µm to support these.

There are a number of ways of creating a SOI wafer. One of the most common is separation by implantation of oxygen (SIMOX) [31]. In this process, oxygen is implanted into the top of the silicon wafer. This is done by electrostatically accelerating oxygen ions and directing them into the wafer, where they form a buried oxide (BOX) layer. The wafer is subsequently annealed at a temperature of ∼ 1350 °C. As a result, a layer of silicon dioxide (silica) is formed which acts as an insulator, or cladding for the purposes of waveguides.

The waveguides are then formed by using lithography to remove the excess silicon from the top layer to leave rectangular strips. These are generally called nanophotonic waveguides and have a width of 300 – 500 nm [32]. However, this width can be increased arbitrarily and ridge waveguides, such as the ones studied in Chapter 8, can have widths > 1 µm.

Unlike silicon-core fibres, which have very smooth boundaries between core and cladding, SOI waveguides have rough sidewalls, which can cause scattering of the light propagating through them, which is a source of loss. I will cover this in more detail in Section 8.1.1 when I focus on ridge waveguides for the purposes of comparison with silicon-core fibres.

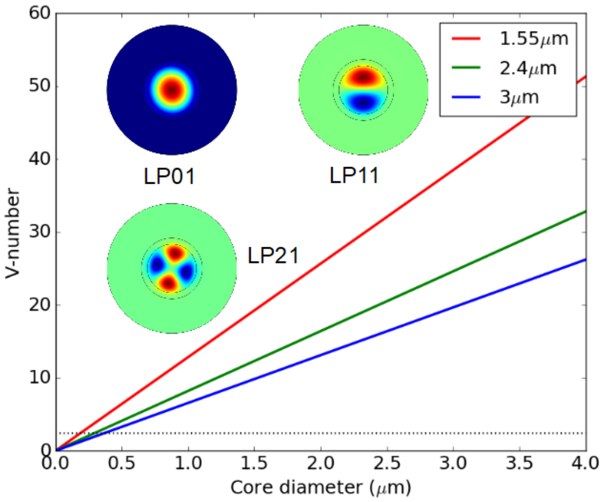

FIGURE 2.5: V-number vs core diameter for 3 wavelengths, as labelled. The horizontal dashed line shows the single-mode cut-off condition, V = 2.405. The inset images are some of the first linearly polarised mode field profiles generated in Comsol.

2.4 Modal confinement

Due to the boundary conditions between the core and cladding in a step-index fibre (i.e., H_z and E_θ should be continuous), there are only certain allowed distributions of the electric field in a fibre, in terms of its polarisation. Those distributions that maintain their shape during propagation are called modes (as opposed to superpositions of modes, which do not). There are usually a number of modes supported by a fibre, depending on its diameter and the carrier frequency of the electric field. To determine how many, a concept called the V-number is introduced [20]: $V = k_0 a\sqrt{n_1^2 - n_0^2}$ where a is the fibre radius and n_1 and n_0 are the core and cladding refractive indices respectively (given by the Sellemeier equations for silicon [22] and silica [33]). Fig. 2.5 shows how the V-number of silicon fibres changes with diameter for 3 different wavelengths, 1.55, 2.4 and 3 µm.

When $V < 2.405$, the fibre only supports one mode, the fundamental mode. As the graph shows, however, this cut-off point occurs for extremely small core diameters of between 0.19 and 0.37 µm, so the fibres that are studied in this thesis, which have core diameters ranging from 0.9 to 5.7 µm, are technically multimode fibres. However, for the simulations contained herein it is assumed that the pulses are propagating only in the fundamental mode. In [34] it was shown that by careful coupling of the light into a a-Si:H fibre with 5.7 µm core diameter, > 98% of it can be contained in the fundamental mode, despite the fact that such a large core can support thousands of modes. I recreate the simulation that shows this in Section 4.2 which is the only time I explicitly include higher-order modes.

To calculate the propagation constant β the eigenvalue equation for the fundamental (HE_{11}) mode is used [35]:

$$\left\{ \frac{J_1'(u)}{uJ_1(u)} + \frac{K_1'(w)}{wK_1(w)} \right\} \left\{ \frac{J_1'(u)}{uJ_1(u)} + \frac{n_0^2 K_1'(w)}{n_1^2 wK_1(w)} \right\} = \left(\frac{\beta}{kn_1} \right)^2 \left(\frac{V}{uw} \right)^4 \tag{2.5}$$

where J_1 and K_1 are Bessel functions of order 1 and $'$ denotes a derivative (e.g. $J_1'(u) = \mathrm{d}J_1/\mathrm{d}u$), $u = a\sqrt{k_0^2 n_1^2 - \beta^2}$, $w = a\sqrt{\beta^2 - k_0^2 n_0^2}$.

The propagation constant can be written as a Taylor series [20]:

$$\beta(\omega) = \beta_0 + \beta_1(\omega - \omega_0) + \frac{\beta_2}{2!}(\omega - \omega_0)^2 + \frac{\beta_3}{3!}(\omega - \omega_0)^3 + ... \tag{2.6}$$

where $\beta_0 = \beta(\omega_0)$ and $\beta_n = \mathrm{d}^n\beta/\mathrm{d}\omega^n$ at $\omega = \omega_0$.

$\beta(\omega)$ determines the rate of phase change of ω due to its propagation distance (see Section 2.6). 1 / β_1 is the group velocity, v_g of the carrier frequency. Although the other frequencies in a pulse have different propagation constants, they group around the carrier, so that the pulse as a whole travels at v_g. The spread of these phase velocities in the pulse is governed by β_2, the group velocity dispersion (GVD) term, and generally the most important term for describing pulse dynamics. Generally, a waveguide is characterised by its dispersion profile, and Figure 2.6 shows the GVD across a range of wavelengths that I calculated by solving Eq. (2.5) and differentiating it twice for 3 different silicon fibre core diameters. Finally, β_3 is the third order dispersion (TOD) parameter, which can be treated as a perturbation on β_2. Of course there are an infinite series of higher-order dispersion terms, and the number needed depends on how wide the spectrum is around the carrier (or pump) wavelength (i.e. the broader the spectrum, the more terms are typically required).

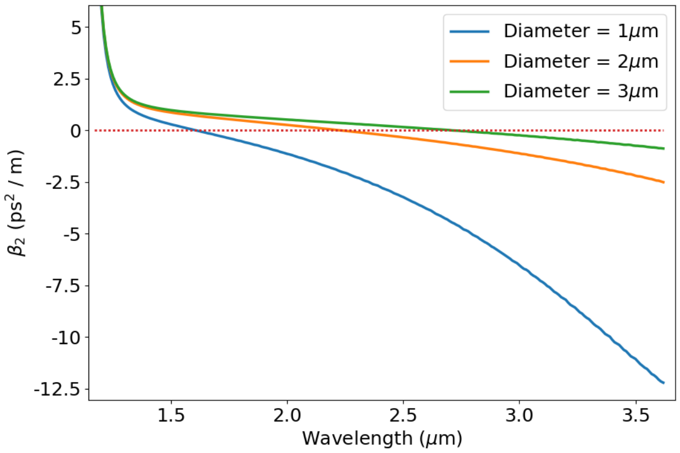

FIGURE 2.6: The dispersion profile of 3 silicon fibres of labelled diameters

The modal fields are then given by [36]:

$$E_x = -jA\beta\frac{a}{u}\left[\frac{(1-s)}{2}J_0\left(\frac{u}{a}r\right)\cos(\phi) - \frac{(1+s)}{2}J_2\left(\frac{u}{a}r\right)\cos(2\theta+\phi)\right] \tag{2.7}$$

$$E_y = jA\beta\frac{a}{u}\left[\frac{(1-s)}{2}J_0\left(\frac{u}{a}r\right)\sin(\phi) + \frac{(1+s)}{2}J_2\left(\frac{u}{a}r\right)\sin(2\theta+\phi)\right] \tag{2.8}$$

$$E_z = AJ_1\left(\frac{u}{a}r\right)\cos(\theta+\phi) \tag{2.9}$$

in the core and:

$$E_x = -jA\beta \frac{aJ_1(u)}{wK_1(w)} \left[\frac{(1-s)}{2} K_0 \left(\frac{w}{a} r \right) \cos(\phi) + \frac{(1+s)}{2} K_2 \left(\frac{w}{a} r \right) \cos(2\theta + \phi) \right] \tag{2.10}$$

$$E_y = jA\beta \frac{aJ_1(u)}{wK_1(w)} \left[\frac{(1-s)}{2} K_0 \left(\frac{w}{a} r \right) \sin(\phi) - \frac{(1+s)}{2} K_2 \left(\frac{w}{a} r \right) \sin(2\theta + \phi) \right] \tag{2.11}$$

$$E_z = A \frac{J_1(u)}{K_1(w)} K_1 \left(\frac{w}{a} r \right) \cos(\theta + \phi) \tag{2.12}$$

in the cladding, where A is the field amplitude, J_n and K_n are Bessel functions of order n, $J'(n)$ and $K'(n)$ are their derivatives,

$$s = \frac{n \left(\frac{1}{u^2} + \frac{1}{w^2} \right)}{\left[\frac{J_n'(u)}{uJ_n(u)} + \frac{K_n'(w)}{wK_n(w)} \right]} \tag{2.13}$$

and $s_1 = \beta^2/(k^2 n_1^2)s$, $s_0 = \beta^2/(k^2 n_0^2)s$.

The LP01 (fundamental) and two of the higher-order modes (LP11 and LP21) are shown in Fig. 2.5. Note that LP01 mode is a scalar approximation to the fully-vectorial HE11 mode defined by the above equations, which is valid in the weakly guiding limit as discussed in Section 2.5.

This means that the electric field polarisation is assumed to be strictly perpendicular to the direction of the propagation. This means that $E_z = 0$ and the polarisation is all in the E_t-direction, where t is transverse (i.e. in the x,y plane). Thus, $E_z/E_t = 0$. In reality, it is small but nonzero, and grows as the wavelength increases and becomes comparable to the waveguide dimensions. This has an effect on the strength of the nonlinear interaction, which will be examined further in Sec. 2.5.3.

Furthermore, the assumption of linear polarisation means that the direction is constant in the transverse plane. In fact, this is used in the derivation of the Nonlinear Schrödinger Equation (Sec. 2.5.1), in which x is defined as the direction of polarisation.

To check how good this assumption is, it is instructive to look at the electric field as calculated by Comsol and in particular the ratio of E_x/E_y or vice versa. The polarisation direction in Comsol is arbitrary (due to circular symmetry) and so both field-components will have some distribution. The ratio shows how much the polarisation varies from its average direction.

Fig. 2.7 shows the fundamental mode for four wavelengths in a silicon-core fibre, with core diameter of 1700 nm, from 2.1 – 5.5 µm. The left plots show the modulus of the field, which can be seen to become increasingly distorted as the wavelength increases, spilling out of the core. The field strength also decreases to about a quarter over the wavelength range, showing that the longer wavelengths are poorly guided. This is to be expected due to the size of the wavelength relative to the core dimension, and in the fibre tapers simulated later on, the core size is generally doubled to facilitate the generation of these longer wavelengths. The middle pair of plots shows the E_y and E_x field respectively, and these become correspondingly distorted. Interestingly, the E_x field seems to lose its shape entirely. Nonetheless, the ratio of E_y/E_y remains fairly constant throughout, becoming seemingly less pronounced at longer wavelengths, but this is more due to the weakening of the field-strength and spillage into the cladding. The maximum ratio is 10 in these plots. It is most appararent in the top mode where the field is strongest, but still only occurs at the

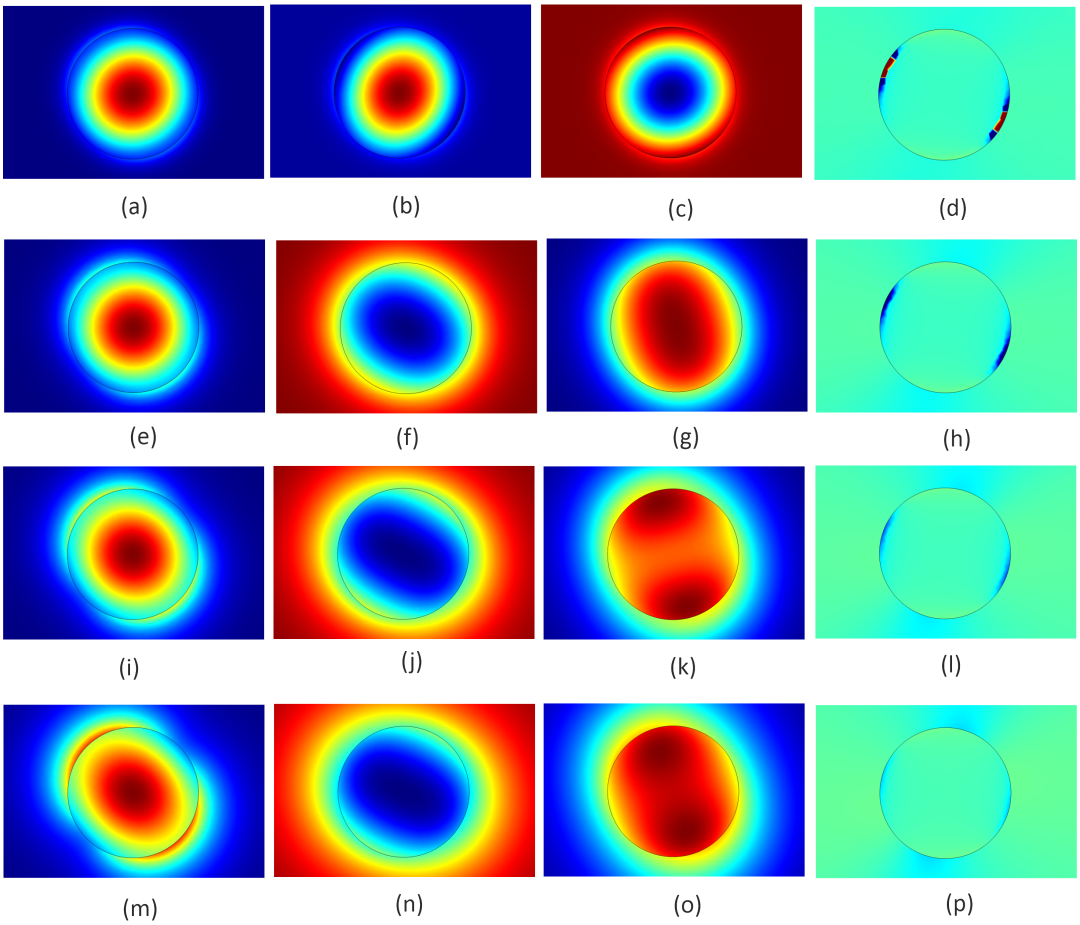

FIGURE 2.7: Electric field polarisation for the fundamental mode in a silicon-core fibre with diameter of 1700 nm. Left-right: electric field norm, x-polarisation, y-polarisation, ratio of y-polarisation / x-polarisation (colour scale is ±10). Fundamental mode wavelengths are (a) – (d): 2.1 µm, (e) – (h): 3.5 µm, (i) – (l): 4.5 µm and (m) – (p): 5.5 µm.

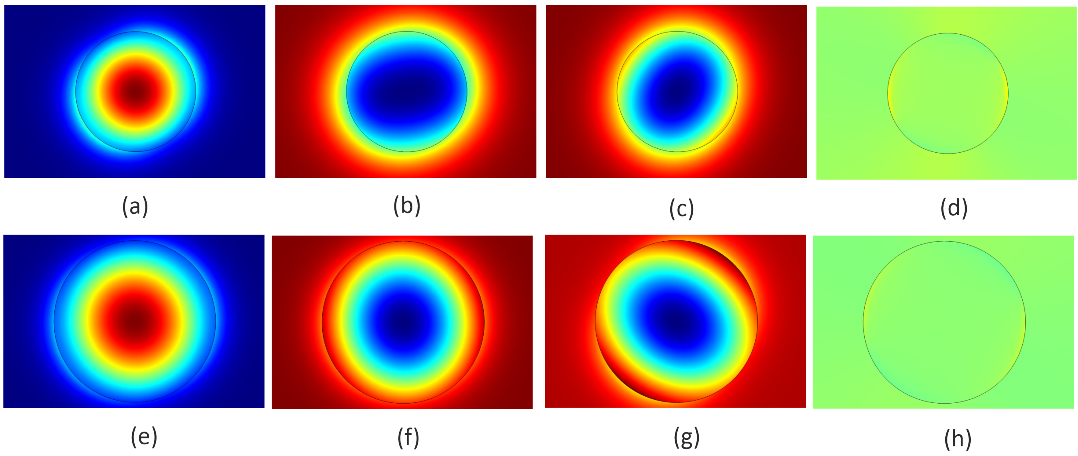

FIGURE 2.8: Electric field polarisation for the fundamental mode at a wavelength of 5.5 µm in silicon-core fibres with diameters of (a) – (d): 2600 nm and (e) – (h): 3500 nm. Left-right: electric field norm, x-polarisation, y-polarisation, ratio of y-polarisation / x-polarisation (colour scale is ±10).

core-cladding interface. This is a good indication that the mode is indeed mostly linearly-polarised.

Fig. 2.8 (top row) shows the mode at 5.5 µm in a silicon-core fibre with 2600 nm diameter as a point of contrast, which is much less distorted and appears mostly linear. The field strength is 40% that of the 2.1 µm mode in the 1700 nm. Actually, for generating wavelengths beyond 4.5 µm in the taper designs, diameters of > 3500 nm are used, which support such wavelengths much more comfortably (as shown in the bottom row).

2.4.1 Ridge waveguide modes

The majority of this thesis is concerned with silicon-core fibres, but silicon-on-insulator (SOI) ridge waveguides are also considered, which have a rectangular cross-section, a silica undercladding and air overcladding.

The equations are omitted here for brevity, and modes are solved using a finite difference method in Comsol. The important thing to note is that the rectangular shape means there two distinct directions for polarisation of the electric and magnetic fields. This leads to two categories of modes, transverse electric (TE) and transverse magnetic (TM) modes. These have different propagation constants and effective areas. These are shown in Fig. 2.9.

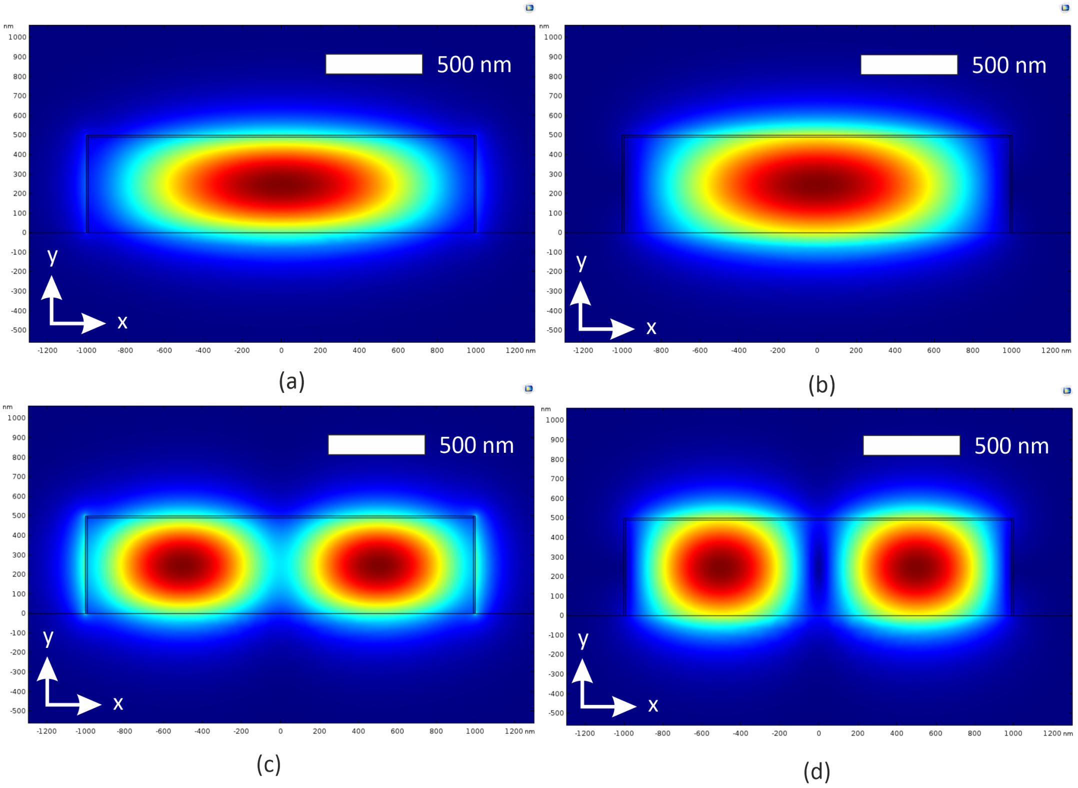

FIGURE 2.9: Fundamental modes in a 500 x 2000 nm SOI ridge waveguide at 2.1 µm. (a) Electric field (norm) of TE mode, with $n_{\text{eff}} = 3.08$, (b) magnetic field (norm) of TE mode, (c) electric field (norm) of TM mode, with $n_{\text{eff}} = 2.94$, and (d) magnetic field (norm) of TM mode.

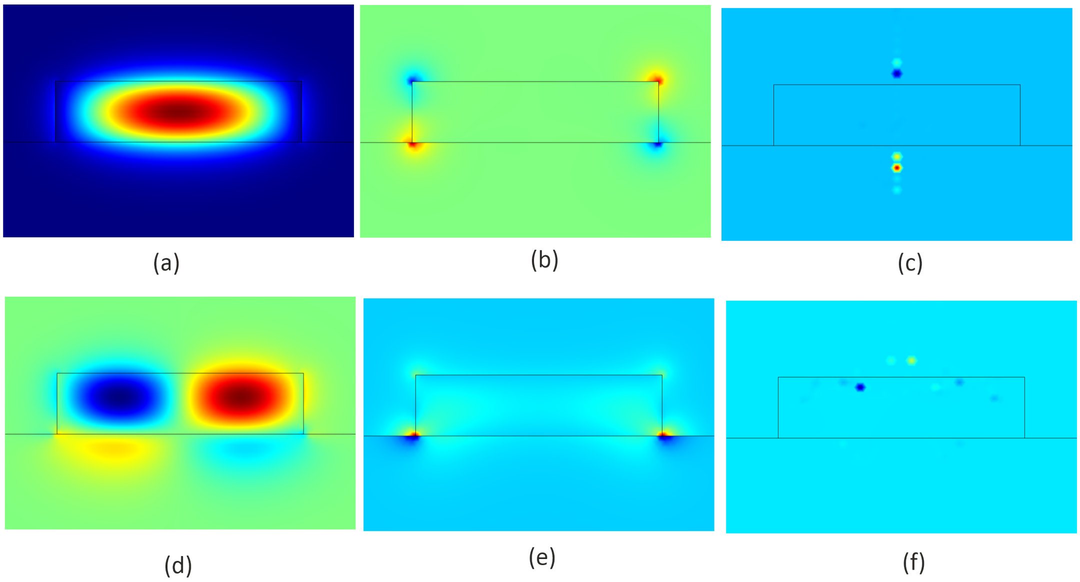

FIGURE 2.10: Fundamental modes in a 500 x 2000 nm SOI ridge waveguide at 2.1 µm. (a) Electric field (x-component, E_x) of TE mode, (b) Electric field (y-component, E_y) of TE mode, (c) Ratio of E_x/E_y for TE mode, (d) Electric field (x-component, E_x) of TM mode, (e) Electric field (y-component, E_y) of TM mode, (f) Ratio of E_x/E_y for TM mode.

Fig. 2.10 shows that despite the small thickness of the ridge waveguide relative to the wavelength, the majority of the electric field is polarised in the x-direction with the y-components confined to the corners of the waveguide. This is most likely because the width of the waveguide is much closer to the wavelength. The ratio of E_x/E_y shows that for the TE-mode, the polarisation is indeed linear across the waveguide, with the exception of small artifacts in the silica under-cladding and air over-cladding, which may be due to the mesh settings. In the TM-mode, there is a more noticeable y-component to the field, and thus some of the artifacts in the ratio appear in the waveguide core.

Nonetheless, the TE mode is preferred for nonlinear optics as the nonlinear interaction is stronger. This means that coupling light in to a ridge waveguide is harder as the polarisation needs to be matched, unlike with a fibre where the circular symmetry means that the fundamental mode is polarisation-independent.

2.4.2 Vector vs scalar modes

The above discussion has assumed that the electric fields confined within the waveguides are perpendicularly polarised i.e. there is no z-component (where z is the direction of propagation). In reality, there is a z-component that increases with wavelength and becomes non-trivial when the wavelength is comparable with the waveguide dimensions. As a result, the nonlinear effect on the light will increase, however the amount of propagating power, proportional to the Poynting vector (which in turn is proportional to the amount of light polarised in the transverse direction) will decrease. This will be discussed further in Sec. 2.5.3.

2.5 The Generalised Nonlinear Schrödinger Equation

Pulse propagation is modelled by using the generalised nonlinear Schrödinger equation (GNLSE). This is adapted from the NLSE derived for silica fibres, which can be extended for other materials. In the case of silicon, this means adding nonlinear absorption (TPA, 3PA etc) and free carrier absorption.

2.5.1 Derivation

We start with Maxwell's Equations:

$$\nabla \times \mathbf{E} = -\frac{\partial \mathbf{B}}{\partial t} \tag{2.14}$$

$$\nabla \times \mathbf{H} = \mathbf{J} + \frac{\partial \mathbf{D}}{\partial t} \tag{2.15}$$

$$\nabla \cdot \mathbf{D} = \rho_f \tag{2.16}$$

$$\nabla \cdot \mathbf{B} = 0 \tag{2.17}$$

where $\mathbf{E}$ and $\mathbf{H}$ are the electric and magnetic field vectors, $\mathbf{D}$ and $\mathbf{B}$ are the electric and magnetic flux densities, and $\mathbf{J}$ and ρ_f are the current and charge densities respectively. As there are no free charges in an optical fibre, these last two densities are zero.

We can also use the following two constitutive relations given in [20]:

$$\mathbf{D} = \epsilon_0 \mathbf{E} + \mathbf{P} \tag{2.18}$$

$$\mathbf{B} = \mu_0 \mathbf{H} + \mathbf{M} \tag{2.19}$$

where ϵ_0 is the vacuum permittivity, μ_0 is the vacuum permeability, and $\mathbf{P}$ and $\mathbf{M}$ are the electric and magnetic polarisations, the latter of which is also zero as a fibre is a non-magnetic medium.

We can then eliminate $\mathbf{B}$ and $\mathbf{D}$ as follows. First, take the curl of both sides of Eq. (2.14), substituting $\mathbf{B} = \mu_0 \mathbf{H}$ as we go:

$$\begin{aligned} \nabla \times \nabla \times \mathbf{E} &= \nabla \times \left(-\frac{\partial \mathbf{B}}{\partial t} \right) \\ &= -\frac{\partial}{\partial t} \left(\nabla \times \mu_0 \mathbf{H} \right) \\ &= -\mu_0 \frac{\partial}{\partial t} \left(\nabla \times \frac{\partial \mathbf{D}}{\partial t} \right) \\ &= -\mu_0 \frac{\partial}{\partial t} \left(\epsilon_0 \frac{\partial \mathbf{E}}{\partial t} + \frac{\partial \mathbf{P}}{\partial t} \right) \\ &= -\mu_0 \epsilon_0 \frac{\partial^2 \mathbf{E}}{\partial t^2} - \mu_0 \frac{\partial^2 \mathbf{P}}{\partial t^2} \end{aligned}$$

Now we can just substitute $\epsilon_0 \mu_0 = 1/c^2$ and we get:

$$\nabla \times \nabla \times \mathbf{E} = -\frac{1}{c^2} \frac{\partial^2 \mathbf{E}}{\partial t^2} - \mu_0 \frac{\partial^2 \mathbf{P}}{\partial t^2} \tag{2.20}$$

The electric polarisation $\mathbf{P}$ can be split into linear and nonlinear components $\mathbf{P_L}$ and $\mathbf{P_{NL}}$. As mentioned in Sec. 2.7, these are governed by the optical susceptibility tensor χ, which can be split up into different orders, $\chi^{(1)}$ which governs the linear response, $\chi^{(2)}$ which only applies to non-symmetric crystals and so is zero for silica and silicon, and $\chi^{(3)}$ which is the lowest-order nonlinear response and as such the dominant one (higher orders are negligible and can be ignored). $\mathbf{P_L}$ and $\mathbf{P_{NL}}$ are related to $\chi^{(1)}$ and $\chi^{(3)}$ as follows:

$$\mathbf{P_L}(\mathbf{r}, t) = \epsilon_0 \int_{-\infty}^{t} \chi^{(1)}(t - t') \cdot \mathbf{E}(\mathbf{r}, t') \mathrm{d}t' \tag{2.21}$$

$$\begin{aligned} \mathbf{P_{NL}}(\mathbf{r}, t) &= \epsilon_0 \int_{-\infty}^{t} \mathrm{d}t_1 \int_{-\infty}^{t} \mathrm{d}t_2 \int_{-\infty}^{t} \mathrm{d}t_3 \\ &\times \chi^{(3)}(t - t_1, t - t_2, t - t_3) \vdots \mathbf{E}(\mathbf{r}, t_1) \mathbf{E}(\mathbf{r}, t_2) \mathbf{E}(\mathbf{r}, t_3) \end{aligned} \tag{2.22}$$

We can make the assumption that $\mathbf{P_{NL}}$ can be added as a perturbation later, such that we can just deal with the linear part. This can be done by Fourier transforming both sides of Eq. (2.20). To apply this to $\mathbf{P_L}$, we use the convolution theorem Eq. (2.4). As such,

$$\tilde{\mathbf{P_L}} = \epsilon_0 \tilde{\chi}^{(1)}(\omega) \cdot \tilde{\mathbf{E}} \tag{2.23}$$

and Eq. (2.20) becomes:

$$\nabla \times \nabla \times \tilde{\mathbf{E}} = -\frac{1}{c^2}\frac{\partial^2 \tilde{\mathbf{E}}}{\partial t^2} - \epsilon_0 \mu_0 \frac{\partial^2 \tilde{\chi}^{(1)}(\omega) \cdot \tilde{\mathbf{E}}}{\partial t^2} \tag{2.24}$$

The Fourier transform is defined as in Eq. (2.1).

So, using $\partial \tilde{\mathbf{E}}/\partial t = \mathrm{i}\omega \tilde{\mathbf{E}}$, Eq. (2.24) simplifies to:

$$\nabla \times \nabla \times \tilde{\mathbf{E}}(\mathbf{r}, \omega) = \epsilon(\omega)\frac{\omega^2}{c^2}\tilde{\mathbf{E}}(\mathbf{r}, \omega) \tag{2.25}$$

where $\epsilon(\omega) = 1 + \tilde{\chi}^{(1)}(\omega)$ is the frequency-dependent dielectric constant. This can be related to the refractive index $n(\omega)$ and the absorption coefficient $\alpha(\omega)$ by using $\epsilon = (n + \mathrm{i}\alpha c/2\omega)^2$. The absorption is assumed to be small and can thus be neglected, giving the approximation $\epsilon \approx n^2$.

We can simplify the LHS of Eq. (2.20) by subsitituting Eq. (2.23) into Eq. (2.18) and using $\tilde{\chi}^{(1)} \approx n^2 - 1$:

$$\begin{aligned}
\nabla \cdot \tilde{\mathbf{D}} &\approx \epsilon_0 \nabla \cdot \tilde{\mathbf{E}} + \nabla \cdot \tilde{\mathbf{P}_\mathbf{L}} \\
&\approx \epsilon_0 \nabla \cdot \tilde{\mathbf{E}} + \epsilon_0 (n^2 - 1)\nabla \tilde{\mathbf{E}} \\
&= \epsilon_0 (1 + n^2 - 1)\nabla \cdot \tilde{\mathbf{E}} \\
&= n^2 \epsilon_0 \nabla \cdot \tilde{\mathbf{E}} = 0
\end{aligned}$$

As $n^2 > 0$ and $\epsilon_0 > 0$, $\nabla \cdot \tilde{\mathbf{E}} = 0$ and thus $\nabla \cdot \mathbf{E} = 0$. The following relation can thus be used:

$$\nabla \times \nabla \times \mathbf{E} \equiv \nabla(\nabla \cdot \mathbf{E}) - \nabla^2 \mathbf{E} = -\nabla^2 \mathbf{E} \tag{2.26}$$

and now Eq. (2.20) becomes:

$$\nabla^2 \mathbf{E} - \frac{1}{c^2}\frac{\partial^2 \mathbf{E}}{\partial t^2} = \mu_0 \frac{\partial^2 \mathbf{P_L}}{\partial t^2} + \mu_0 \frac{\partial^2 \mathbf{P_{NL}}}{\partial t^2} \tag{2.27}$$

in which $\mathbf{P_{NL}}$ is included. It will nonetheless be treated as a small purturbation when solving Eq. (2.27). Other simplifying assumptions used are that optical field maintains its polarisation during propagation, and that the field can be assumed to be quasi-monochromatic (i.e. its bandwidth is much smaller than the carrier frequency). These assumptions are valid for silica fibres and become less so for silicon, but in practice the resulting equation still works well.

As mentioned in Sec. 2.6, the slowly varying approximation is used, so the electric field and polarisation can be written as follows:

$$\mathbf{E}(\mathbf{r}, t) = \frac{1}{2}\hat{x}[E(\mathbf{r}, t)\exp(-\mathrm{i}\omega_0 t) + \text{c.c.}] \tag{2.28}$$

$$\mathbf{P_L}(\mathbf{r}, t) = \frac{1}{2}\hat{x}[P_L(\mathbf{r}, t)\exp(-\mathrm{i}\omega_0 t) + \text{c.c.}] \tag{2.29}$$

$$\mathbf{P_{NL}}(\mathbf{r}, t) = \frac{1}{2}\hat{x}[P_{NL}(\mathbf{r}, t)\exp(-\mathrm{i}\omega_0 t) + \text{c.c.}] \tag{2.30}$$

We can subsitite Eqs. (2.28) and (2.29) into Eq. (2.21) to give:

$$\begin{aligned}
\frac{1}{2}\hat{x}[P_L(\mathbf{r},t)\exp(-\mathrm{i}\omega_0 t)+\text{c.c.}] &= \epsilon_0\int_{-\infty}^{\infty}\chi^{(1)}(t-t')\cdot\frac{1}{2}\hat{x}[E(\mathbf{r},t')\exp(-\mathrm{i}\omega_0 t)+\text{c.c.}]\mathrm{d}t' \\
\implies P_L(\mathbf{r},t) &= \epsilon_0\int_{-\infty}^{\infty}\chi^{(1)}(t-t')\cdot E(\mathbf{r},t')\exp(-\mathrm{i}\omega_0 t')\exp(\mathrm{i}\omega_0 t)\mathrm{d}t' \\
&= \epsilon_0\int_{-\infty}^{\infty}\chi^{(1)}(t-t')\cdot E(\mathbf{r},t')\exp[\mathrm{i}\omega_0(t-t')]\mathrm{d}t'
\end{aligned}$$

It would be more useful if the integral was in the frequency domain rather than the time domain, which can be achieved by Fourier transforming and then inverse-transforming the RHS, using the convolution theorem Eq. (2.4) in the first step with:

$$\begin{aligned}
P_L(\mathbf{r},t) &= \epsilon_0 u(t) \\
\text{where } u(t) &= (f*g)(t), \\
f(t-t') &= \chi^{(1)}(t-t'), \\
g(t') &= E(\mathbf{r},t')\exp[\mathrm{i}\omega_0(t-t')]
\end{aligned}$$

Now we can apply the theorem:

$$\begin{aligned}
\tilde{u}(\omega) &= \tilde{f}(\omega)\cdot\tilde{g}(\omega) \\
&= \tilde{\chi}^{(1)}(\omega)\cdot\tilde{g}(\omega) \\
&= \tilde{\chi}^{(1)}(\omega)\int_{-\infty}^{\infty}E(\mathbf{r},t')\exp[\mathrm{i}\omega_0(t-t')]\exp(\mathrm{i}\omega t')\mathrm{d}t' \\
&= \tilde{\chi}^{(1)}(\omega)\int_{-\infty}^{\infty}E(\mathbf{r},t')\exp[\mathrm{i}(\omega-\omega_0)t']\exp(\mathrm{i}\omega_0 t)\mathrm{d}t' \\
&= \tilde{\chi}^{(1)}(\omega)\tilde{E}(\mathbf{r},\omega-\omega_0)\exp(\mathrm{i}\omega_0 t) \qquad (2.31)
\end{aligned}$$

Finally, we apply an inverse Fourier transform such that:

$$\begin{aligned}
P_L(\mathbf{r},t) &= \epsilon_0\mathcal{F}^{-1}\{\tilde{u}(\omega)\} \\
&= \frac{\epsilon_0}{2\pi}\int_{-\infty}^{\infty}\tilde{\chi}^{(1)}(\omega)\tilde{E}(\mathbf{r},\omega-\omega_0)\exp(\mathrm{i}\omega_0 t)\exp(-\mathrm{i}\omega t)\mathrm{d}\omega \\
&= \frac{\epsilon_0}{2\pi}\int_{-\infty}^{\infty}\tilde{\chi}^{(1)}(\omega)\tilde{E}(\mathbf{r},\omega-\omega_0)\exp[-\mathrm{i}(\omega-\omega_0)t]\mathrm{d}\omega \qquad (2.32)
\end{aligned}$$

To solve for $\mathbf{P_{NL}}(\mathbf{r},t)$, we can subsitute Eq. (2.28) into Eq. (2.22) and make the simplifying assumption that the nonlinear response is instantaneous. Thus, the time-dependent integrals can be replaced by a product of delta functions with the form $\delta(t-t_i)$ and the equation reduces to:

$$\mathbf{P_{NL}}(\mathbf{r},t) = \epsilon_0\chi^{(3)}\vdots\mathbf{E}(\mathbf{r},t)\mathbf{E}(\mathbf{r},t)\mathbf{E}(\mathbf{r},t) \qquad (2.33)$$

I write out the full solution to this in Appendix B. The result of this is:

$$P_{NL}(\mathbf{r},t) \approx \epsilon_0\epsilon_{NL}E(\mathbf{r},t) \qquad (2.34)$$

where

$$\epsilon_{NL} = \frac{3}{4}\chi^{(3)}_{xxxx}|E(\mathbf{r},t)|^2 \tag{2.35}$$

Now, we want to get Eq. (2.27) into the frequency domain, to get it into the form of the Helmholtz wave equation. To do this, we treat ϵ_{NL} as a constant (i.e. not dependent on electric field intensity), which is valid according to the slowly varying envelope approximation. We substitute in Eqs. (2.28), (2.32) and (2.34) as follows:

$$\begin{aligned} \nabla^2\tilde{E} - \frac{1}{c^2}\frac{\partial^2\tilde{E}}{\partial t^2} - \mu_0\frac{\partial^2 P_L}{\partial t^2} - \mu_0\frac{\partial^2 P_{NL}}{\partial t^2} &= 0 \\ \Longrightarrow \nabla^2\tilde{E} + \frac{\omega^2}{c^2}\tilde{E} + \mu_0\omega^2\tilde{P_L} + \mu_0\epsilon_0\epsilon_{NL}\omega^2\tilde{E} &= 0 \end{aligned} \tag{2.36}$$

To solve $\tilde{P_L}$, recall that $P_L = \epsilon_0\mathcal{F}^{-1}\{\tilde{u}(\omega)\}$ where $\tilde{u}(\omega)$ is defined as in Eq. (2.31). Thus, $\tilde{P_L} = \mathcal{F}\{\epsilon_0\mathcal{F}^{-1}\{\tilde{u}(\omega)\}\} = \epsilon_0\tilde{u}(\omega)$. We can use the definition of the Fourier transform $\tilde{E}(\mathbf{r},\omega-\omega_0)$ as follows:

$$\begin{aligned} \tilde{E}(\mathbf{r},\omega-\omega_0) &= \int_{-\infty}^{\infty} E(\mathbf{r},t)\exp(\mathrm{i}(\omega-\omega_0)t)\mathrm{d}t \\ \Longrightarrow \tilde{P_L}(\omega) &= \epsilon_0\tilde{\chi}^{(1)}(\omega)\tilde{E}(\mathbf{r},\omega-\omega_0)\exp(\mathrm{i}\omega_0 t) \\ &= \epsilon_0\tilde{\chi}^{(1)}(\omega)\int_{-\infty}^{\infty} E(\mathbf{r},t)\exp(\mathrm{i}(\omega-\omega_0)t)\mathrm{d}t\exp(\mathrm{i}\omega_0 t) \\ &= \epsilon_0\tilde{\chi}^{(1)}(\omega)\int_{-\infty}^{\infty} E(\mathbf{r},t)\exp(\mathrm{i}\omega t - \mathrm{i}\omega_0 t + \mathrm{i}\omega_0 t)\mathrm{d}t \\ &= \epsilon_0\tilde{\chi}^{(1)}(\omega)\int_{-\infty}^{\infty} E(\mathbf{r},t)\exp(\mathrm{i}\omega)t)\mathrm{d}t \\ &= \epsilon_0\tilde{\chi}^{(1)}(\omega)\tilde{E}(\mathbf{r},\omega) \end{aligned}$$

Now we can plug this value of $\tilde{P_L}(\omega)$ into Eq. (2.36) to get

$$\nabla^2\tilde{E} + \epsilon(\omega)k_0^2\tilde{E} = 0 \tag{2.37}$$

where $k_0 = \omega/c = 2\pi/\lambda$ (where λ is the free-space wavelength) and

$$\epsilon(\omega) = 1 + \tilde{\chi}^{(1)}_{xx}(\omega) + \epsilon_{NL} \tag{2.38}$$

which is defined as the nonlinear dielectric constant. This can be approximated as [20]:

$$\epsilon = (n+\Delta n)^2 \approx n^2 + 2n\Delta n \tag{2.39}$$

where Δn is a small perturbation defined as:

$$\Delta n = \bar{n}_2|E|^2 + \frac{\mathrm{i}\tilde{\alpha}}{2k_0} \tag{2.40}$$

where $\tilde{n}$ and $\tilde{\alpha}$ are the intensity-dependent nonlinear-index and absorption coefficients:

$$\tilde{n} = n + \bar{n}_2|E|^2,\ \tilde{\alpha} = \alpha + \alpha_2|E|^2 \tag{2.41}$$

In Eq. (2.41), α_2 is the TPA coefficient. $\bar{n}_2$ and α_2 relate to the real and imaginary components of $\chi^{(3)}_{xxxx}$ as follows [20]:

$$\bar{n}_2 = \frac{3}{8n}\mathrm{Re}\left(\chi^{(3)}_{xxxx}\right),\ \alpha_2 = \frac{3\omega_0}{4nc}\mathrm{Im}\left(\chi^{(3)}_{xxxx}\right) \tag{2.42}$$

We can now use separation-of-variables to split Eq. (2.37) into two parts, by using a solution of the form

$$\tilde{E}(\mathbf{r}, \omega - \omega_0) = F(x,y)\tilde{A}(z, \omega - \omega_0)\exp(\mathrm{i}\beta_0 z) \tag{2.43}$$

where $\tilde{A}(z, \omega - \omega_0)$ is a function of z that varies slowly relative to the central frequency ω_0. This is referred to as an 'envelope' function. $\beta_0 = k_0/n$ is the wavenumber inside the fibre (i.e. compressed by the refractive index). The two parts become:

$$\frac{\partial^2 F}{\partial x^2} + \frac{\partial^2 F}{\partial y^2} + \left[\epsilon(\omega)k_0^2 - \tilde{\beta}^2\right] F = 0 \tag{2.44}$$

$$\frac{\partial^2 \tilde{A}}{\partial z^2} + 2\mathrm{i}\beta_0\frac{\partial \tilde{A}}{\partial z} + \left(\tilde{\beta}^2 - \beta_0^2\right)\tilde{A} = 0 \tag{2.45}$$

where an eigenvalue $\tilde{\beta}$ is introduced which can be solved using the eigenvalue formula Eq. (2.5).

A major simplification is made in Eq. (2.45) by assuming that because the 'envelope' function $\tilde{A}(z, \omega - \omega_0)$ varies slowly relative to z, the second-derivative $\partial^2\tilde{A}/\partial z^2$ can be ignored. This is called the 'slowly varying envelope approximation' (SVEA).

Eq. (2.44) can be solved by using first-order perturbation theory [37, 20]. In the first step, $\epsilon \approx n^2$ is used, and the eigenvalue is just the wavenumber $\beta(\omega)$. Then the effects of the $2n\Delta n$ term are included, which does not affect $F(x,y)$ but adds a perturbation to the eigenvalue which becomes:

$$\tilde{\beta}(\omega) = \beta(\omega) + \Delta\beta(\omega) \tag{2.46}$$

where

$$\Delta\beta(\omega) = \frac{\omega^2 n(\omega)}{c^2\beta(\omega)}\frac{\iint_{-\infty}^{\infty}\Delta n(\omega)|F(x,y)|^2\mathrm{d}x\mathrm{d}y}{\iint_{-\infty}^{\infty}|F(x,y)|^2\mathrm{d}x\mathrm{d}y} \tag{2.47}$$

The electric field can now be written as a combination of Eqs. (2.28) and (2.43):

$$\mathbf{E}(\mathbf{r}, t) = \frac{1}{2}\left\{F(x,y)A(z,t)\exp[\mathrm{i}(\beta_0 z - \omega_0 t)] + \mathrm{c.c.}\right\} \tag{2.48}$$

Eq. (2.45) can be rearranged as follows:

$$\begin{aligned}\frac{\partial \tilde{A}}{\partial z} &= \frac{\mathrm{i}}{2\beta_0}\left(\tilde{\beta}^2 - \beta_0^2\right)\tilde{A} \\ &\approx \mathrm{i}[\beta(\omega) + \Delta\beta(\omega) - \beta_0]\tilde{A}\end{aligned} \tag{2.49}$$

in which the approximation $\tilde{\beta}^2 - \beta_0^2 \approx 2\beta_0(\tilde{\beta} - \beta_0)$ was used.

We now want to use the inverse Fourier transform to get Eq. (2.49) into the time domain. We use the Taylor series expansion Eq. (2.6) around ω_0 for both $\beta(\omega)$ and $\Delta\beta(\omega)$. The Fourier transform is carried out over $\omega - \omega_0$, and this can be replaced with the differential operator $\mathrm{i}(\partial/\partial t)$ to form:

$$\frac{\partial A}{\partial z}+\sum_{n=1}^{\infty}\frac{\mathrm{i}^{n-1}\beta_n}{n!}\frac{\partial^n A}{\partial t^n}=\mathrm{i}\Delta\beta_0 A \tag{2.50}$$

where $\Delta\beta_0 = \Delta\beta(\omega = \omega_0)$. This can be calculated using Eq. (2.47), assuming that the value of Δn is similar enough in the core and cladding that it can be taken outside the integral. It is further assumed that $F(x,y)$ does not vary over the pulse bandwidth, and the approximation $\beta(\omega) \approx n(\omega)\omega/c$ is used. We then introduce the nonlinear parameter γ, defined as:

$$\gamma(\omega_0)=\frac{\omega_0 n_2}{cA_{\text{eff}}},\; n_2=\frac{2\bar{n}_2}{\epsilon_0 nc} \tag{2.51}$$

where A_{eff} is the effective area of the mode:

$$A_{\text{eff}}=\frac{(\iint_{-\infty}^{\infty}|F(x,y)|^2\mathrm{d}x\mathrm{d}y)^2}{\iint_{-\infty}^{\infty}|F(x,y)|^4\mathrm{d}x\mathrm{d}y} \tag{2.52}$$

where $F(x,y)$ is given by Eqs. (2.7) and (2.8) in the core and Eqs. (2.10) and (2.11) in the cladding. The effective area is a measure of how strongly confined the mode is in the fibre, and is generally smaller than the fibre core area. A smaller effective area means a higher intensity of light, and thus a stronger Kerr nonlinearity. For silicon fibres, due to the high index contrast, as the core diameter gets smaller, the z-component of the field becomes non-negligible, so the effective area (defined by its transverse components) is smaller than if the two-dimensional field approximation as given in [20] (Eqs 2.2.12 and 2.2.13) is used. At a small enough diameter ($<$ 0.4 µm), the effective area diverges even further from the overlap integral (Eq. 2.52), as the vectorial nature of the fields and the variation of n_2 between core and cladding have to be fully accounted for [11]. However, the smallest diameter of fibre studied in this thesis is 0.9 µm, which justifies the use of Eq. (2.52).

In Sec. 2.5.3 I calculate the effective area in Comsol for a number of diameters and wavelengths using the full vectorial equation and compare this to the scalar effective area.

Eq. (2.50) can now be written as follows:

$$\frac{\partial A(z,t)}{\partial z}=i\sum_{n=1}^{\infty}\frac{i^n\beta_n}{n!}\frac{\partial^n A}{\partial t^n}+i\gamma(\omega_0)\left|A(z,t)\right|^2 A(z,t)-\frac{\alpha}{2}A(z,t) \tag{2.53}$$

This is the GNLSE as used for silica, in which TPA is negligible, and so the approximation $\bar{\alpha} \approx \alpha$ was used. For silicon, the $\alpha_2|E|^2$ term needs to be reintroduced. We can write out Δn to include it explicitly:

$$\begin{aligned}\Delta n &= \bar{n}_2|E|^2+\frac{\mathrm{i}\alpha}{2k_0}+\frac{\mathrm{i}\alpha_2}{2k_0}|E|^2\\ &= \left(\bar{n}_2+\frac{\mathrm{i}\alpha_2}{2k_0}\right)|E|^2+\frac{\mathrm{i}\alpha}{2k_0}\end{aligned} \tag{2.54}$$

This means that n_2 would become:

$$
\begin{aligned}
n_{2s} &= \frac{2\bar{n}_2}{\epsilon_0 n c} + \frac{\mathrm{i}\alpha_2}{\epsilon_0 n k_0 c} \\
\implies \gamma_s(\omega_0) &= \frac{\omega_0}{c A_{\text{eff}}}\left(\frac{2\bar{n}_2}{\epsilon_0 n c} + \frac{\mathrm{i}\alpha_2}{\epsilon_0 n \omega_0}\right)
\end{aligned}
$$

However, it is customary to leave n_2 and thus γ unchanged, such that they relate only to the real part of $\chi^{(3)}$, and define a separate term β_{TPA} to deal with TPA:

$$\beta_{\text{TPA}} = 2\mathrm{i}A_{\text{eff}}\,\mathrm{Im}(\gamma_s) = \frac{2\mathrm{i}A_{\text{eff}}\alpha_2}{\epsilon_0 n c} \tag{2.55}$$

This term can then be included in the GNLSE as follows:

$$
\begin{aligned}
\frac{\partial A(z,t)}{\partial z} = i\sum_{n=1}^{\infty}\frac{i^n\beta_n}{n!}\frac{\partial^n A}{\partial t^n} &+ i\gamma(\omega_0)\left|A(z,t)\right|^2 A(z,t) \\
&- \frac{\beta_{\text{TPA}}}{2A_{\text{eff}}}\left|A(z,t)\right|^2 A(z,t) - \frac{\alpha}{2}A(z,t)
\end{aligned} \tag{2.56}
$$

As mentioned in Sec. 2.2, as photons are absorbed by electrons in the TPA process, the excited electrons become unbound ('free') charge carriers i.e. free-carriers. These can absorb further photons in a process called free-carrier absorption (FCA) which needs to be included in the GNLSE. This can be included as an additional loss term σ_f such that the GNLSE becomes [38, 24, 39]:

$$
\begin{aligned}
\frac{\partial A(z,t)}{\partial z} &= i\sum_{n=1}^{\infty}\frac{i^n\beta_n}{n!}\frac{\partial^n A}{\partial t^n} + i\gamma(\omega_0)\left|A(z,t)\right|^2 A(z,t) \\
&- \frac{\beta_{\text{TPA}}}{2A_{\text{eff}}}\left|A(z,t)\right|^2 A(z,t) - \frac{1}{2}(\sigma_f + \alpha_l)A(z,t)
\end{aligned} \tag{2.57}
$$

where α is relabelled as α_l to make it clear that it accounts for linear loss. $\sigma_f = \sigma(1 + \mathrm{i}\mu)$. σ is the FCA cross section ($1.45 \times 10^{-21}\mathrm{m}^2$ in crystalline silicon [38] or $1 \times 10^{-20}\mathrm{m}^2$ in amorphous silicon [34] at 1.55 µm), μ is the free-carrier dispersion (FCD) parameter ($\mu = 2k_c k_0/\sigma$ where $k_c = 1.35 \times 10^{-27}\mathrm{m}^3$ [34]) and N_2 is the free carrier density, where

$$\frac{\partial N_2(z,t)}{\partial t} = \frac{\beta_{\text{TPA}}}{2h\nu_0}\frac{\left|A(z,t)\right|^4}{A_{\text{eff}}^2} - \frac{N_2(z,t)}{\tau_f}, \tag{2.58}$$

h is the Planck constant, ν_0 is the (non-angular) centre frequency, and τ_f is the free-carrier lifetime, which is typically 87 ns for wavelengths affected by TPA.

A similar approach can be followed to include higher orders of photon absorption. The simulations in this thesis include 3PA in the GNLSE to give:

$$
\begin{aligned}
\frac{\partial A(z,t)}{\partial z} = i\sum_{n=1}^{\infty}\frac{i^n\beta_n}{n!}\frac{\partial^n A}{\partial t^n} &+ i\gamma(\omega_0)\left|A(z,t)\right|^2 A(z,t) \\
- \frac{\beta_{\text{TPA}}}{2A_{\text{eff}}}\left|A(z,t)\right|^2 A(z,t) &- \frac{\beta_{\text{3PA}}}{3A_{\text{eff}}^2}\left|A(z,t)\right|^4 A(z,t) - \frac{1}{2}(\sigma_f + \alpha_l)A(z,t)
\end{aligned}
$$

and the FCA resulting from this process is included in σ_f such that $\sigma_f = \sigma(1 + i\mu)(N_2 + N_3)$. The free-carrier parameters at 2.5 µm, which is affected by 3PA, are $\sigma = 3.7 \times 10^{-21}\mathrm{m}^2$ for the cross section and $\mu = 4.7$ [9]. N_3 builds up across the pulse as:

$$\frac{\partial N_3(z,t)}{\partial t} = \frac{\beta_{3\mathrm{PA}}}{3h\nu_0}\frac{|A(z,t)|^6}{A_{\mathrm{eff}}^3} - \frac{N_3(z,t)}{\tau_f}, \tag{2.59}$$

The free-carrier lifetime τ_f is 10 ns at 2.5 µm [9].

Finally, the frequency-dependence of γ needs to be taken into account, as this becomes significant when the pulse spectrum broadens into a SC. This can be added as a perurbation γ_1, which is applied in the frequency domain as [20]:

$$\frac{\gamma_1(\omega_0)}{\gamma(\omega_0)} = \frac{1}{\omega_0} + \frac{1}{n_2}\left(\frac{\mathrm{d}n_2}{\mathrm{d}\omega}\right)_{\omega=\omega_0} - \frac{1}{A_{eff}}\left(\frac{\mathrm{d}A_{eff}}{\mathrm{d}\omega}\right)_{\omega=\omega_0}. \tag{2.60}$$

This is applied to the electric field amplitude in the time domain by using the Fourier-transform property $\mathcal{F}\{\partial^n A(t)\partial t^n\} = (-i\omega)^n A(\omega)$ and is included in the full GNLSE for silicon as used in this study [20, 38, 24, 39]:

$$\begin{aligned}\frac{\partial A(z,t)}{\partial z} &= i\sum_{n=1}^{\infty}\frac{i^n\beta_n}{n!}\frac{\partial^n A}{\partial t^n} + i\left(\gamma(\omega_0) + i\gamma_1\frac{\partial}{\partial t}\right)|A(z,t)|^2 A(z,t)\\ &- \frac{\beta_{\mathrm{TPA}}}{2A_{\mathrm{eff}}}|A(z,t)|^2 A(z,t) - \frac{\beta_{3\mathrm{PA}}}{3A_{\mathrm{eff}}^2}|A(z,t)|^4 A(z,t) - \frac{1}{2}\left(\sigma_f + \alpha_l\right)A(z,t)\end{aligned} \tag{2.61}$$

2.5.2 Multi-mode GNLSE

The GNLSE can be extended to include multiple modes. As mentioned in Sec. 2.4, I assume single-mode propagation throughout the thesis, with the exception of the simulation in Sec. 4.2 in which I recreate one of the simulations from [34]. In that case, the GNLSE is as follows:

$$\begin{aligned}\frac{\partial A_\nu}{\partial z} &= -(\beta_1^{(\nu)} - \beta_1)\frac{\partial A_\nu}{\partial t} - i\sum_{n=2}^{\infty}\frac{i^n\beta_n}{n!}\frac{\partial^n A_\nu}{\partial t^n}\\ &+ i\gamma'(\omega_0)\left(R_{\nu\nu}|A_\nu|^2 + 2\sum_{\nu\neq\mu}R_{\mu\nu}|A_\mu|^2\right)A_\nu\\ &+ i\gamma_1\frac{\partial}{\partial t}|A_\nu|^2 A_\nu - \frac{\beta_{\mathrm{TPA}}}{2A_{\mathrm{eff}}^{(\nu)}}|A_\nu|^2 A_\nu - \frac{1}{2}\left(\sigma_f + \alpha_l\right)A_\nu,\\ &\nu = 1, 2, \ldots\end{aligned} \tag{2.62}$$

In this version I have omitted the z and t arguments for ease of reading, and also omitted the 3PA term as it does not apply at the 1.54 µm wavelength in the simulation.

The ν subscript designates the mode, such that any number of modes can be simulated, where each mode propagates separately according to its own propagation constant and nonlinear interaction, with two key additional terms. The first term governs the 'walk-off' between modes, which travel at different group velocities. Thus, $1/\beta_1$ is the group velocity of the fundamental mode.

The second additional term, which contains the sum, governs XPM, in which each mode modifies the refractive index of each other mode (designated μ). For this term, γ is replaced with $\gamma' = k_0 n_2$ i.e. omitting the effective area. This is done because an overlap integral needs to be introduced to specify the strength of interaction between modes. This is defined as:

$$R_{\mu\nu} = \frac{\iint_{-\infty}^{\infty} |F_\mu(x,y)|^2 |F_\nu(x,y)|^2 \mathrm{d}x\mathrm{d}y}{\iint_{-\infty}^{\infty} |F_\mu(x,y)|^2 \mathrm{d}x\mathrm{d}y \iint_{-\infty}^{\infty} |F_\nu(x,y)|^2 \mathrm{d}x\mathrm{d}y}. \tag{2.63}$$

For each mode, the effective area is included in the $R_{\nu\nu}$ term (i.e. its overlap with itself) which reduces to $1/A_{\mathrm{eff}}^{(\nu)}$.

The number of free carriers implicitly contained in the σ_f term is also affected by the overlap of modes in the following way:

$$\frac{\partial N_c}{\partial t} = \frac{\beta_{\mathrm{TPA}}}{2h\nu_0}\left(\sum_{\nu} R_{\nu\nu}^2 |A_\nu|^4 + 2\sum_{\nu\neq\mu} R_{\nu\nu} R_{\mu\nu} |A_\mu A_\nu|\right) - \frac{N_c}{\tau_c}, \tag{2.64}$$
$$\nu = 1, 2, ...$$

2.5.3 Vector vs scalar effective area

To check that this assumption is indeed justified, I recalculated the effective area in Comsol for a number of diameters and wavelengths using the full vectorial equation [11]:

$$A_{\mathrm{eff}} = \frac{|\int (\mathbf{E}\times\mathbf{H}^*)\cdot\hat{z}\,\mathrm{d}A|^2}{\int |(\mathbf{E}\times\mathbf{H}^*)\cdot\hat{z}|^2\,\mathrm{d}A} \tag{2.65}$$

This can be simplified as follows:

$$\begin{aligned}
(\mathbf{E}\times\mathbf{H}^*) &= (E_x\cdot\hat{x} + E_y\hat{y} + E_z\hat{z}) \times (H_x^*\hat{x} + H_y^*\hat{y} + H*_z\,\hat{z}) \\
&= E_x H_x^*(\hat{x}\times\hat{x}) + E_x H_y^*(\hat{x}\times\hat{y}) + E_x H_z^*(\hat{x}\times\hat{z}) \\
&+ E_y H_x^*(\hat{y}\times\hat{x}) + E_y H_y^*(\hat{y}\times\hat{y}) + E_y H_z^*(\hat{y}\times\hat{z}) \\
&+ E_z H_x^*(\hat{z}\times\hat{x}) + E_z H_y^*(\hat{z}\times\hat{y}) + E_z H_z^*(\hat{z}\times\hat{z}) \\
&= E_x H_y^*\hat{z} - E_x H_z^*\hat{y} - E_y H_x^*\hat{z} + E_y H_z^*\hat{x} + E_z H_x^*\hat{y} - E_z H_y^*\hat{x} \\
\Longrightarrow\ (\mathbf{E}\times\mathbf{H}*)\cdot\hat{z} &= E_x H_y^* - E_y H_x^*
\end{aligned}$$

So, Eq. 2.65 becomes:

$$A_{\mathrm{eff}} = \frac{|\int E_x H_y^* - E_y H_x^*\,\mathrm{d}x\mathrm{d}y|^2}{\int |E_x H_y^* - E_y H_x^*|^2\,\mathrm{d}x\mathrm{d}y} \tag{2.66}$$

These are the results I got, compared with the scalar approximation:

Fig. 2.11 shows that the difference between the full vectorial effective area and the scalar approximation is less than 10 % for core diameters of 2600 nm and above, even with wavelengths out to 5.5 µm, which is the longest wavelength looked at in the fibre taper designs later. The difference becomes much more significant with a core diameter of 1700 nm, but this is the smallest diameter (the waist) in the taper designs, and wavelengths > 4 µm are not generated there. Thus, the results obtained

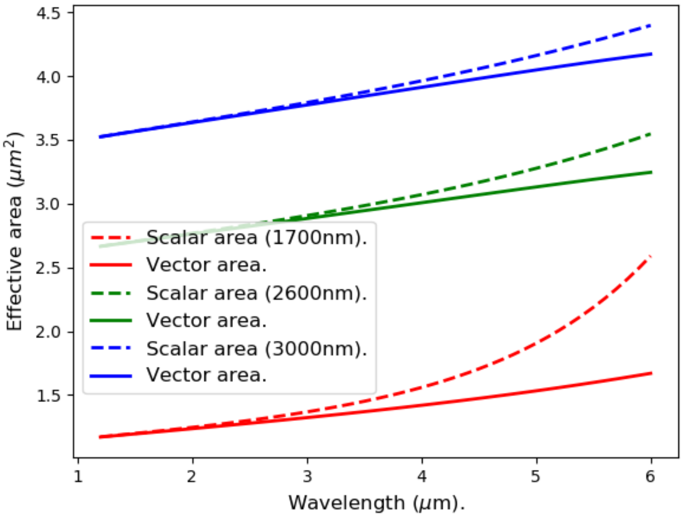

FIGURE 2.11: Scalar and vector effective area for the fundamental mode with silicon core fibre diameters of 1700, 2600 and 3000 nm for wavelengths of 1.2 – 6 µm.

with the scalar approximation for the effective area are still valid for the fibre taper designs.

I did, however, also look at ridge waveguides, as mentioned previously, and the smallest dimension (the thickness) in these cases is 500 nm, which is much smaller than the pulse wavelengths studied, thus the z-component of the field would be expected to become much more significant. I also calculated the vectorial effective area for ridge waveguides:

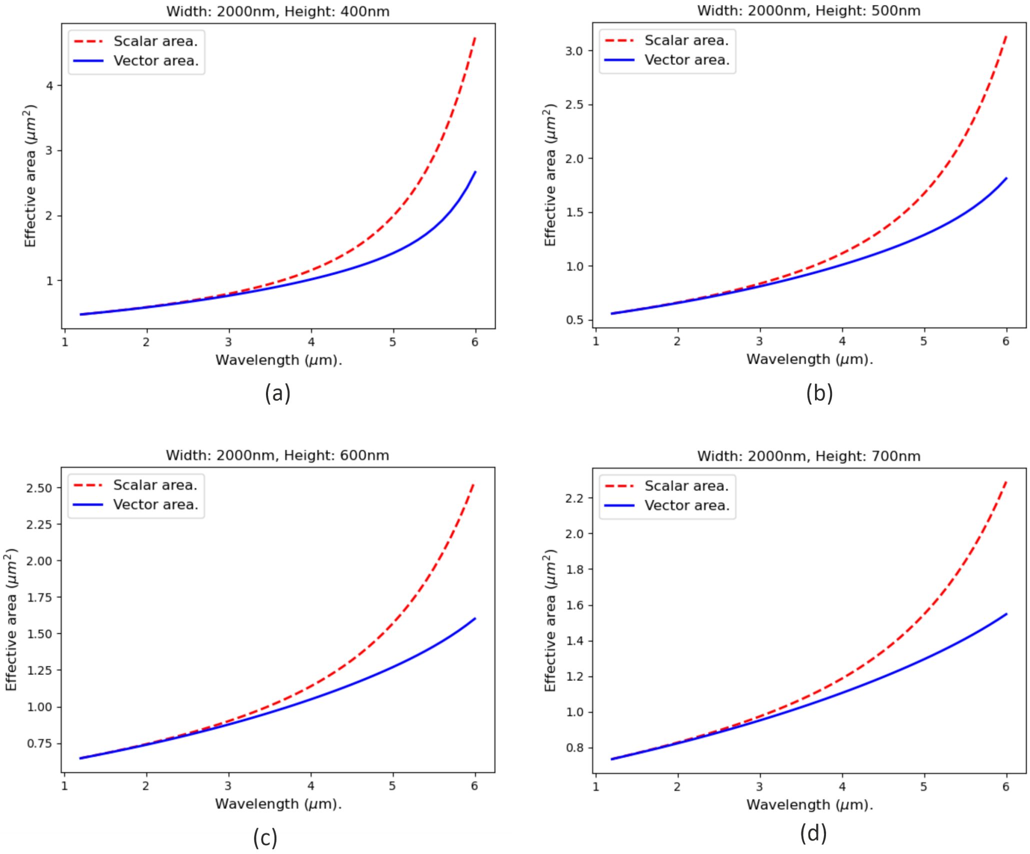

(a) (b)

(c) (d)

FIGURE 2.12: Scalar vs vector effective areas for ridge waveguides with 2000 nm width and heights of (a) 400 nm, (b) 500 nm, (c) 600 nm and (d) 700 nm.

Fig. 2.12 shows that, with a ridge waveguide width of 1 µm and a height of 400 nm, the vector effective area increases significantly more with wavelength than the scalar approximation. The difference is already 10 % by 3.73 µm and increases to nearly 80 % by 6 µm. However, the longest wavelengths looked at in ridge waveguides in this thesis is 4.5 µm, and the smallest height simulated is 500 nm. In that case, the difference is 18 %. However, a width close to 2 µm is only used for generating wavelengths up to 3.75 µm, so the results obtained are within tolerance.

For generating wavelengths of up to 4.5 µm, a width of ≈ 2.5 µm is used. Fig. 2.13 shows the vectorial effective area compared with the scalar approximation for ridge waveguides of this thickness and the same height range of 400 – 700 nm.

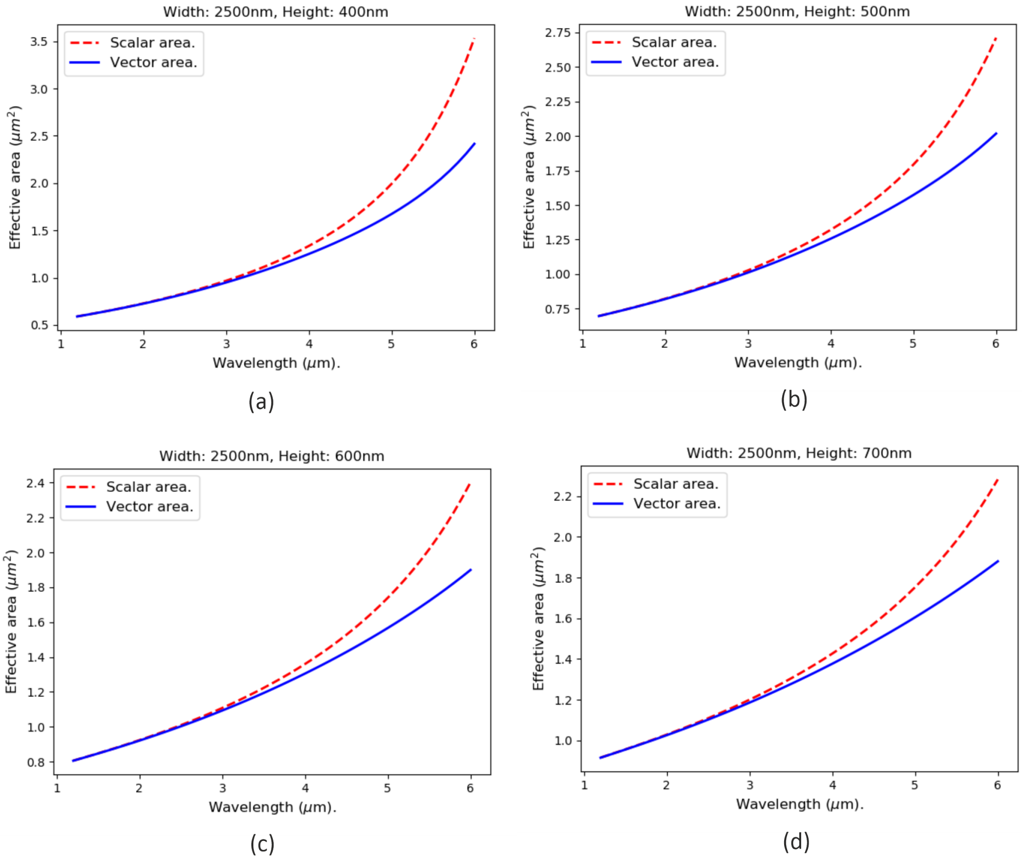

FIGURE 2.13: Scalar vs vector effective areas for ridge waveguides with 2500 nm width and heights of (a) 400 nm, (b) 500 nm, (c) 600 nm and (d) 700 nm.

Fig. 2.13 shows that even with a height of 400 nm, the difference between the vectorial effective area and the scalar approximation is less than 10% up to 4.4 µm, and with a height of 500 nm, 4.65 µm.

Therefore, for the ridge waveguides studied later in Chapter 8, the scalar approximation of the effective area is a reasonable one.

2.5.4 Solving the GNLSE: The Split Step Fourier Method

The code implements the split-step Fourier method (SSFM). This processes the linear part of the equation (dispersion and linear loss) in the frequency domain and the nonlinear part in the time domain. Thus, the GNLSE is split into two operators, a linear operator $\hat{L}$ and a nonlinear operator $\hat{N}$ so that

$$\frac{\partial A_\nu}{\partial z} = (\hat{L} + \hat{N})A(z,t) \tag{2.67}$$

$$\hat{L} = i\sum_{n=1}^{\infty} \frac{i^n \beta_n}{n!}\frac{\partial^n}{\partial t^n} - \frac{\alpha(\omega)}{2} \tag{2.68}$$

$$\hat{N} = i\gamma_0 \left(|A(z,t)|^2 + i\frac{\gamma_1}{\gamma_0}\frac{1}{A}\frac{\partial}{\partial t}(|A(z,t)|^2 A) \right) \\ - \frac{\beta_{\text{TPA}}}{2A_{\text{eff}}}|A(z,t)|^2 - \frac{\beta_{\text{3PA}}}{3A_{\text{eff}}^2}|A(z,t)|^4 - \frac{1}{2}\sigma_f \tag{2.69}$$

where γ_1 is defined as above and $\gamma_0 = \gamma(\omega_0)$. In my code, the $1/A$ factor in the self-steepening term caused numerical errors and so I have used the technique described in [21], which is to set

$$\frac{1}{A}\frac{\partial}{\partial t}(|A(z,t)|^2 A) = A^*\frac{\partial A}{\partial t} + \frac{\partial |A(z,t)|^2.}{\partial t} \tag{2.70}$$

The SSFM processes each operator separately in the following (non-symmetric) manner [20]:

$$A(z+h,t) \approx \exp\left(\frac{h}{2}\hat{L}\right)\exp\left(\int_z^{z+h}\hat{N}(z')\mathrm{d}z'\right)A(z,t) \tag{2.71}$$

where the integral is approximated by $\exp(h\hat{N})$. This produces a phase error of size h which is the spatial step size. It is, however, straightforward to improve this to second-order (h^2) by symmetrising the process as follows [40]:

$$A(z+h,t) \approx \exp\left(\frac{h}{2}\hat{L}\right)\exp\left(\int_z^{z+h}\hat{N}(z')\mathrm{d}z'\right)\exp\left(\frac{h}{2}\hat{L}\right)A(z,t) \tag{2.72}$$

I have implemented a third-order scheme by not approximating the integral in Eq. 2.72 by $h\hat{N}(z)$ but instead using [41]:

$$\int_z^{z+h}\hat{N}(z')\mathrm{d}z' \approx \frac{h}{2}[\hat{N}(z) + \hat{N}(z+h)] \tag{2.73}$$

This first estimates $\hat{N}(z+h)$ by using the second-order scheme, which is then fed into the third-order scheme to obtain an accuracy of (h^3). I also implemented a fourth-order scheme invented by Hult, the interaction picture (IAP) method [42] but my initial tests showed little improvement over the third-order method.

For computational efficiency, I later implemented an adaptive step-size Runge Kutta method that solves the GNLSE using the Cash-Karp method, which gives fifth-order accuracy [43]. (See Appendix A).

2.5.5 Code testing

I have implemented two tests within the code to ensure that the results I obtained are sensible, even though numerical errors can never be completely ruled out. The first is checking that energy is conserved (when setting $\alpha = 0$), simply by calculating the total input and output power by integrating the modulus squared of the pulse over the time window. The relative error should be very small, e.g. $< 10^{-6}$, where the relative error is defined as $1 - |A|^2_{\text{out}}/|A|^2_{\text{in}}$. The second test is to check that a fundamental soliton propagates unchanged, by setting $\beta_2 < 0$, all higher dispersion terms to zero, switching off self-steepening and loss terms, and $P_0 = |\beta_2|/(T_0^2 \cdot \gamma)$. This is done by comparing the input and output pulses after every propagation step to obtain a relative error. The errors accumulate with the number of steps, so it is not enough to simply double the number of steps when doubling propagation length. When error testing, I set the condition that the error should be less than 4.5×10^{-6} at 10% of the propagation length (such that the full length does not have to be run before a warning is raised). I settled on this value by trial and error, which involved looking at different simulations with varying lengths and ascertaining when no further improvement to the output was achieved by increasing the number of steps. This test helps to reduce errors which will become magnified when larger pulse powers, higher orders of dispersion and additional nonlinearities are all included.

Higher-order dispersion terms can be tested by offsetting the pulse from the centre frequency and comparing its shape evolution to a pulse with known value of β_2. In this way, it can be ensured that the higher-order terms are producing the correct dispersion effect across the spectrum.

2.6 Pulse propagation

There are two useful terms which indicate over what lengths dispersion and nonlinearity become significant. The dispersion (L_{D}) and nonlinear (L_{NL}) lengths are defined as follows [44]:

$$L_{\mathrm{D}} = \frac{t_0^2}{|\beta_2|} \tag{2.74}$$

$$L_{\mathrm{NL}} = \frac{1}{\gamma P_0} \tag{2.75}$$

For this study it is assumed that the light travels in a packet consisting of a carrier frequency (ω_0) which is modulated in time to form an envelope. This modulation produces a range of frequencies around the carrier, and the field can be written [20]:

$$\boldsymbol{E}(\boldsymbol{r},t) = \frac{1}{2}\hat{x}F(x,y)A(z,t)\exp[\mathrm{i}(\beta_0 z - \omega_0 t)] + \mathrm{c.c.} \tag{2.76}$$

where r is the spatial component, $A(z,t)$ is the field amplitude, z is the propagation direction and t is time. $\beta_0 = k_0 n_{\mathrm{eff}}$ is the propagation constant where n_{eff} is the effective refractive index at ω_0 which depends on its refractive indices in the core and cladding material as well as the fibre diameter (see Section 2.4) and $k_0 = 2\pi/\lambda_0$ is the wave-vector in free-space of the carrier wavelength λ_0.

In this case the polarisation is in the $\hat{x}$-direction, and the strength of the field varies as a function $F(x,y)$. Generally speaking, in a uniformly circular fibre the polarisation direction is arbitrary, and it can vary across the (x,y)-plane, but in the following only linearly polarised fields will be considered for simplicity.

This assumption is essentially valid for the fibres and waveguides studied in this thesis, as shown in Figs. 2.7 – 2.10. It is further assumed, however, that there is negligible polarisation in the z-direction, but this is shown to be a good approximation in Sec. 2.5.3.

Propagation of the wave-fronts occurs in the z-direction, and these have a spatial phase which depends on β_0 and a phase in time which depends on ω_0.

$A(z,t)$ is also referred to as the envelope, which is assumed to vary slowly in time relative to ω_0, so this model is termed the slowly-varying envelope approximation (SVEA). This is a valid approximation as the optical cycle time for the frequencies studied in this thesis, which range from 55 – 250 (THz) (i.e. 5.5 µm down to 1.2 µm), ranges from 4 – 20 fs, while the shortest pulse lengths looked at are 100 fs.

This envelope is initially assumed to be a Gaussian pulse where [45]:

$$A(0,t) = \exp\left(-\frac{t^2}{2t_0^2}\right) \tag{2.77}$$

where t_0 is the half-width (where intensity reaches $1/e$) and $t_0 = t_{\mathrm{FWHM}}/1.665$, where the full width half maximum (FWHM) is the width where the intensity is half, which is the more commonly used pulse width given in the literature.

Assuming that the pulse propagates free from any nonlinear effects and is only affected by the GVD parameter β_2, then $A(z,t)$ satisifies the linear partial differential equation:

$$\mathrm{i}\frac{\partial A}{\partial z} = \frac{\beta_2}{2}\frac{\partial^2 A}{\partial t^2} \tag{2.78}$$

We can use the inverse Fourier transform, defined in Eq. (2.2), to transform this into an ordinary differential equation:

$$\mathrm{i}\frac{\partial \tilde{A}}{\partial z} = -\frac{1}{2}\beta_2\omega^2\tilde{A} \tag{2.79}$$

This has the solution

$$\tilde{A}(z,\omega) = \tilde{A}(0,\omega)\exp\left(\frac{\mathrm{i}}{2}\beta_2\omega^2 z\right) \tag{2.80}$$

Inserting this solution into the inverse Fourier transform equation gives:

$$A(z,t) = \frac{1}{2\pi}\int_{-\infty}^{\infty}\tilde{A}(0,\omega)\exp\left(\frac{\mathrm{i}}{2}\beta_2\omega^2 z - \mathrm{i}\omega t\right)\mathrm{d}\omega \tag{2.81}$$

The initial shape of the Gaussian pulse can now be inserted into the Fourier transform definition of $\tilde{A}(0,\omega)$ to give:

$$\tilde{A}(0,\omega) = \int_{-\infty}^{\infty}\exp\left(-\frac{t^2}{2t_0^2} + \mathrm{i}\omega t\right) \tag{2.82}$$

This can be solved using the identity [20]

$$\int_{-\infty}^{\infty}\exp(-ax^2 - bx)\mathrm{d}x = \sqrt{\frac{\pi}{a}}\exp\left(\frac{b^2}{4a}\right) \tag{2.83}$$

where $a = 1/2t_0^2$ and $b = -\mathrm{i}\omega$, and inserted into Eq. (2.81) to give:

$$A(z,t) = \frac{1}{2\pi}\sqrt{2t_0^2\pi}\int_{-\infty}^{\infty}\tilde{A}(0,\omega)\exp\left(-\frac{t_0^2\omega^2}{2} + \frac{\mathrm{i}}{2}\beta_2\omega^2 z - \mathrm{i}\omega t\right)\mathrm{d}\omega \tag{2.84}$$

We can use the identity Eq. (2.83) again with $a = t_0^2/2 - \mathrm{i}\beta_2 z/2$ and $b = \mathrm{i}t$ to give:

$$A(z,t) = \frac{t_0}{(t_0^2 - \mathrm{i}\beta_2 z)^{1/2}}\exp\left[-\frac{t^2}{2(t_0^2 - \mathrm{i}\beta_2 z)}\right] \tag{2.85}$$

Eq. (2.85) shows how the amplitude and phase changes with propagation in the z-direction. This pulse then gains a phase-shift as it propagates, such that

$$A(z,t) = |A(z,t)|\exp[\mathrm{i}\phi(z,t)] \tag{2.86}$$

where

$$-\frac{\partial\phi}{\partial t} = \delta\omega(t) = \frac{\mathrm{sgn}(\beta_2)(z/L_\mathrm{D})}{1+(z/L_\mathrm{D}))^2}\frac{t}{t_0^2} \tag{2.87}$$

$\delta\omega(t)$ is the chirp, which represents how the spectral content varies across the pulse in the time domain. A positive value means that the frequency increases from the leading to the trailing edge, while a negative chirp is the opposite. Fig. 2.14 shows how the intensity and frequency chirp of a guassian pulse changes as it propagates up to $4L_\mathrm{D}$ in both the normal and anomalous dispersion regimes.

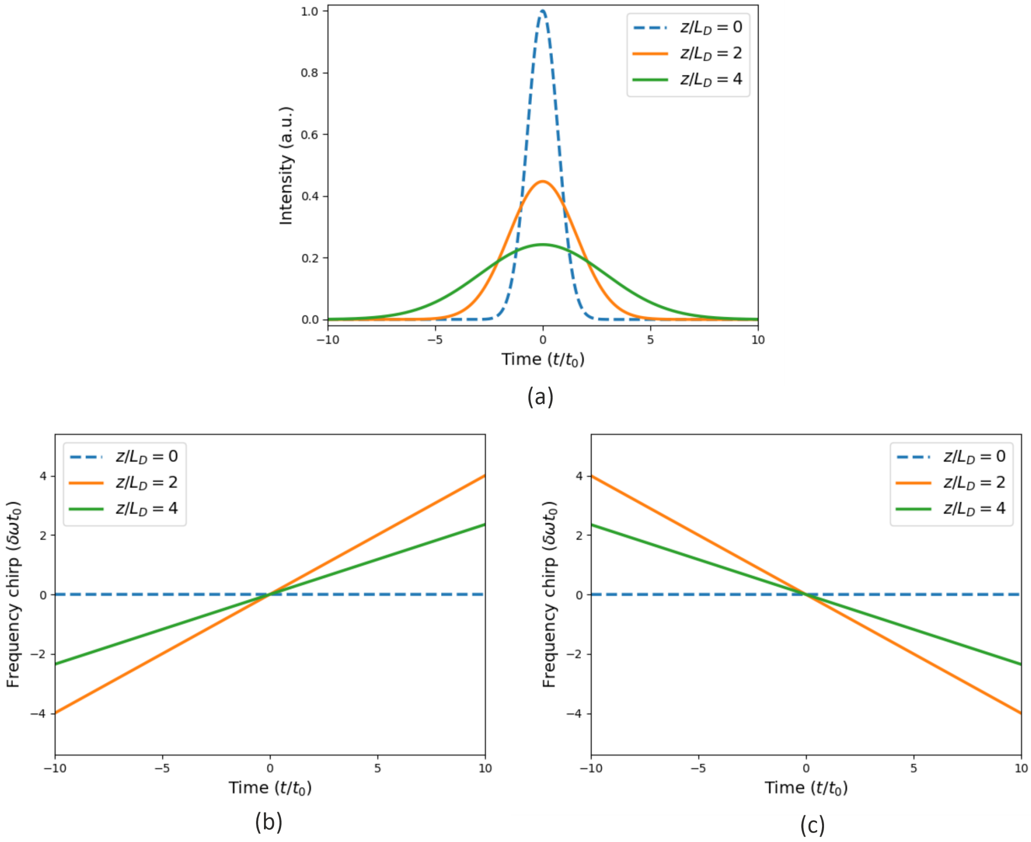

(a)

(b)

(c)

FIGURE 2.14: Gaussian pulse at L_D = 0, 2 and 4. (a) Intensity profile, (b) frequency chirp in the normal dispersion regime and (c) frequency chirp in the anomalous dispersion regime.

If the pulse starts with an initial chirp, this is defined as $C \propto \delta\omega(t)$ such that:

$$A(0,t) = \exp\left(-\frac{(1+\mathrm{i}C)}{2}\frac{t^2}{t_0^2}\right) \tag{2.88}$$

Another common pulse shape is the hyperbolic secant, which maintains its shape as it propagates (so it is called a 'soliton'). This will be covered in Section 3.1.1.

2.7 Nonlinear processes

As pulses propagate, they are modified by nonlinear interaction with the material, which for materials such as silica and silicon is dominated by the third-order susceptibility tensor, $\chi^{(3)}$. ($\chi^{(1)}$ governs the linear response, which is also included in the study, whereas $\chi^{(2)}$ governs the nonlinearity of non-symmetric crystals and is not applicable for silicon [38]).

Whereas $\chi^{(1)}$ is a vector (a tensor of order-1), $\chi^{(3)}$ is a tensor of order-3 and so it cannot be muliplied directly with the electric field. It has 81 elements (d^o) where d is the number of dimensions (3: the spatial ones) and o is the tensor order (also 3). Thus a triple dot product has to be applied (see Appendix B) which reduces the number of elements down to 3.

There are two main types of third-order nonlinearity: the Kerr and Raman responses. Whereas the Raman effect is a delayed vibrational response and thus only applies under certain conditions (see Sec. 2.7.2), the Kerr effect is an instantaneous electronic response and operates by changing the refractive index of the medium in response to the intensity of the field, i.e. $\tilde{n} = n_{\text{eff}} + n_2|E|^2$ [20]. The Kerr coefficient n_2 is related to χ^3 as follows [46]:

$$n_2(\omega) = \frac{3}{4\epsilon_0 c n(\omega)^2}\chi^{(3)'}_{\text{eff}}(\omega) \tag{2.89}$$

where ϵ_0 is the vacuum permittivity and $\chi^{(3)'}_{\text{eff}}$ is the real part of the third-order susceptibility. (In silicon, as with other semiconductors, the imaginary part of χ^3 governs multi-photon absorption so $\beta_{\text{TPA}} \propto \text{Im}(\chi^3)$ - see Section 2.5.)

One of the main consequences of this refractive index modification is self-phase modulation (SPM) which means that a pulse becomes chirped as the rate of change of the refractive index follows the shape of the pulse intensity. So as the intensity increases at the leading edge of the pulse, the refractive index continually increases, thus continually slowing down the phase velocity of the frequencies in that part of the pulse, effectively lowering those frequencies. The opposite occurs at the trailing edge: the refractive index continually decreases, and the phase velocity continually increases, raising the frequencies. Thus, the spectral content varies across the centre of the pulse in the time domain, from lowest frequencies to highest. On its own, this would have no impact, but group velocity dispersion (GVD) takes over. This is a linear effect whereby different frequencies travel at speeds determined by their refractive indices. In the 'normal' dispersion regime, lower frequencies propagate faster than higher ones, which causes the pulse to spread out in time anyway (and also chirps it) but in this case, SPM is acting in the same 'direction' and causes even more rapid broadening. However, in the so-called 'anomalous' dispersion regime, the higher frequencies travel faster, which alone causes broadening, but with the right pulse intensity, SPM can counteract this and a pulse can maintain it shape, travelling as a 'soliton', as described in Section 3.1.1. If pulses occur at different frequencies but overlap in time, they will also modify the each others' refractive indices, in an effect called cross-phase modulation (XPM).

2.7.1 Phase-matching and four wave mixing

The phase of a wave depends not only on its frequency but also on its wave-vector, which in a medium is modified by the refractive index. Thus, waves of different frequencies can phase-match, and a process called four wave mixing (FWM) occurs if four such waves match according to the following condition [47]:

$$\omega_{p1} + \omega_{p2} - \omega_s - \omega_i = 0. \tag{2.90}$$

$$\Delta k = \beta_{p1} + \beta_{p2} - \beta_s - \beta_i = \tilde{n}_{p1}k_{p1} + \tilde{n}_{p2}k_{p2} - \tilde{n}_s k_s - \tilde{n}_i k_i = 0 \tag{2.91}$$

where $p1$ and $p2$ are pumps 1 and 2 ($\omega_{p2} > \omega_{p1}$)) and s and i refer to signal and idler, such that $\omega_s < \omega_{p1}$ and $\omega_i > \omega_{p2}$. As different wavelengths travel at different speeds (due to different refractive indices), waves tend to move out of phase with each other and as such this condition is quite hard to satisfy.

Effectively the result is that two photons of frequencies ω_{p1} and ω_{p2} are absorbed by an electron, which then emits two photons of different frequencies ω_s and ω_i. This is non-degenerate FWM because all four frequencies are different. However, the pumps can have the same frequency, and in this (degenerate) case, the two pump photons (of the same frequency such that $\omega_{p1} = \omega_{p2}$) are converted to a signal photon of lower frequency ω_s and an idler of higher frequency ω_i, such that $\omega_i - \omega_{p1} = \omega_{p1} - \omega_s$. Fig. 2.15 illustrates these processes. Note that the diagram only represents the frequencies of the photons involved, but as Eq. 2.91 shows, the momenta of all four has to sum to zero.

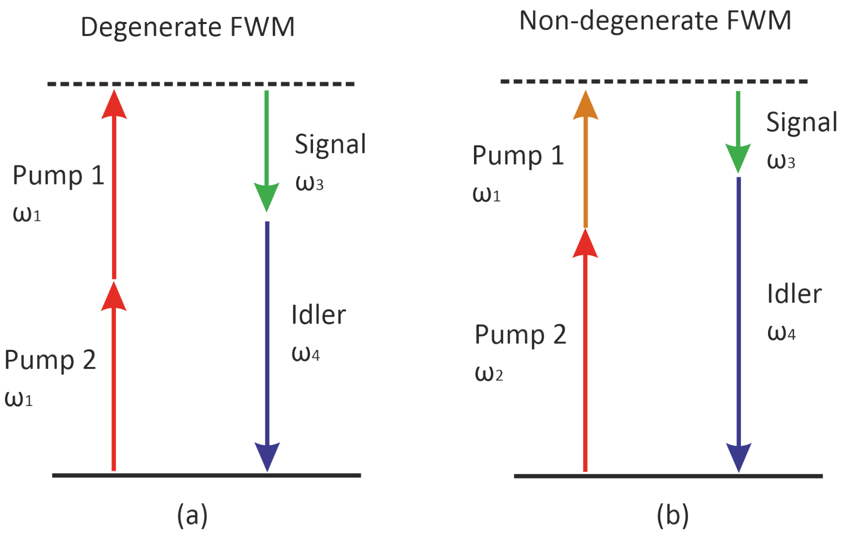

FIGURE 2.15: Energy diagram of FWM process showing frequencies of pumps, signal and idler in (a) degenerate FWM and (b) non-degenerate FWM.

The effective indices of different wavelengths are changed by the nonlinearity, which means that when certain dispersion conditions are met, the nonlinearity can create additional phase-matching conditions.

We can see how this happens by starting with Eq. (2.61) but simplifying it by removing all dispersion terms, self-steepening and linear and nonlinear loss to leave just the nonlinear effect:

$$\mathrm{i}\frac{\partial A}{\partial z} = -\gamma |A|^2 A \tag{2.92}$$

We can look at a CW with power P_0 and frequency ω_0 which has amplitude:

$$A(z,t) = \sqrt{P_0}\exp(-\mathrm{i}\omega_0 t) \tag{2.93}$$

Thus,

$$\begin{aligned}\frac{\partial A}{\partial z} &= -\mathrm{i}\gamma|A|^2A \\ &= \mathrm{i}\gamma P_0A \end{aligned} \tag{2.94}$$

It can be seen that the solution is therefore:

$$\begin{aligned}A(z,t) &= A(0,t)\exp(\mathrm{i}\gamma P_0z) \\ &= A(0,t)\exp(\mathrm{i}\phi_{\mathrm{NL}}z)\end{aligned} \tag{2.95}$$

where $\phi_{\mathrm{NL}} = \gamma P_0$. This is the nonlinear phase shift. If we now assume that the power of pumps P_1 and P_2 in Eq. (2.91) is much greater than the power of signal and idler (P_s, P_i) such that the nonlinearity only has significant effect on the pumps, then we get an *effective* phase-mismatch [47]:

$$\kappa = \Delta k + \gamma(P_1 + P_2) \tag{2.96}$$

Thus, phase-matching occurs when $\kappa = 0$.

As γ, p_1 and p_2 are positive, this can only occur when Δk is negative. To calculate Δk, we can use Eq. (2.91).

By picking a reference frequency ω_0 halfway between ω_{p1} and ω_{p2}, we can write the propagation constant for each wavelength as a Taylor expansion:

$$\begin{aligned}\beta(\omega_n) = \beta_0 + \beta_1(\omega_n-\omega_0) + \frac{\beta_2}{2!}(\omega_n-\omega_0)^2 \\ + \frac{\beta_3}{3!}(\omega_n-\omega_0)^3 + \frac{\beta_4}{4!}(\omega_n-\omega_0)^4 ...\end{aligned} \tag{2.97}$$

where $n = p1, p2, s, i$ and $\beta_m = \mathrm{d}^m\beta/\mathrm{d}\omega^m|_{\omega=\omega_0}$.

When each propagation constant is written out in this way, substituting $\omega_{p2} - \omega_0 = -(\omega_{p1}-\omega_0)$ and $\omega_i - \omega_0 = -(\omega_s - \omega_0)$, and inserting it into Eq. (2.91), the odd-numbered β_m terms vanish and we are left with only even terms:

$$\begin{aligned}\Delta k = \beta_2[(\omega_{p1}-\omega_0)^2 + (\omega_s-\omega_0)^2] \\ + \frac{2\beta_4}{4!}\left[(\omega_{p1}-\omega_0)^4 + (\omega_s-\omega_0)^4\right] + ...\end{aligned} \tag{2.98}$$

It should thus be clear that at least one of these even-numbered β terms must be negative. So, for example, β_2 can be positive (the normal dispersion regime) as long as β_4 is negative. In the simplest case, β_2 is negative (the anomalous dispersion regime) such that $-\beta_2 = |\beta_2|$, β_4 is negligible and the pumps have the same frequency (i.e. $\omega_{p1} = \omega_{p2} = \omega_0$ and $p1 = p2 = P_0$). Thus, $\kappa = 0$ when

$$|\beta_2|(\omega_s-\omega_0)^2 = 2\gamma P_0 \tag{2.99}$$

$$\omega_s - \omega_0 = \sqrt{\frac{2\gamma P_0}{|\beta_2|}} \tag{2.100}$$

Thus, sidebands form either side of the pump, with a frequency separation of ω_S. This process of MI arises from amplification of quantum noise (photons of arbitrary frequency spontaneously emitted by electrons), and can cause the breakup of a continuous wave (CW) into a train of pulses, or a long pulse into shorter pulses.

2.7.2 A note on the Raman effect

The Raman response occurs when electrons are excited by photons, but then vibrate, losing some of their energy via phonons before re-radiating the rest of the energy (the Stokes process). Thus pump frequencies are downshifted to a signal frequency, which follows a gain spectrum peaking around 15.6 THz lower than the pump (in silicon). This process can occur spontaneously, or it can be stimulated by an existing signal wave, and thus can be used for intentional frequency conversion or signal gain (stimulated Raman scattering: SRS). A higher frequency can also be produced (the Anti-Stokes process), but is thermodynamically less likely because it requires a phonon giving energy to an electron at just the right moment. Fig. 2.16 illustrates these processes.

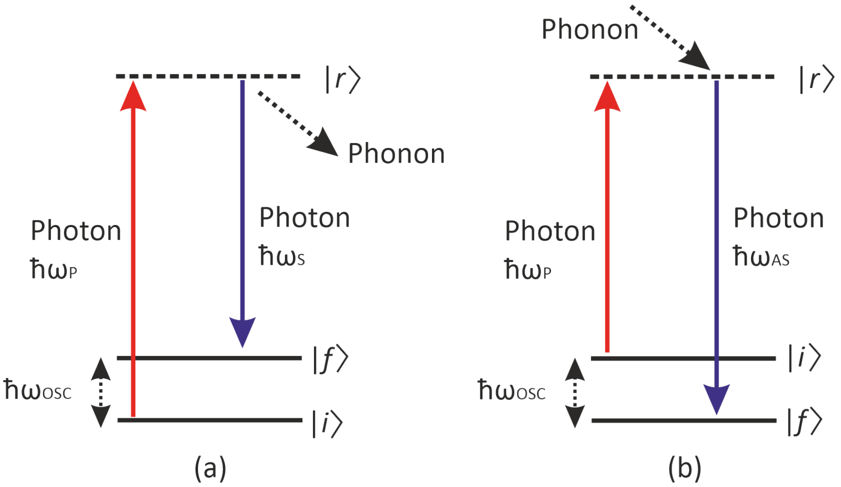

FIGURE 2.16: Energy diagram of spontaneous Raman scattering. Initial electron energy state is labelled as i, final state as f and virtual Raman state as r. $\hbar\omega_{\mathrm{OSC}}$ is the vibrational energy of the phonon involved in each process, $\hbar\omega_{\mathrm{P}}$ is the pump photon, $\hbar\omega_{\mathrm{S}}$ is the emitted photon in the Stokes process (a) and $\hbar\omega_{\mathrm{AS}}$ in the Anti-Stokes process (b). Adapted from Fig. 1 in [48].

For the purposes of this study, the Raman effect in silicon is ignored because it has a very narrow gain bandwidth of 105 GHz [38]. The response time of the Raman effect (i.e. the time the electric field needs to be applied to trigger the effect) is inversely proportional to the gain bandwidth, which means a response time in silicon of ≈ 3 ps (as opposed to silica which has a response time of 32 fs [49] corresponding to a gain bandwidth of 10.6 THz). Although the SC studied in this thesis can span up to nearly ten times the Raman shift frequency of 15.6 THz, the pulses studied have widths of 100 – 150 ps, so are much too short to be affected by this process. In Chapter 6 C.W.s are looked at for the purpose of wavelength conversion, but the frequency spacing of the pumps is 30 THz, so will not stimulate the Raman response.

Furthermore, when the Raman response is included in the GNLSE, the gain bandwidth and shift frequency are used to calculate the maximum strength of the reponse relative to the Kerr effect.

The nonlinear response term $\mathrm{i}\gamma(\omega_0)A(z,t)|A(z,t)|^2$ in Eq. (2.61) is replaced with [20]:

$$\mathrm{i}\gamma(\omega_0)A(z,t)\int_0^\infty R(t')|A(z,t-t')|^2\mathrm{d}t' \tag{2.101}$$

where $A(t,t-t')$ takes into account the delay in the vibrational response, $R(t) = (1-f_\mathrm{R})\delta(t) + f_\mathrm{R}h_\mathrm{R}(t)$, f_R is the fractional contribution of the delayed Raman response to nonlinear polarisation P_NL and $h_\mathrm{R}(t)$ is the Raman response function. This is written as:

$$h_\mathrm{R}(t) = \left(\tau_1^{-2}+\tau_2^{-2}\right)\tau_1\exp\left(\frac{-t}{\tau_2}\right)\sin\left(\frac{t}{\tau_1}\right) \tag{2.102}$$

where $\tau_1 = 1/\Omega_\mathrm{R}$, Ω_R is the vibrational Raman frequency and τ_2 is the damping time of vibrations (or response time). For silica these values are set to be $\tau_1 = 12.2\,\mathrm{fs}$ and $\tau_2 = 32\,\mathrm{fs}$ [49], whereas in silicon they are set as $\tau_1 = 10\,\mathrm{fs}$ and $\tau_2 = 3\,\mathrm{ps}$ [38].

The Raman gain g_R is then related to the imaginary part of the Fourier transform of h_R:

$$g_\mathrm{R}(\Delta\omega) = \frac{f_\mathrm{R}\omega_0}{cn(\omega_0)}\chi^{(3)}_{xxxx}\mathrm{Im}[\tilde{h}_\mathrm{R}(\Delta\omega)] \tag{2.103}$$

Using measured values of peak Raman gain, Eqs. (2.102) - (2.103) can be used to estimate that the fractional contribution of the vibrational Raman effect to the total nonlinear response is 0.18 in silica, whereas in silicon it is only 0.043 [50].

2.8 Conclusion

In this Chapter I have introduced the optical properties of silicon, the structure of silicon-core fibres, the equations governing the modes confined by fibres and the equation used to solve the propagation of light pulses through the fibres, the GNLSE. I have also discussed the basics of SPM and FWM.

In the next chapter I will look at how these nonlinear effects combine together with dispersion to produce spectral broadening of pulses as they propagate, ultimately resulting in SC generation.

Chapter 3

Supercontinuum generation dynamics in silicon-core fibres

Having introduced the GNLSE and the basic nonlinear processes in the previous chapter, in this chapter the dynamics of SC generation in silicon-core fibres will be studied. This is important because understanding these dynamics will help with designing fibre tapers which will extend the long-wavelength edge of a SC.

3.1 Supercontinuum Generation

A supercontinuum is generated by a combination of nonlinear processes. In this chapter I study these effects individually and in combination in order to better understand SC generation.

Initially the spectrum is broadened by SPM, FWM or both. Following this, under the right conditions (see following sections), a pulse which forms a higher-order soliton (see Sec. 3.1.1) can separate into several fundamental solitons in a process called soliton fission (see Sec. 3.1.2), which then can be shifted in frequency by FWM where the phase-matching is governed by third-order dispersion (TOD), causing new components to appear in the spectrum, thus broadening it. Higher order solitons are pulses with higher powers than fundamental (first-order) ones, and evolve periodically. They can be thought of as consisting of multiple fundamental solitons which can be separated by perturbation [51].

3.1.1 Solitons

Solitons, as previously mentioned, occur when dispersion is counteracted by nonlinearity. This only occurs in the anomalous dispersion regime, i.e. when $\beta_2 < 0$ The simplest type of soliton, or first-order, occurs when the pulse envelope has a hyperbolic secant shape:

$$A(0,t) = \operatorname{sech}\left(\frac{t}{t_0}\right) \exp\left(-\frac{\mathrm{i}Ct^2}{2t_0^2}\right) \tag{3.1}$$

and

$$P_0 = \frac{|\beta_2|}{t_0^2 \cdot \gamma} \tag{3.2}$$

where P_0 is the peak power of the pulse and t_0 is the pulse width. When these terms are balanced in this way, the pulse propagates unchanged in both time and spectrum, hence the term ‘soliton’.

Higher-order solitons are solutions to the GNLSE that have long-term propagation stability, as with fundamental solitons, but rather than maintaining their temporal and spectral properties, they periodically oscillate or 'breathe' [44]. The order of a soliton is given by N in the solution

$$P_0 = \frac{|\beta_2| N^2}{t_0^2 \cdot \gamma} \tag{3.3}$$

where fundamental solitons have order ($N = 1$). Fig. 3.1 shows one period ($\pi L_D/2$) of a second-order soliton.

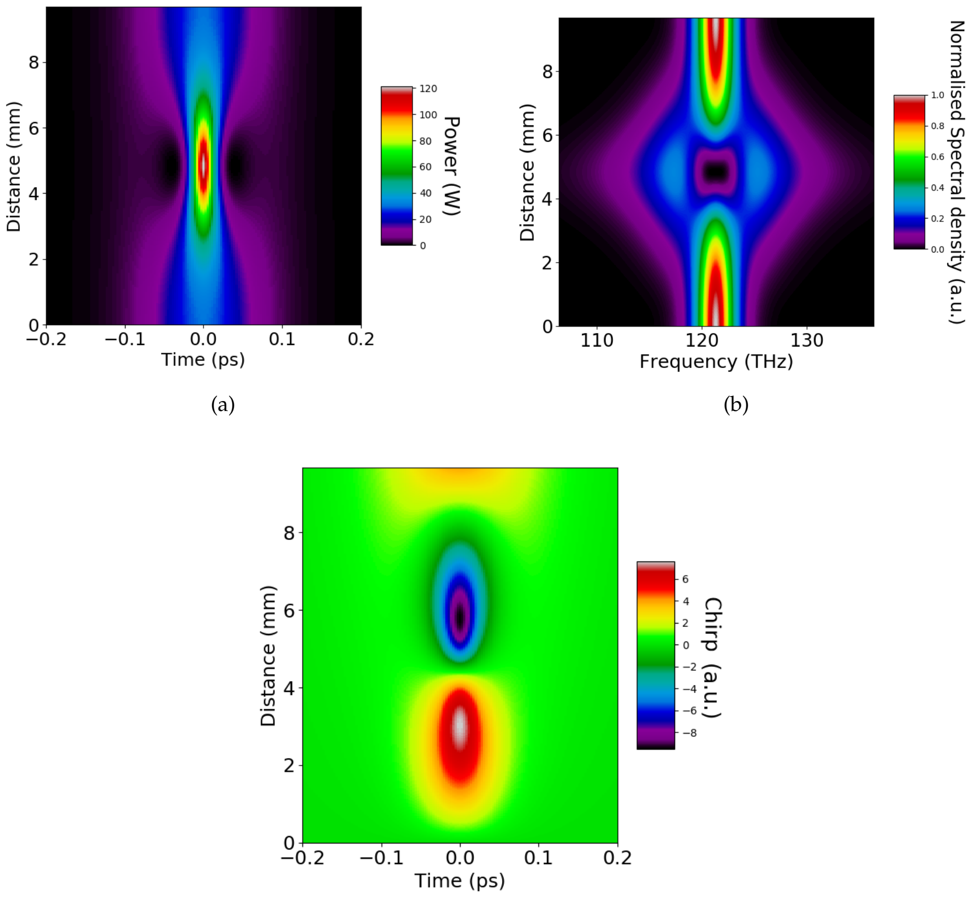

(a)

(b)

(c)

FIGURE 3.1: Periodic evolution of a second-order soliton in (a) time, (b) spectrum and (c) chirp. $\lambda = 2.47\,\mu\text{m}$, $\gamma = 2 \times 10^{-3}\text{W}^{-1}\text{m}^{-1}$, $\beta_2 = -0.02\text{ps}^2/\text{m}$, $T_0 = 100\,\text{fs}$, $N = 2$

Initially, SPM dominates, creating lower frequencies on the leading edge and higher on the trailing edge, giving the pulse a positive chirp. Anomalous GVD then acts on this, slowing down the lower frequencies and speeding up the higher frequencies relative to the group velocity. This contracts the pulse width. However, GVD does not stop here, and the lower and higher-frequency parts of the pulse are pulled and pushed respectively past each other, thus switching the chirp of the pulse to negative. At this point, SPM lowers the higher frequencies on the leading edge and raises the lower ones on the trailing edge, thus reducing the chirp and narrowing the bandwidth. By the end of the soliton period, SPM has narrowed the spectrum back to its original bandwidth and GVD has broadened the pulse width back to its original width, and the opposite contributions to chirp have cancelled out. The entire process then repeats, unless there is some perturbation which can cause soliton fission.

In the case of third-order solitons (see Fig. 3.2), the change in phase and corresponding chirp caused by the interplay of SPM and GVD becomes more complicated. SPM increases the chirp, which broadens the spectrum if the chirp is already positive or narrows it if the chirp is negative. At this point, anomalous GVD responds in the opposite way by compressing the spectrum if the chirp is positive and broadening it if the chirp is negative. As a result, the pulse will oscillate in a repeating pattern in time and spectrum.

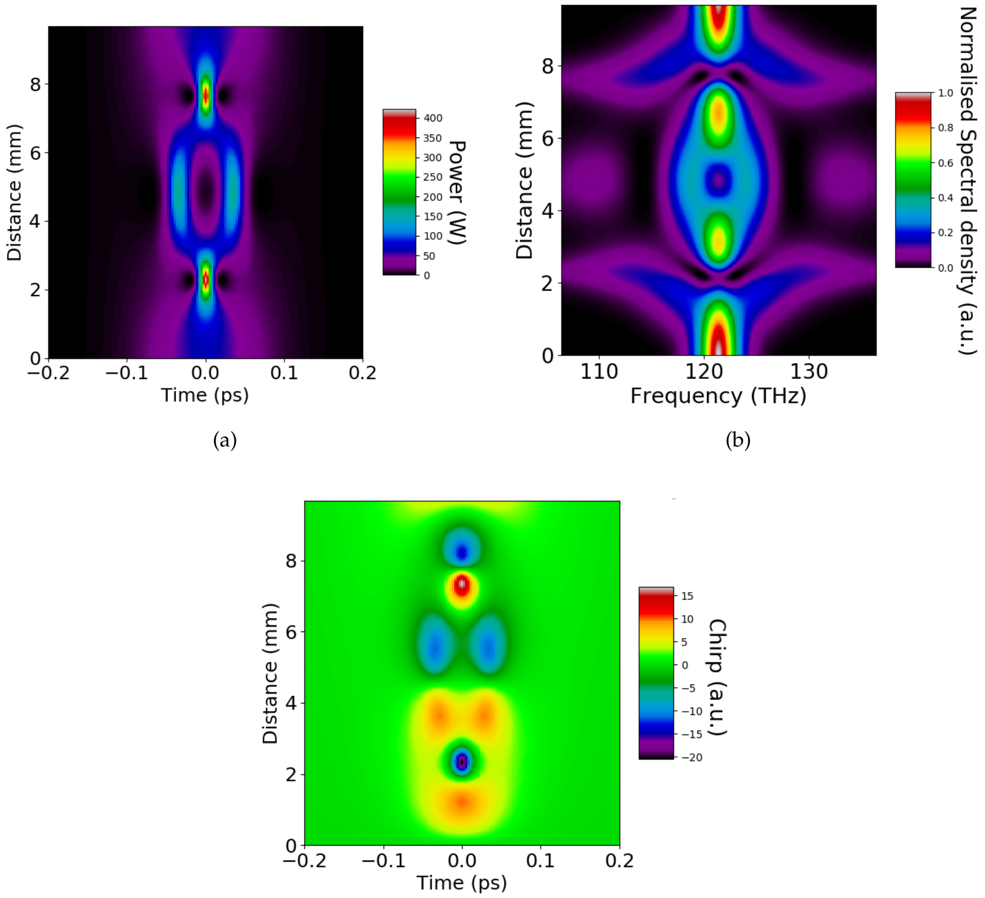

(a) (b)

(c)

FIGURE 3.2: Periodic evolution of a third-order soliton in (a) time, (b) spectrum and (c) chirp. $\lambda = 2.47\,\mu\text{m}$, $\gamma = 2 \times 10^{-3}\text{W}^{-1}\text{m}^{-1}$, $\beta_2 = -0.02\text{ps}^2/\text{m}$, $T_0 = 100\,\text{fs}$, $N = 3$

3.1.2 Broadening via SPM and soliton fission

When pulses are very short ($< 100\,\text{fs}$), initial broadening is dominated by SPM because the change in intensity of the pulse with respect to time is greater than with a longer pulse of the same peak power.

Before the dispersion length L_D, as defined in Eq. (2.74) is reached, SPM dominates over dispersion and thus the pulse broadens in frequency and narrows in time, which also means the peak power increases, and with high enough power, a higher order soliton forms. If the broadening causes enough of the spectrum to cross over the zero-dispersion wavelength (ZDW) from the anomalous dispersion regime into the normal dispersion regime, however, some of the energy of the pulse will dissipate as Cherenkov radiation [52]. This is also known as a dispersive wave (DW) because the resulting pulse can only disperse in this regime (i.e. it cannot form a soliton). This perturbation will cause the pulse to break up into a number of lower-order solitons.

The following simulations show pulse propagation through a-Si:H fibres, as they have high nonlinearity and low TPA which means the nonlinear processes are clearly discernible.

Fig. 3.3 shows the propagation through a 3 mm length of a 1.7 µm-diameter a-Si:H fibre, for a pulse with a 50 fs width and 175 W peak power. This corresponds to soliton order $N = 2.4$ (where $N = \sqrt{L_{\mathrm{D}}/L_{\mathrm{NL}}}$ and the nonlinear length L_{NL} is defined in Eq. **??**). Thus a second-order soliton forms and then when the soliton fission length $L_{\mathrm{fiss}} = L_{\mathrm{D}}/N$ (0.78 mm) is reached, a DW is emitted (seen in the time evolution plot Fig. 3.3 (a) as the right-most purple band) and the soliton fissions into two fundamental solitons, with the new soliton moving faster than the main one which is delayed. Fig. 3.3 (b) shows the spectrum at the fission length, and the DW is seen at 1.71 µm.

The phase-matching between the DW and soliton can be analysed as follows. Let the phase of a wave at frequency ω and the phase of a soliton (with frequency ω_s) be defined as:

$$\phi(\omega) = \beta(\omega)z - \omega\left(\frac{z}{v_g}\right) \tag{3.4}$$

$$\phi(\omega_s) = \beta(\omega_s)z - \omega_s\left(\frac{z}{v_g}\right) + \frac{1}{2}\gamma P_s z \tag{3.5}$$

where P_s is the peak power of the soliton, which gains a nonlinear phase-shift of $\gamma P_s z/2$ as it propagates. A DW can be emitted with a frequency ω when the phase-matching condition $\phi(\omega) = \phi(\omega_s)$ is met i.e. when

$$\begin{aligned} \beta(\omega)z - \omega\left(\frac{z}{v_g}\right) &= \beta(\omega_s)z - \omega_s\left(\frac{z}{v_g}\right) + \frac{1}{2}\gamma P_s z \\ \implies \beta(\omega) &= \beta(\omega_s) + \beta_1(\omega - \omega_s) + \frac{1}{2}\gamma P_s \end{aligned} \tag{3.6}$$

We can substitute the Taylor expansion Eq. (2.97) of $\beta(\omega)$ up to order 4, exanding around ω_s, into Eq.(3.6) to get:

$$\begin{aligned} \beta(\omega_s) + \beta_1(\omega - \omega_s) + \frac{1}{2}\beta_2(\omega - \omega_s)^2 + \frac{1}{6}\beta_3(\omega - \omega_s)^3 &+ \frac{1}{24}\beta_4(\omega - \omega_s)^4 \\ = \beta(\omega_s) + \beta_1(\omega - \omega_s) &+ \frac{1}{2}\gamma P_s \\ \implies \frac{1}{2}\beta_2(\omega - \omega_s)^2 + \frac{1}{6}\beta_3(\omega - \omega_s)^3 + \frac{1}{24}\beta_4(\omega - \omega_s)^4 - \frac{1}{2}\gamma P_s &= 0 \end{aligned} \tag{3.7}$$

In the case where β_4 is negligible, and defining $\Omega = \omega - \omega_s$ as the angular frequency separation between the soliton and the DW, this becomes:

$$\beta_2\Omega^2 + \frac{\beta_3}{3}\Omega^3 - \gamma P_s = 0 \tag{3.8}$$

The solution for Ω can be approximated as [53]:

$$\Omega = -\frac{3\beta_2}{\beta_3} + \frac{\gamma P_s \beta_3}{3\beta_2^2}, \tag{3.9}$$

Fig. 3.3 (c) shows the evolution of the spectrum, showing that the higher-intensity soliton shifts to a longer wavelength, and correspondingly its emitted DW is shifted to shorter wavelength. Fig. 3.3 (d) shows the two solitons at the end of the 3 mm fibre, and the DW which is a wide hump with low power at around 0.5 ps.

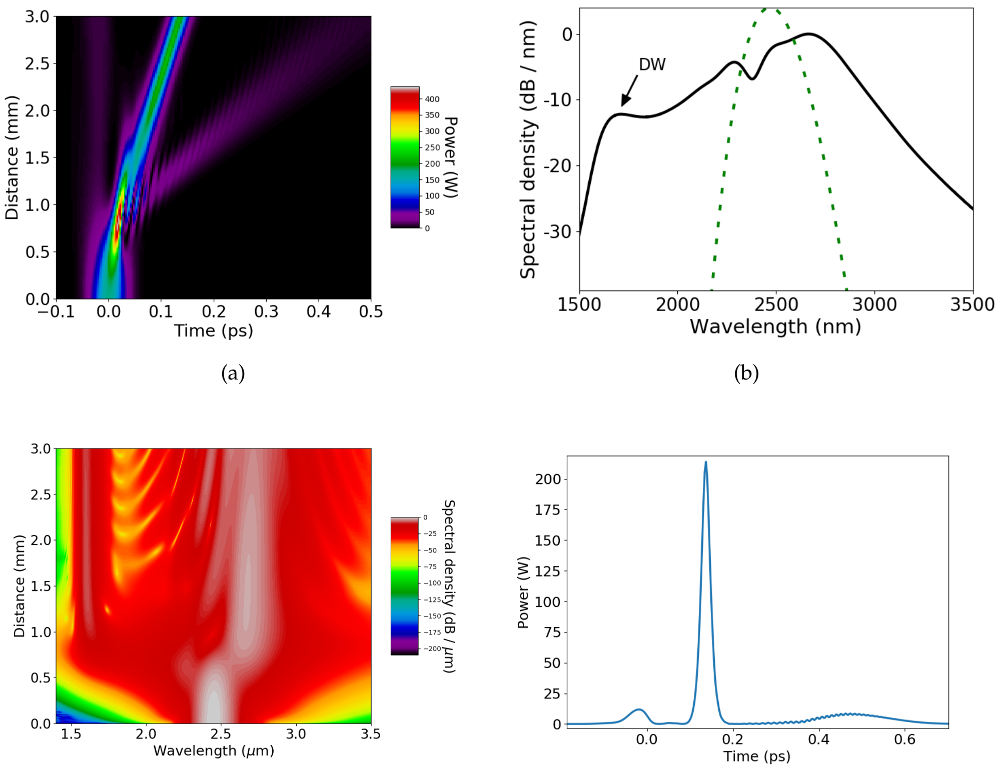

(a)

(b)

(c)

(d)

FIGURE 3.3: (a) Evolution of a second-order soliton propagating through 3 mm of an a-Si:H fibre, fissioning and releasing a DW. (b) The spectrum at the point of fission (c) Evolution of the spectrum (d) The pulses and DW at the end of the fibre

3.1.3 Pulse break-up when Four Wave Mixing dominates

Dispersive waves can be generated in a different manner when longer input pulses are used, provided that the soliton-order $\gg 10$ [54]. In this case, FWM is the dominant source of spectral broadening, and if the spectrum crosses the ZDW, a DW can arise out of this phase-matched process.

Fig. 3.4 shows a 1.7 μm-diameter, 2 cm long a-Si:H fibre, pumped at 2.47 μm (in the anomalous region), which is approximately 0.31 μm away from the ZDW (2.16 μm), with 2 ps-long pulses, long enough that FWM dominates over SPM.

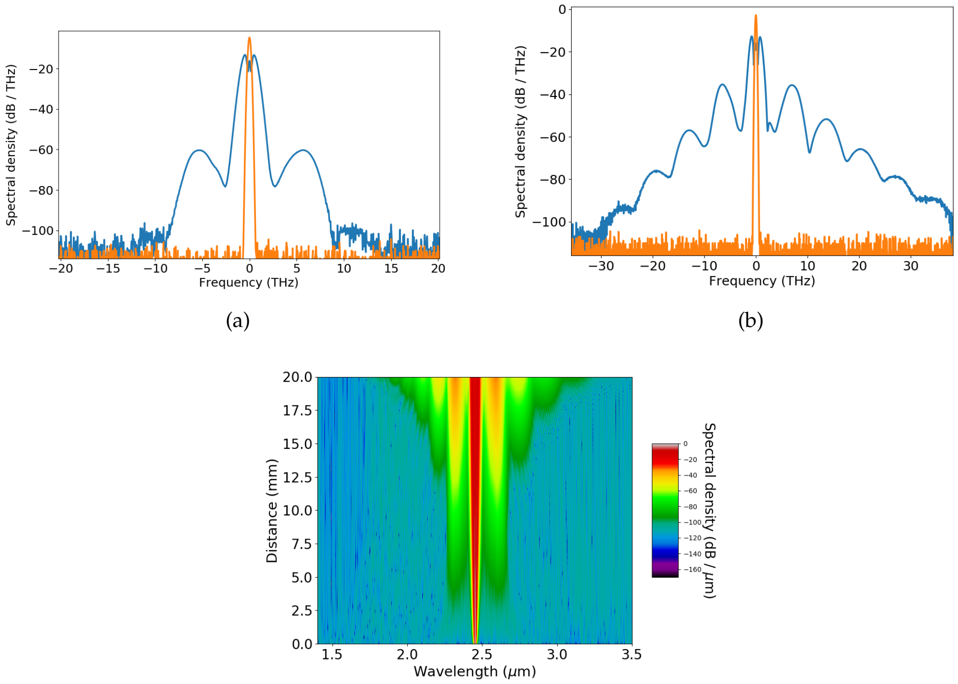

(a)

(b)

(c)

FIGURE 3.4: (a) Spectrum produced by 20 W, 2 ps-long pulses at 20 mm, showing the first FWM sidebands. (b) 30 W pulses, showing cascaded FWM. (c) Spectral evolution showing cascaded FWM happening with propagation distance.

Fig. 3.4 (a) shows the output pulse spectrum with 20 W peak power, where FWM peaks appear at $\pm\omega = \sqrt{2\gamma P_0/|\beta_2|} = 6.08$THz. Then, at 30 W in Fig. 3.4 (b, c), cascaded FWM occurs with 7 THz intervals. These processes are governed by MI, which amplifies the noise, and at a high enough power (40 W), this process breaks up the pulse into several shorter pulses. This is accompanied by the emission of a dispersive wave in the normal dispersion regime, at 1.73 μm, which occurs at the end of the fibre.

To show the process more clearly, Fig. 3.5 shows pulse propagation with 75 W peak power, so that the DW can be seen appearing at around 12 mm and then persisting along the fibre.

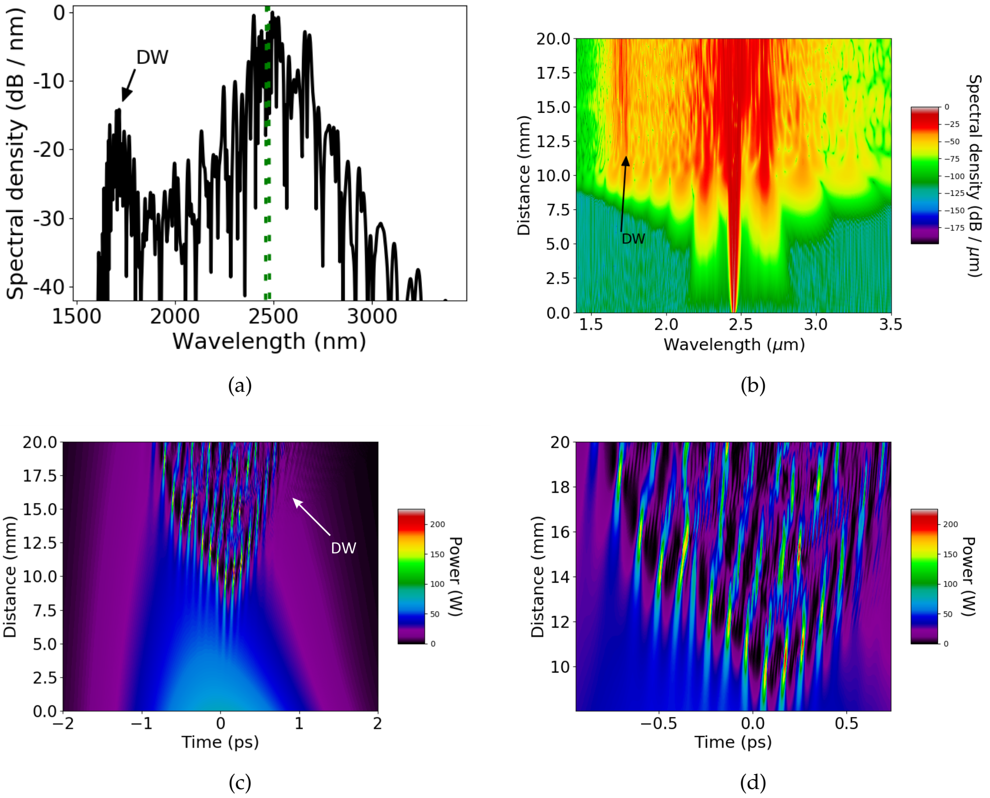

FIGURE 3.5: (a) Spectrum produced by 75 W, 2 ps-long pulses at 20 mm, showing the dispersive wave. (b) Spectral evolution (c) Time evolution showing breakup of pulse into sub-pulses (d) Propagation of sub-pulses (close-up of (c)).

With this peak power, the soliton order is 63.5, and the soliton fission length is 3.95 cm, so it is clear that the DW is not caused by soliton fission. In any case, it is clear that it does not occur in the same way as with soliton fission, where the wave appears at the edge of the spectrum and then shifts to a shorter wavelength, but rather emerges out of the phase-matched FWM processes already occurring. Thus it does not form such a strong band, but it is clearly present. The breakup of pulses in the time domain looks different to soliton fission as well, with pulse delay being much less pronounced and no sign of solitons passing through each other. It is also harder to see the dispersive wave, with the only indication being a faint band of streaks moving up and to the right at around 15 mm and 1 ps in Fig. 3.5 (c). However, this is not surprising as the DW itself in the wavelength domain is only slightly more pronounced than the surrounding material, and appears to consist of multiple bands. This entire spectrum is very noisy because the FWM process starts by amplifying noise. Thus a SC produced in this manner is not coherent in the time domain between pulses.

3.2 Simulations of SC generation in a p-Si fibre

The following simulations were conducted originally to compare with experiments being conducted at Southampton with a 15 mm-long p-Si fibre with 2 μm core diameter. These were inconclusive, but the simulations show a range of the nonlinear processes involved in SC generation, so are useful for study here. Fig. 3.6 shows the calculated dispersion-curve for this fibre.

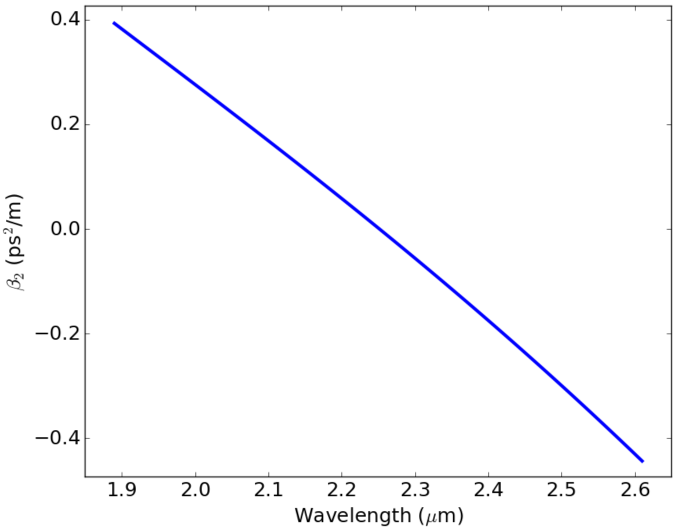

FIGURE 3.6: Calculated dispersion-curve of 2 µm-diameter p-Si fibre

The ZDW is at 2.25 µm. The simulations use 2.4 µm pulses with a peak power of ∼600 W and FWHM of 200 fs. Table 3.1 shows the full set of parameters used.

Parameter	Value
$\lambda(\mu m)$	2.4
$n_2(cm^2/GW)$	1.04×10^{-4}
$A_{eff}(\mu m^2)$	1.23
$\beta_{3PA}(cm^3/GW^2)$	2.66×10^{-3}
$\beta_2(ps^2/m)$	-5.866
$\beta_3(ps^3/m)$	5.578×10^{-3}
$\beta_4(ps^4/m)$	-2.594×10^{-5}
$\beta_5(ps^5/m)$	1.866×10^{-7}
L (mm)	15
α (dB/cm)	2
T_{FWHM} (fs)	200
P_0	585W

TABLE 3.1: Parameters used for the 2 µm-diameter p-Si fibre

.

3.2.1 Numerical simulation of SC generation dynamics

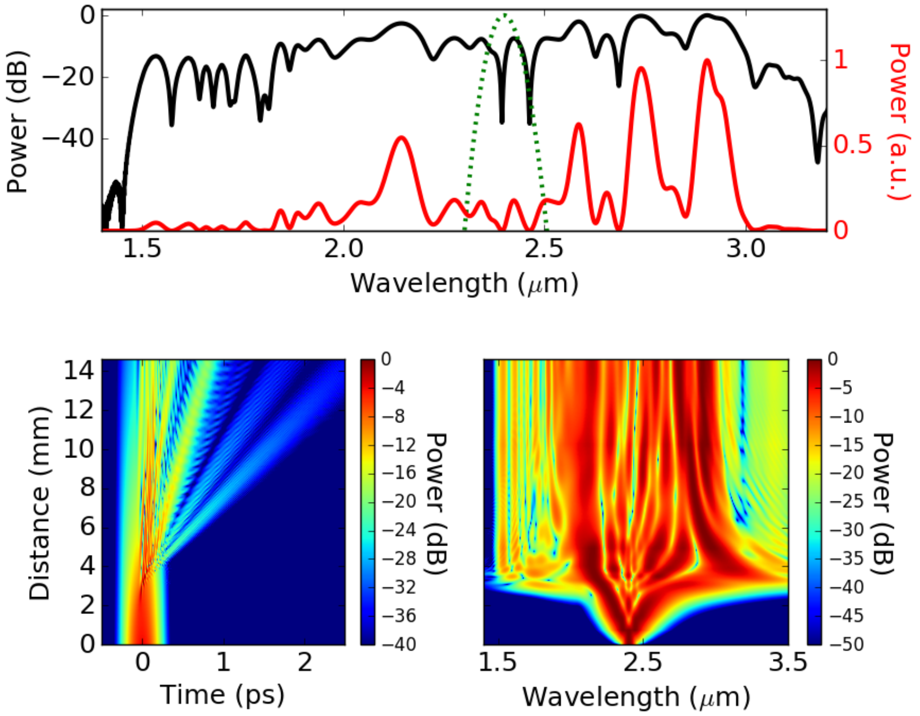

FIGURE 3.7: Simulation of 200 fs pulses with 587 W peak power (10 mW average) through a 15 mm-long, 2 μm-diameter p-Si fibre. (a) Output spectrum (green dashed line shows input). (b) Temporal evolution of the pulses. (c) Spectral evolution.

Figure 3.7 shows the output of the full simulation. To analyse the dynamics, spectrograms were produced at periodic intervals along the fibre length and studied to gain insight into the interplay between time and frequency characteristics of the pulses as they propagate.

A spectrogram is defined as [55]:

$$S(\omega, \tau) = \left| \int_{-\infty}^{\infty} E(t)R(t-\tau)\exp(-\mathrm{i}\omega t)\mathrm{d}t \right|^2 \tag{3.10}$$

where $R(t-\tau)$ is a gating function with a shape such as a Gaussian, with a width τ. The gate can be thought of as a time-dependent Fourier transform that shows how the frequency components of a pulse vary according to position in the time domain. This is useful as it can highlight where specific wavelengths are separating from the rest of the pulse, as is the case with DWs.

The temporal resolution is inversely related to the width of the pulse, and the spectral resolution has the opposite relationship, so some trial and error is needed to find a gate width that shows a useful relationship between the time and frequency domains. In the following figures, a Gaussian window with a 0.03 ps width was used.

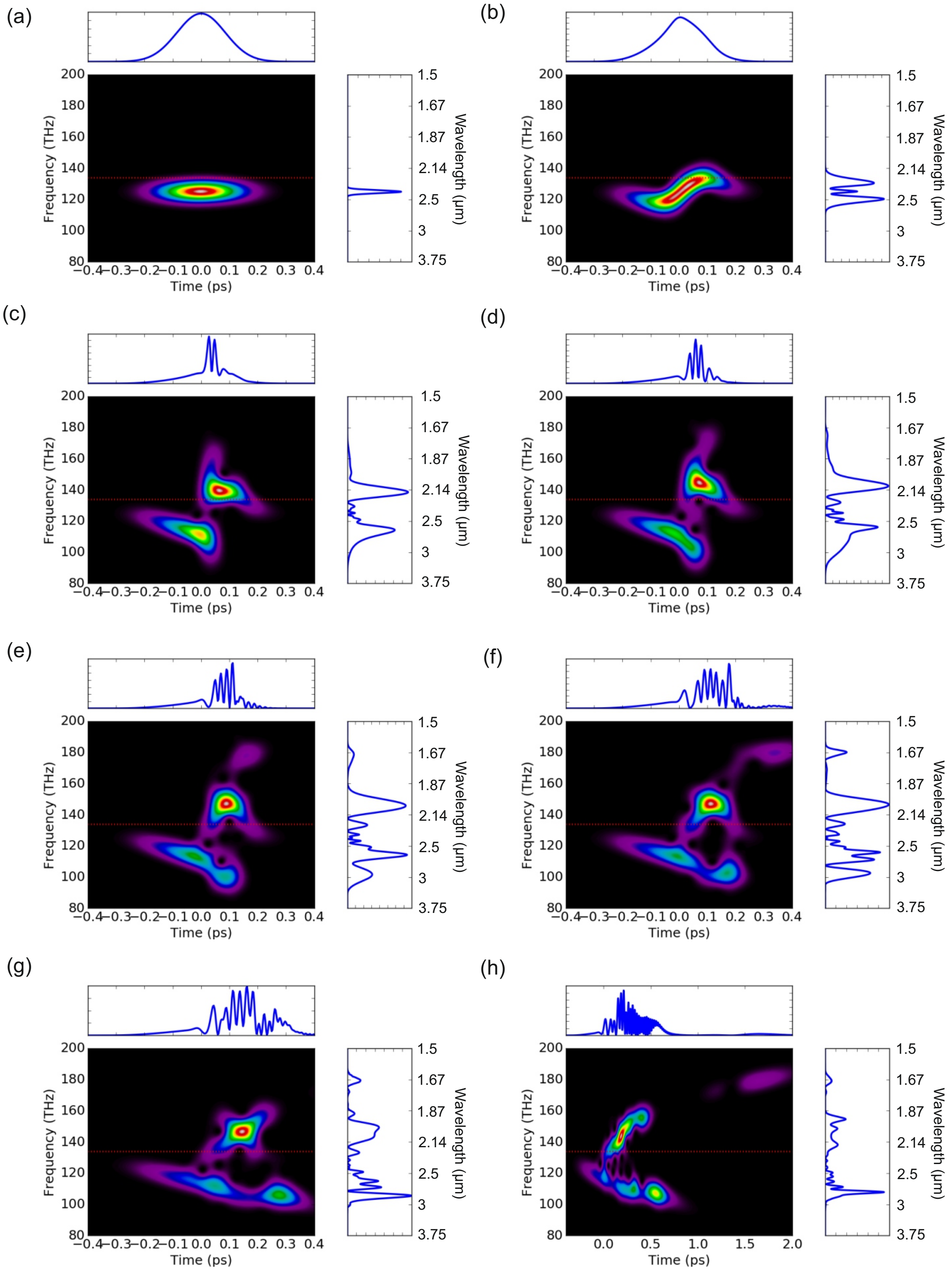

FIGURE 3.8: Spectrograms showing evolution of pulse propagation at (a) input (b) 2.2 mm (c) 3.5 mm (d) 4.22 mm (e) 4.8 mm (f) 6.1 mm (g) 7.5 mm and (h) output. The red dashed-line shows the zero-dispersion frequency. The normal dispersion regime is above it and anomalous below.

The implementation in the code defines $R(t_w) = \exp[-t_w^2/(2\tau^2)]$ in which t_w is the time-window used in the GNLSE-solver, but shifted such that it starts halfway through the pulse window. A series of slices is calculated, each one as

$$\mathcal{F}\left\{\exp\left(-\frac{t_w^2}{2\tau^2}\right)E(t)\right\}. \tag{3.11}$$

where t_w shifts back one time-step for the next slice, such that the gating function effectively scans across the entire time-window. The modulus squared is applied to the entire 2D array, and plotted as shown in Fig. 3.8.

Initially the pulse spectrum lies entirely in the anomalous dispersion region (see Figure 3.8 (a)), as the pump is at 2.4 µm (125 THz) and the ZDW (the red dashed-line in the spectrograms) is at 2.24 µm (133.84 THz). The spectral width (FWHM) is 2.2 THz. The horizontal and symmetrical oval shape shows that the pulse is not chirped, i.e. all parts of the pulse contain the same range of frequencies. The pulse starts broadening due to SPM, giving it a positive chirp, and part of the spectrum crosses over the ZDW, as shown in Figure 3.8 (b). The chirp is shown by the tilting of the central part of the shape from bottom left to top right (i.e. the frequencies in the trailing edge of the pulse are higher than in the leading edge). Treating the input pulse as a HO soliton (of order $N = 22$) means the soliton fission length is ~3.9 mm, but by 3.5 mm, approximately half of the pulse spectrum has entered the normal dispersion regime and so only a fraction of the component solitons remain intact. These components nonetheless begin to separate at ~4.2 mm (Figure 3.8 (d)), and the lower half of the spectrogram shows the onset of this splitting. The soliton with highest peak power can be discerned clearly in Figure 3.8 (e) as a peak at ~100 THz and 0.1 ps in the lower half of the spectrogram. This soliton then adjusts its shape as it is perturbed by higher-order dispersion, which it does by shaking off energy in the form of Cherenkov-like radiation. The frequency of this radiation is ~180 THz, which is phase-matched with the soliton (at ~100 THz) according to Eq. (3.9), where $\beta_2 = -0.6\,\mathrm{ps}^2/\mathrm{m}$ and $\beta_3 = 3.7 \times 10^{-3}\,\mathrm{ps}^3/\mathrm{m}$ so the first term is dominant, giving a frequency separation between the soliton and DW of (2π)80 THz, matching the observed separation in the spectrogram. The second term gives only a small correction for a soliton with peak power of a 500 W of (2π)1.5 THz. The energy build-up at the phase-matched frequency, in the form of a dispersive wave, is seen in Figure 3.8 (e) as a peak in the top half of the spectrogram (at around 0.15 ps), corresponding to a wavelength of $\sim$ 1.67 µm. The DW propagates at a lower group velocity than the soliton, so it gets increasingly delayed until they stop overlapping (Figure 3.8 (f)) and no more energy can be transferred. After this, the soliton gets delayed (but to a lesser extent than the DW) Figure 3.8 (g). Figure 3.8 (h) shows the final state of the pulses, in which it can be observed that the DW is delayed by 1.75 ps relative to the leading edge of the pulse, and the primary soliton (from which the DW had been emitted) has almost completely separated from the rest of the pulse.

3.3 Conclusion

In this chapter, I have shown various nonlinear processes that are involved in SC generation, such as SPM, soliton fission, FWM and MI. The combination of these processes are analysed in a full simulation of a p-Si fibre with the aid of spectrograms. This study will help during the design of tapered fibres later in the thesis, as the design choices will require taking the different processes into account.

In the next chapter, I compare some simulations with experimentally measured spectra in a fixed-diameter fibre, ridge waveguide and a tapered fibre, in order to show that the code solving the GNLSE works as expected and produces reasonable predictions.

Chapter 4

Code validation: experimental comparison

4.1 Introduction

In the previous chapters the GNLSE was introduced, and nonlinear effects were discussed and simulated both individually and in combination in the process of SC generation. In this chapter, some of the initial tests of the model are shown. In order to ensure that it was producing sensible results, I simulated a few examples of silicon fibres and waveguides and compared these with the measured spectral outputs.

4.2 Multi-mode silicon-core fibre

When developing the pulse-propagation model, the first test was to replicate the simulations carried out in [34]. In that paper, two a-Si:H fibres with core diameters of 1.7 and 5.7µm were fabricated. Pulses with a wavelength of 1.54µm were coupled in and the output spectra measured. A series of simulations was then run with different proportions of light in the first four linearly polarised modes to ascertain how much the higher-order modes would contribute to the spectral width and shape.

In the case of the 12 mm long 5.7 µm diameter fibre, which can contain a large number of modes, it was nonetheless concluded that the best agreement was found when assuming $> 98\%$ of the light was in the fundamental mode. Fig. 4.1 shows the original simulation from the paper, overlaid on the measured spectra, and my recreation of that simulation. The parameters used for the simulation are shown in Table 4.1

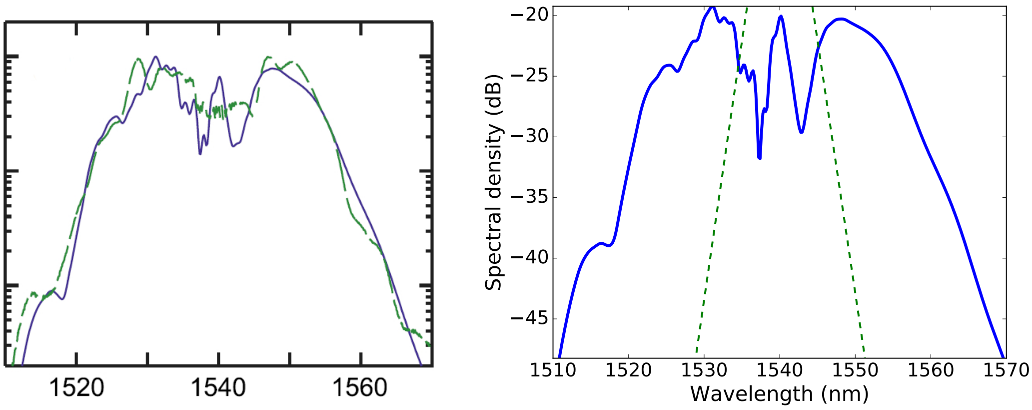

(a)

(b)

FIGURE 4.1: Simulations of 1.54 µm pulses propagating through a 12 mm long a-Si:H core fibre with 5.7 µm diameter core. (a) Original simulation from [34] (blue line) overlaid on measured spectra (green dashed line). (b) Output from my simulation (green dashed line is input pulse for reference).

Parameter	**Value**	**Parameter**	**Value**
$\lambda(\mu\text{m})$	1.54	R_{11} $(\times 10^{11}\text{m}^{-2})$	0.816
$n_2(\text{cm}^2/\text{GW})$	1.8×10^{-4}	R_{12} $(\times 10^{11}\text{m}^{-2})$	0.682
$\beta_{\text{TPA}}(\text{cm}/\text{GW})$	0.8×10^{-3}	R_{13} $(\times 10^{11}\text{m}^{-2})$	0.666
σ (m^2)	1×10^{-20}	R_{14} $(\times 10^{11}\text{m}^{-2})$	0.662
k_c (m^3)	1.35×10^{-27}	R_{22} $(\times 10^{11}\text{m}^{-2})$	1.011
Power in LP_{01} mode (%)	98.7	R_{23} $(\times 10^{11}\text{m}^{-2})$	0.795
Power in LP_{02} mode (%)	0.8	R_{24} $(\times 10^{11}\text{m}^{-2})$	0.767
Power in LP_{03} mode (%)	0.3	R_{33} $(\times 10^{11}\text{m}^{-2})$	1.043
Power in LP_{04} mode (%)	0.2	R_{34} $(\times 10^{11}\text{m}^{-2})$	0.815
$\beta_1^{(2)} - \beta_1^{(1)}$ (ps/m)	87.79	R_{44} $(\times 10^{11}\text{m}^{-2})$	1.035
$\beta_1^{(3)} - \beta_1^{(1)}$ (ps/m)	253.51	L (mm)	12
$\beta_1^{(4)} - \beta_1^{(1)}$ (ps/m)	507.80	α (dB/cm)	3
$\beta_2^{(1)}(\text{ps}^2/\text{m})$	0.998	τ_c (ns)	87
$\beta_2^{(2)}(\text{ps}^2/\text{m})$	0.856	t_0 (fs)	390
$\beta_2^{(3)}(\text{ps}^2/\text{m})$	0.55		
$\beta_2^{(4)}(\text{ps}^2/\text{m})$	0.1		

TABLE 4.1: Parameters used for simulation of the multi-mode a-Si:H fibre as studied in [34].

The agreement between measured spectrum and the original simulation is good, and my pulse-propagation model successfully recreated the spectral output. This shows that my model works as expected. Furthermore, as concluded in [34], the majority of spectral broadening and shape can be assumed to occur due to light propagating in the fundamental mode of a silicon-core fibre, and this is the assumption carried forward throughout this thesis.

One caveat should be noted, however, which is that the nonlinear interaction (or walk-off) length between the modes is shorter than the total length of the fibre. This is calculated as [56]:

$$L_W = \frac{t_0}{d_{mn}} \tag{4.1}$$

where $d_{mn} = \beta_1^{(m)} - \beta_1^{(n)}$ is the walk-off parameter (i.e. the difference in group velocities of modes m and m). Taking the values from Table 4.1, walk-off lengths between between the LP$_{01}$ mode and LP$_{02}$, LP$_{03}$ and LP$_{04}$ are ≈ 4.4 mm, 1.5 mm and 0.8 mm respectively. This means that there is no interaction between the modes after the first third of the fibre. There will be other set-ups where the nonlinear interaction length is much longer, however it is proportional to pulse length, so will likely be even shorter for most of the scenarios considered later, which involve pulse lengths of 150 fs.

4.3 SOI waveguide

This simulation was originally conducted in order to see if including wavelength-dependent TPA would make a significant difference to the result. It did not, due to the low peak power of the pulses, but it is included here as the simulation nonetheless matches very closely with the authors' simulation and measured experimental output. I later look at simulations of tapered SOI waveguides in Chapter 8, so this comparison offers a suitable check.

The simulation is of pulse propagation in an a-Si:H rectangular waveguide, as studied by Leo et al. in [14]. The waveguide parameters used by the authors are given in Table 4.2. I extracted the dispersion parameters from Fig. 2 in [14] which is reproduced as Fig. 4.2. I also included wavelength-dependent TPA (see Sec. 5.3.1) in the simulation, but this had negligible impact.

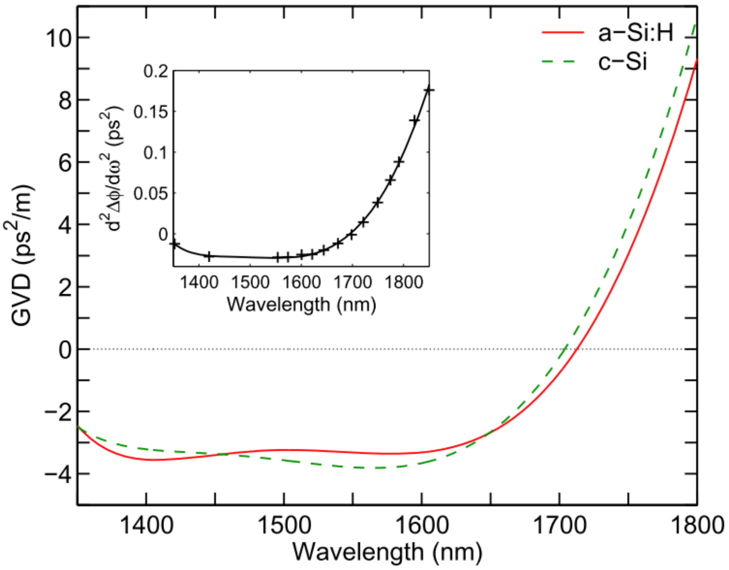

FIGURE 4.2: Measured dispersion curve of the waveguide studied in [14] (Reproduced from their Fig. 2). The red line is the a-Si:H dispersion, green-dashed is for a c-Si waveguide of similar dimensions. The inset shows the curvature of measured phase-difference between the waveguide and a reference-path, from which GVD was calculated.

Parameter	**Value**
$\lambda(\mu\mathrm{m})$	1.575
$n_2(\mathrm{cm}^2/\mathrm{GW})$	1.35×10^{-4}
$A_{\mathrm{eff}}(\mu\mathrm{m}^2)$	0.07
$\beta_{\mathrm{TPA}}(\mathrm{cm}/\mathrm{GW})$	0.434×10^{-3}
$\mathrm{d}\beta_{\mathrm{TPA}}/\mathrm{d}\omega$ $(\mathrm{cm}/\mathrm{GW}/(2\pi\cdot\mathrm{THz}))$	1.254×10^{-3}
$\beta_2(\mathrm{ps}^2/\mathrm{m})$	-3.356
$\beta_3(\mathrm{ps}^3/\mathrm{m})$	-8.19×10^{-4}
$\beta_4(\mathrm{ps}^4/\mathrm{m})$	1.94×10^{-4}
$\beta_5(\mathrm{ps}^5/\mathrm{m})$	-8.3×10^{-6}
L (mm)	10
α (dB/cm)	2.65
T_{FWHM} (fs)	180

TABLE 4.2: Parameters used for simulation of the 220nm by 500nm a-Si:H waveguide studied in [14] by Leo et al.

In their experiments, Leo et al. pumped 180 fs (FWHM) pulses at 1575 nm through the a-Si:H waveguide with peak pump powers up to 13 W. SC generation in this wavelength region is difficult to achieve because of the loss caused by TPA, and so their measured spectra were a good test case to compare with simulations. The results of their modelling agreed reasonably well with the experiments, but there was a slight discrepancy in that the height of the DW around 1900 nm was higher than that measured. Fig. 4.3 shows their simulation (a) and mine (b).

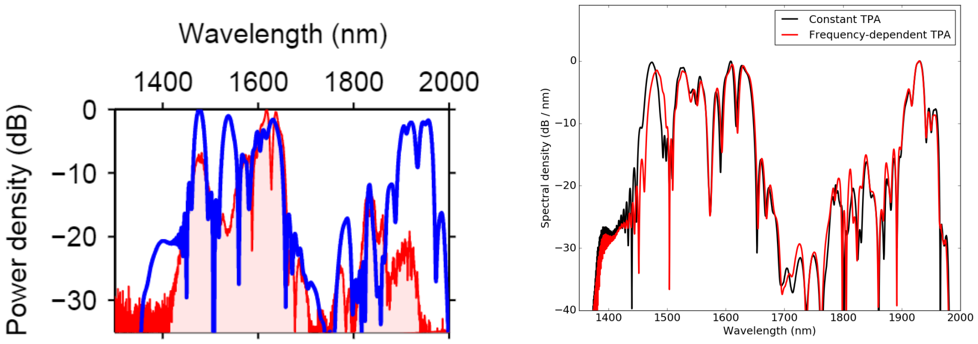

(a)

(b)

FIGURE 4.3: (a) Simulation of 13 W pulses from [14] (Fig. 3b) (b) Output of my simulation of the 13 W pulses, with and without TPA frequency-dependence.

Firstly, it is interesting to note that two features in the current simulation match the measured output more closely than the original simulation. One is the double peak around 1620 nm, and the second is the drop-off near 1400 nm, where the original simulation has a shelf. These differences are minor, however, and are presumably due to different estimates of higher orders of dispersion from their measured profile (see Fig. 4.2). The more noticeable discrepancies in both cases are the presence of a peak around 1525 nm in the simulations that is absent in the experiment, and the greater height of the DW around 1900 nm in the simulations.

The TPA would actually be lower around this DW (so could not account for its reduction in the experiment), but a higher value at a shorter wavelength may affect the soliton emitting the DW. This soliton may be at 1525 nm and is suppressed in the experiment, but attributing this to higher TPA is problematic because this would also affect the 1475 nm peak which is clearly present in experiment and modelling. As can be seen, however, including frequency-dependence of TPA makes virtually no difference on either side of the spectrum, except for a slight red-shifting of this short-wavelength peak. This experiment is not a good candidate for ascertaining the impact of the wavelength-dependence of TPA because the pump in the middle of the TPA band, where its value is high and as such it would affect the pump significantly before much spectral broadening can occur. In addition, the pump power in this case is low, so its impact would likely be hard to determine anyway. In Sec. 5.4 a much better example is shown with higher peak power in this region, as well as an example where the pump lies near the edge of the TPA band.

Although there are some minor discrepancies between simulation and experiment, the overall agreement is very good, and most importantly, my simulation matches closely that of the authors. This is further confirmation that the pulse propagation model is behaving as expected and can thus be used to make predictions.

4.4 Tapered p-Si fibre

By tapering a fibre, the dispersion properties can be varied with propagation distance. This can, for example, allow a dispersive wave to be pushed further away from the soliton that generates it by shifting the ZDW, thus broadening the overall SC. Also, a taper can be useful as the length of the smallest diameter-part can be minimised, while keeping the overall fibre length long enough to be manageable. This is important because with a small waist where the nonlinearity is high, spectral broadening can occur very rapidly (over a length ~ 1 mm) but the spreading of the mode into the cladding can cause high loss, so it is desirable to increase the core diameter after broadening so as to preserve the spectrum for output coupling. Furthermore, it is easier to free-space couple the light to a larger core diameter, so a coupling lens with lower magnification is needed than with a smaller core. Therefore, a potential source of loss is reduced such that a lower pump power is needed.

The following simulations serve as a crucial test of my pulse-propagation model, as the dispersion and nonlinear parameters are varied with propagation length, adding complexity to the output. Establishing that the model works is important as predictions are made later in the thesis about the output of silicon-core fibre tapers that are yet to be fabricated and tested.

4.4.1 Modelling a taper

These simulations were carried out concurrently to the fabrication and testing of a 14.6 mm long p-Si taper by H. Ren at the University of Southampton. This was tapered after being drawn by the MCD method. A number of SC were generated with different input peak powers which are reported on in [57]. Fig. 4.4 (a) shows a sketch of the taper and (b) shows a more accurate taper profile in terms of its diameter and the corresponding ZDW.

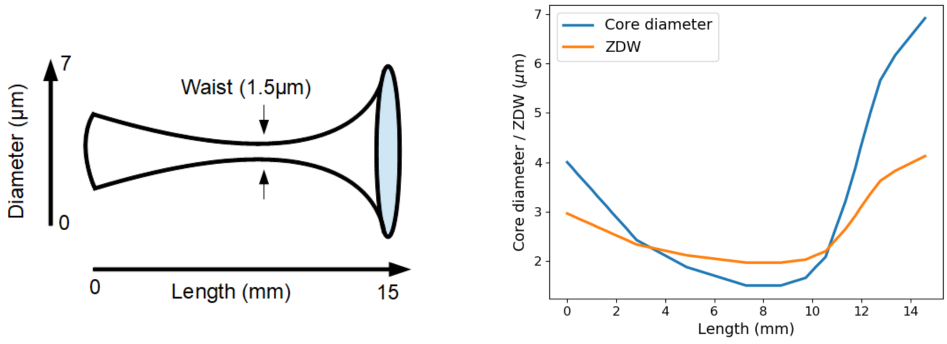

(a)

(b)

FIGURE 4.4: (a) Sketch of the taper (not to scale) (b) Variation of core diameter and ZDW with fibre length.

The taper was pumped with 200 fs pulses with a carrier wavelength of 2.4 µm and peak powers ranging from 20 W - 266 W. The fixed parameters used in the simulation are shown in Table 4.3.

Parameter	**Value**
$\lambda(2.4\,\mu\text{m})$	2.4
$n_2(\text{cm}^2/\text{GW})$	1.04×10^{-4}
$\beta_{3\text{PA}}(\text{cm}^3/\text{GW}^2)$	2.66×10^{-2}
L (mm)	14.6
α (dB/cm)	2
T_{FWHM} (fs)	200
P_0 (W)	20 - 266

TABLE 4.3: Parameters used for the tapered-diameter p-Si fibre

In order to simulate this and study the dynamics in the taper, it was modelled as a number of 200 µm-long constant-diameter sections (which is shown in Section 4.4.2 to provide a good approximation). For each of these, the dispersion coefficients $\beta_2 - \beta_5$ and effective area of the fundamental mode were calculated using Comsol (to simulate the modal field-distribution) and Matlab (to automate Comsol and output derivatives of the propagation constant, i.e. higher-order dispersion terms). This was then read into the GNLSE implementation in Python so that the parameters varied with propagation distance. The spectral output of the experiments are shown in Fig. 4.5 along with the spectral output of my simulations, and the simulated temporal and spectral evolution of 266 W peak power pulses.

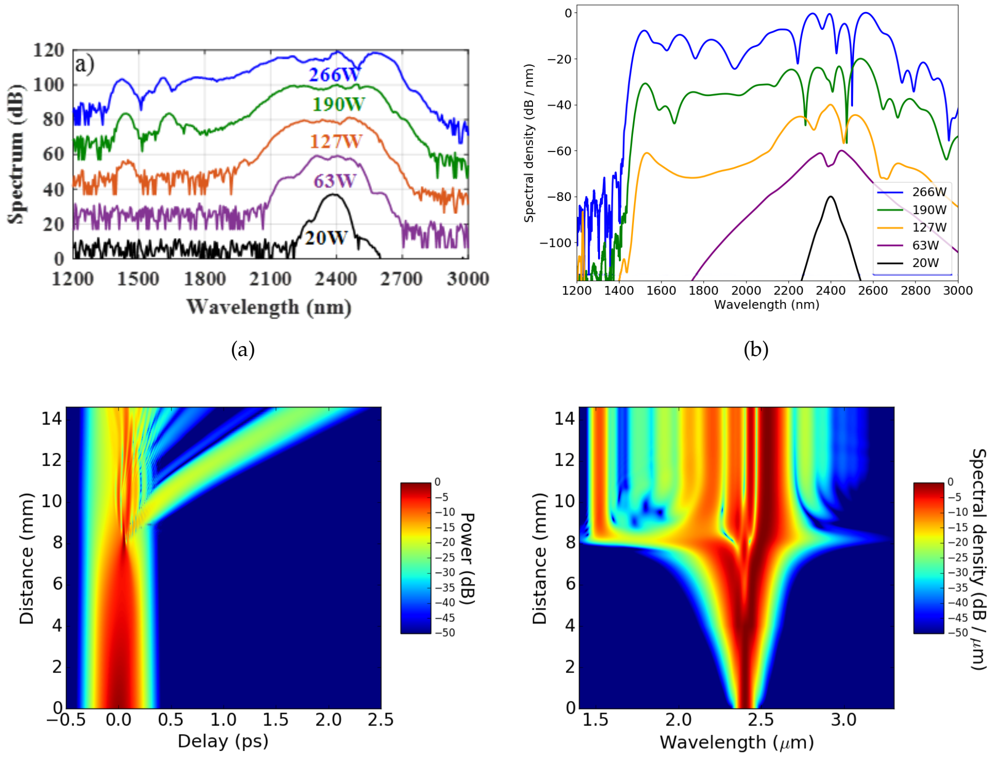

(a) (b)

(c) (d)

FIGURE 4.5: (a) Measured spectral output of p-Si tapered fibre from [57] by Ren et al. The pulses are 200 fs long and pumped at 2.4 μm with labelled peak powers. (b) Spectral output of my simulations with corresponding peak powers. (c) Temporal evolution of the 266 W peak power pulses. (d) Spectral evolution of 266W pulses.

The qualitative agreement with experiment is good. The dispersive wave appears with an input peak pump power of 127 W, and grows more prominent with additional power. Furthermore, as the power increases, additional peaks appear below 2 μm. There is a minor discrepancy between simulation and experiment, which is the precise position of the DW, which appears at 1.4 μm in the measured spectra but at 1.5 μm in the simulations. This is likely due to an incorrect estimate of the ZDW, which may be caused by unknown effects of the CaO interface layer on higher orders of dispersion.

4.4.2 Test of flat sections to approximate taper

To test that the use of 200 μm sections is a reasonable approximation, I checked the stability of the output spectra when longer sections were used (corresponding to larger core diameter steps). Figure 4.6 shows the propagation of a 266 W pulse with the same parameters as above, with 200 μm-sections (labelled '1x' in the figure) and then with sections twice as long, then five and ten times the length.

Figure 4.6 shows that the approximation is reasonable, as it is robust when the resolution is decreased. The spectra for sections twice as long is indistinguishable from the original approximation. With sections five times as long there is a noticeable difference but not a critical one, and even with sections ten times as long (which

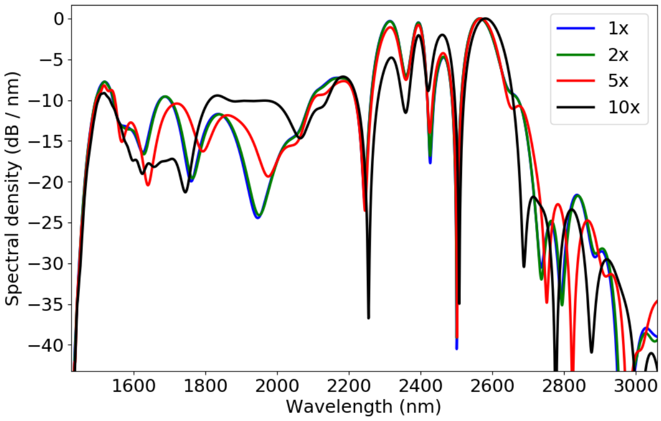

FIGURE 4.6: 266 W pulse propagating through the taper approximated with 200 µm-sections (1x) and then longer sections as labelled

means there are only eight sections) the difference is significant, but the dispersive wave is still in the correct position.

4.4.3 Discussion

A taper was successfully used to generate an SC while avoiding loss for two reasons: (1) the taper broadens out after the spectral broadening has occurred, minimising evanescent field interaction with the cladding and interface layer, and (2) the length of the fibre after SC generation is also minimised, so other loss mechanisms in the core such as free-carriers have less length over which to cause loss. The propagation of pulses through the taper was then modelled with fairly good agreement, and the model is robust against small changes in diameter, so it can be used to study other taper profiles and design new ones.

4.5 Conclusion

In this chapter, three pulse propagation simulations have been shown: an a-Si:H fibre, in which three additional LP modes were included although the propagation was dominated by the fundamental mode; a SOI ridge waveguide; and a tapered p-Si core fibre. In all cases, the agreement between simulation and experiment is good, such that the propagation code can be assumed to operating correctly and thus can be used to make reasonable predictions.

In the next chapter, I look at the wavelength-dependent parameters that are included in the GNLSE and discuss how I use them. The modification of the TPA term to make it wavelength-dependent is also discussed, and two examples are shown, one where it is not applicable and one where it is.

Chapter 5

Making the GNLSE more wavelength-dependent

5.1 Introduction

In the previous chapter I looked at the standard GNLSE, which is only partially wavelength-dependent, in that it incorporates the change in the nonlinear coefficient γ by including a self-steepening term. In this chapter I show how I have modified the code solving the equation to incorporate wavelength-dependent linear and nonlinear loss (TPA and 3PA) into the simulations studied in this thesis.

5.2 Frequency-dependent linear loss

The dominant source of linear loss in silicon-core fibres is from the core material, where the fundamental mode is mostly confined. However, at longer wavelengths the mode spreads further into the silica cladding, causing significant loss beyond 4 µm. At this point the loss in pure silica is already > 10 dB/cm [58] and continues to increase with wavelength, so as a larger fraction of the mode interacts with it, the more contribution to the loss it will make.

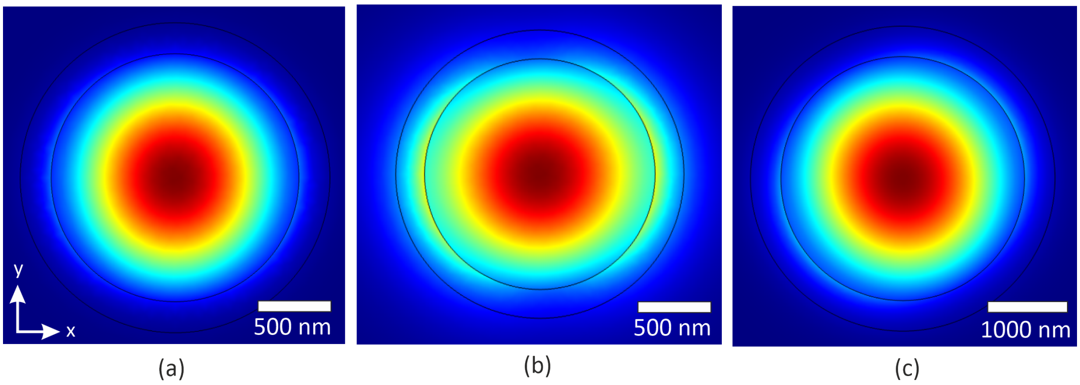

(a) (b) (c)

FIGURE 5.1: Fundamental mode in a silicon-core fibre, with CaO interface layer and silica cladding, solved by Comsol for (a) 2.1 µm with 1700 nm core diameter, (b) 4.5 µm with 1700 nm core diameter and (c) 4.5 µm with 3000 nm core diameter.

In order to include the wavelength-dependent linear loss in the simulations of silicon-core fibres, I needed to include the wavelength-dependent silica loss in the Comsol model of the fibre cross-section, which was also used to calculate the dispersion coefficients and effective areas according to diameter and wavelength. Fig. 5.1 shows the electric field of some of the fundamental modes found by Comsol. It shows the degree to which the mode spills out into the cladding (which includes the interface layer which is a mixture of CaO and silica). For example, with a core diameter of 1700 nm, the mode at 2.1 µm (a) has minimal overlap with the cladding, whereas at 4.5 µm (b) it has significant overlap, such that the cladding will cause noticeable loss. However, increasing the core diameter to 3000 nm (c) reduces this overlap and the corresponding loss.

The linear loss for the silica cladding was included in the model as the imaginary part of the refractive index, as extracted from [58]. The relevant figure from that paper is shown in Fig. 5.2 (b) over which is overlaid the values that I used in the model. (a) shows a more detailed plot of those values.

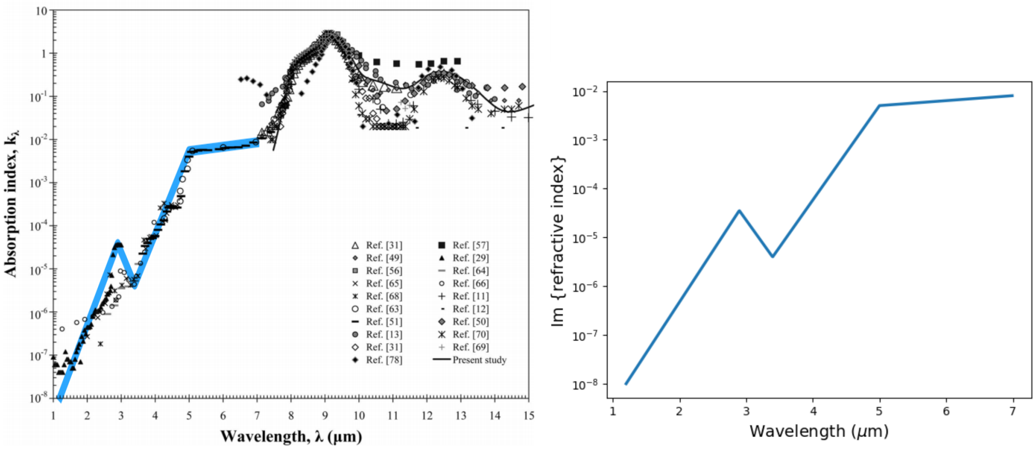

(a) (b)

FIGURE 5.2: Imaginary refractive index of silica. (a) Figure from [58], which plots the values recorded from numerous studies. The values I used are overlaid in blue. (b) The values used in the Comsol fibre model.

The Comsol model then returns an effective refractive index for the fundamental mode when it finds a solution. This includes an imaginary part, giving an effective modal linear loss which can be extracted into a value α (in dB/cm) by using

$$\alpha = \mathrm{Im}(n) \log_{10}(e) \times \frac{0.4\pi}{\lambda \times 10^{-6}}, \tag{5.1}$$

where n is the effective index of the fundamental mode and λ is the wavelength in microns.

Of course the dominant source of linear loss is from the bulk material itself. There is a scarcity of optical loss measurements for this, and thus measurements that are reported are for specific waveguide or fibre structures, which already include losses from scattering and cladding and also depend on the crystal grain sizes. Nonetheless, by looking at a number of sources [59], [13], [60], some reasonable estimates can be made, as shown in Table 5.1.

Wavelength (µm)	**Linear loss (dB/cm)**
1.55	3
2.1	0.8
3	0.05

TABLE 5.1: Estimates of material linear optical loss in bulk p-Si.

A line based on these values can then be added to the cladding losses estimated using Comsol, resulting in the loss profiles plotted in Fig. 5.3 for silicon-core diameters of 1700 – 3000 nm. The dotted lines show the contribution from cladding loss alone, which dominates for wavelengths > 3µm.

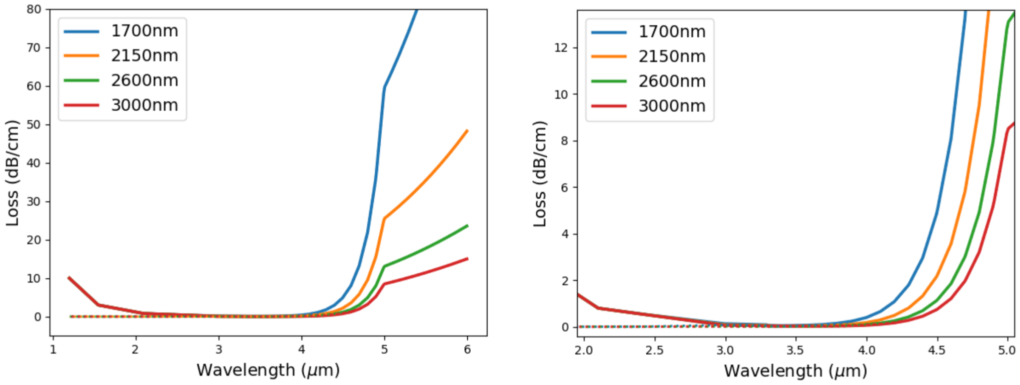

(a)

(b)

FIGURE 5.3: Linear loss for silicon-core fibres with core diameters from 1700 nm – 3000 nm. Wavelength-dependent loss for (a) 1 – 6 µm and (b) 2 – 5 µm to show more detail. Dotted lines show contribution from cladding loss alone.

This linear loss envelope is included directly in the code by turning α_l in Eq. 2.52 into $\alpha_l(\omega)$. As the term is applied directly in the frequency domain, an array can be specified rather than a constant to map loss values onto their position in this domain. In order to test that it is working correctly, I ran some simulations of continuous wave (CW) propagation through 1 cm lengths of fibre with the diameters shown in Fig. 5.3. I switched off the nonlinear loss terms such as TPA and FCA and used a low power pulse of 1 W in order to minimise any nonlinear phase-matching effects that happen with higher input powers.

I used four wavelengths: 1.55, 2.1, 3 and 4.5 µm, with the frequency window centred on 2.1 µm in all cases to ensure that the loss was being applied across the frequency window. For the first three wavelengths I only look at one diameter because the material loss from the core dominates. However, for 4.5 µm, the cladding loss is the dominant source of loss and so core diameter makes a significant difference.

I recorded the losses in power at the end of the fibre propagation simulation and compared these with the calculated linear loss values L_{calc} where

$$L_{\text{calc}} = P_{\text{in}}\left(1 - 10^{-\alpha/10}\right), \tag{5.2}$$

$P_{\text{in}} = 1$ W is the input power and α is the loss coefficient in dB/cm. Fig. 5.4 shows the power loss in each simulation and Table 5.2 summarises the findings.

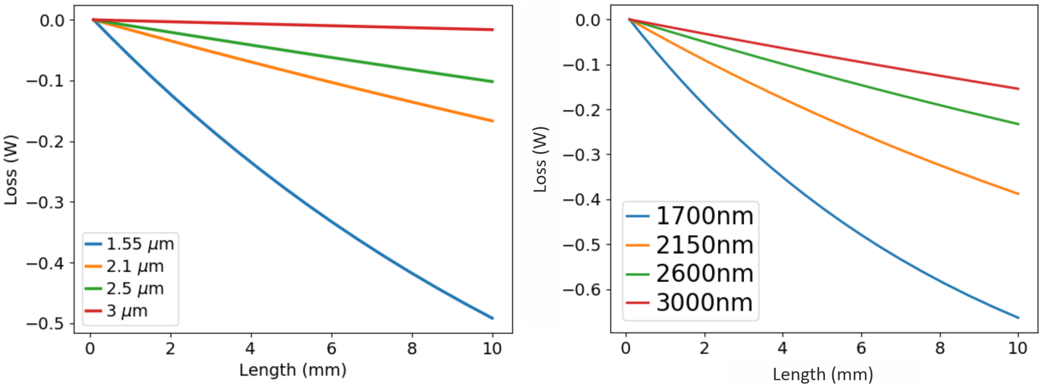

(a) (b)

FIGURE 5.4: Average power loss in simulations of a 1 W power CW propagating through a 1 cm length of silicon-core fibre with: (a) 2600 nm core diameter at wavelengths of 1.55 – 3 μm where the dominant source of loss is the silicon core material; (b) labelled core diameters at 4.5 μm where the dominant source of loss is the overlap with the silica cladding. The spectral window is centred on 2.1 μm but the other CW wavelengths are offset to demonstrate that the linear loss envelope is working.

Wavelength (μm)	**Diameter (nm)**	**Loss (dB / cm)**	**1 cm loss (calculated)**	**1 cm loss (simulation)**
1.55	2600	3	0.5 W	0.49 W
2.1	2600	0.8	0.17 W	0.17 W
2.5	2600	0.47	0.10 W	0.10 W
3	2600	0.05	0.01 W	0.02 W
4.5	1700 2150 2600 3000	5.1 2.1 1.17 0.75	0.69 W 0.38 W 0.24 W 0.16 W	0.66 W 0.39 W 0.23 W 0.15 W

TABLE 5.2: Linear loss values for wavelengths from 1.55 – 4.5 μm and expected power losses for a 1 W CW propagating through 1 cm of silicon-core fibres with labelled diameters.

As Table 5.2 shows, the simulated power losses are in good agreement with the calculated losses, so I am confident that the linear loss term in the code is behaving as expected.

It is interesting to note that, although the linear loss values for 4.5 μm are quite high, they do drop below 1 dB/cm when the silicon-core diameter reaches 3000 nm, which is promising for wavelength conversion to wavelengths in this region, as will be explored in Chapter 6.

5.3 Wavelength dependence of TPA

TPA is wavelength-dependent, and thus it should have an impact on SC generation because it causes some frequencies to be absorbed more strongly than others. This is not generally included in simulations, so I modified the GNLSE to ascertain whether or not it should be included. If it could be shown to have a significant effect, then it may also be necessary to include the frequency-dependence of 3PA as this would affect SWIR SC generation.

In this section the effect will be tested to make sure it behaves as expected. First, the wavelength-dependence is included in the GNLSE as a derivative at the pump wavelength. Then this is replaced with a fully specifiable envelope function to increase the accuracy of the effect.

5.3.1 Including the wavelength-dependent TPA term as a derivative

The frequency-dependent term to adjust TPA was implemented in a similar manner to the self-steepening term which adjusts γ as:

$$\begin{aligned}\beta_{\mathrm{TPA}}(\omega-\omega_0)(|A|^2A) &= \beta_{\mathrm{TPA}}(\omega_0)(|A|^2A) + i\frac{\mathrm{d}\beta_{\mathrm{TPA}}}{\mathrm{d}\omega}\Big|_{\omega=\omega_0}\frac{\partial(|A|^2A)}{\partial t} \\ &= \beta_{\mathrm{TPA}}(\omega_0)(|A|^2A) + i\frac{\mathrm{d}\beta_{\mathrm{TPA}}}{\mathrm{d}\omega}\Big|_{\omega=\omega_0}\mathcal{F}^{-1}\left\{-i(\omega-\omega_0)\mathcal{F}(|A|^2A)H(\omega)\right\} \quad (5.3)\end{aligned}$$

where $H\omega)$ is a Heaviside step function that has a value of 1 for wavelengths up to 2.2 µm, at which point it switches to zero such that there are no negative values of TPA.

This addition to the GNLSE was tested by comparing the effect of TPA on a pulse propagating with a frequency offset from the centre of the simulation window, which is achieved by modifying the phase (ϕ) of the Gaussian pulse in the following way:

$$A(0,t)\exp(-i\phi) = \exp\left(-\frac{t^2}{2t_0^2}\right)\exp(-i(\omega-\omega_0)t). \quad (5.4)$$

In this test the central frequency was set corresponding to a wavelength of 2.2 µm, and TPA was defined as zero. The frequency-dependent TPA term was set such that its value at 1.55 µm should be 0.46 cm/GW. This value was taken from the curve fit to Lin et al. in Fig. 4(a) from [46], which is reproduced here as Fig. 5.5.

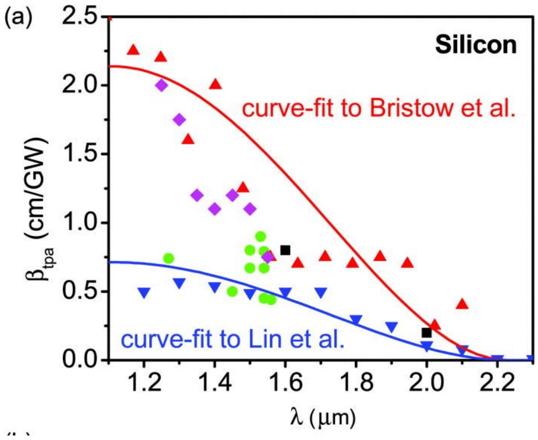

FIGURE 5.5: Measured values of TPA in silicon, reproduced from Fig. 4 (a) in [46].

To confirm this, a 75 W peak power, 200 fs pulse was propagated for 5 mm with the parameters in Table 5.3 (where test A, B and C correspond to (a), (b) and (c) of Fig. 5.6). The output of the pulse is shown in Fig. 5.6 (a) with frequency-dependent TPA included, (b) with a flat level of TPA corresponding to the target value and (c) with TPA switched off. It is clear that the offset pulse is modified correctly and thus the frequency-dependent TPA term works. Fig. 5.6 (d) shows the profile of TPA by wavelength used.

Parameter	**Test A**	**Test B**	**Test C**
β_{TPA} (cm/GW)	0	0.46	0
$d\beta_{\text{TPA}}/d\omega$ (cm/GW/(2π·THz))	1.254×10^{-3}	0	0
λ (centre of window) (μm)	2.2		
λ (pump) (μm)	1.55		
n_2(cm^2/GW)	5.52×10^{-5}		
A_{eff}(1.4 μm^2)	1.4		
L (mm)	5		
α (dB/cm)	2		
T_{FWHM} (fs)	200		
P_0 (W)	75		

TABLE 5.3: Parameters used for the frequency-dependent TPA test, where the centre of the frequency window corresponds to 2.2 μm. The parameters for 'Test B' and 'Test C' are the same as for 'Test A' except where listed.

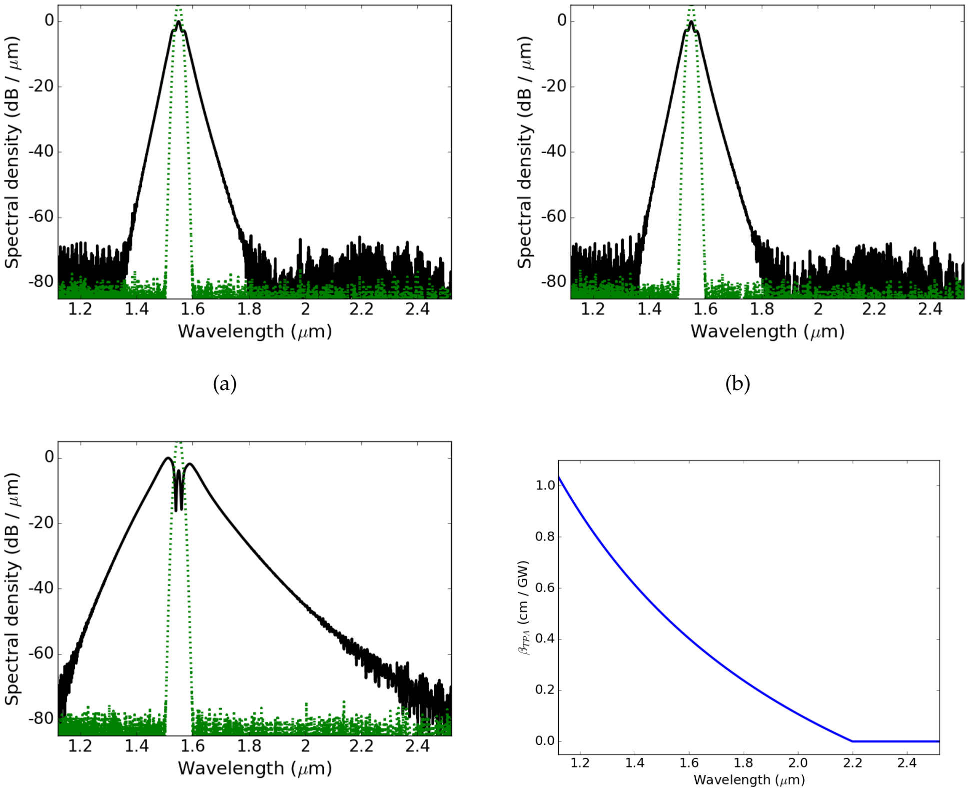

(a)

(b)

(c)

(d)

FIGURE 5.6: Simulations of a 75 W, 200 fs pulse propagating through 5 mm of p-Si fiber, which has a carrier wavelength of 1.55 µm (the centre of the frequency window corresponds to 2.2 µm), with (a) frequency-dependent TPA, (b) constant TPA defined to produce a matching value and (c) TPA switched off as a point of comparison. (d) TPA values by wavelength.

5.3.2 Including wavelength-dependent TPA as an envelope function

I originally included wavelength-dependent TPA as a constant derivative term applied at the pump wavelength, as explained in the previous section, but I also applied a Heaviside step-function H in order to prevent negative values occurring beyond 2.2 µm. I realised that this step function, applied as an array or envelope across the entire frequency domain, could be modified to produce the precise shape of the TPA envelope. Not only does this make the values at each wavelength more accurate (as it does not assume a linear curve) but it also removes the need to change the value of the derivative at different pump wavelengths. It can be applied in the same manner regardless of the centre wavelength of the window, meaning it can be used in cases where the pump is at the edge of the TPA window or even beyond it. This is important as the TPA will have an effect on the short-wavelength side of a SC generated by a pump that is not itself affected.

This simplifies the TPA term in Eq. 5.3 so it is now solved as follows:

$$\beta_{\mathrm{TPA}}(\omega-\omega_0)(|A|^2A) = i\mathcal{F}^{-1}\left\{-i(\omega-\omega_0)\mathcal{F}(|A|^2A)H_{\mathrm{TPA}}(\omega)\right\} \tag{5.5}$$

$H_{\mathrm{TPA}}(\omega)$ is the envelope function applied directly in the frequency domain, with values taken from [46] as shown in Fig. 5.7.

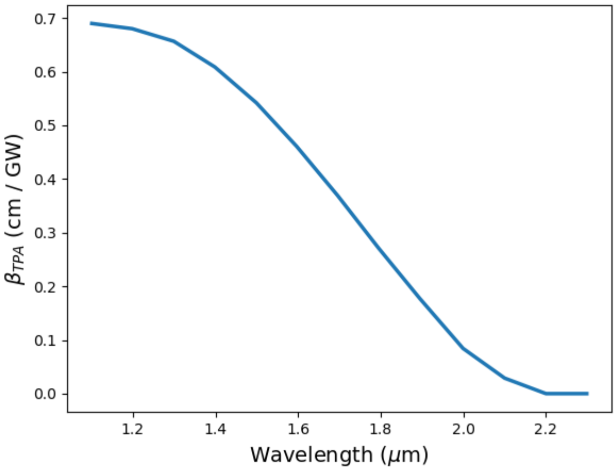

FIGURE 5.7: Values of TPA used in the code.

I tested that this modification works with the same procedure as described in Sec. 5.3.1 and got the same results.

In the previous chapter, the code was tested by comparing the results of simulations with existing experiments, to make sure that the results are sensible. The simulation of the SOI ridge waveguide included the wavelength-dependent TPA. However, the peak power in that case was very small (13 W) and the pump was in the middle of the TPA range, such that the value was high at the pump and so wavelength-dependence of the effect was barely perceptible.

It would be useful to have experiments with high input powers (in the multi-kW region) where the pumps lie at 1.55 µm (in the middle of the TPA band) and at 2.1 µm (near the edge) in order to compare the effects of the wavelength-dependence of TPA in the limit. In the absence of this, I have simulated these cases in order to estimate the scale of the effect.

5.4 The impact of wavelength-dependent TPA on multi-kW pulses at 1.55 and 2.1 µm

In the following simulations, I have implemented a function in the code which integrates over specified wavelength ranges at each step, and normalises them according to the total input average power (which depends on the pulse width, peak power and an assumed repetition rate of 100 MHz). This means that changes to specific wavelength regions can be seen which may not be apparent by simply looking at the spectrum. This technique is crucial to results in future chapters, where the goal is to maximise the average power in specific target wavelength ranges.

Both sets of comparisons use pulses with a width of 150 fs and peak power of 5 kW, and are propagated through 10 mm lengths of p-Si fibre. The difference in the sets is the centre wavelength of the pulses (1.55 and 2.1 µm) and the core diameters (2000 and 2625 nm).

5.4.1 5 kW pulses at 1.55 µm

In this first comparison, the pulses are propagated through 10 mm lengths of p-Si fibre with a core diameter of 2000 µnm. In the first case, the TPA is set as a constant and in the second, the TPA envelope is used. The simulations are shown in Fig. 5.8.

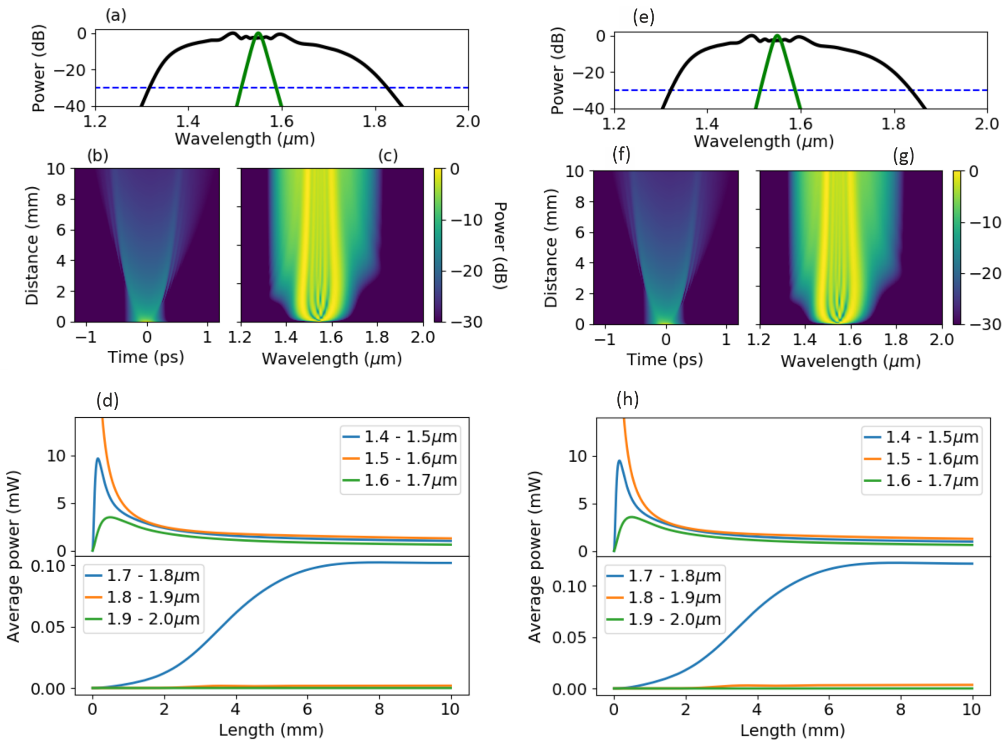

FIGURE 5.8: Simulations of 150 fs, 5 kW pulses at 1.55 μm propagating through a 10 mm length of p-Si fibre with 2000 nm core diameter. (a – d) Constant TPA. (e – h) Wavelength-dependent TPA. (a, e) Input and output spectra. (b, f) Temporal pulse evolution. (c, g) Spectral pulse evolution. (d, h) Evolution of average power in labelled wavelength ranges.

The simulations in Fig. 5.8 show that there is no distinguishable difference between the case where TPA is constant and that where it varies with wavelength. This can be simply attributed to the fact that TPA is high enough at the pump to clamp that wavelength and prevent any appreciable spectral broadening from occurring. Thus, there is not enough power in the surrounding wavelength ranges on which varying levels of TPA could act.

5.4.2 5 kW pulses at 2.1 μm

The next comparison uses pulses with the same width and peak power but centred at 2.1 μm, which is near the edge of the TPA band. Thus, it would be expected that the clamping effects would be much less significant on the pump itself but would manifest in the short-wavelength side of the SC generated.

In these simulations, the fibre has a length of 10 mm and core diameter 2625 nm diameter, chosen as it allows for FWM-based transfer to wavelengths > 3.5 μm (as will be explained in Chapter 7). Again, in the first case the TPA is kept constant at the value for the pump and in the second, the full TPA envelope is included.

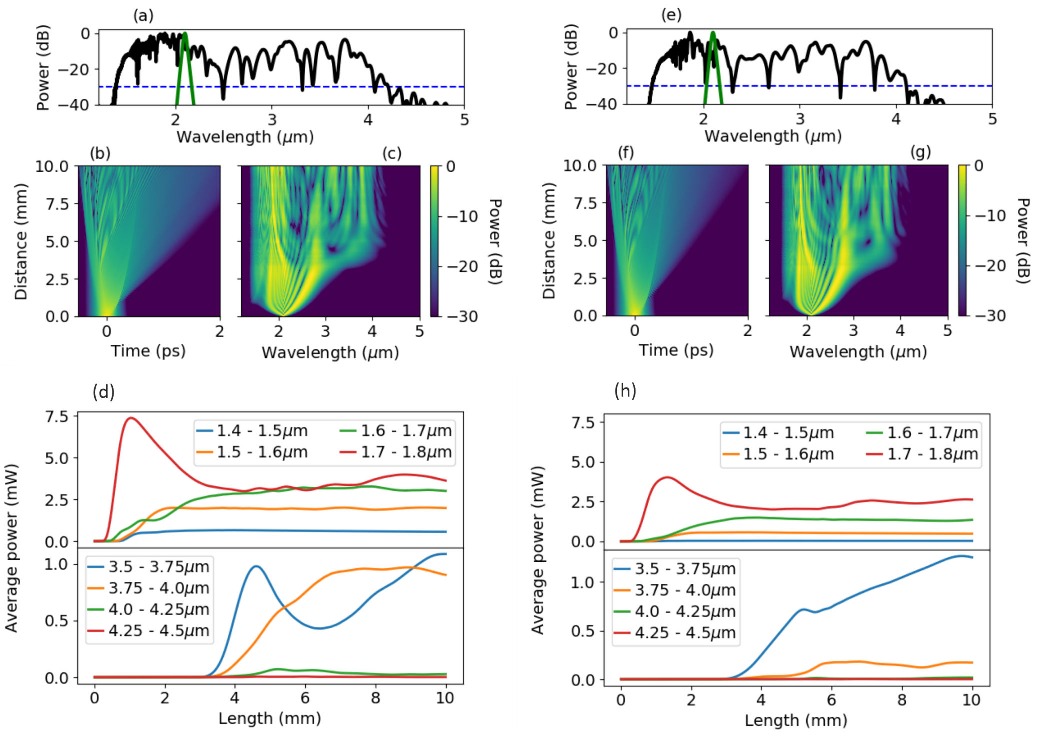

FIGURE 5.9: Simulations of 150 fs, 5 kW pulses at 2.1 µm propagating through a 10 mm length of p-Si fibre with 2625 nm core diameter. (a – d) Constant TPA. (e – h) Wavelength-dependent TPA. (a, e) Input and output spectra. (b, f) Temporal pulse evolution. (c, g) Spectral pulse evolution. (d, h) Evolution of average power in labelled wavelength ranges.

In this case, the wavelength-dependent TPA has a significant impact. The average power in the wavelength ranges spanning 1.4 – 1.8 µm is clamped by around half, which is an expected effect as the TPA is much higher at these wavelengths than at the pump. What is perhaps surprising is that some of the wavelengths longer than 2.2 µm, where there is no TPA acting at all, are affected. In particular, the 3.75 – 4 µm range is cut by an order of magnitude. This can be explained by assuming that power is transferred to this range by FWM, in which one of the pumps lies in the short wavelength ranges clamped by TPA. The phase-matching conditions for such transfers are covered in great detail in Chapter 7, where silicon core fibre tapers are designed to optimise these conditions. As the simulations here show, it is thus crucial to include the wavelength-dependent TPA in the pulse propagation equations, as loss in one part of the spectrum can impact other parts.

5.5 Three-photon absorption

Three-photon-absorption has a much smaller impact than TPA, but is included for completeness. It is included as an envelope function in a similar manner to TPA, as shown in Eq. 5.6. The values for this, taken from [61], are shown in Fig. 5.10.

$$\beta_{3\text{PA}}(\omega-\omega_0)(|A|^4A) = i\mathcal{F}^{-1}\left\{-i(\omega-\omega_0)\mathcal{F}(|A|^4A)H_{3\text{PA}}(\omega)\right\} \tag{5.6}$$

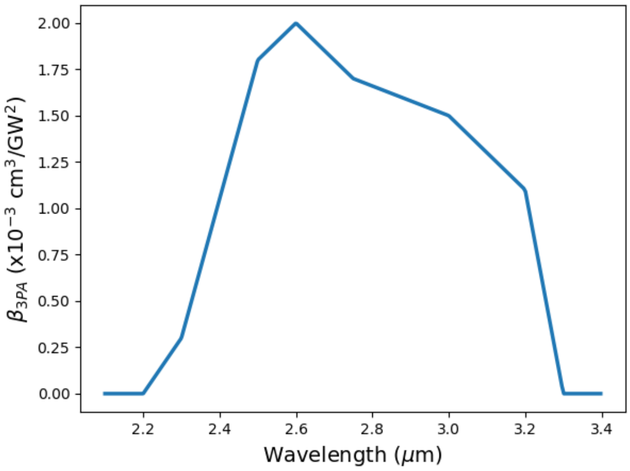

FIGURE 5.10: Values of 3PA used in the code.

5.6 Self steepening

The self-steepening term, as defined in Eq. (2.60), accounts for how the nonlinear coefficient term γ changes with wavelength around the pump and contains three sub-terms, which depend on ω, $n_2(\omega)$ and $A_{\text{eff}}(\omega)$. The first and dominant term is precisely proportional to ω, so is easy to include. The last term is dependent on $A_{\text{eff}}(\omega)$, which changes roughly linearly with wavelength, as shown in Fig. 5.11.

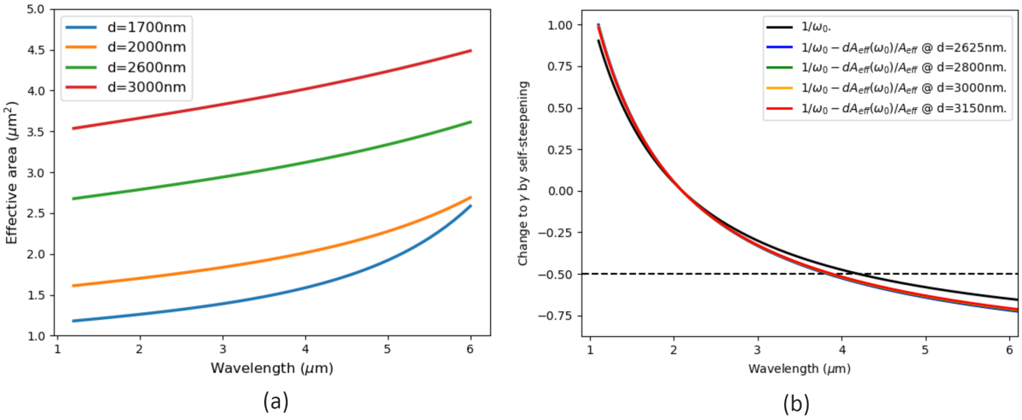

FIGURE 5.11: (a) Wavelength dependent area the fundamental mode in silicon-core fibres with core diameters of 1700 – 3000 nm. (b) Change to γ by including the wavelength-dependent effective area in the self-steepening term, Eq. (2.60).

Fig. 5.11 (a) shows how the effective area changes with wavelength for silicon-core fibres with core diameters from 1700 – 3000 nm. It can be seen that the change is mostly linear with wavelength, with the exception of the 1700 nm core fibre for wavelengths > 4 µm. However, this will have no impact on the fibre tapers simulated in Chapter 7 because this size of diameter is only used for the waist, where the wavelengths generated are < 3.5 µm. It will be shown that longer wavelengths are generated in the up-taper and end-facet section where diameters are > 2000 nm.

Fig. 5.11 (b) shows how the nonlinear term γ is modified by self-steepening. It can be seen that the wavelength-dependent effective area makes only a modest change beyond the purely frequency-dependent term $1/\omega_0$. However, it has a much more significant effect for SOI ridge waveguides, as the cross-sectional area is much smaller. This is will be covered in more detail in Chapter 8.

The remaining term in Eq. (2.60), proportional to n_2, the intrinsic material nonlinearity, does not vary linearly with wavelength, at least not for silicon across the wavelength range covered by simulations in this thesis, 1.55 – 5.5 µm.

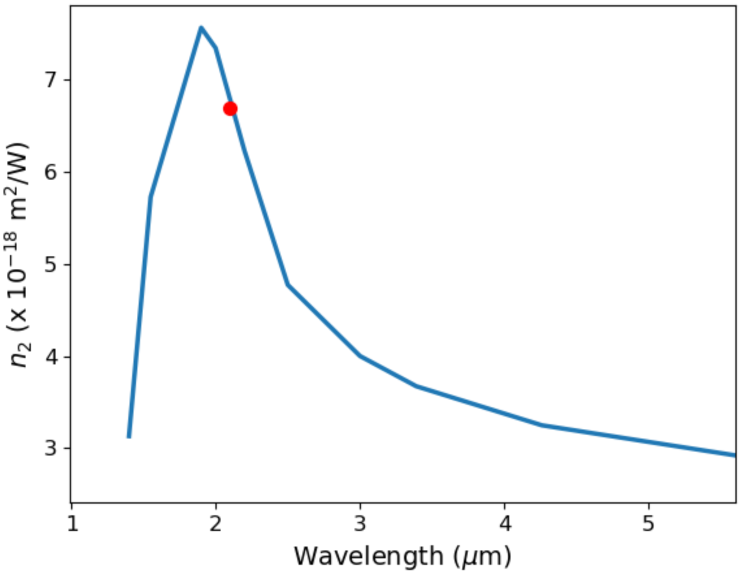

FIGURE 5.12: Material nonlinear coefficient n_2 in silicon by wavelength. The red dot indicates the value at 2.1 µm.

Fig. 5.12 shows this very clearly. Many of the simulations are conducted with a pump wavelength of 2.1 µm, and as the SC produced can span from 1.55 µm to beyond 4 µm, there is no linear derivative term that can account for this. A Taylor expansion could potentially be used, but as the self-steepening term acts on a Fourier transform of the pulse amplitude across the entire time window, adding additional terms to this would increase the numerical errors. It would require significant further investigation to quantify this and ascertain whether this approach would be justified when the contribution of wavelength-dependence to this term may be relatively small. I have therefore omitted the $n_2(\omega)$ self-steepening term for the purposes of this thesis.

5.7 Conclusion

In this chapter I have looked at the effects of adding wavelength-dependence to linear loss caused by cladding absorption and TPA, and shown that these effects can be accurately modelled in the code and have a significant impact. I have also added wavelength-dependent 3PA and the change in effective area to the nonlinear term.

In the following chapter, I will look at how wavelength conversion in silicon-core fibres can be extended to longer wavelengths by connecting a second fibre to change the dispersion profile and thus open up new phase-matching conditions. This will lay the groundwork for moving on to designing full tapers for extending the long wavelength edge of a SC.

Chapter 6

Two-diameter fibre system for wavelength conversion

6.1 Introduction

One of the main applications of nonlinear optics is wavelength conversion. A seed (signal) and pump are coupled into a fibre or waveguide, and if phase-matching conditions allow, energy is transferred from the pump to the seed and also to an idler frequency on the side of the pump opposite the signal.

The output frequency can be tuned by shifting the frequency of the pump and/or seed, so the output range is limited by the tuning ranges of these inputs, assuming that a single fibre or waveguide with fixed diameter or width is used. However, it is possible that by varying the diameter or width longitudinally, the output bandwidth can be extended. In this chapter I investigate this by changing the fibre diameter to tune these phase matching conditions.

6.1.1 A note on terminology

In some investigations, the term signal is used to refer to the input seed frequency and the idler is the generated output frequency, regardless of their frequency relation to the pump. This can be confusing, so in what follows I will use the terms signal and idler depending on their wavelength relative to the pump. The convention I use is that an idler has a shorter wavelength (or higher frequency) and a signal has a longer wavelength (or lower frequency). As in this case I am looking at conversion from a shorter to a longer wavelength, the input seed is thus referred to as the idler.

6.2 Investigation into extending the wavelength conversion range

The scenario investigated here is as follows. The seed wavelength is 1.82 µm and the pump is at 2.2 µm. The goal is to generate an output signal in the free space communications wavelength band (between 3.6 and 4 µm) but the seed (idler) and pump are too close together in the frequency domain to be able to generate this target with a fixed-diameter fibre. To reach this target, a cascaded wavelength generation process will need to be used, so the phase matching conditions will need to be changed along the pulse propagation length to facilitate this.

6.2.1 Proposed solution: connecting two fibres

The scheme for generating a longer wavelength with the 2.2 µm pump is as follows. Two fibres are connected together, such that a signal wavelength is generated by the pump and idler in the first fibre in a degenerate FWM process. When the signal reaches its peak, the three wavelengths are sent into the second fibre, which has a diameter chosen such that this signal now acts as a second pump in a non-degenerate FWM process in the second fibre, phase-matched with the original pump and idler to produce a new (target) signal. (Alternatively, the idler from the first fibre can act as a second pump in the second fibre to produce a new idler.)

To phase-match with all three existing waves, we need to fulfil Eqs. (2.91) – (2.98). Having chosen whether the target is a signal or idler, finding the correct diameter to use is straightforward. The dispersion curve ($\beta(\omega)$) is calculated (using a finite element method in Comsol) for a range of diameters centred on the input fibre diameter. The exact diameter can then be calculated by interpolation.

6.2.2 First fibre: seeded degenerate FWM

The optimum diameter for the first fibre depends on the wavelengths of the pump and seed (idler or signal). For generating a longer wavelength, the seed will be at a shorter wavelength than the pump, so is defined as the idler and the output will be the signal.

For degenerate-FWM in the first fibre, I only look at the simple case where the pump, signal and idler all lie in the anomalous dispersion regime. In silicon-core fibres, the ZDW therefore lies at a wavelength shorter than the idler. This is shown in Fig. 6.1 (a).

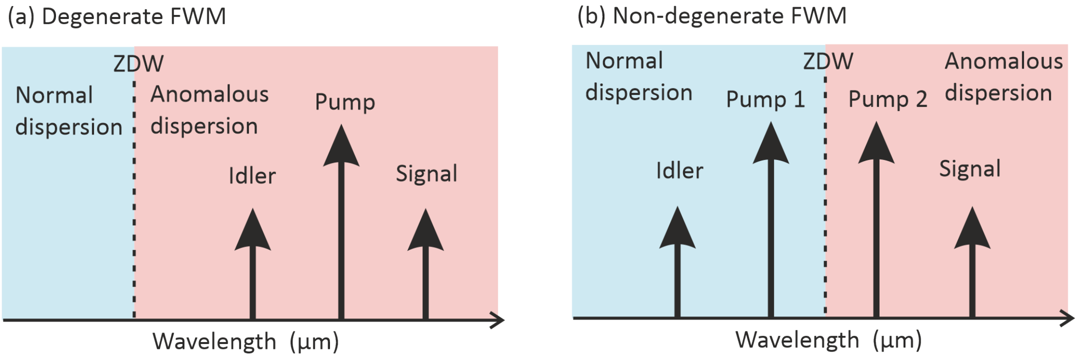

FIGURE 6.1: Position of ZDW relative to pump/s, signal and idler when higher-order dispersion terms are small for (a) degenerate and (b) non-degenerate FWM.

As mentioned in Section 2.7.1, modulation instability sidebands cluster around an optimum wavelength. This is given by Eq. 2.100 but this is an oversimplification as it assumes that higher-order dispersion terms are negligible. A more accurate equation is:

$$\Delta\beta = 2\beta_p - \beta_s - \beta_i - 2\gamma P = 0. \tag{6.1}$$

This is solved numerically to find the optimum diameter.

It should be noted that this Equation ignores the effects of loss, which means that the only depletion of the pump is due to transfer of power to the signal and idler. In reality, linear and nonlinear losses will have an effect, such that rate of power transfer will be different to the rate of pump depletion. The optimum diameter will likely be different to that calculated in the idealised case. As will be shown in Sec. 6.3, this is indeed the case, and simulations which include all relevant losses are used to find the best diameter.

6.2.3 Second fibre: non-degenerate FWM using output from first fibre

As mentioned previously, in the first fibre it is assumed that the three wavelengths lie in the anomalous dispersion regime. But for non-degenerate FWM (i.e. with four different wavelengths) in the second fibre, two of these must be in the normal dispersion regime, such that there is one pair on either side of the ZDW. This is shown in Fig. 6.1 (b).

Therefore, the ZDW has to move to a longer wavelength to fulfil this condition. For generating a wavelength longer than the original signal, the ZDW will need to be positioned in between the pump (which will become pump 1) and the original signal (which will become pump 2). The target will become the new signal in this scenario. For generating a wavelength shorter than the original idler, the ZDW will need to be positioned in between the idler and pump (which will become pumps 1 and 2 respectively) and the target will be a new idler. In either case, a larger diameter will be required to shift the ZDW to a longer wavelength, as shown in Fig. 2.6.

The fulfilment of these phase-matching conditions can be explained in the following way [62]:

The phase-matching conditions for non-degenerate FWM are generally satisfied when the pumps are spaced roughly symmetrically around the ZDW. This is the case because, due to the size and circular geometry of the fibres, the rate of change of the dispersion is relatively linear.

This can be understood by recalling Eqs. (2.91) – (2.98). The leading order of Δk vanishes if $\beta_2 = 0$, i.e. if the pumps are equally spaced around the ZDW. The fibre geometry means that the higher-order terms in Eq. 2.97 are negligible and so the majority of phase-matched solutions do indeed follow this pattern.

However, as we will see later (in Chapter 8), for ridge waveguides where the higher order dispersion terms cannot be so readily ignored, the phase-matching conditions become more complicated.

6.3 Optimising the core diameter of the first fibre

As mentioned in the previous section, finding the optimum diameter for the second fibre is a straightforward matter of solving Eqs. (2.91) – (2.98). For the first fibre, which uses degenerate FWM, finding the optimal diameter requires more investigation.

For the purposes of this proof-of-principle design, I looked at a pump wavelength of 2.2 µm (the edge of the TPA-band) and a target signal wavelength of 3.8 µm (as this is a potentially useful wavelength for free-space communications). The frequency-separation between these is 60 THz, so the seed (idler) is positioned with frequency 30 THz higher than the pump, corresponding to 1.9 µm. The pump and seed will generate an intermediate signal at 2.8 µm in the first fibre section, and then these will be phase-matched in the second section to generate the 3.8 µm target.

The simulations are done with a CW pump with 40 W power and a seed with 8 W, which are easily achievable with commercially available lasers [63]. The results are also applicable for long pulses of > ps.

Fig. 6.2 shows the phase-matching curves ($\Delta\beta$) for a pump at 2.2 µm with powers of 0 W and 40 W in a fibre with a core diameter of 1935 nm.

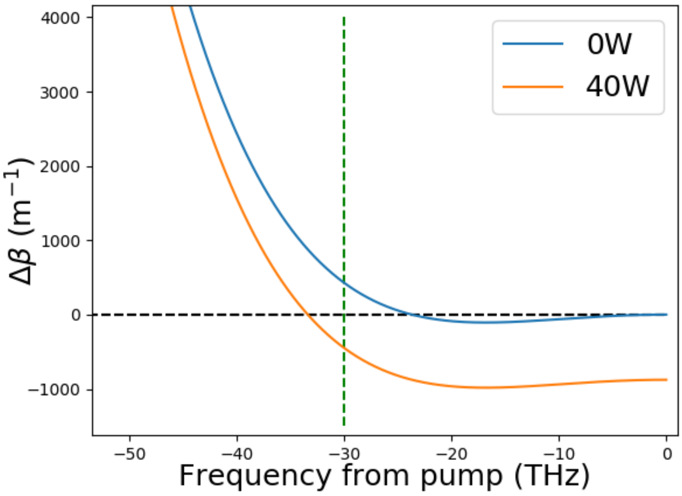

FIGURE 6.2: Nonlinear phase-matching with a diameter of 1935 nm and pump at 2.2 µm with power of 40 W and the limit of 0 W. Green-dashed line shows target frequency-separation of 30 THz.

The phase-mismatch $\Delta\beta$ is shown in the frequency-domain as the waves are equally spaced in this domain (unlike in the wavelength domain). With no pump power, the phase-matching is purely dependent upon dispersion, and the optimum frequency-separation is at 24 THz. As the pump power increases, this phase-matched frequency-separation increases, until at 40 W, it lies at 33 THz. This is higher than the 30 THz required, but as the pump depletes due to wavelength conversion as well as losses, the phase-matching conditions will approach the zero-power case. The green-dashed line in the figure shows the 30 THz target, at which point $|\Delta\beta|(0\,\text{W}) \sim |\Delta\beta|(40\,\text{W})$. Most of the time the pump power will lie somewhere between these two, so will maintain a relatively low phase-mismatch. Simulations which include pump depletion due to propagation loss show that this diameter is indeed the optimum one in terms of transferring the most power to the intermediate signal at 2.79 µm. Three of these simulations are shown in Fig. 6.3.

The simulations in Fig. 6.3 show that the maximum amount of power (8.952 W) is generated with a core diameter of 1937 nm, whereas only 8.589 W is generated with a core diameter of 1947 nm and 6.852 W with a core diameter of 1927 µm.

In order to generate the maximum power at the target wavelength in the second fibre, however, it does not make sense to couple in the original three wavelengths at the point where the intermediate signal reaches its peak. This is because the original pump power drops below that of the idler at 6 mm, at which point they are both at 13.4 W, and the intermediate signal is at 7.94 W. As this is close to the maximum it seems like a sensible cut-off point at which to couple in the wavelengths to the second fibre.

As this cut-off point does not rely on the peak of the signal being reached, it means that there is more tolerance in the core diameter of the first fibre. For example, with a core diameter of 1947 nm, at 6.85 mm, the pump and idler cross when the power in each is 12.95 W, at which point the signal power is 7.11 W. The power levels are very similar at this length in the 1927 nm core fibre. Thus, the overall output is

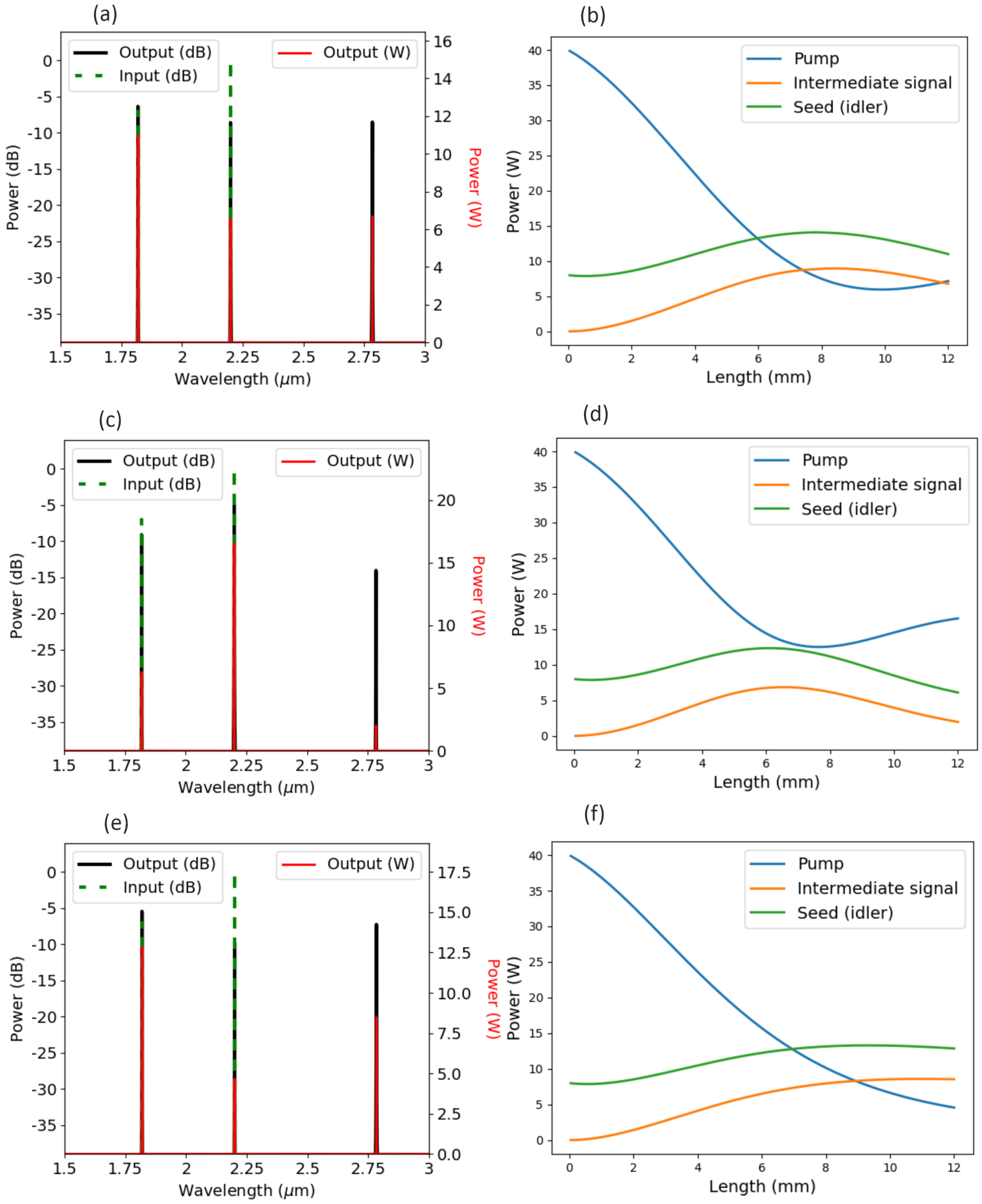

FIGURE 6.3: Simulations of 40 W pump at 2.2 µm and 8 W seed at 1.82 µm propagating through 12 mm lengths of p-Si fibre with core diameters of (a, b) 1925 nm, (c, d) 1935 nm and (e, f) 1945 nm. Each simulation shows the spectral output (a, c, e) and the evolution of power (b, d, f) in the pump, seed, and generated signal at 2.79 µm.

likely to be affected very little by fabrication intolerance in the first fibre, as will be shown in Section 6.4.1.

6.3.1 Optimum core diameter for second fibre

For the particular set of wavelengths looked at here, the optimum core diameter for the second fibre is 2578 nm, at which point the ZDW is at 2.55 µm, close to halfway between the pump at 2.2 µm and the intermediate signal at 2.79 µm. It is not exactly halfway, so there is a small contribution from higher-order dispersion terms. Nonetheless, for this diameter, the phase-mismatch between the four wavelengths is minimised.

The tolerance for variation to this diameter is lower, as at diameters of 2568 and 2588 nm (i.e. ± 10 nm) the phase mismatch increases to 0.3/mm, which means that the waves will undergo a relative phase-shift of π at $\sim$ 10 mm. As will be seen in Section 6.4.1, with the addition of losses in the simulation, this translates to a peak in power transfer to the target at $\sim$ 8 mm into the second fibre, whereas with the optimum diameter the transfer continues for a further 10 mm which doubles the target power output.

6.4 Simulations of the two-fibre design

The following simulations use the GNLSE, as outlined in Sec. 2.5. The input parameters were a 40 W CW pump at 2.2 µm and 8 W CW seed (labelled 'Pump 2') at 1.82 µm. Fig. 6.4 shows the output when these pumps are propagated through two fibres of diameter 1937 nm and 2578 nm with corresponding lengths of 6.85 mm and 19 mm.

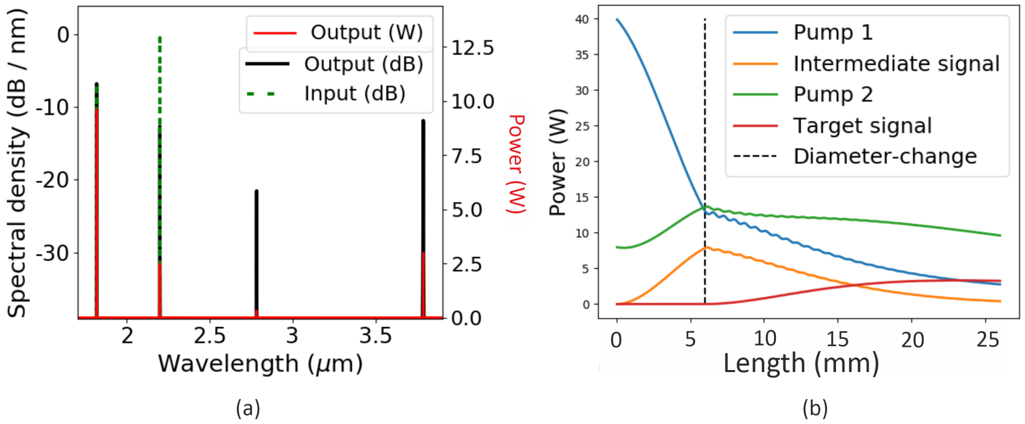

FIGURE 6.4: (a) Spectral output of two-fibre system. (b) Evolution of pump (Pump 1), seed (Pump 2), intermediate signal and target wavelength signal.

As Fig. 6.4 shows, the two input pumps produce an intermediate signal at 2.79 µm which reaches a peak of 7 W. The three wavelengths then phase-match with the target of 3.8 µm in the second fibre, which reaches a peak output of 3 W. The efficiency of the conversion from input pump and seed to output target is 6.25 %, i.e. the power output at the target wavelength is 6.25 % of the total power input of the pump and seed.

6.4.1 Stability analysis

As mentioned in Section 6.3.1, the phase-matching conditions in the second fibre are highly sensitive to variations in the diameter, so I conducted a stability analysis whereby I varied the diameter of each section by 10 nm to account for standard fabrication intolerances. Fig. 6.5 shows the evolution of the target wavelength power with each combination of these diameter changes.

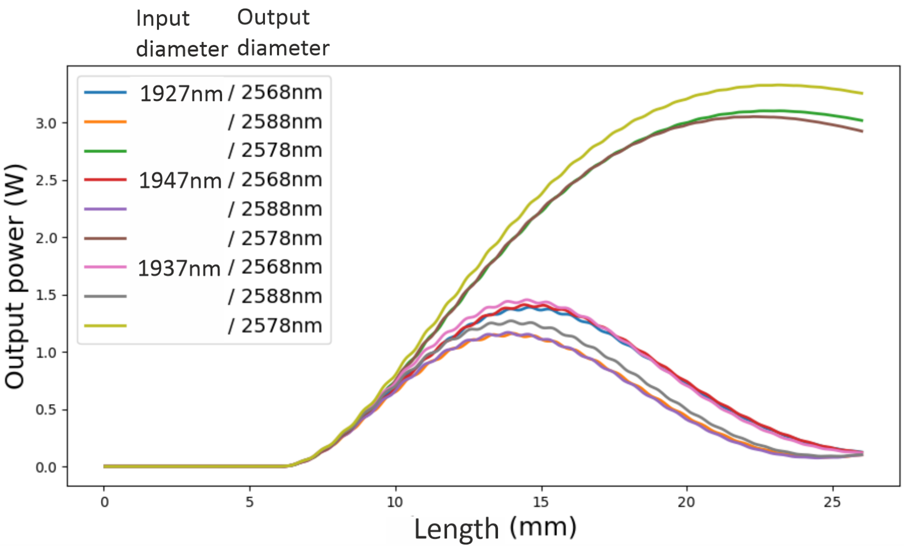

FIGURE 6.5: Conversion to the target wavelength when input and output diameters are varied by a ± 10 nm range. The labels show the diameters of the first / second fibre in each case.

The analysis shows that the output power is not particularly sensitive to changes in the input diameter, as this is optimised to phase-match to a degenerate FWM process. However, the output power is extremely sensitive to the diameter of the second fibre, as the conversion in this section relies on non-degenerate FWM. The conversion to the target is halved with a variation of 10 nm either way and this conversion also peaks at a much shorter length (14 mm) than the optimised one (26 mm), so almost no output would be seen at this longer length unless the fabrication was perfect. However, if the lower output was acceptable, the overall length could be shortened to 14 mm to guarantee an output of at least 1 W (or 2 % of input) at 3.8 µm.

6.5 Conclusion

The primary purpose of the work in this chapter has been to show a proof-of-principle example of how wavelength conversion can be achieved with a two-step process using two different kinds of FWM (degenerate and non-degenerate). Although the wavelengths for the simulations in this chapter were chosen with the goal of an immediate practical application, the target wavelength region (for free-space communications) can be reached with existing pumps and seeds in a straightforward single-step wavelength-conversion process with higher efficiency.

Nonetheless, a useful design principle has been shown: that three wavelengths generated by one nonlinear process in one fibre can be used to generate a fourth wavelength in a second fibre with appropriate phase-matching conditions. This principle can be extended to multiple groups of wavelengths, as are produced in a supercontinuum (SC). The next chapter will demonstrate through simulations that this process can be exploited to extend the width of a SC generated in a silicon fibre taper, and more importantly, boost the usable average power in the long wavelength edge of this SC.

Chapter 7

Fibre tapers for boosting longer wavelengths in a supercontinuum

7.1 Introduction

In the previous chapter, I looked at how two fibres with different diameters can be used to generate a new wavelength in a two-step process: degenerate FWM in the first fibre followed by non-degenerate FMW in the second, which opens up new phase-matching conditions. This approach of using a second diameter to change the phase-matching conditions (in this case using a larger second diameter to reach a longer wavelength range) can be adapted for SC generation.

In this chapter, the design is expanded into a full taper-shape, with a down-taper from a large input facet to a waist region, an up-taper, and a fixed-diameter end section. The down-taper and waist replaces the first fixed-diameter section in the wavelength-conversion design. In this case, several processes (self-phase modulation and soliton fission as well as degenerate FWM) produce initial spectral-broadening. The up-taper then introduces new phase-matching conditions for non-degenerate FWM-based conversion to progressively longer wavelengths. This process culminates in the fixed-diameter end facet, which is optimised to maximise the number of phase-matching conditions to a particular target wavelength range. The taper design is shown to work with a range of input powers, improving the efficiency of conversion to several output wavelength ranges out to 5.5 µm.

7.2 Motivation

The width of a supercontinuum (SC) is measured as either the frequency or wavelength range between its edges, defined as the points in the spectrum which drop below a threshold relative to the peak. This threshold is often set at the -20 or -30 dB level. However, this does not give any indication of the usable power in any given wavelength range, which could alternatively be expressed as a signal-to-noise ratio. If the purpose of the SC generation is for spectroscopy, for example, one or the other of these metrics is crucial.

Some of the papers that have focused on the amount of average power in this way are [64, 65], which have looked at SC generation for spectroscopy of greenhouse gases, for which the 3 – 5 µm region (the first mid-IR atmospheric window) is particularly important as it contains many of the absorption lines of such gases [66]. They achieve usable amounts of power in the first half of this window (3 – 4 µm) by pumping high-power lasers at 1.55 µm through a silicon-on-insulator (SOI) waveguide in the first case [64] and 2.1 µm through a silicon-dioxide ridge platform in the second [65]. The first achieves an output of 0.3 mW across the 3 – 4 µm wavelength range, whereas the second can achieve 1 mW, but with a peak pump power > 10 kW.

This chapter shows that silicon-core fibre tapers can produce similar output average powers across the entire greenhouse gas absorption region but with relatively modest (< 10 kW peak) powers. Initially, I investigate the role of the taper profile to obtain flat and efficient SC in a silicon-core fibre taper that extends across the 3 – 4.5 µm region by optimizing the FWM phase-matching conditions. The long wavelength edge is then extended out to 5.5 µm.

A key goal is to achieve output SC spectra at practical power levels using standard commercially available fibre laser pump sources, such as the 2.1 µm one used in [65], from which I use the pulse parameters. The taper is designed to have large input and output diameters to maximize the coupling efficiencies, with a waist such that the ZDW is close to the pump in order to enhance the efficiency of the nonlinear processes. However, in contrast to conventional tapers, the design is asymmetric such that the up-tapered output section can be carefully engineered to access new phase-matching conditions for FWM, thus extending the long wavelength substantially beyond what could be achieved with a straight waveguide.

Having designed four tapers which target progressively longer 0.25 µm wavelength ranges covering the 3.5 – 4.5 µm region, I then look at extending the target ranges still further, out to 5.5 µm.

7.3 Taper design principles

Each taper design is optimised for a different peak pump power, starting with 1 kW for the first target wavelength range (3.5 – 3.75 µm), increasing to 5 kW for the 4.25 – 4.5 µm range and then up to 10 kW in the second half of the chapter where 5.25 – 5.5 µm is targeted. These input peak powers are established by simulating pulse propagation through fibres with a constant diameter to ascertain the maximum average power generated in the target ranges, thus setting a benchmark against which to measure the performance of the taper in this region. The primary goal is to search for designs that maximise the spectral width of the supercontinuum, whilst retaining a high spectral density in the mid-infrared region of interest.

The tapers are divided into three sections, a down-taper (1), up-taper (2) and constant-diameter end facet (3), as shown in Fig. 7.1. Section (1) has a large input facet in order to couple the light into the fibre with minimal loss, and then tapers down towards the waist diameter. As the light propagates in this section, it undergoes initial spectral broadening via self-phase modulation (SPM). At the waist diameter, the nonlinearity reaches its maximum, and part of the spectrum crosses the zero-dispersion wavelength (ZDW), triggering soliton fission which speeds up this broadening. Section (2) is an up-taper, where the increasing diameter opens up new phase-matching conditions for non-degenerate FWM, which acts to improve the transfer of power to increasingly longer wavelengths. This up-taper culminates in Section (3), the end-facet, where the diameter is optimised for phase-matching to the target wavelength range. The larger the diameter, the longer the wavelengths that can be phase-matched to in this manner. For each design, the total length of the tapered structure and the individual sections are fixed, but the diameters of the individual sections are allowed to vary (for example, increasing the input diameter allows for larger peak powers which are needed to reach longer wavelengths). This approach was arrived at by an extensive numerical search through the design space, simulating pulse propagation through tapers with different section lengths as well as different diameters.

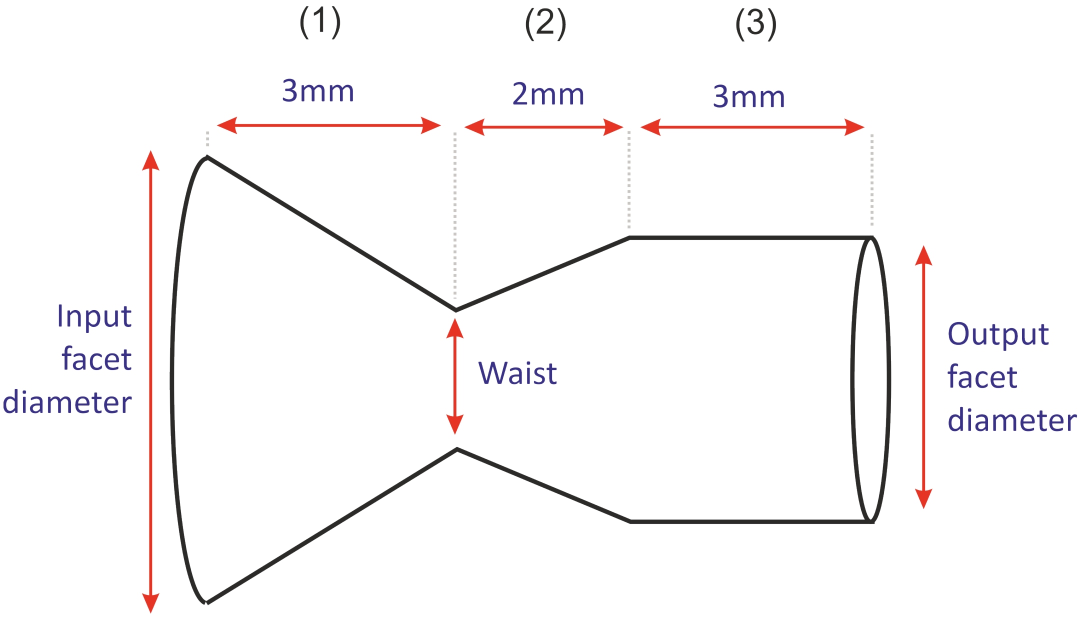

FIGURE 7.1: Schematic showing taper design: (1) down-taper, (2) up-taper, and (3) constant diameter end facet.

When deciding upon appropriate length scales for each section in the taper designs, the main factor I took into account was the nonlinear length, defined as $L_{\mathrm{NL}} = 1/\gamma P$. For mid-infrared light propagation, silicon core diameters on the order of a few micrometers $\sim 1.5 - 4\,\mu$m are desired so that the pump is positioned close to the ZDW and that the interaction with the silica cladding, which is lossy at these wavelengths, is minimised. Such diameters correspond to nonlinear parameters γ in the range $3 - 22\,\mathrm{W}^{-1}\mathrm{m}^{-1}$. The properties of the pump laser used in my investigations are modelled on typical values for a 2.1 µm fibre laser, with a pulse duration of 150 fs, peak powers in the range $1 - 5$ kW, and a repetition rate of 100 MHz [67]. Thus, for these values of γ and P_0, typical nonlinear lengths are in the range $0.01 - 0.3$ mm, so it can be assumed that significant nonlinear effects will occur over lengths of $\sim$1 mm. The peak power drops rapidly with pulse propagation, due to linear and nonlinear losses, and most of my simulations show that the SPM broadening reaches a maximum at lengths $\sim$3 mm. As silicon-core fibre tapers as short as 8 mm [30] have been demonstrated, I set this as the total length, divided into a 3 mm down-taper (where most of the SPM occurs), 2 mm up-taper (where cascading FWM occurs) and 3 mm end-facet (to maximise phase-matching for FWM-based transfer of power to the target wavelength-range). This design is shown in Fig. 7.1.

It would be possible to design tapers with much shorter length (say 3 – 5 mm), but these would be extremely difficult to fabricate and so would have limited practical interest. The overall length is reduced slightly however, for designs targeting the 4.5 – 5.5 µm region, to $\sim$6.5 mm, because as the peak input powers approach 10 kW, the nonlinear length is reduced.

7.3.1 Controlling the initial broadening in the down-taper

The fibre design starts with a down-tapered region, from the input facet to the waist, to facilitate efficient coupling of the fibre-based pump source into the narrow waist.

During this transition, SPM initiates spectral broadening. Then, in the waist region, the red edge of the spectrum crosses the ZDW, triggering soliton fission which facilitates further broadening.

However, if too much power crosses the ZDW, the solitons that form in the anomalous dispersion region are of too high an order. Thus, when soliton fission occurs, two problems arise: (1) the solitons recoil too far toward shorter wavelengths, wasting power that could otherwise be transferred to longer wavelengths. (2) The dispersive wave generation spreads to longer wavelengths too rapidly, which means power does not build up in the target output wavelength ranges. Furthermore, it does not build up in the central part of the spectrum, so there is no stable source of pumps for later transfer to the target ranges.

Some examples of these processes happening in non-optimised taper designs are shown in Figs. 7.2 and 7.3 where in the first case, with an input peak power of 2 kW, the input facet diameter is too small, and in the second, with 3 kW peak power, the waist is too small.

Fig. 7.2 (a – c) shows the output spectrum, temporal and spectral evolution of the pulse propagation. Fig. 7.2 (d) shows how the 0.25 µm ranges in 3 – 4 µm evolve along the length of the taper. It shows that the first three ranges peak closely together, with more power being transferred to the 3.25 – 3.5 µm range and significantly less to the 3.5 – 3.75 µm range. Even the power that is transferred here is not contained and so fails to act as a pump for the target range (3.75 – 4 µm). Thus, the cascading power transfer does not happen and too little power is transferred to the target region. Fig. 7.2 (e) shows the taper profile (i.e. how the core diameter changes with length). In this case the input diameter is too small, causing the initial spectral broadening to occur over too short a length. The design with a more optimal input diameter is shown in Section 7.5.2.

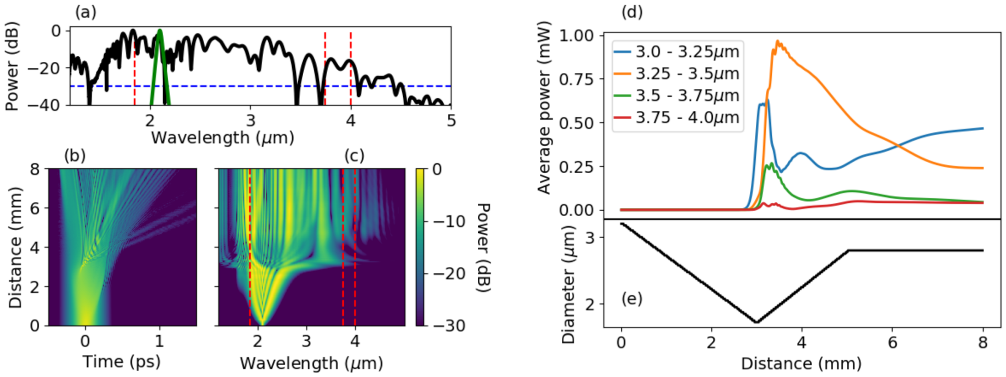

FIGURE 7.2: Simulation of 2 kW pulses through a non-optimal taper design. In this case, the input facet (3200 nm) is too small, causing too much soliton fission in the early stages of spectral broadening. (a) Output spectrum. (b) Temporal evolution of the pulses. (c) Spectral evolution. (d) Evolution of average power in 0.25 µm wavelength bands. (e) Profile of the taper showing how the diameter changes with length.

Fig. 7.2 (c) shows spectral broadening, due to soliton fission, extending down to 1.2 µm. This happens shortly after SPM broadens the spectrum past the 1.85 µm point shown as a dashed red line. As a result, the long-wavelength side of the spectrum also broadens too quickly, and the spectrum breaks up before FWM can transfer sufficient power to the target region. The output spectrum actually extends beyond the target region (also shown by red-dashed lines), but the power is not contained and thus the maximum level reached in the 3.75 – 4 µm range is 0.08 mW. Furthermore, this occurs at 6 mm propagation length.

The simulation results for the second non-optimal design (where the waist is too small) are shown in Fig. 7.3.

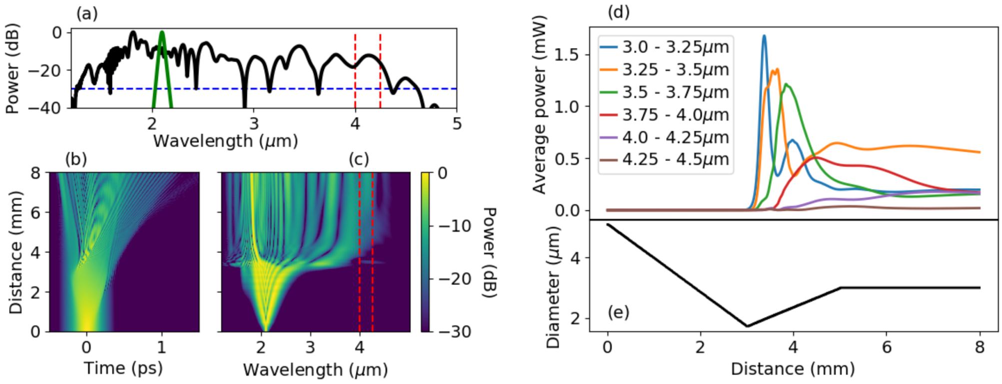

FIGURE 7.3: Simulation of 3 kW pulses through a non-optimal taper design. In this case, the waist (1700 nm) is too small, causing too much soliton fission in the early stages of spectral broadening. (a) Output spectrum. (b) Temporal evolution of the pulses. (c) Spectral evolution. (d) Evolution of average power in 0.25 µm wavelength bands. (e) Profile of the taper showing how the diameter changes with length.

Fig. 7.3 (a – c) shows the output spectrum, temporal and spectral evolution of the pulse propagation. It can be seen in Fig. 7.3 (b) and (c) that soliton fission occurs at 3 mm (i.e. when the waist is reached). The spectral evolution plot shows a soliton breaking away to a shorter wavelength, while a corresponding dispersive wave carries away energy to a longer wavelength. Thus, some of the useful power is lost before the bulk of the wavelength conversion to the target range (4 - 4.25 µm) happens in the output facet. Fig. 7.3 (d) shows that the average power in the target range increases, but then peaks (at 0.16 mW) before the end of the taper and starts to drop again. Fig. 7.3 (e) shows the taper profile. The design with a more optimal waist diameter is shown in Section 7.5.2.

Based on these results, when optimising the output facet diameter (see Section 7.3.2) to maximise the FWM-based transfer to the target wavelength ranges, I filter the space of available solutions to the phase-matching condition such that the short-wavelength pump lies at $\lambda > 1.85$ µm. Thus, when simulating different taper designs, initial spectral broadening beyond this limit indicates that power is wasted because shorter wavelengths will not be able to serve as pumps for the transfer to the targets. Thus, the input and/or the waist diameter will need to be adjusted.

Nonetheless, a limited amount of soliton fission is necessary to provide additional spectral broadening to that produced by SPM, so for lower input powers (1 – 2 kW) the waist diameter is set to 1700 nm (where the ZDW is at the input wavelength, 2.1 µm). The goal is to produce a reasonably broad intermediate spectrum, but with an evenly distributed spectral density. This will act as a range of pumps in the up-taper and end-facet to transfer power to the longer-wavelength target ranges.

To control the initial SPM and limit the degree of subsequent soliton fission, the input facet and waist diameters are both increased with higher input powers. Unlike most tapers, in which the waist is held constant over some length to maximise a particular nonlinear process, our design transitions immediately into the up-tapered region to start continuously shifting the FWM phase-matching conditions to progressively longer wavelengths. The up-taper section of the design ends when the optimum diameter is reached for FWM wavelength conversion to the targeted wavelength region.

In the second half of the chapter, I look at additional designs to push the target output wavelength ranges beyond 4.5 µm. As the pumps needed to generate these also get longer in wavelength, the designs begin to reduce the waist diameter in order to gradually reintroduce additional soliton fission in the early stages of spectral broadening.

7.3.2 Optimising the end-facet diameter for phase-matching to the target

This is the most important section of the design, as it is the point at which phase-matching to the target region is maintained. In order to determine the optimum output diameter for the different taper designs, I calculated the phase-matching conditions for all combinations of pumps in the 1.2 – 4.5 µm range for each diameter (sampling pump wavelengths at 25 nm intervals). I was then able to use this dataset to obtain the number of phase-matched solutions depending on where the pump, signal and idler wavelengths lie. Fig. 7.4 shows the positions of pairs of phase-matched pumps (short and long wavelength plotted as black and yellow points respectively) and the corresponding idlers for four signal wavelength ranges, (a) 3.5 – 3.75 µm, (b) 3.75 – 4 µm, (c) 4 – 4.25 µm and (d) 4.25 – 4.5 µm. In all cases, only pump wavelengths that are longer than 1.85 µm are considered for the non-degenerate FWM processes. Although solutions do exist with pumps at shorter wavelengths, they are not useful because they are only generated by excessive soliton fission in the waist region (as explained in Section 7.3.1). Fig. 7.5 summarizes the results of this analysis, showing the usable bandwidth of the generated pumps. The maximum bandwidth corresponds to the point where the phase-matched pumps reach the short-wavelength edge of the target spectral range, and this indicates the optimum output diameter for maximal transfer of power to the target range.

The phase-matching conditions for non-degenerate FWM are generally satisfied when the pumps are spaced roughly symmetrically around the ZDW, as explained in Section 6.2.3. Thus, having set lower limits to the position of the short-wavelength pump (1.85 µm) and the target wavelength range of the output signal, the number of solutions should reach its maximum when the ZDW lies halfway between these limits.

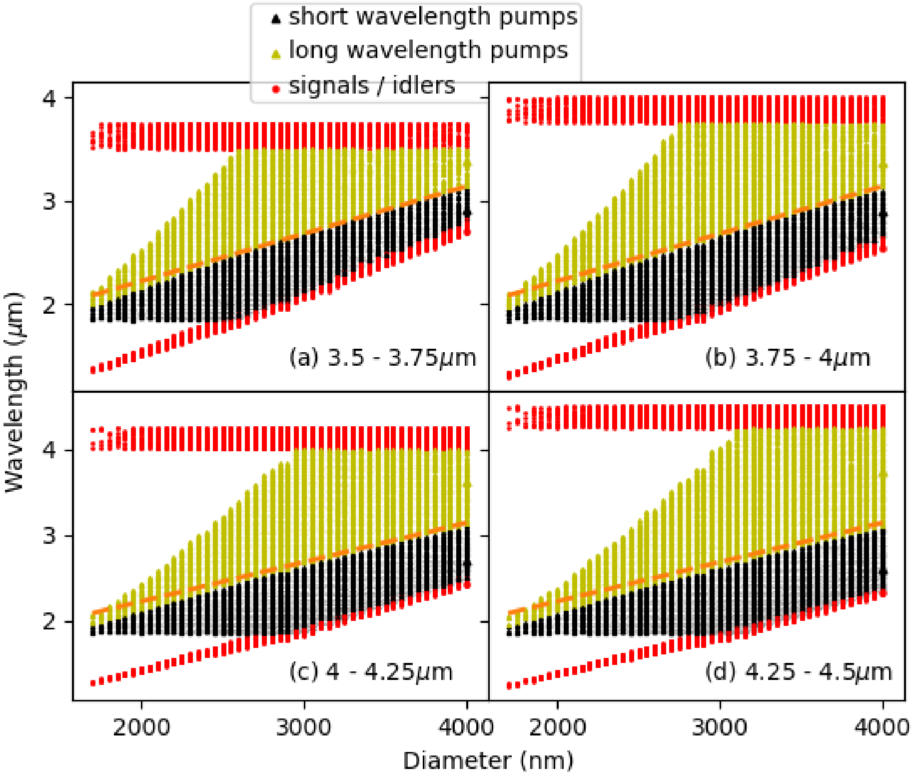

FIGURE 7.4: Four wave mixing phase-matched solutions where pumps have $\lambda > 1.85\,\mu m$ and signals are in the target ranges (a) 3.5 - 3.75 μm, (b) 3.75 - 4 μm, (c) 4 – 4.25 μm and (d) 4.25 – 4.5 μm. Orange dashed line shows the zero-dispersion wavelength. Note how the short-wavelength pumps and long-wavelength pumps tend to cluster either side of the ZDW.

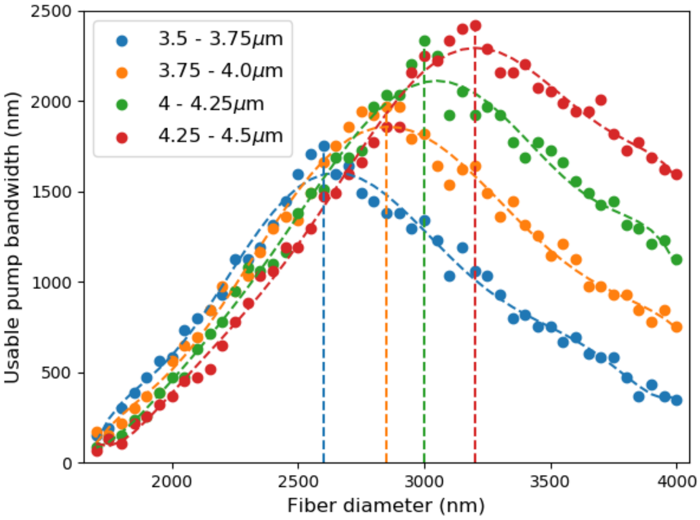

FIGURE 7.5: Bandwidth of phase-matched solutions for non-degenerate FWM where the pumps exist at wavelengths longer than 1.85 μm for target signals in the labelled wavelength ranges. The peaks correspond to the diameters where the pump wavelength range starts to overlap with the target range.

Indeed, Fig. 7.4 shows that the majority of the long wavelength pumps (yellow points) cluster above the ZDW (shown by the orange dashed line), and the short-wavelength ones (black points) cluster below it. It can be seen that the ZDW increases with diameter, and as it reaches the halfway point between the lower pump limit and the lower edge of the target wavelength range, the available phase-matched solutions for FWM to occur 'fill-in' the space between these limits. This means that FWM can draw from pumps across the entire spectrum to transfer to the target wavelength range, and thus the 'density' of solutions, corresponding to the usable pump bandwidth, is maximised, as shown in Fig. 7.5. The position of these peaks indicates the output facet core diameter required for maximising the output in the required range. So for maximising power in the 3.5 – 3.75 µm range, the diameter should be ~ 2600 nm, for the 3.75 – 4 µm range, ~ 2800 nm and so on.

7.4 Fixed-diameter fibre simulations

Before designing tapers and assessing their efficiency, I needed a set of benchmarks to compare them with. The benchmarks are simply the maximum amount of average power generated in a given target wavelength range in a fixed-diameter silicon fibre. A set of simulations were conducted for straight fibres with core diameters covering the range 1 – 4 µm. The pulses are centred at 2.1 µm, have a width of 150 fs and a repetition rate of 100 MHz. These are typical parameters achievable using a commercially available fibre laser such as the one used in [65]. Thus, as shown in Table 7.1, 1 kW peak input power corresponds to 18 mW average power.

In each case, I extracted the average power within each 0.25 µm spectral window covering the entire greenhouse gas absorption region (3 – 4.5 µm) for every propagation step. Thus, it was possible to ascertain the maximum average power transferred to each window along the propagation length. As the maximum transfer to any spectral window always occurred at a propagation length shorter than 20 mm, this length was used for every simulation. From these simulations, I found that generating a SC extending out to 3.5 µm was easily achievable in all fibre diameters with a peak power of 1 kW, so we concentrated only on the remaining four 0.25 µm ranges covering 3.5 – 4.5 µm.

Fig. 7.6 shows the results of this study. The maxima of the target ranges according to input power are summarised in Table 7.1. It can be seen that for the first three target ranges, the maximum average power is ~ 0.02 mW, and so the goal of each taper design is to boost this by an order-of-magnitude, i.e. to 0.2 mW (shown as a black dashed line in Fig. 7.6). The exception to this is for the 4.25 – 4.5 µm range, where with 4 kW peak input power, the maximum output average power is 0.008 mW, which is due to a combination of increased TPA at the pump and increased separation between pump and target. It was found that taper designs were unable to boost this level up to the benchmark, so the input peak power was increased to 5 kW.

This 0.2 mW level across a 0.25 µm bandwidth is somewhat arbitrary, but it was necessary to establish a target, and more importantly it should provide a usable amount of power for spectroscopy applications ([64] for example claims that 0.3 mW across a 1 µm bandwidth is sufficient). The results are discussed in the following section.

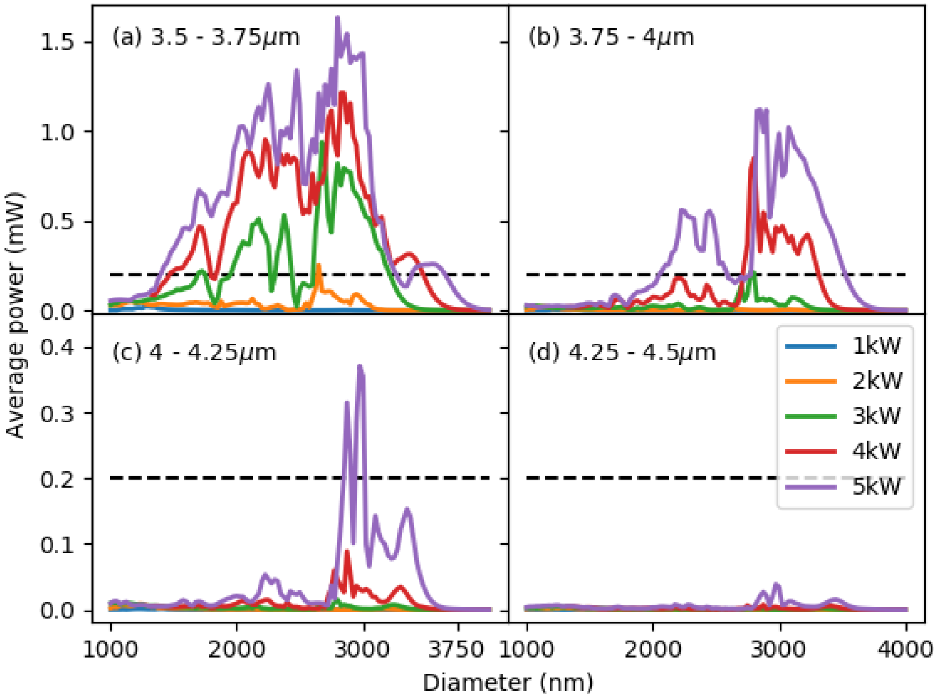

FIGURE 7.6: Complete results from fixed-diameter simulations, showing maximum average power levels transferred, with input peak pump powers of 1 – 5 kW, to the target wavelength ranges (a) 3.5 – 3.75 µm, (b) 3.75 - 4 µm, (c) 4 – 4.25 µm and (d) 4.25 – 4.5 µm. Dashed black lines show the benchmark level of 0.2 mW.

Input power		**Target**	
Peak (kW)	**Average (mW)**	**λ Range (µm)**	**Maximum power output (mW)**
1	18	3.5 – 3.75	0.022
2	36	3.75 – 4	0.021
3	54	4 – 4.25	0.015
4	72	4.25 – 4.5	0.008
5	90	4.25 – 4.5	0.039

TABLE 7.1: Maximum average power transferred with fixed-diameter fibres of any length to the 0.25 µm target ranges with labelled input powers.

7.5 Taper Simulation Results and Discussion

7.5.1 3.5 – 3.75 µm target window with 1 kW pulses

As explained in Section 7.4, with 1 kW peak power input pulses (18 mW average power), the bulk of the SC power in any fixed diameter length of fibre occurs at wavelengths shorter than 3.5 µm. As shown in Table 7.1, the maximum average power obtained in the 3.5 – 3.75 µm window with a fixed diameter fibre is 0.022 mW.

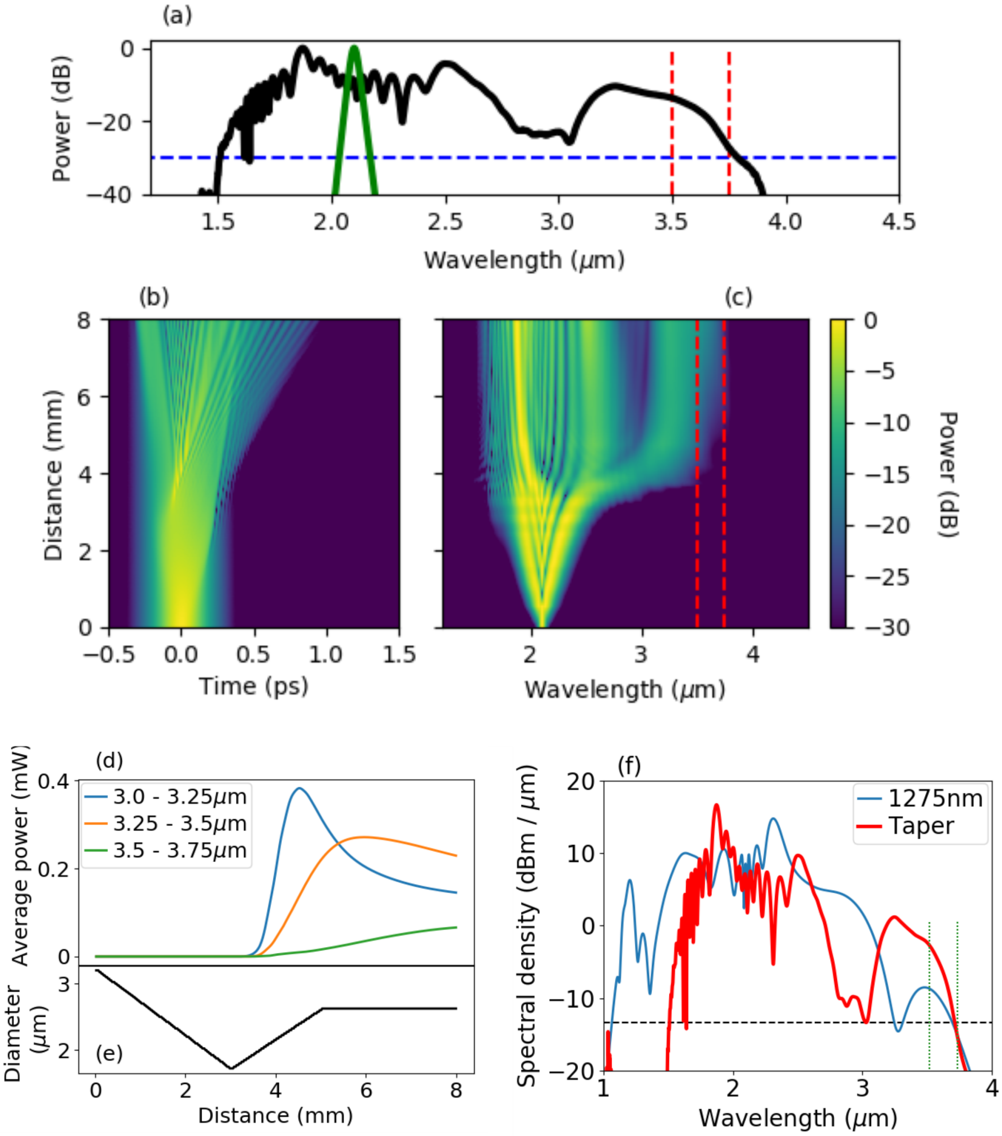

FIGURE 7.7: 1kW (18mW) pulses. (a) Output spectrum. (b) Temporal evolution. (c) Spectral evolution. (d) Evolution of average power in 250nm spectral ranges between 3 and 3.75μm. (e) Taper profile. (f) Comparison of taper output with fixed diameter fibre (1275nm) at length where power in the 3.5 - 3.75 μm range is highest.

By using our taper design (Fig. 7.1) with an input diameter of 3200nm, waist of 1700nm and output facet diameter (2625 nm) that maximises phase-matching to the target range (as shown in Fig. 7.5), we can generate a SC with 0.066 mW across 3.5 – 3.75 μm, which is a threefold improvement. The overall SC spans 1.2 octaves (1.64 – 3.75 μm) with a total average power of 8.3 mW. Fig. 7.7 shows the spectral output (a), as well as the evolution of the pulses in the temporal (b) and spectral (c) domains.

Fig. 7.7(d) shows how the average power evolves in the 0.25 μm spectral windows from 3 – 3.75 μm, mapped against the taper profile below in (e). This evolution shows that the average power peaks in progressively longer wavelength windows as the light propagates along the length. In particular, it can be seen that the average power in the 3.25 – 3.5 μm window peaks near the end of the up-taper region before dropping as the power in the target range (3.5 – 3.75 μm) rises in the final straight section of the taper. This is evidence for FWM-based transfer of power from the shorter to the longer wavelength range along the end facet.

Finally, Fig. 7.7(f) shows a spectral density plot obtained using the tapered structure, compared with the output from a length of fixed diameter fibre (with core diameter of 1275 nm) in which the most average power in the target region is generated. This gives a clear indication that the tapered design can be used to improve the transfer of power to a specific spectral window.

7.5.2 3.75 – 4 µm target range with 2 kW pulses

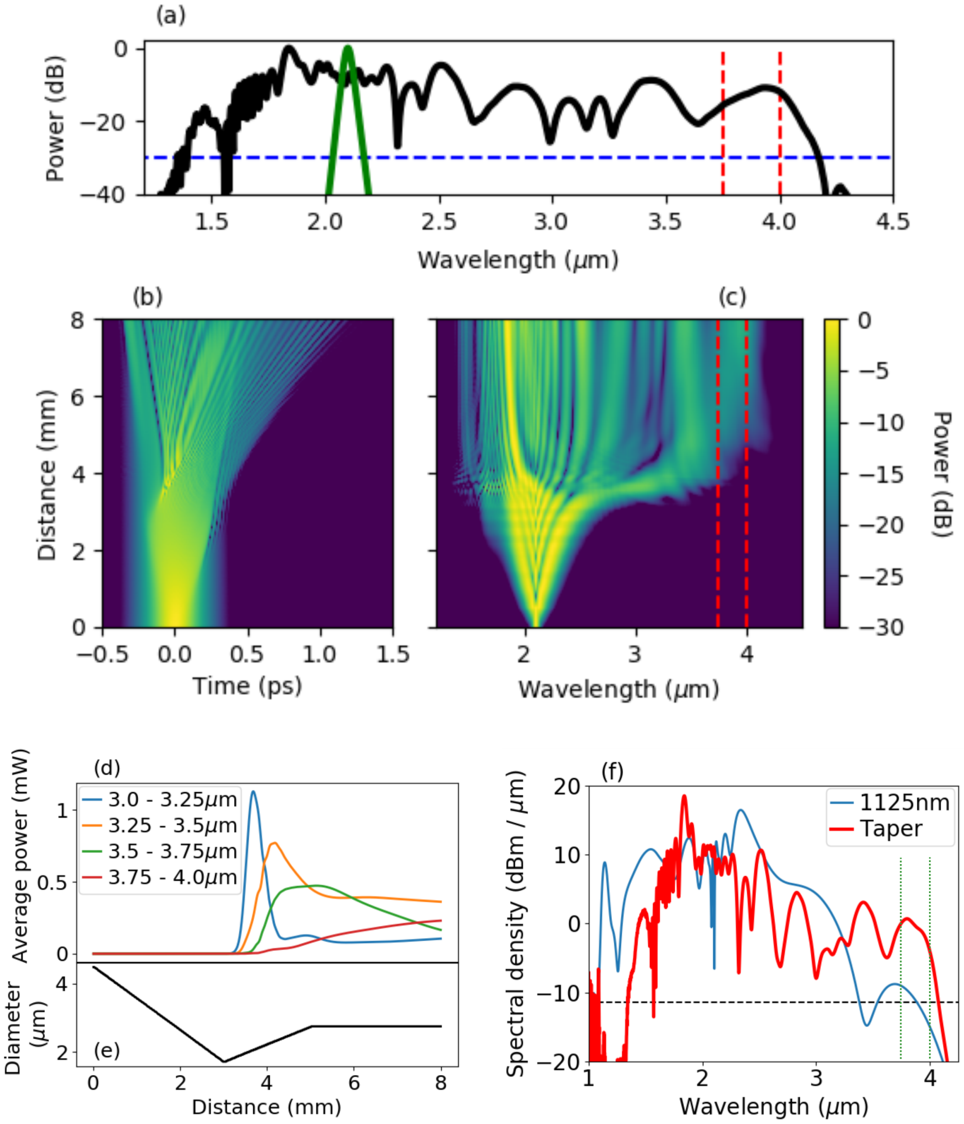

FIGURE 7.8: 2 kW (36 mW) pulses. (a) Output spectrum. (b) Temporal evolution. (c) Spectral evolution. (d) Evolution of average power in 0.25 µm spectral ranges between 3 and 4 µm. (e) Taper profile. (f) Comparison of taper output with fixed diameter fibre (1125nm) at length where power in the 3.75 - 4 µm range is highest.

For input pulses with a 2 kW peak power (36 mW average power), the SC in a single diameter extends only to $\sim$ 4 µm at the -30 dB level. The maximum power transferred to the 3.75 – 4 µm window with any length of a fixed diameter is 0.021 mW. The output facet diameter was set to 2800 nm to maximise phase-matching to this target range (see Fig. 7.5). However, without increasing the input diameter, the higher input power causes soliton fission to occur too early, as the simulation shown in Fig. 7.2 illustrates.

I found that a much larger input facet diameter (4475 nm) is required to slow down the rate of SPM-induced spectral broadening, limiting the amount of the spectrum crossing the ZDW in the waist region, which is kept at 1700nm. The simulation is shown in Fig. 7.8.

Now it can be seen that the larger input facet ensures that the initial spectral broadening is contained. The wavelength ranges shown in Fig. 7.8 (d) peak in an orderly succession, showing that power is transferred in a cascading fashion. A more significant amount of power is transferred to the 3.5 – 3.75 µm region, and is maintained for around a mm as the up-taper transitions to the end-facet, so is able to act as a pump source, allowing for efficient FWM conversion (0.23 mW) to the target region. This is an order of magnitude improvement over the best fixed-diameter case.

The power in the 3.5 – 3.75 µm window, although depleted, is still 0.166 mW at the end of the taper, and the average power across the entire 3 – 4 µm region is 0.8 mW, which is sufficient power for use in practical spectroscopy applications. As a point of reference, this represents a conversion efficiency (CE) of 2.2 % in this region, which is five times higher than the 0.4 % CE achieved in systems that have utilised much higher peak powers, such as the > 6 kW used in an aluminium nitride photonic chip waveguide [68]. The overall SC spans 1.4 octaves, from 1.6 – 4.18 µm, with total average power of 11.8 mW.

Fig. 7.8 (f) shows the spectral density output from the fixed diameter (1125 nm) for which power in the 3.75 – 4 µm range is maximised, compared with the output from the taper. It is clear that the power is cut off at around 3.75 µm in the fixed diameter fibre. Thus, the power in these pulses is not being transferred very efficiently to longer wavelengths. The taper design introduces new phase-matching conditions that are not otherwise available, allowing for effective redistribution of the spectrum to the target region.

7.5.3 4 – 4.25 µm target range with 3 kW pulses

For input pulses with a 3 kW peak power, the power transfer to the 4 – 4.25 µm window attainable with a fixed diameter fibre is limited to 0.015 mW, so this is the range I wanted to boost.

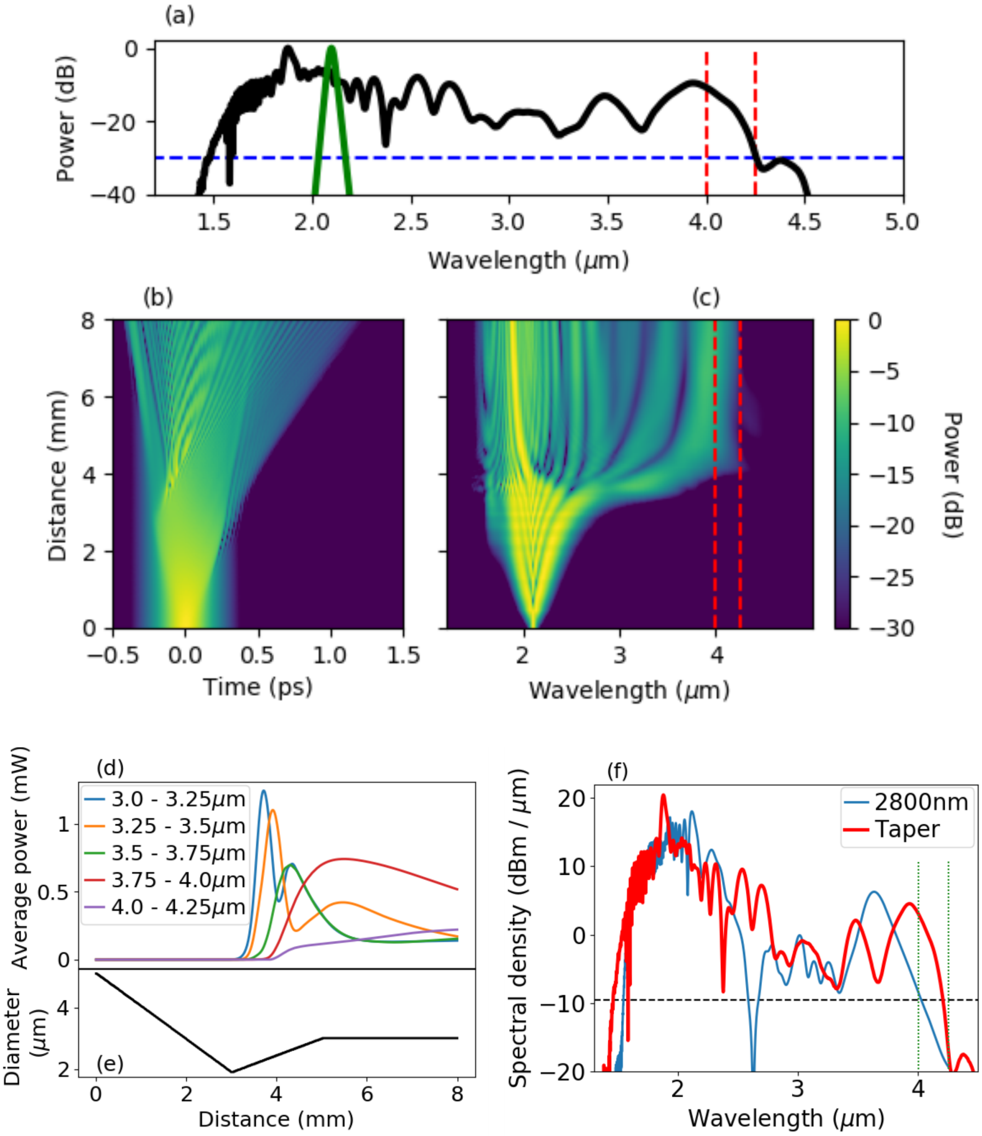

FIGURE 7.9: 3 kW (54 mW) pulses. (a) Output spectrum. (b) Temporal evolution. (c) Spectral evolution. (d) Evolution of average power in 0.25 μm spectral ranges between 3 and 4.25 μm. (e) Taper profile. (f) Comparison of taper output with fixed diameter fibre (2800nm) at length where power in the 4 - 4.25 μm range is highest.

The output diameter was increased to 3000 nm to optimise the phase-matching conditions for transfer to the target range (see Fig. 7.5), and the input diameter was increased to 5100 nm. However, even this increase in diameter was insufficient to limit the amount of spectral power crossing the ZDW before the taper waist was reached. Thus, too much soliton fission occurred, dispersing the spectral energy, as shown in Fig. 7.3.

Therefore, I increased the waist diameter to 1875 nm in order to push the ZDW further from the pump. From Fig. 7.9 it is clear that with this increase in the waist diameter, the soliton fission is more limited, and thus the energy is contained in the middle of the spectrum until the FWM process is able to take over in the up-taper and end facet. It can also be seen in Fig. 7.9 (c) that more power is transferred to the 3.75 - 4 μm range in the up-taper, which then acts as a pump source for the target range. The target power increases steadily right until the end of the taper, reaching a higher peak (0.221 mW) than in the previous design. This is an order-of-magnitude improvement on the power reached in this region with a fixed-diameter fibre.

7.5.4 4.25 – 4.5 µm target range with 5 kW pulses

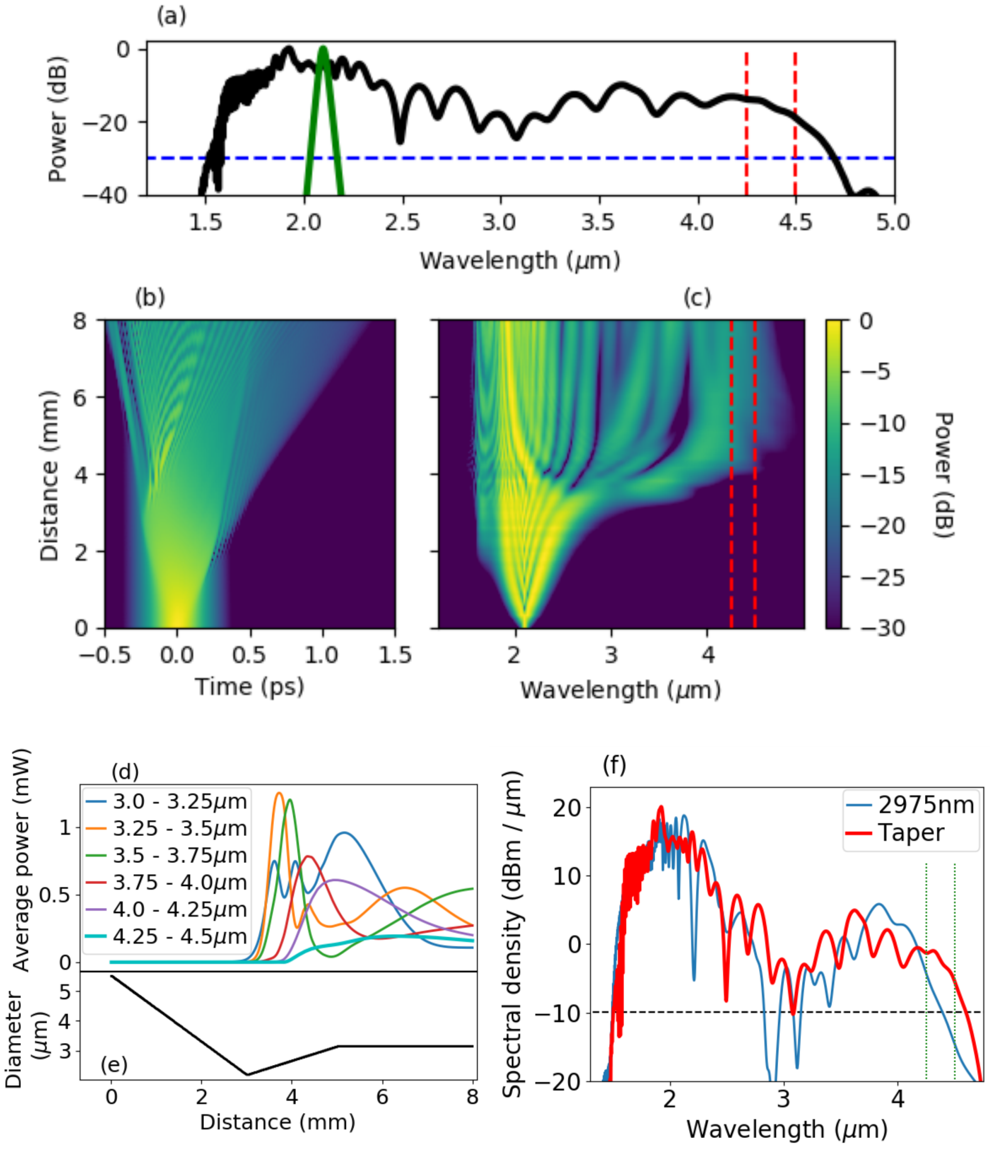

FIGURE 7.10: 5 kW (90 mW) pulses. (a) Output spectrum. (b) Temporal evolution. (c) Spectral evolution. (d) Evolution of average power in 0.25 µm spectral ranges between 3 and 4.5 µm. (e) Taper profile. (f) Comparison of taper output with fixed diameter fibre (2975nm) at length where power in the 4.25 - 4.5 µm range is highest.

The maximum average output power achievable in the 4.25 – 4.5 µm spectral window with a fixed diameter fibre is 0.039 mW, which was obtained in a fibre with a diameter of 2975 nm (see Table 7.1). To boost this range, I increased the taper input diameter to 5500 nm, the waist to 2175nm, and set the output facet diameter to 3150nm to optimise phase-matching to the target region. The output average power in this region is boosted to 0.159 mW, a fourfold improvement. The overall SC extends from 1.6 – 4.7 µm (1.5 octaves), as shown in Fig. 7.10.

7.5.5 Discussion

Table 7.2 summarises the results in this section.

Input power		Taper diameters (nm)			Generated target		
Peak (kW)	**Avg. (mW)**	**Input**	**Waist**	**Output**	**λ Range (µm)**	**Power output (mW)**	**Boost factor**
1	18	3200	1700	2625	3.5 - 3.75	0.066	3
2	36	4475	1700	2800	3.75 - 4	0.23	11
3	54	5100	1875	3000	4 - 4.25	0.221	14.7
5	90	5500	2175	3150	4.25 - 4.5	0.159	4.1

TABLE 7.2: Summary of taper parameters used for each peak input power, and average power transferred to the target wavelength range in each case.

It shows that with a low input peak power (1 kW), the taper design offers a threefold improvement in the average power conversion to the target wavelength range. With 2 – 3 kW, the improvement is a more significant order-of-magnitude. The wavelength conversion with a 5 kW input is more modest, as nonlinear losses have a clamping effect, but nonetheless the average power transferred to the target region is still a fourfold improvement over that achievable with a fixed diameter fibre.

These results show that a silicon-core tapered fibre could be used to generate power in the greenhouse gas absorption region that is comparable to that generated in [64] and [65] but with less input power, potentially allowing for a compact spectroscopy solution.

7.6 Extending the wavelength range out to 5.5 µm

The biggest source of loss in silicon fibres and waveguides for wavelengths > 4 µm is cladding loss, whereby the mode spreads into the silica cladding and is thus subject to the increased losses of this material. For a fibre with a large enough core diameter however, the mode can be confined almost entirely to the silicon core itself with very little cladding interaction. Thus, the possibility of using the entire transparency window of silicon (out to 8 µm) opens up, as explored in [60]. In this section, I will explore the possibility of extending the SC generation to at least 5.5 µm with the same design principles as before, i.e. using an up-taper and a fixed-diameter end-facet to maximise FWM to the target wavelengths and build up sufficient average power for spectroscopy applications. I also use the same pulse parameters to see how much long-wavelength transfer can be attained before needing to consider a longer-wavelength pump source.

As explained previously, the goal is not simply to extend the long-wavelength edge of the SC, which has been achieved multiple times, but to increase the average power in those longer wavelengths such that it has a signal-to-noise ratio suitable for broadband gas spectroscopy.

7.6.1 Phase-matching solutions

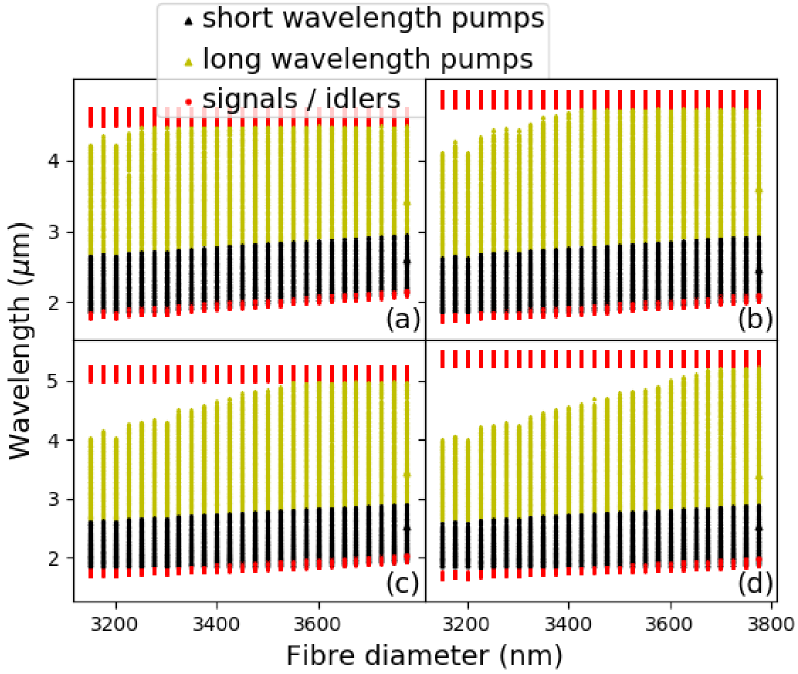

FIGURE 7.11: Four wave mixing phase-matched solutions where pumps have $\lambda > 1.85\,\mu m$ and signals are in the target ranges (a) 4.5 - 4.75 µm, (b) 4.75 - 5 µm, (c) 5 – 5.25 µm and (d) 5.25 – 5.5 µm. Black triangles represent the short wavelength pumps, yellow triangles represent the long wavelength pumps, and red circles represent the generated signals and idlers.

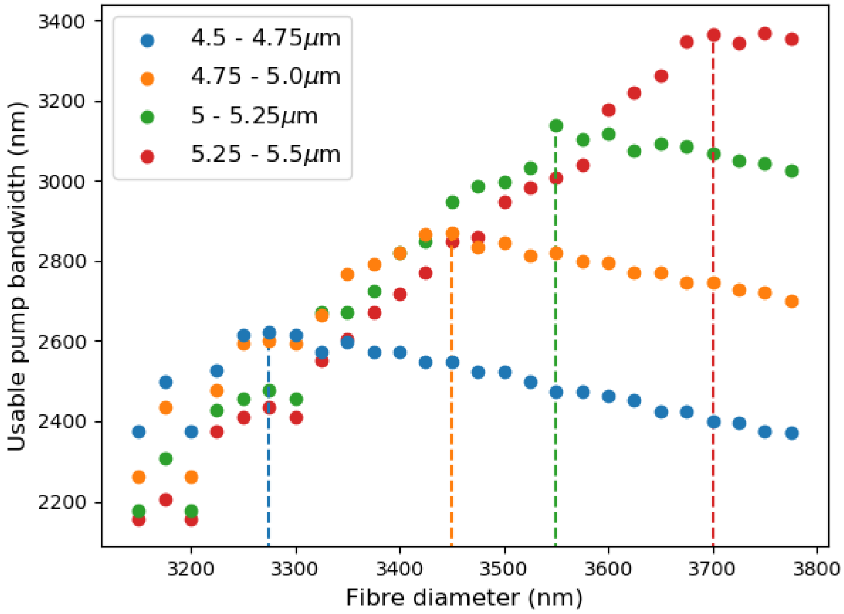

FIGURE 7.12: Bandwidth of phase-matched solutions for non-degenerate FWM where the pumps exist at wavelengths longer than 1.85 µm for target signals in the labelled wavelength ranges.

As before, the design process starts with identifying the core diameter at which the maximum possible bandwidth can be used as pump sources for FWM-based power transfer to the target wavelength ranges. Fig. 7.11 shows the positions of the pumps, signals and idlers where the phase-matching condition is fulfilled. Fig. 7.12 shows the corresponding usable pump bandwidth. The peaks (indicated with dashed lines) correspond to the diameters where the pump wavelength range starts to overlap with the target range and thus indicate what the output facet core diameter should be for each range.

7.6.2 Fixed-diameter simulations

Again, as before, the target for improvement depends on the average power that can be produced in the wavelength bands of interest with lengths of fixed-diameter silicon fibre. Fig. 7.13 shows the results of 20 mm lengths of fibre pumped with 150 fs pulses, centred at 2.1 μm with a repetition rate of 100 MHz and peak powers ranging from 6 to 10 kW. Table 7.3 summarises these results.

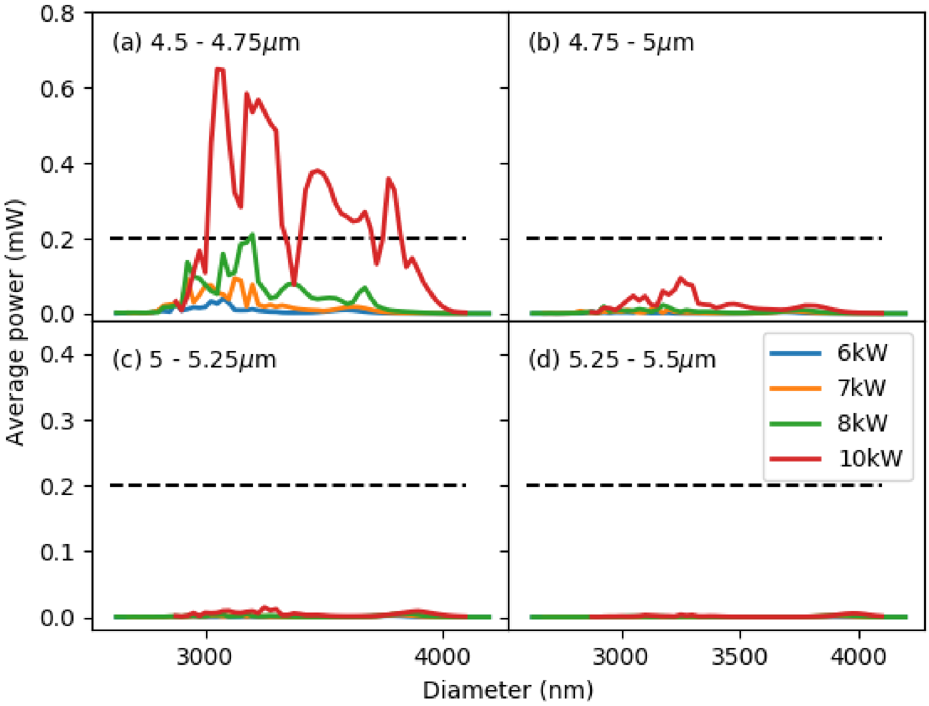

FIGURE 7.13: Results from fixed-diameter simulations with input powers of 6 – 10 kW, showing power transferred to (a) 4.5 – 4.75 μm, (b) 4.75 – 5 μm, (c) 5 – 5.25 μm and (d) 5.25 – 5.5 μm.

Input power		**Target**	
Peak (kW)	**Average (mW)**	**λ Range (µm)**	**Maximum power output (mW)**
6	108	4.5 – 4.75	0.041
7	126	4.75 – 5	0.012
8	144	5 – 5.25	0.006
10	180	5.25 – 5.5	0.006

TABLE 7.3: Maximum average power transferred with fixed-diameter fibres of any length to the 0.25 µm target ranges with labelled input powers.

The simulations show that increasing the input peak power from 6 to 10 kW produces a significant increase in the 4.5 - 4.75 µm range, but a much more modest increase in the 4.75 - 5 µm range. There is then an almost negligible increase in the last two ranges.

These results give a sense of the 'horizon' of achievable long-wavelength powers when pumping with fixed-diameter fibres. The peak pump power could be boosted beyond 10 kW, but at this point TPA is already extremely limiting. This is indicated by the results of these simulations, which show that the difference between average power generated in the 5 – 5.25 and 5.25 – 5.5 µm ranges is negligible when increasing the input peak power from 8 to 10 kW.

Extending the SC beyond this point would therefore require a longer wavelength pump, but the investigation in this chapter is focussed on the limits of what is achievable with a pump centred at 2.1 µm.

7.6.3 Taper design simulations

The following results provide a snapshot of the improvements that can be achieved for these longer wavelengths with taper designs based on those explored earlier in this chapter and keeping the pulse parameters the same. Note that the input facet diameter in all of these designs is 5500 nm.

7.6.4 4.5 – 4.75 µm target range with 6 kW pulses

The trend of increasing the output facet diameter to optimise FWM phase-matching to the target wavelength range continues with the design for 6 kW pulses. The output diameter is set to 3325 nm, but the input diameter (5500 nm) and waist (2150 nm) are kept at approximately the same as for the 5 kW design. This breaks the trend of increasing the input and/or waist diameters, which means that in order to reach wavelengths beyond 4.5 µm, the early spectral broadening (dominated by soliton fission) is becoming more important. This is because the pump wavelengths need to be longer in order to generate the even longer signal wavelengths.

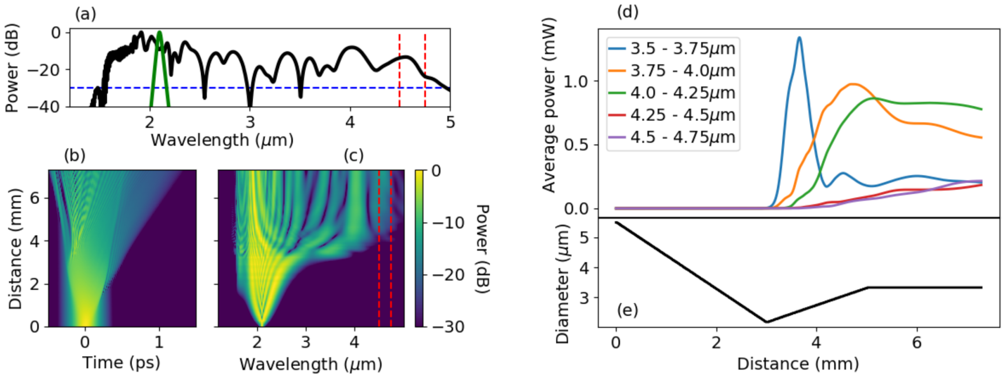

FIGURE 7.14: Simulation of 6 kW pulses through a taper designed to optimise average power output in the 4.5 – 4.75 μm wavelength range. (a) Output spectrum. (b) Temporal evolution of the pulses. (c) Spectral evolution. (d) Evolution of average power in 0.25 μm wavelength bands. The target band is the purple line. (e) Profile of the taper showing how the diameter changes with length.

The simulation of pulses propagating through this design is shown in Fig. 7.14. The power transferred to the target range is 0.21 mW, which occurs at a length of 7.3 mm as shown by the purple line in Fig. 7.14 (d). Thus the end-facet is reduced to a length of 2.3 mm. This reduction in length is due to the fact that the longer wavelength target requires increased soliton fission in the initial part of the taper. As a result, the overall energy is less contained and the entire broadening process occurs over a shorter length.

7.6.5 4.75 – 5 μm target range with 7 kW pulses

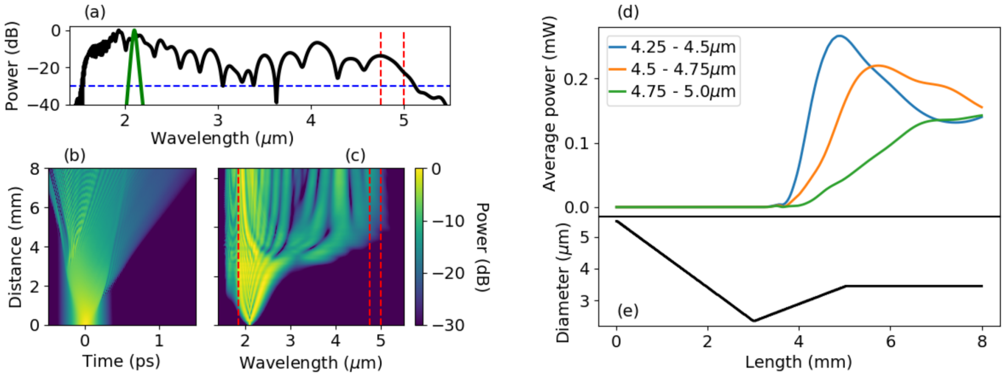

FIGURE 7.15: Simulation of 7 kW pulses through a taper designed to optimise average power output in the 4.75 – 5 μm wavelength range. (a) Output spectrum. (b) Temporal evolution of the pulses. (c) Spectral evolution. (d) Evolution of average power in 0.25 μm wavelength bands. The target band is the green line. (e) Profile of the taper showing how the diameter changes with length.

With the power increased to 7 kW in order to reach the next target wavelength range, the waist diameter is increased to 2325 nm and the output facet is increased to 3450 nm to maximise phase-matching to the target wavelength range. The input facet is kept at 5500 nm.

Fig. 7.15 shows the simulation output of this taper design. The average power generated in the 4.75 – 5 µm target range is shown by the green line in Fig. 7.15 (d). Note that this line appears to be continuing to increase at the end of the fibre but this is in fact the peak. The maximum average power in this range is 0.142 mW which is an order-of-magnitude improvement over a fixed-diameter fibre with this peak input power and is 50% higher than the maximum output with a fixed diameter even when the input peak power is increased to 10 kW (red line in Fig. 7.13 (b)).

7.6.6 5 – 5.25 µm target range with 8 kW pulses

With this design, although the output facet diameter is increased to 3550 nm to optimise phase-matching to the target wavelength range, the output in the target range is maximised when the waist diameter is actually decreased to 2025 nm, based on simulations run with a range of waist diameters. As the target range gets further away from the pump, the early soliton fission that occurs with a smaller waist becomes increasingly useful to accelerate the initial spectral broadening. With target ranges closer to the pump, this early broadening needed to be controlled to allow shorter wavelengths to build up before being used as pump sources, but now the increased early broadening is needed to reach the longer wavelengths that will serve as pumps.

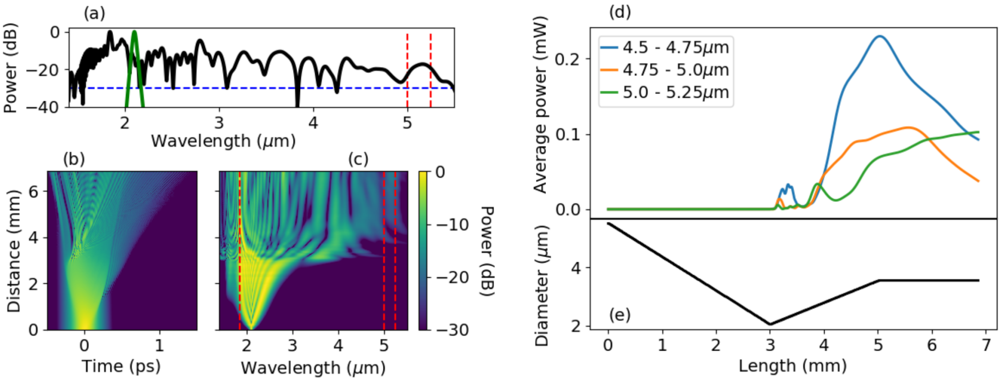

FIGURE 7.16: Simulation of 8 kW pulses through taper designed to optimise average power output in the 5 – 5.25 µm wavelength range. (a) Output spectrum. (b) Temporal evolution of the pulses. (c) Spectral evolution. (d) Evolution of average power in 0.25 µm wavelength bands. The target band is the green line. (e) Profile of the taper showing how the diameter changes with length.

Fig. 7.16 shows the simulation output of the taper best-optimised to target the 5 - 5.25 µm range. The input peak power has been increased to 8 kW and the maximum average output power in the target range is 0.102 mW, shown as the green line in Fig. 7.16 (d). This is considerably lower than the desired 0.2 mW ‘benchmark’ level, but nonetheless is more than an order-of-magnitude improvement over the power produced in this range with a fixed diameter, with 8 kW or even 10 kW peak input power.

7.6.7 5.25 – 5 µm target range with 10 kW pulses

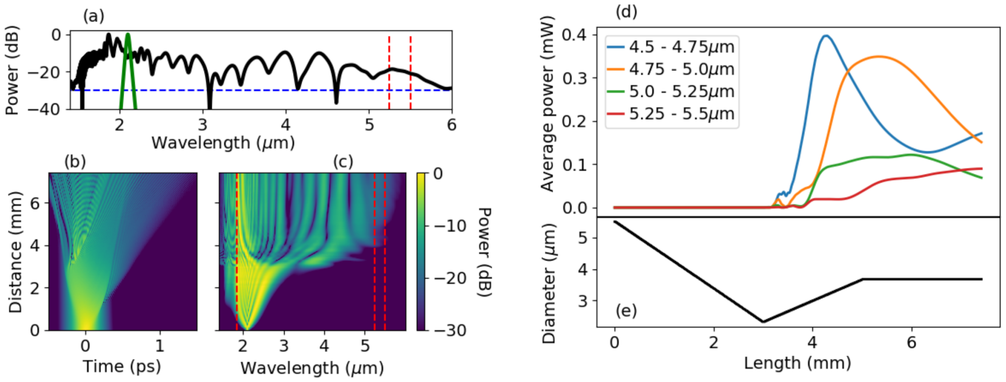

FIGURE 7.17: Simulation of 10 kW pulses through a taper designed to optimise average power output in the 5.25 – 5.5 µm wavelength range. (a) Output spectrum. (b) Temporal evolution of the pulses. (c) Spectral evolution. (d) Evolution of average power in 0.25 µm wavelength bands. The target band is the red line. (e) Profile of the taper showing how the diameter changes with length.

Fig. 7.17 shows the output of a design optimised to generate power in the 5.25 – 5.5 µm wavelength range. The output facet diameter is 3675 nm to optimise the phase-matching conditions for transfer to the target wavelength range, and it was found that the target power was maximised when the waist was increased from the previous design, to 2300 nm. This balances out the increased input power, is still a slightly slightly smaller waist than for the 7 kW taper design due to the increased separation between pump and target.

The output is 0.09 mW, which is an order-of-magnitude higher than that achievable with a fixed diameter fibre. Nonetheless, it is clear that at this point the returns from increased input power are significantly diminished. This is in part due to the increased separation between the pump and the target wavelength range, but also due to TPA at the pump wavelength, which is relatively small but nonetheless has an effect proportional to the square of the pump power.

7.6.8 Discussion

Table 7.4 summarises the results of this section.

Input power		**Taper diameters (nm)**			**Generated target**		
Peak (kW)	**Avg. (mW)**	**Input**	**Waist**	**Output**	**λ Range (µm)**	**Power output (mW)**	**Boost factor**
6	108	5500	2150	3325	4.5 - 4.75	0.21	5.1
7	126	5500	2325	3450	4.75 - 5	0.142	11.8
8	144	5500	2025	3550	5 - 5.25	0.102	17
10	180	5500	2300	3675	5.25 - 5.5	0.09	15

TABLE 7.4: Summary of taper parameters used for each peak input power, and average power transferred to the target wavelength range in each case.

This section has explored the potential for shifting power in the SC generation to longer wavelengths, and has shown that this is possible even while exploring a small subset of the design space. Although improvements of an order-of-magnitude in the average output power in the target wavelength ranges even out to 5.5 µm are made by using a tapered design, it seems that this is the limit of what can be achieved with a pump at 2.1 µm.

This is supported by the fact that the early spectral broadening needs to be boosted by reducing the taper waist for the last two target wavelength ranges (5 – 5.25 µm and 5.25 – 5.5 µm). It is also indicated by Fig. 7.13 (c) and (d) which show that power transferred to these last two target ranges with a fixed diameter is negligible, and increasing the peak power from 8 to 10 kW makes no noticeable difference. The tapers looked at here which target these ranges do offer a significant improvement, but from a lower baseline.

Future work would look at a larger region of the design space, and using a longer wavelength input pump (around 3 µm), for which available power has been increased significantly in recent years. It has been shown in a very interesting work ([60]) that a SC could indeed be generated with a silicon-core fibre taper pumped at 3 µm that extends out to the 8 µm silicon transparency limit. However, a detailed analysis of the average power generated in specific target wavelength ranges near this limit has yet to be conducted.

7.7 Conclusion

In this Chapter I have looked at eight taper designs, each optimised according to input power in order to boost the output power on the long-wavelength side of the supercontinuum generation to a level that is not attainable with a fixed diameter fibre. The simulations show that the principle of using a tapered waveguide to extend the long-wavelength edge of a SC is sound. In particular, I have shown that silicon-core tapered fibres offer a solution which could generate a usable amount of output power (of around 0.2 mW per 0.25 µm spectral band) in the greenhouse-gas absorption region of the mid-IR (2.7 – 4.3 µm), with modest input powers and pulse widths that are readily available in a portable set-up.

Although there have been various demonstrations of multiwatt average output powers in this absorption window, they typically require very high peak powers of tens of kilowatts and sub-100 fs pulses. Thus my design is unique in that practical levels of mid-IR light could be generated using conventional fibre-laser sources with $\ll 10$ kW peak power, offering a much more efficient solution. The CE from the pump laser to the 3 – 4 µm range (covering the majority of the greenhouse absorption peaks) can reach 2.2 %, which is 5 times higher than existing solutions for a portable spectroscopy platform using similar input powers because these are limited by fixed-width waveguides. Furthermore, the silicon-core fibre-based design offers straightforward integration with standard glass fibre components, as they can spliced directly together, allowing for an all-fibre solution to mid-IR spectroscopy.

The SC achievable with these taper designs, pumped at 2.1 µm, can be extended out to 5.5 µm, with nearly 0.1 mW in the last 0.25 µm range of the SC. However, further extension of a mid-IR SC out towards the silicon transparency limit of 8 µm would likely require a longer pump wavelength of ≈ 3 µm.

Chapter 8

Applying the taper model to ridge waveguides

Having demonstrated in the previous chapter that a longitudinally tapered silicon-core fibre structure can effectively boost the long-wavelength edge of a SC, it is worth investigating how effectively this design strategy would work in a ridge platform.

In this chapter, a range of taper designs with two different layer thicknesses for silicon-on-insulator (SOI) ridge waveguides are studied, and the effects of wavelength-dependent area and the phase-matching conditions allowed by the dispersion parameters are considered.

8.1 Merits of SOI ridge platform vs silicon-core fibres

Ridge waveguides are an alternative geometry to that of fibres which have the advantage of being integrated with other waveguides, optical and electronic components on a single silicon chip. They also offer increased nonlinearity due to tighter modal confinement. This means that tapers based on this platform have the potential to generate mid-IR wavelengths with greater efficiency than tapers based on the fibre platform. Moreover, as fibres have only one degree of freedom, their diameter, the phase-matching conditions can only be changed based on this. Therefore, the diameters which offer FWM conditions to transfer spectral energy from the body of a SC to its long-wavelength edge can be fairly large (> 3 µm) which means that the input peak powers needed are of the order of > 3 kW when generating usable average powers beyond 4 µm. With the ridge platform, however, there are two degrees of freedom (height and width) which means that there are multiple geometries that can offer these phase-matching conditions. Thus, smaller heights can be favoured, decreasing the effective area and thus requiring smaller input peak powers of < 3 kW.

However, one of the drawbacks of a smaller cross-section is that coupling light into and out of ridge waveguides is more difficult than with the larger cross-section offered by a fibre. Not only does the light need to be focussed to a narrower spot-size, but a rectangular cross-section supports two perpendicularly polarised modes (TE and TM), so the input polarisation needs to be matched to one of these. Fibres are circularly symmetric, so are polarisation-agnostic.

8.1.1 Accounting for sidewall scattering and linear loss

Another issue that arises with ridge waveguides is surface roughness along the sidewalls that arises during the lithography process that removes the surrounding silicon, causing scattering of the field which overlaps these regions. This is exacerbated when the over-cladding is air as opposed to silica which would provide a smoothing effect. This is not a problem for silicon-core fibres because the the flow of the silica around the core during the drawing process produces a smooth surface. To include scattering loss when using Comsol to solve the fundamental mode in a given ridge waveguide, I have used the approach outlined in [69]. There, they simply add sidewall sections to the main waveguide which have the same real refractive index but include an additional imaginary component to simulate the loss. This term is actually arbitrary and depends on the thickness of the sidewall sections and the mesh set-up, but once it is set such that the output loss value matches the expected one, it can be used to produce values for wavelengths where they have not been measured.

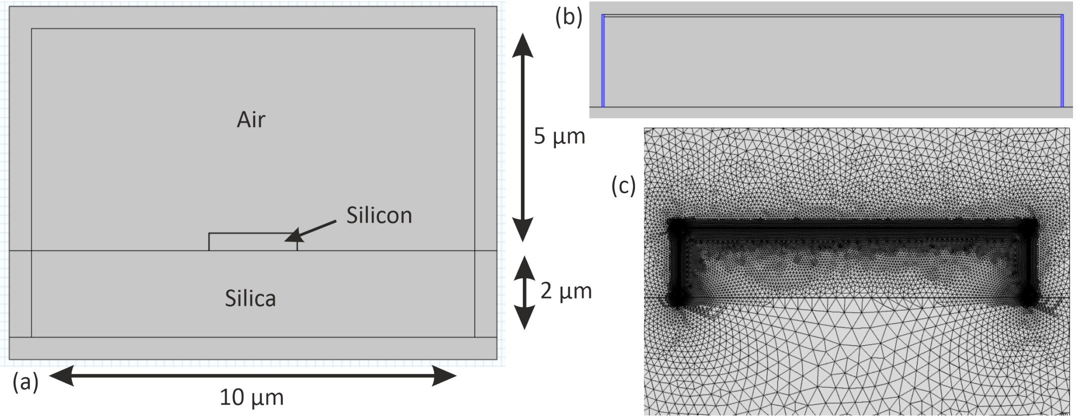

FIGURE 8.1: Comsol model used for calculating dispersion, effective area and linear loss parameters for the ridge waveguides. (a) Whole geometry showing silica under-cladding, silicon core and air over-cladding. (b) Core, with highlighted regions showing where the sidewalls are modelled. (c) The mesh used around the core.

Fig. 8.1 shows the model set up in Comsol. Some trial and error was needed to set an appropriate value for the imaginary refractive index in the sidewalls, because the model is in 2D and thus does not depend on propagation length. I used the linear loss measurements plotted in [70] to test that the model produced sensible outputs. These loss measurements are high and many improvements have been made to reduce these losses since the work was carried out [71]. However, the important result from this work is that there is an exponential relationship between the linear loss and the waveguide width. For a 200 nm thick waveguide, the linear loss at 1.54 µm is negligible with a width > 3.5 µm. However, this loss then increases to $\sim$4 dB/cm with a 1.5 µm width, 10 dB/cm with a 1 µm width and > 30 dB/cm for 0.5 µm width. As mentioned, these are high loss values, but I decided it was best to assume the maximum value for scattering loss for the simulations conducted here. As it turns out, for the longer wavelengths and thicker waveguides studied in this chapter, the scattering loss becomes negligible.

I tested the Comsol model with this wavelength and compared 1.5 µm and 1 µm widths. With 10 nm sidewalls, I adjusted the imaginary part of the refractive index to produce a loss of 10 dB/cm for 1 µm width and 3 dB/cm for 1.5 µm width. As noted in [69], changing the sidewall width does not change the ratio of these results, but only the absolute values, such that the imaginary component needs to be adjusted.

As noted above, with the ridge waveguide thickness increased to at least 500 nm and with most of the wavelengths in the SC simulated in this chapter lying beyond the 2.1 µm pump, the sidewall scattering loss becomes negligible. As with silicon-core fibres, the biggest source of linear loss for wavelengths > 3 µm is from interaction of the fundamental mode with the silica cladding, for which the losses significantly increase beyond 4 µm.

I included this cladding loss in the model as the imaginary refractive index value, extracted from [58]. When the fundamental mode is solved by the model, the overall propagation loss is included in the imaginary part of the effective index, which can be converted to a loss figure in dB/cm.

Fig. 8.2 shows the loss profiles for two widths at 500 nm thickness, and one at 600 nm thickness. The loss increases noticeably beyond 4 µm, but is still a manageable level of < 3 dB/cm. However, beyond 4.5 µm, the loss becomes prohibitive.

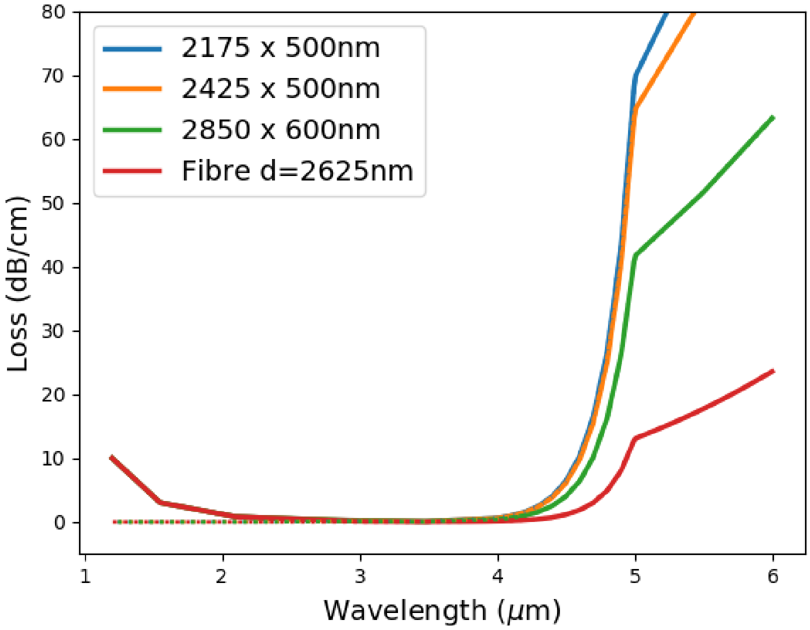

FIGURE 8.2: Linear loss by wavelength for ridge waveguides with 500 nm and 600 nm thickness. Linear loss for a 2625 nm diameter fibre is also plotted for comparison.

8.1.2 Including wavelength-dependent effective area

The Comsol model is also used to calculate the effective area at different wavelengths, and this can be used to calculate the wavelength-dependent effective area self-steepening term used in Eq. 2.61. Fig. 8.3 shows the effective area for a range of wavelengths with a 500 nm thick waveguide and also the effect on γ of the self-steepening term on ridge waveguides with 500 and 600 nm thickness.

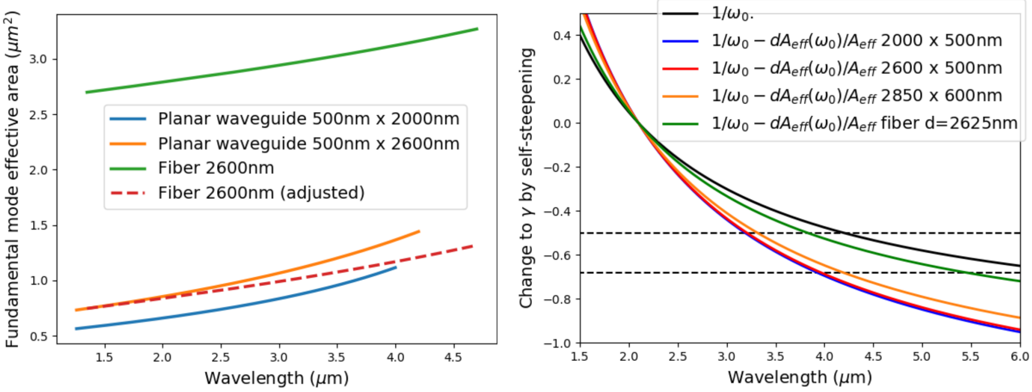

(a) (b)

FIGURE 8.3: (a) Effective area of the fundamental mode in SOI waveguides with 500 nm thickness, compared with a silicon-core fibre with diameter of 2600 nm. The dashed red line shows the fibre line adjusted for ease of comparison. (b) Self steepening in SOI waveguides with thicknesses of 500 and 600 nm, compared with a silicon-core fibre with 2625 nm diameter. Black line shows the purely frequency-dependent self-steepening term. Blue and red lines show the correction to this when including wavelength-dependent effective area for 500 nm thick waveguides with widths of 2000 nm and 2600 nm respectively, and orange line shows the correction for a 600 nm thick waveguide with width of 2850 nm. Green line shows the correction for a fibre with 2625 nm diameter for comparison. The dashed lines show the point when self-steepening reduces γ by -50% and -68%. This latter level is only reached at 5.5 µm for the fibre whereas it occurs at 3.95 µm in the ridge waveguides.

It is clear that the wavelength-dependent effective area has a more significant effect than for a fibre with the smallest output facet diameter looked at in the previous chapter. For reference, the dashed lines show the point at which self-steepening reduces γ by -50% and -68%. This lower level corresponds to the level in the fibre at 5.5 µm, which was the longest wavelength targeted in the fibre taper designs. This large reduction in γ occurs at 3.95 µm in the ridge waveguides, which means that generation of wavelengths beyond 4 µm is likely to be highly inefficient. This will indeed be demonstrated in the results section where simulations ignoring the wavelength-dependent area self-steepening term will be compared with those including it. There is a modest reduction in this effect with a 600 nm waveguide, so this ridge thickness will also be tested.

8.2 Ridge taper design process

One of the advantages of using a ridge platform over a fibre one is that the longitudinal profile can be much more arbitrary. With a fibre, the taper has to be drawn out, which limits the exact shape attainable. It also sets a minimum length on the taper, which is why the designs were mostly 8 mm long in the previous chapter. With a ridge platform, however, the shape is defined by lithography, which means that the length can be shorter and the design itself can have any chosen profile.

Designing a taper takes some trial and error, testing a multitude of shapes and simulating pulse propagation through them. There are certain guidelines provided by analytic analysis, such as the ZDW for a particular cross-section, and the phase-matching conditions available for a particular target range, but beyond this, the only way to really know how the spectrum will change over the length of the waveguide is to simulate it. As time-consuming as this is, it is still more efficient and cost-effective than manufacturing every waveguide profile and measuring light propagation. This stage should only be conducted once the design stage is complete.

8.2.1 Optimising the waveguide thickness

The taper principles worked out for silicon-core fibers should also work for ridge waveguides. However, care is required because the rectangular cross-section introduces a second ZDW which changes the phase-matching conditions on the long-wavelength side. The non-degenerate FWM process with pumps either side of the first ZDW can only transfer power to wavelengths shorter than the second ZDW.

The standard thickness of silicon waveguides is 220 nm, but this is for telecoms wavelengths. For extending into the mid-IR, a thickness of at least 300 nm is needed [72].

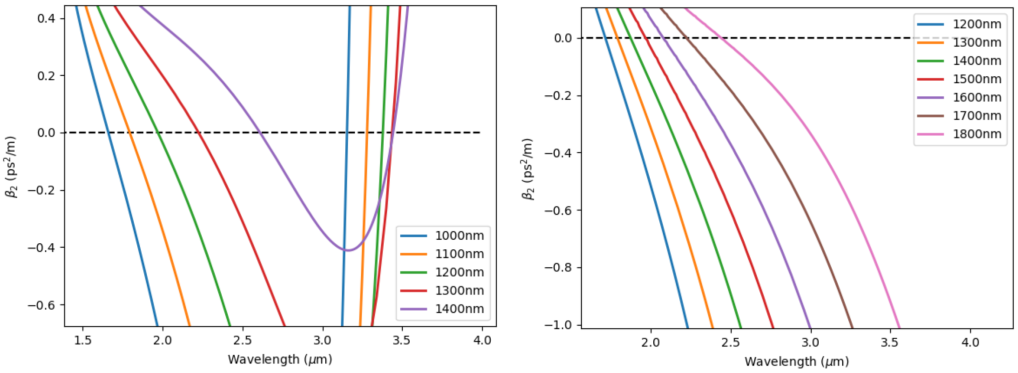

(a) (b)

FIGURE 8.4: Dispersion curves for a ridge waveguide with (a) 300 nm thickness with widths of 1000 nm – 1400 nm and (b) 400 nm thickness with widths of 1200 nm – 1800 nm.

Looking at Fig. 8.4 (a), it can be seen that with a thickness of 300 nm, the dispersion curves have two ZDWs at wavelengths shorter than the target ranges which start at 3.5 µm. The taper design principles discussed in the last chapter and applied here rely on pumps either side of the ZDW, with the short-wavelength pump and idler lying in the normal dispersion regime and the long-wavelength pump and signal lying in the anomalous regime. This second ZDW thus rules out such FWM processes from occurring.

With a thickness of 400 nm (b), the second ZDW disappears, which means that phase-matching conditions are possible, but the first ZDW needs to be close to 2.5 µm (i.e. in the middle of the usable bandwidth for pump sources). This occurs with widths of less than 2000 nm, which mean that the modes of these longer wavelengths will be too tightly confined, causing high scattering and cladding losses, as shown in Fig. 8.5.

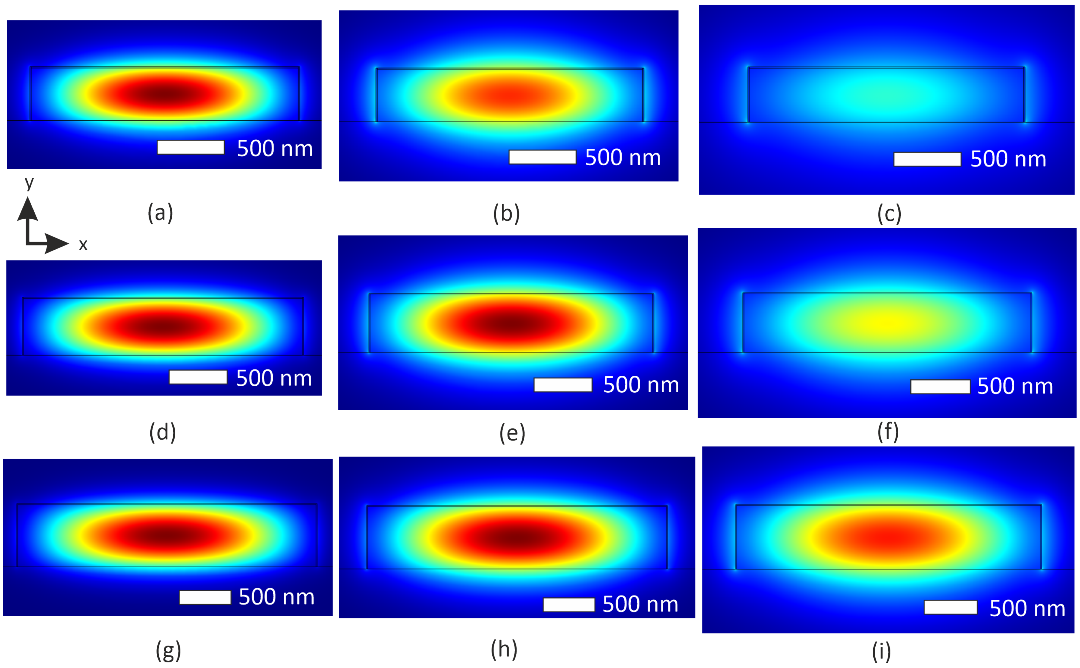

FIGURE 8.5: Fundamental mode profiles, as generated by Comsol. Top row: modes in a 400 x 2000 nm waveguide at (a) 2.1 µm, (b) 3.3 µm and (c) 4.5 µm. Middle row: modes in a 500 x 2425 nm waveguide at (d) 2.1 µm, (e) 3.3 µm and (f) 4.5 µm. Bottom row: modes in a 600 x 2850 nm waveguide at (g) 2.1 µm, (h) 3.3 µm and (i) 4.5 µm. Note that the width is increased along with the thickness in each case to account for the dimensions where the appropriate phase-matching conditions are met for FWM-based transfer to the target regions.

Fig. 8.5 shows the fundamental mode profiles solved in Comsol at three wavelengths: 2.1 µm (the pump), 3.3 µm (an intermediate wavelength) and 4.5 µm (the edge of the furthest target wavelength range). In each case the width is set such that the ZDW lies in the correct region for the phase-matching conditions needed in the end-facet. It can be seen that the longest wavelength is barely confined with a 400 nm thick waveguide (top row), and only starts to be reasonably confined in a 500 nm one (middle row), and this is the thickness I use for the initial designs. Clearly the confinement is better still with 600 nm thickness (bottom row) and this waveguide thickness will also be studied in this chapter.

I thus assume that the minimum waveguide thickness that could produce wavelengths out to 4.5 µm is 500 nm. I will start with designing tapers with this thickness, and then consider a 600 nm thick waveguide base.

The ridge taper design settled on for 500 nm thick waveguides is much simpler than for the fibre tapers, as shown in Fig. 8.6.

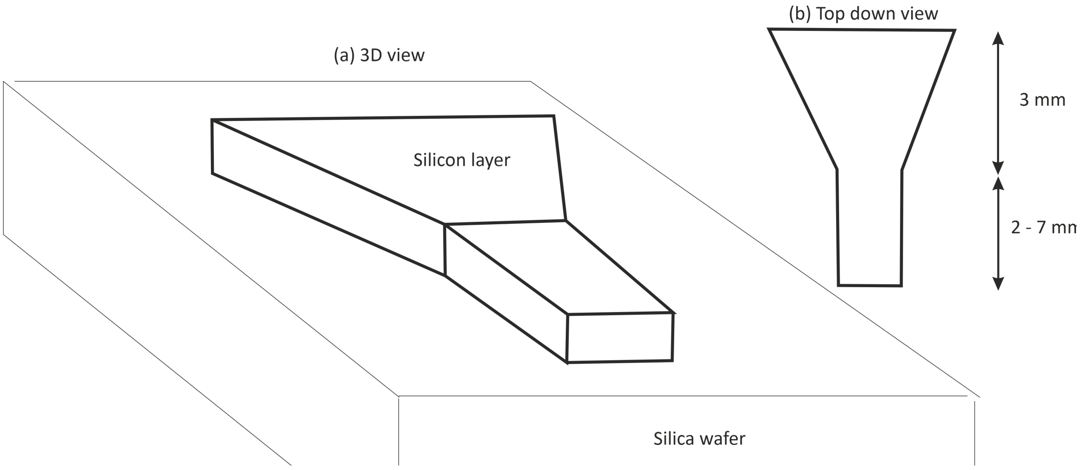

FIGURE 8.6: Design of SOI ridge waveguide taper. (a) 3D view. (b) Top-down view.

This is because the widths that provide the maximum bandwidth for FWM phase-matching to the target wavelength bands lies in the range 2175 - 2425 nm. The width where the ZDW is at the pump wavelength, 2.1 µm, is 2000 nm. As this is so close to the output widths required, there does not seem to be an advantage to tapering down to 2000 nm and then back up again. The designs that seem to work the best are those that start with a large input width (> 3000 nm) and then taper down to the output width, which is then maintained for some length to allow the FWM process to transfer energy to the target wavelength range.

8.3 500 nm thick waveguides

In this section ridge waveguides with 500 nm thickness are studied to find the widths where phase-matching to the target wavelength ranges 3.5 – 3.75 µm, 3.75 – 4 µm, 4 – 4.25 µm and 4.25 – 4.5 µm are optimal. Taper designs that incorporate these output widths are then simulated and the outputs in these ranges are compared with the maximum power levels transferred in fixed-width waveguides to see if the tapers successfully boost these power levels.

8.3.1 Phase matching conditions

The dispersion curves for 500 nm thick SOI waveguides with widths from 2000 – 2900 nm are shown in Fig. 8.7.

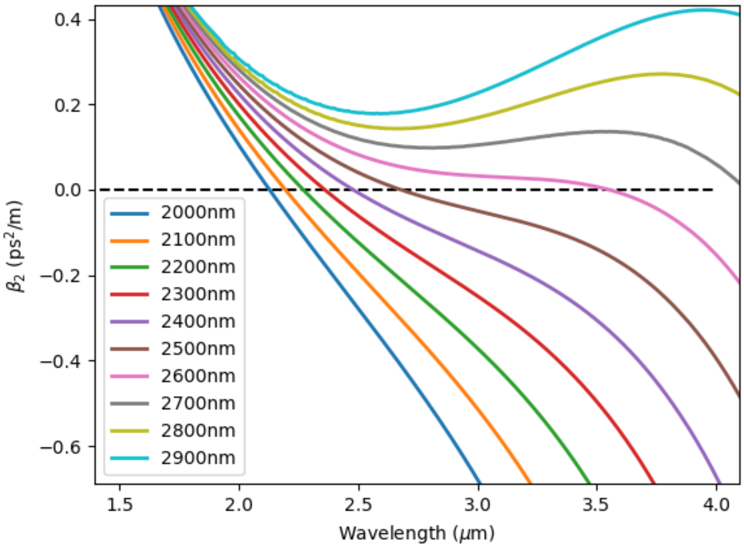

FIGURE 8.7: Dispersion curves for 500 nm thick SOI ridge waveguides with widths of 2000 – 2900 nm.

It can be seen that the dispersion curves in Fig. 8.7 become less linear as the width increases, with the curve becoming less steep with longer wavelengths as if there will be a second ZDW, but then the curve dives down again. This means there is not a second ZDW before the edge of the target wavelength ranges at 4.5 µm, which allows for phase-matching solutions to the target wavelength ranges. However, the ZDW wavelength increases rapidly for widths > 2400 nm.

As with the fibre tapers, the optimum output diameters correspond to the point where FWM phase-matching solutions ‘fill-in’ the gap between the target wavelength range and the lower pump limit. This was 1.85 µm for fibres, but for ridge tapers the limit is decreased to 1.7 µm. It may be that the increased self-steepening allows the spectrum to broaden further towards short wavelengths without triggering runaway soliton fission. In any case, the actual design process is iterative, in that the optimum width is ascertained by looking at the phase-matching solutions, but these depend on the lower pump limit. Testing taper designs with simulations then reveals which widths tend to produce the most average power in the target ranges, and this can then indicate which lower pump limit is actually producing a sensible result. It will be seen in the simulations in Sec. 8.4 that the short-wavelength SPM lobe broadens down to 1.7 µm and remains fixed there.

Fig. 8.8 shows the distribution of FWM phase-matched solutions and Fig. 8.9 shows the number of solutions found, with local peaks indicated by dashed lines which correspond to the widths where the pump wavelength range starts to overlap with the target wavelength range.

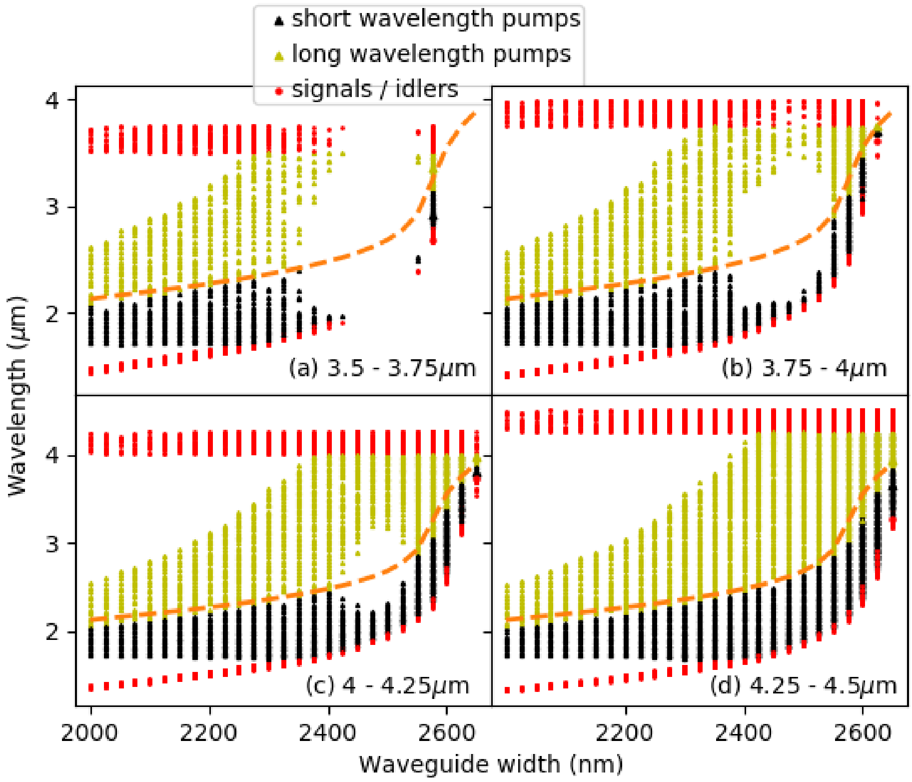

FIGURE 8.8: Four wave mixing phase-matched solutions where pumps have $\lambda > 1.7\,\mu$m and signals are in the target ranges (a) 3.5 - 3.75 µm, (b) 3.75 - 4 µm, (c) 4 – 4.25 µm and (d) 4.25 – 4.5 µm. Orange dashed line shows the zero-dispersion wavelength. Black triangles represent the short-wavelength pumps, yellow triangles the long-wavelength pumps and red circles the signals and idlers.

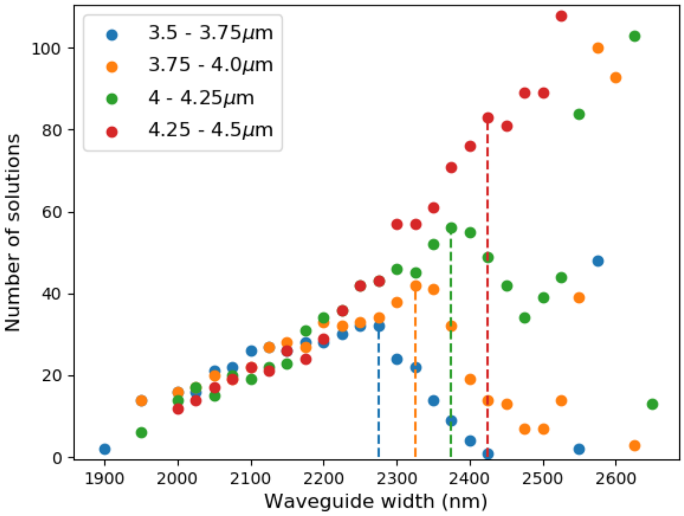

FIGURE 8.9: Number of phase-matched solutions for non-degenerate FWM where the pumps exist at wavelengths longer than 1.7 µm for target signals in the labelled wavelength ranges. The peaks (indicated with dashed lines) correspond to the waveguide widths where the pump wavelength range starts to overlap with the target range.

With phase-matching conditions constrained by a lower pump limit of 1.7 µm, the optimum widths for maximising the number of phase-matched solutions are 2275 nm, 2325 nm, 2375 nm and 2425 nm for power transfer to the target wavelength ranges 3.5 – 3.75 µm, 3.75 – 4 µm, 4 – 4.25 µm and 4.25 – 4.5 µm respectively.

Fig. 8.9 shows these optimum widths as vertical dashed lines. But whereas for fibres the peak in number of solutions corresponded to the maximum usable pump bandwidth, this is not the case for ridge waveguides. The solutions do increase with width, as expected, reaching a local maximum before dropping off again as the bandwidth decreases (due to the move to longer wavelengths of the shortest wavelength pump).

It will be noted that there are 'holes' in Fig. 8.8 (a – c). This is not a sampling error (the grid size was increased to test this) but rather due to the sensitivity of the phase-matching conditions to the higher-order dispersion terms. These play an increasing role at widths > 2400 nm, where the change in ZDW wavelength clearly increases at an accelerated rate with width. This means that, given a combination of wavelengths for the two pumps, signal and idler, a small change in position of one of these will result in a bigger change in the positions of the others than is the case where the dispersion curve is more 'linear' (i.e. higher-order terms are smaller).

Fortunately, these gaps in the spread of phase-matched solutions for each target range do not appear until the widths have increased beyond the point at which the usable pump bandwidth meets the lower edge of each range. This means that there is sufficient 'density' of solutions for each of the optimum widths indicated in Fig. 8.9.

However, after widths of 2500 nm, the number of solutions increases again, such that even as the usable bandwidth decreases, the 'density' of solutions increases, which can be seen in Fig. 8.9 as the number of solutions increasing after the optimum width has been reached. This is because, as the ZDW approaches very close to the lower edge of each target wavelength range, the dispersion curve becomes highly linear over the reduced usable pump bandwidth, which means that small changes in each pump wavelength result in small changes to signal and idler. Needless to say, these larger widths are less useful as the usable pump bandwidth is so small, so the bulk of the initial spectrum will not be converted to the target wavelength ranges.

8.3.2 Fixed width simulations

As with the fibre taper design process, I started by looking at the power transferred to the target wavelength ranges when pumping through fixed width waveguides. The simulations all use a length of 15 mm to ensure that power in each range reaches a maximum before the end but these peak points usually occur in the first 10 mm. The maximum average power is then extracted to use as a benchmark against which improvement by tapering the waveguide can be compared. Following the last chapter, I keep the target average power level at 0.2 mW, but the input peak powers are smaller because the nonlinear interaction is increased by the smaller effective area in these waveguides. Fig. 8.10 shows the complete results of these simulations, which are summarised in Table 8.1.

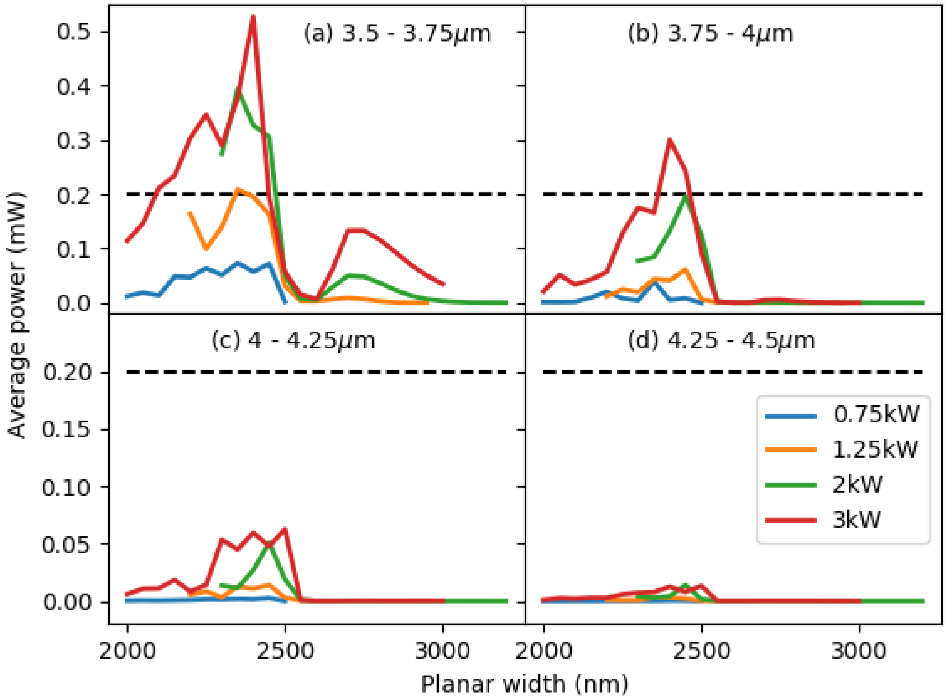

FIGURE 8.10: Complete results from fixed-width 500 nm thick ridge waveguide simulations, showing maximum average power levels transferred, with input peak pump powers of 0.75 – 3 kW, to the target wavelength ranges (a) 3.5 – 3.75 µm, (b) 3.75 - 4 µm, (c) 4 – 4.25 µm and (d) 4.25 – 4.5 µm. Dashed black lines show the benchmark level of 0.2 mW.

Input power		**Target**	
Peak (kW)	**Average (mW)**	**λ Range (µm)**	**Maximum power output (mW)**
0.75	13.5	3.5 – 3.75	0.08
1.25	22.5	3.75 – 4	0.061
2	36	4 – 4.25	0.051
3	54	4.25 – 4.5	0.014

TABLE 8.1: Maximum average power transferred with fixed-width 500 nm 15 mm long ridge waveguides to the 0.25 µm target ranges with labelled input powers.

Fig. 8.10 shows that increasing the input peak power increases the output average power in the first two wavelength ranges, 3.5 – 3.75 µm and 3.75 – 4 µm. However, the increase in the 4 – 4.25 µm range shows significant clamping, with the maximum average output only increasing from 0.052 mW to 0.063 mW with a peak input power increase from 2 to 3 kW. This is likely because the self-steepening created by the wavelength-dependent effective area reduces γ by 68% at wavelengths beyond 4 µm, as mentioned previously.

At the end of Section 8.4, the impact of this effect will be demonstrated by comparing the outputs when the wavelength-dependent effective area term is included and omitted in both a fixed-width waveguide and a tapered waveguide targeting this target region.

8.4 500 nm thick tapered waveguide results

In this section, four different ridge taper designs are simulated, each with an output width chosen to maximise the transfer of power to the four target wavelength ranges, as indicated in Fig. 8.9. The downward taper length is kept at 3 mm in each case, but the length of the output section varies depending on the point at which maximum power is transferred to the target range in each case.

As with the fibre taper work, the input peak power is increased as the target wavelength range gets further away from the pump, and comparisons are made with the benchmark average power levels established in the previous section.

8.4.1 3.5 – 3.75 µm with 0.75 kW pulses

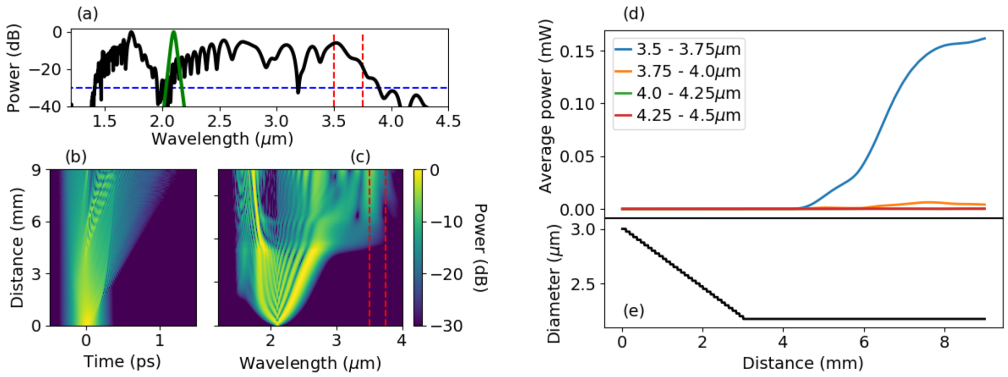

FIGURE 8.11: Simulation of 0.75 kW pulses through a 9 mm long 500 nm thick ridge taper consisting of 3 mm down-taper from 3000 nm down to an output fixed-width section with a width of 2175 nm. (a) Output spectrum. (b) Temporal pulse evolution. (c) Spectral pulse evolution. (d) Evolution of average powers in the 3.5 – 3.75 µm, 3.75 – 4 µm, 4 – 4.25 µm and 4.25 – 4.5 µm wavelength ranges. (e) Profile of the taper width over its length.

The simulation in Fig. 8.11 shows that a taper design with 3000 nm input width and 2175 nm output width works effectively at transferring spectral power to the 3.5 – 3.75 µm range, with the average power in this region starting to increase significantly after 4 mm (1 mm into the end section) and then continuing to increase over 5 mm, reaching a maximum of 0.169 mW at the end of the taper. This is a twofold improvement over the maximum output power achievable with a fixed width waveguide pumped with the same input power. Furthermore, this is an improvement of 2.5 times the average power produced in this range by a fibre taper (see previous chapter) pumped with 1 kW peak input power. Therefore, for this wavelength range, a ridge waveguide taper offers a significant efficiency improvement over a fibre.

8.4.2 3.75 – 4 µm with 1.25 kW pulses

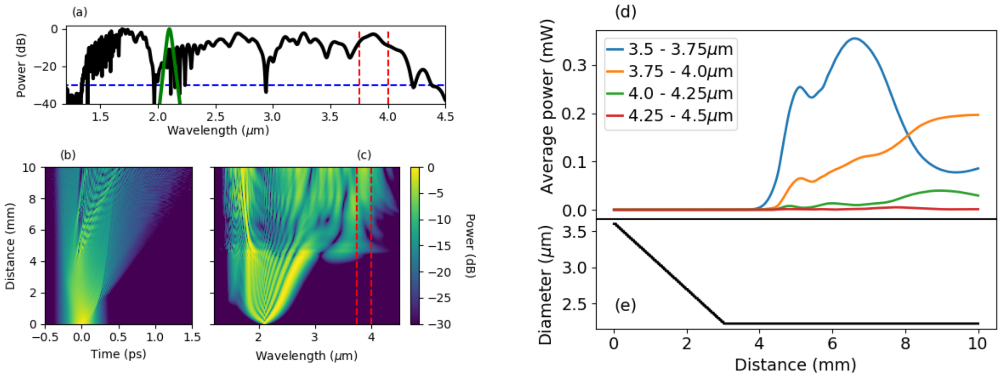

FIGURE 8.12: Simulation of 1.25 kW pulses through a 10 mm long 500 nm thick ridge taper consisting of 3 mm down-taper from 3600 nm down to an output fixed-width section with a width of 2225 nm. (a) Output spectrum. (b) Temporal pulse evolution. (c) Spectral pulse evolution. (d) Evolution of average powers in the 3.5 – 3.75 µm, 3.75 – 4 µm, 4 – 4.25 µm and 4.25 – 4.5 µm wavelength ranges. (e) Profile of the taper width over its length.

The simulation in Fig. 8.12 shows that this taper design with 3600 nm input width and 2225 nm output width is effective for transferring energy to the next target wavelength range, 3.75 – 4 µm. As with the previous design, the FWM-based transfer starts at around 4 mm, and it can be seen that the previous wavelength range, 3.5 – 3.75 µm starts to increase first, eventually dropping after 6 mm while the target range continues to rise, suggesting that a cascaded FWM process is occurring. The average power in this target range peaks at 0.19 mW, a more than threefold improvement over a fixed-width waveguide and again more efficient than a fibre taper, which required a peak input power of 2 kW to attain this level of output.

8.4.3 4 – 4.25 µm with 2.25 kW pulses

Fig. 8.13 shows pulse propagation through a taper design with 3700 nm input width and 2375 output width optimised for power transfer to the 4 – 4.25 µm range. At this point, the self-steepening has become more significant, so pumping with 2 kW of peak input power only produced 0.147 mW average power in the target range. This is still a factor of 3 improvement over the benchmark level recorded for this input peak power. However, increasing this peak input power to 2.25 kW boosts the output average power level to 0.239 mW. This makes this ridge waveguide taper over 30% more efficient than the fibre taper designed for this wavelength range, which required 3 kW peak input power to generate > 0.2 mW in the target range.

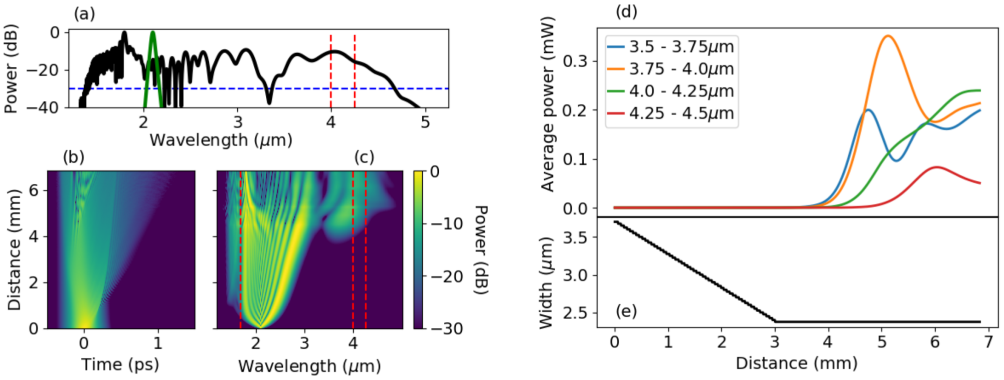

FIGURE 8.13: Simulation of 2.25 kW pulses through a 6.84 mm long 500 nm thick ridge taper consisting of 3 mm down-taper from 3700 nm down to an output fixed-width section with a width of 2375 nm. (a) Output spectrum. (b) Temporal pulse evolution. (c) Spectral pulse evolution. (d) Evolution of average powers in the 3.5 – 3.75 μm, 3.75 – 4 μm, 4 – 4.25 μm and 4.25 – 4.5 μm wavelength ranges. (e) Profile of the taper width over its length.

8.4.4 4.25 – 4.5 μm with 2 – 3 kW pulses

At this wavelength range, the self-steepening effect induced by the wavelength-dependence of the effective area has a significant clamping effect that prohibits any appreciable amount of average power building up in this region. The following simulations demonstrate this by comparing the pulse propagation when the wavelength-dependent effective area term is omitted and included. First, a fixed-width waveguide is studied, and then a taper.

The 2450 nm output width is chosen as this is the width that produces the maximum output average power in the 4.25 – 4.5 μm range with the wavelength-dependent effective area term included in the self-steepening. This peak is 0.014 mW and occurs at a 10 mm length, as shown in Fig. 8.14. However, switching off the wavelength-dependent effective area term has a dramatic effect, as shown in Fig. 8.15. The average power in this range shoots up to 0.15 mW, an order-of-magnitude increase, after only 5 mm. The level of average power in the previous wavelength range, 4 – 4.25 μm, is impacted to a very similar degree, reaching a peak of 0.03 mW with the effect switched on and 0.2 mW with it switched off.

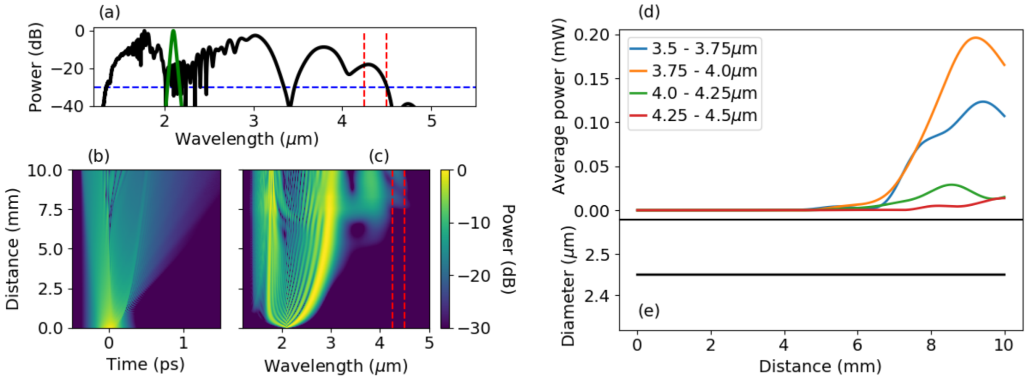

FIGURE 8.14: Simulation of 2 kW pulses through a 10 mm long 500 nm thick 2450 nm wide ridge waveguide with the wavelength-dependent effective area self-steepening term included. (a) Output spectrum. (b) Temporal pulse evolution. (c) Spectral pulse evolution. (d) Evolution of average powers in the 3.5 – 3.75 μm, 3.75 – 4 μm, 4 – 4.25 μm and 4.25 – 4.5 μm wavelength ranges. (e) Profile of the taper width over its length.

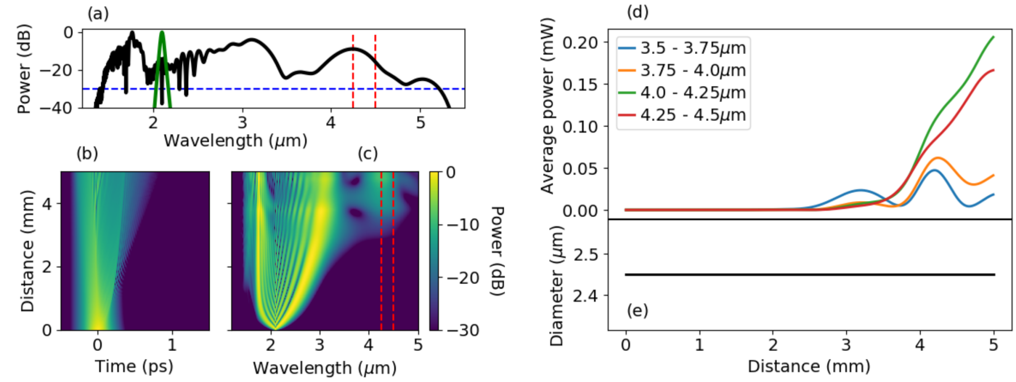

FIGURE 8.15: Simulation of 2 kW pulses through a 5 mm long 500 nm thick 2450 nm wide ridge waveguide with the wavelength-dependent effective area self-steepening term omitted. (a) Output spectrum. (b) Temporal pulse evolution. (c) Spectral pulse evolution. (d) Evolution of average powers in the 3.5 – 3.75 μm, 3.75 – 4 μm, 4 – 4.25 μm and 4.25 – 4.5 μm wavelength ranges. (e) Profile of the taper width over its length.

These simulations of a fixed width indicate the magnitude of the effect of self-steepening induced by the wavelength-dependence of the effective area, but they do not show how this affects a taper design. To demonstrate this, the following simulations show pulse propagation through a design which should work well for the target range, with a down-taper from a large input width (3700 nm) down to an output fixed-width section with a 2425 nm width, chosen to maximise the phase-matching from the bulk of the spectrum to the target wavelength range.

In this case, the input peak power is increased to 3 kW, as the input width is larger than for the fixed width comparison. The taper design does work reasonably well, even with the full self-steepening, boosting the output average power to 0.1 mW after a 2.5 mm end section, which is on the same order-of-magnitude as the target level of 0.2 mW and is nearly an order-of-magnitude improvement over the fixed-width maximum. However, with the wavelength-dependent effective area term omitted, the power level is boosted to 0.4 mW, and this occurs at a much shorter length, 0.7 mm into the end facet.

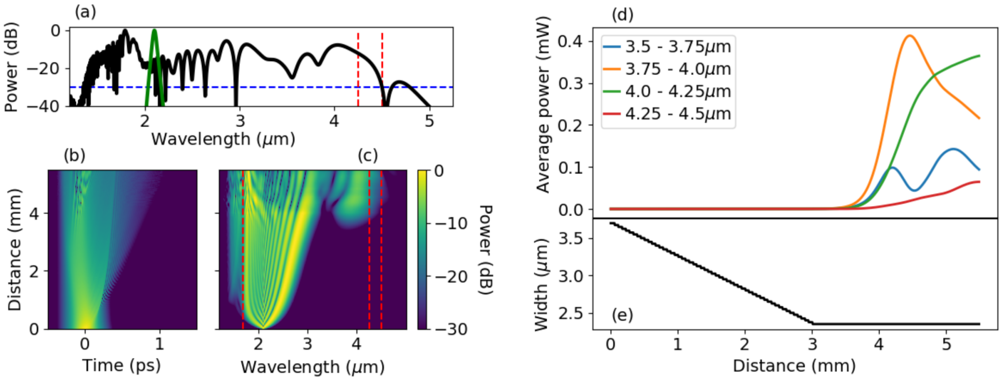

FIGURE 8.16: Simulation of 3 kW pulses through a 5.5 mm long 500 nm thick ridge waveguide taper with the wavelength-dependent effective area self-steepening term included. The input width is 3700 nm and tapers down over 3 mm to an output section of 2425 nm width. (a) Output spectrum. (b) Temporal pulse evolution. (c) Spectral pulse evolution. (d) Evolution of average powers in the 3.5 – 3.75 µm, 3.75 – 4 µm, 4 – 4.25 µm and 4.25 – 4.5 µm wavelength ranges. (e) Profile of the taper width over its length.

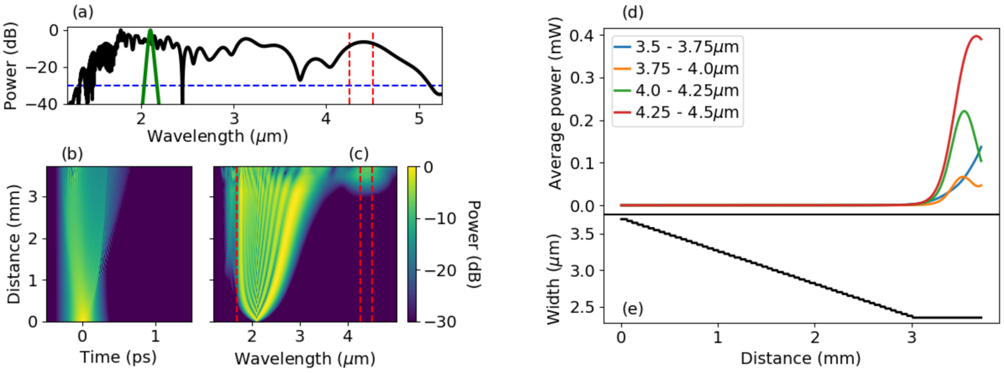

FIGURE 8.17: Simulation of 3 kW pulses through a 3.7 mm long 500 nm thick ridge waveguide taper with the wavelength-dependent effective area self-steepening term omitted. The input width is 3700 nm and tapers down over 3 mm to an output section of 2425 nm width. (a) Output spectrum. (b) Temporal pulse evolution. (c) Spectral pulse evolution. (d) Evolution of average powers in the 3.5 – 3.75 µm, 3.75 – 4 µm, 4 – 4.25 µm and 4.25 – 4.5 µm wavelength ranges. (e) Profile of the taper width over its length.

8.4.5 Discussion

Table 8.2 summarises the results of this section.

Input power		**Taper widths (nm)**		**Generated target**		
Peak (kW)	**Avg. (mW)**	**Input**	**Output**	**λ Range (µm)**	**Power output (mW)**	**Boost factor**
0.75	13.5	3000	2175	3.5 - 3.75	0.169	2.1
1.25	22.5	3600	2225	3.75 - 4	0.19	3.1
2	36	3700	2375	4 - 4.25	0.147	2.9
2.25	40.5	3700	2375	4 - 4.25	0.239	-
3	54	3700	2425	4.25 - 4.5	0.1	7.1

TABLE 8.2: Summary of taper parameters used for each peak input power, and average power transferred to the target wavelength range in each case.

In this section, the taper design principles introduced in the last chapter have been applied to SOI ridge waveguides with 500 nm thickness, albeit with a simplified design. The results of simulations show that for the first three wavelength target ranges (out to 4.25 µm), the SOI tapers are more efficient than the fibre-tapers. The first ridge taper produces more than twice the average power than the fibre taper in the 3.5 – 3.75µm target range with 75 % of the input power, making it 240 % more efficient. The second ridge taper produces 83 % of the output power in the 3.75 – 4 µm range as the fibre taper, but with 62.5 % of the input power, making it 30 % more efficient. And finally, the third ridge taper is also 30 % more efficient at transferring power to the 4 – 4.25 µm range than the fibre taper, as it requires 2.25 kW to generate > 0.2 mW in this range whereas the fibre version required 3 kW. However, the improvement stalls at this point as the self-steepening produced by the wavelength-dependent effective area of the fundamental mode in the SOI waveguides causes a significant drop in strength of the nonlinear interaction needed for FWM-based transfer to the target range 4.25 – 4.5 µm. Increasing the input power further would negate the advantage of having a higher nonlinear interaction strength in a ridge waveguide. Furthermore, the efficiency improvements that have been shown do not take into account the increased coupling loss that would be caused by the stronger coupling lens needed to launch light into a SOI waveguide due to its smaller cross-section.

8.5 600 nm thick ridge waveguides

As the clamping effect on the 4.25 – 4.5 µm wavelength range is so strong in the 500 nm thick waveguides, a better output may be achieved by increasing the waveguide thickness, increasing the effective area and thus reducing the effect of self-steepening. In this section I will look at the prospect of designing ridge waveguide tapers with a thickness of 600 nm.

8.5.1 Phase-matching solutions

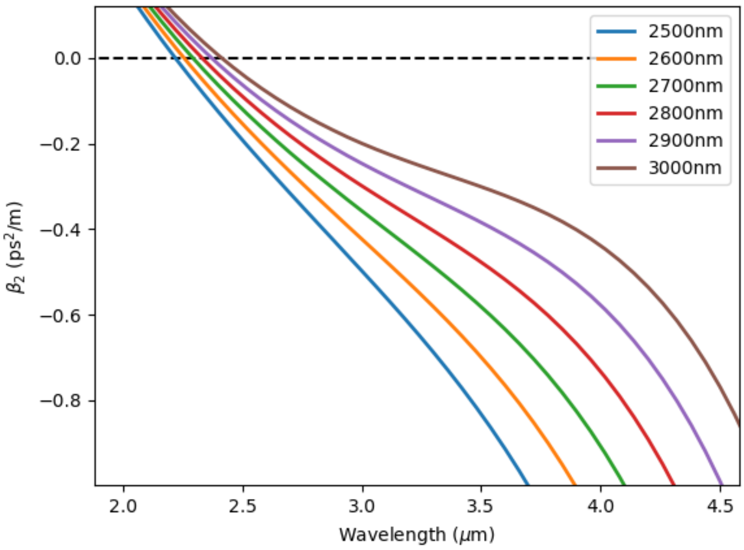

FIGURE 8.18: Dispersion curves for 600 nm thick SOI waveguides with widths in the range 2500 – 3000 nm.

Unfortunately, for a 600 nm thick ridge waveguide, the phase-matching conditions become poorer, and the optimum output width for transferring spectral power to the target wavelength bands becomes unclear. The nature of the dispersion curves means that the point at which the number of solutions reaches a peak does not correspond to the point at which the usable bandwidth is maximised.

This is very different to the pattern seen for 500 nm waveguides, where the number of solutions for each target range increases as more of the bandwidth is covered, reaching a local peak as the spectral range between lower pump limit and lower edge of the target wavelength range before dropping off again. Furthermore, the number of solutions at this peak increases for the next target range, as the pumps have a broader spectral window to cover.

For 600 nm waveguides, the dispersion curves do not favour this pattern. The ZDW increases with width, and the number of solutions initially increases, but then starts to drop again before the potentially usable bandwidth is 'filled-in'. This has the result that, for the last two target wavelength ranges (the ones we were hoping to improve the output for by increasing the thickness and thus lowering the wavelength-dependent effective area) this spectral gap is never 'filled-in' by the pumps.

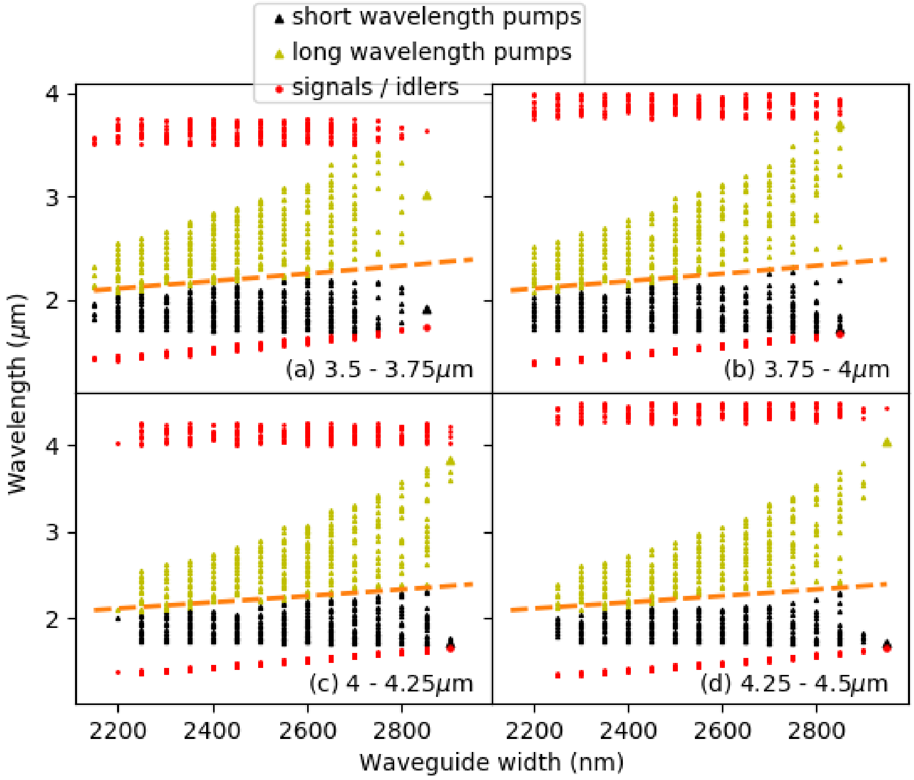

FIGURE 8.19: Four wave mixing phase-matched solutions where pumps have $\lambda > 1.7\,\mu m$ and signals are in the target ranges (a) 3.5 - 3.75 μm, (b) 3.75 - 4 μm, (c) 4 – 4.25 μm and (d) 4.25 – 4.5 μm. Orange dashed line shows the zero-dispersion wavelength.

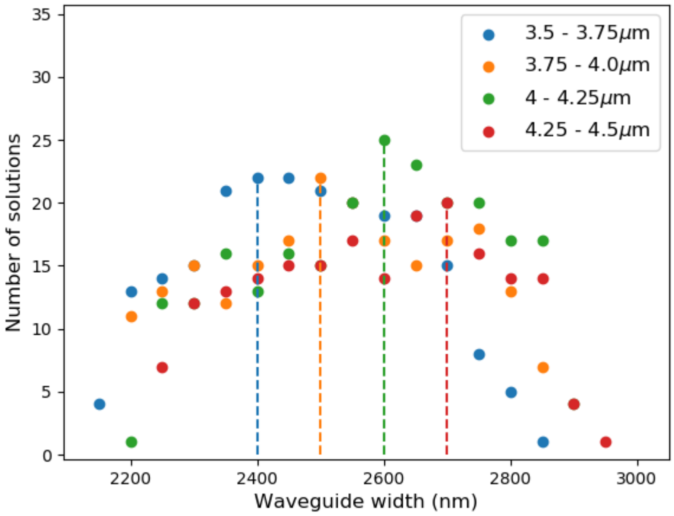

FIGURE 8.20: Number of phase-matched solutions for non-degenerate FWM where the pumps exist at wavelengths longer than 1.7 μm for target signals in the labelled wavelength ranges. The peaks no longer correspond to the waveguide widths where the pump wavelength range starts to overlap with the target range.

For example, for the first wavelength range, 3.5 – 3.75 μm, the highest number of solutions occurs at a width of 2400 nm (with 22 solutions). At this width, the longest pump wavelength is 2.85 µm. This is not a useful pump range if the goal is to maintain a SC while also maximising the power at its long wavelength edge. The number of solutions then drops to 15 at a width of 2700 nm, where the usable bandwidth is 'filled in'. This means that, although the entire spectrum can be used as a pump source, the phase-matched combinations are more spaced out, so the conversion will be less efficient than for the 500 nm thick waveguides, where the number of solutions was 32. These numbers are not the absolute number of solutions but they are proportional to the sampling rate of 25 nm used in the search algorithm.

For longer wavelengths, the situation gets worse: for 3.75 – 4 µm, the maximum number of solutions is again 22, which occurs at a width of 2500 nm. The longest pump wavelength in this case is 2.99 µm. At the point where the solutions span the maximum bandwidth, with a width of 2800 nm, the number of solutions has dropped to 13.

For 4 – 4.25 µm, the maximum number of solutions increases to 25 at a width of 2600 nm, but the longest pump wavelength is 3.07 µm. In this case, the usable bandwidth is not even fully filled in. The closest it gets is with a width of 2850 nm, at which point the number of solutions has dropped to 17 and the longest pump wavelength is 3.77 µm. At a width of 2900 nm, the number of solutions has dropped to 4, and these lie at the extreme edges of the usable bandwidth. So the 'best' width, offering a compromise between 'density' of phase-matched solutions and usable bandwidth coverage is 2850 nm.

Finally, for the 4.25 – 4.5 µm range, the maximum number of solutions is 20, which occurs at a width of 2700 nm, where the longest pump wavelength is 3.33 µm. With a width of 2900 nm, the solutions drop off significantly, so the 'best' width, based on a compromise between number of solutions and covered bandwidth, is once again 2850 nm, for which the number of solutions is 14 and the longest pump wavelength is 3.7 µm.

There are two problems here. (1) The gradual 'thinning-out' of pump combinations that phase-match to the target wavelength ranges and (2) the sudden drop-off in the number of pump combinations that occurs for the last two wavelength ranges.

The first issue can be broadly explained by the dispersion curves, shown in Fig. 8.18, becoming less linear over the spectral range of the long-wavelength pumps (i.e. between the ZDW and the target signal range). As such, a small shift in the pump positions produces a larger shift in the signal (and idler) positions, pushing it out of the target range.

The calculated changes to the signal and idler positions when the short-wavelength pump is offset are shown in Fig. 8.21.

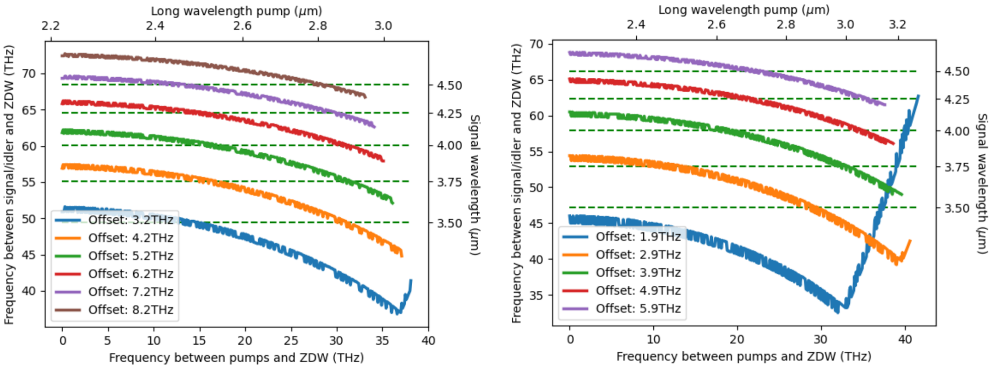

(a) 2500 nm

(b) 2600 nm

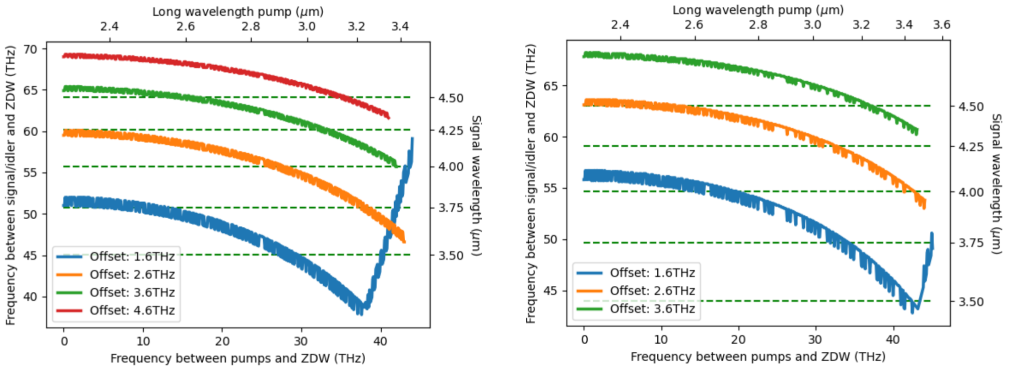

(c) 2700 nm

(d) 2750 nm

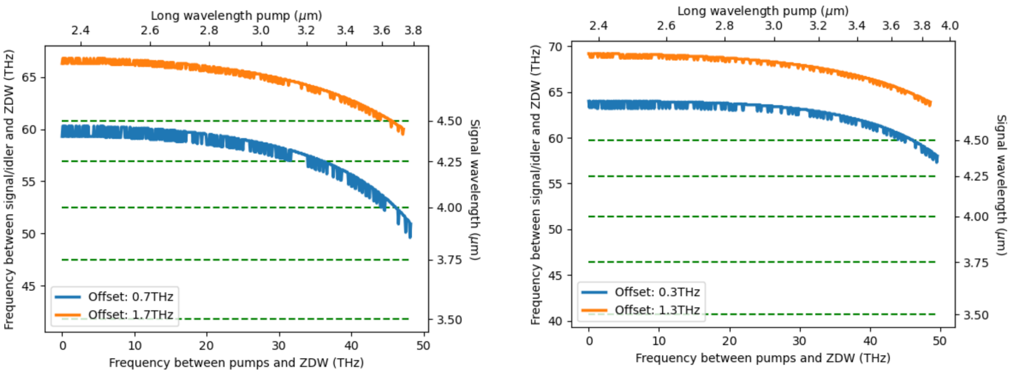

(e) 2850 nm

(f) 2900 nm

FIGURE 8.21: Position of signal wavelength when pumps are spaced around the ZDW with labelled offsets. Ridge waveguides have thickness of 600 nm and widths of (a) 2500 nm, (b) 2600 nm, (c) 2700 nm, (d) 2750 nm, (e) 2850 nm and (f) 2900 nm.

The lines show how the signal wavelength changes when the pumps move away from the ZDW. The pump positions are measured in the frequency domain (although the graphs do show the corresponding wavelengths), and initially are positioned with zero separation from the ZDW. As the dispersion curves are not linear, the solutions do not fall with equal frequency spacing above and below the ZDW, so there is an offset, which is shown in the graphs in THz. The offset is applied to the short wavelength pump (so it starts at a frequency $\omega_{\text{ZDW}} + \omega_{\text{OFFSET}}$) but this is equivalent to a negative offset applied to the long wavelength pump. The pumps are then pushed away from the ZDW at the same frequency rate until the short wavelength pump reaches the lower limit of 1.7 μm. The frequency shift of the long-wavelength pump (which always starts at zero) is shown on the x-axis and the corresponding frequency separation of the signal from the ZDW is shown on the y-axis.

The waveguide widths increase from 2500 nm to 2900 nm, and the offset of each line plotted on the graph is increased by 1 THz from the previous one. Immediately it can be seen that with smaller widths, the frequency shift of the signal is smaller with each offset step than with larger widths. This shows the sensitivity of the phase-matching conditions to a frequency shift in one of the pumps, which increases as the dispersion curve becomes less linear over the range of the pumps. This explains why the number of solutions for phase-matching to a particular target range becomes more sparse.

The second problem relates to the specific shape of the dispersion curve, which at widths > 2850 nm bends up towards the ZDW and then back down again in such a way that the pump combinations across almost the entire usable bandwidth phase-match to a very limited range of signals. The blue line in Fig. 8.21 (f) shows this very clearly. It starts beyond the last target wavelength range at the minimum pump separation from the ZDW, and remains at this wavelength for the first 30 THz (approx. 3 µm), before finally moving towards the ZDW near the edge of the usable bandwidth. The signal position only crosses into the target wavelength range at around 3.8 µm before reaching a limit of 4 µm as the short-wavelength pump reaches 1.7 µm. This explains why there are just a few odd pump solutions shown in Fig. 8.19 at a width of 2900 nm, appearing at the extreme edges of the potentially usable pump bandwidth.

These two problems mean that for the last two target wavelength ranges, 600 nm thick ridge waveguides are not a viable platform. Two taper designs are nonetheless tested in Sec. 8.7 with output widths of 2700 nm and 2850 nm to see if any significant boosting occurs in the 4 – 4.5 µm region.

8.6 Fixed-width simulations

Before testing different taper designs, it is first necessary to establish the benchmark levels of average power transferred to the target wavelength ranges with fixed-width waveguides. Fig. 8.22 shows the results of this study, which are summarised in Table 8.3.

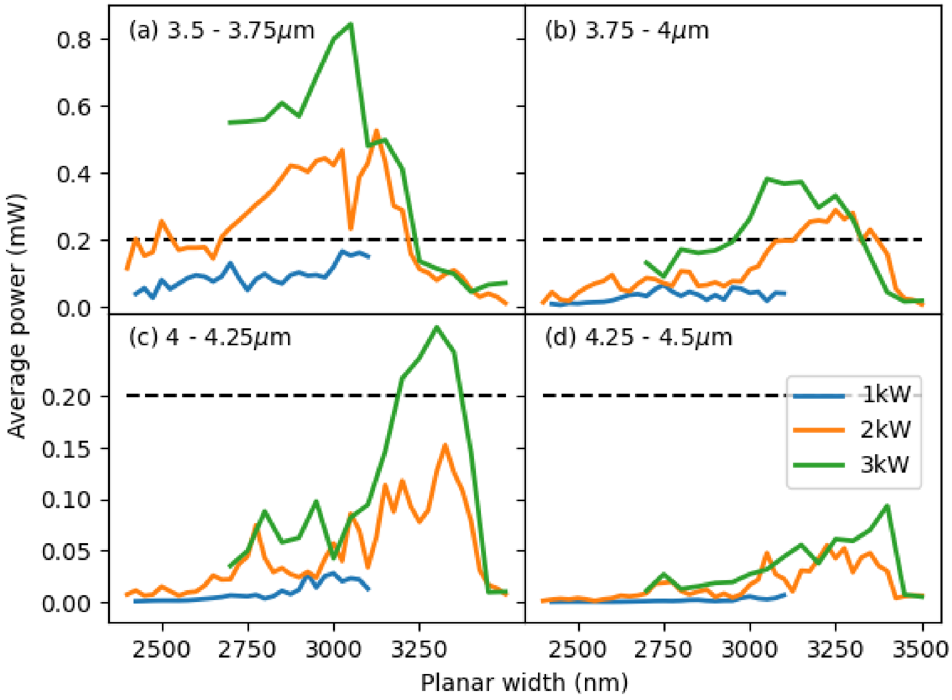

FIGURE 8.22: Complete results from fixed-width 600 nm thick ridge waveguide simulations, showing maximum average power levels transferred, with input peak pump powers of 1 – 3 kW, to the target wavelength ranges (a) 3.5 – 3.75 µm, (b) 3.75 - 4 µm, (c) 4 – 4.25 µm and (d) 4.25 – 4.5 µm. Dashed black lines show the benchmark level of 0.2 mW.

Input power		**Target**	
Peak (kW)	**Average (mW)**	**λ Range (µm)**	**Maximum power output (mW)**
1	18	3.5 – 3.75	0.167
2	36	3.75 – 4	0.288
3	54	4 – 4.25	0.265
3	54	4.25 – 4.5	0.094

TABLE 8.3: Maximum average power transferred with fixed-width 600 nm 15 mm long ridge waveguides to the 0.25 µm target ranges with labelled input powers.

The maximum average power generated in the last two target ranges, 4 – 4.25 µm and 4.25 – 4.5 µm, with a fixed-width 600 nm is actually greater with a 3 kW peak power input than for any fixed-width 500 nm thick waveguide. This is useful to know, as it means that there is less clamping of the these longer wavelengths by the self-steepening effect, as predicted. However, the lack of sufficient 'density' of phase-matched solutions for FWM-based transfer to these wavelength ranges means that I was not available to find a taper design that boosts these power outputs any further, as discussed in the next section.

8.7 Results of taper designs

As the 500 nm thick ridge waveguide tapers seem to work effectively for target ranges out to 4.25 µm, I focused on trying to design a taper for maximising the final wavelength range, 4.25 – 4.5 µm. As discussed in Section 8.5.1, the phase-matching conditions are not satisfactory, and so very poor results are achieved. I tried a number of different designs, none of which worked particularly well. Table 8.4 shows the results from some of these tests.

The following two designs utilise the simple down-taper - end-facet combination that worked for 500 nm waveguides, and have an input width of 4000 nm and output widths of 2700 nm (at which the 'density' of solutions peaks) and 2850 nm (where the pump bandwidth is closest to being 'filled in').

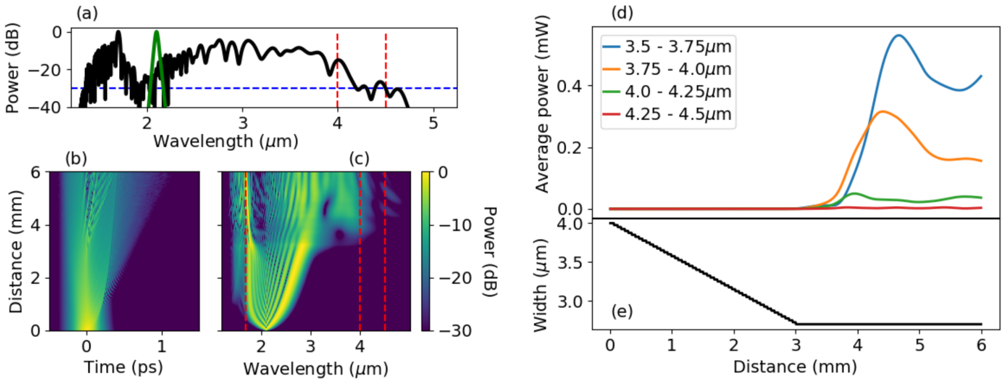

FIGURE 8.23: Simulation of 3 kW pulses through a 6 mm long 600 nm thick ridge taper consisting of 3 mm down-taper from 4000 nm down to an output fixed-width section with a width of 2700 nm. (a) Output spectrum. (b) Temporal pulse evolution. (c) Spectral pulse evolution. (d) Evolution of average powers in the 3.5 – 3.75 µm, 3.75 – 4 µm, 4 – 4.25 µm and 4.25 – 4.5 µm wavelength ranges. (e) Profile of the taper width over its length.

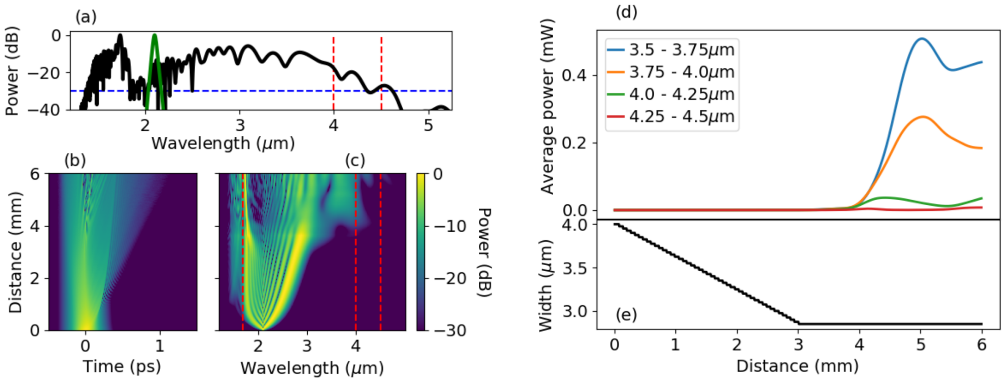

FIGURE 8.24: Simulation of 3 kW pulses through a 6 mm long 600 nm thick ridge taper consisting of 3 mm down-taper from 4000 nm down to an output fixed-width section with a width of 2850 nm. (a) Output spectrum. (b) Temporal pulse evolution. (c) Spectral pulse evolution. (d) Evolution of average powers in the 3.5 – 3.75 µm, 3.75 – 4 µm, 4 – 4.25 µm and 4.25 – 4.5 µm wavelength ranges. (e) Profile of the taper width over its length.

It is clear that neither of these tapers produce an appreciable amount of average power in either of the last two target wavelength bands. This is most likely because the phase-matching conditions for FWM-based transfer from the bulk of the spectrum to these bands do not exist. Thus, despite the lower self-steepening effect caused by the wavelength-dependent effective area, the output power in the 4.25 – 4.5 µm range is actually lower than for the 500 nm thick SOI tapers.

Taper profile		**Maximum average output power (mW)**	
Input width (nm)	**Output width (nm)**	**4 – 4.25µm**	**4.25 – 4.5µm**
4000	2700	0.096	0.015
	2750	0.096	0.012
	2800	0.067	0.007
	2850	0.176	0.022
	2900	0.13	0.021
	2950	0.097	0.05
	3000	0.118	0.041
3500	2700	0.046	0.025
	2750	0.094	0.021
	2800	0.147	0.082
	2850	0.167	0.018
	2900	0.132	0.023
	2950	0.049	0.017
	3000	0.103	0.019

TABLE 8.4: Average output power in the target ranges 4 – 4.25 µm and 4.25 – 4.5 µm with various SOI taper designs with 600 nm thickness.

It can be seen by comparing the results in Table 8.4 with Table 8.3 that none of the taper designs generate more average power in the target ranges than a fixed-width waveguide.

8.8 Thicker waveguides: 700 nm and 800 nm

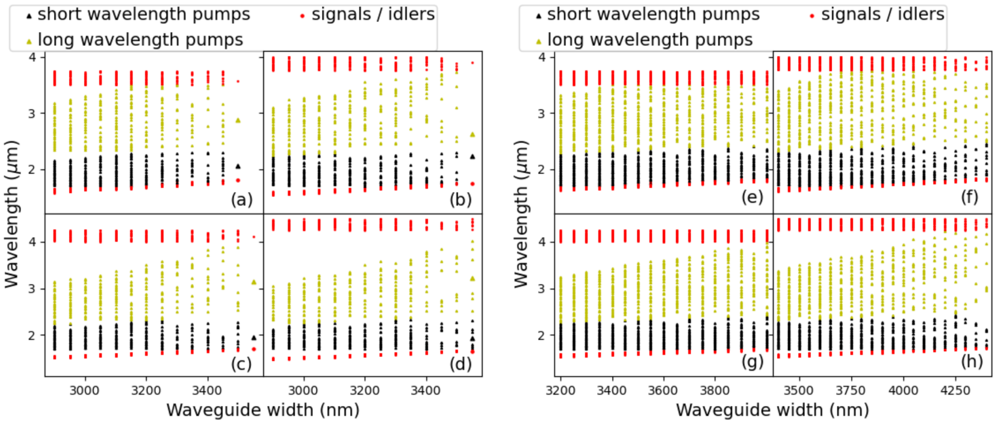

FIGURE 8.25: Four wave mixing phase-matched solutions for 700 nm thick (a – d) and 800 nm thick (e – h) waveguides where pumps have $\lambda > 1.7$ µm and signals are in the target ranges (a, e) 3.5 - 3.75 µm, (b, f) 3.75 - 4 µm, (c, h) 4 – 4.25 µm and (d, h) 4.25 – 4.5 µm.

I also looked at increasing the thickness further, to 700 nm and then 800 nm, to see if the pattern of thinning-out phase-matched solutions is an anomaly, but Fig. 8.25 shows that this is not the case. Particularly for the last target wavelength range, 4.25 – 4.5 µm, shown in (d) and (h), this thinning-out effect is significant, so although the usable bandwidth is 'filled-in', the conversion efficiency will likely be low. Furthermore, as the thickness is increased, the width at which phase-matching would be optimised for this final wavelength range also increases. Thus, the effective area increases and so more input pump power will be needed. In fact for a 4500 nm wide, 800 nm thick ridge waveguide, the effective area (2 μm^2) is on the same order of magnitude as a 3150 nm diameter fibre (4 μm^2). Further increases in ridge thickness (with corresponding width thickness) would thus eliminate any potential efficiency gains, even if the phase-matching solution-spacing improved.

8.9 Conclusion

Ridge waveguides offer the promise of replicating the useful output average powers in the greenhouse gas absorption regions that can be generated with fibre tapers, but with lower input powers. This was demonstrated to be the case with 500 nm thick SOI tapers for wavelengths out to 4.25 µm, where the input powers needed are at least 30% lower than those required for the fibre taper designs studied in the last chapter. This ignores the coupling losses, however, which are likely to be greater for SOI waveguides than for fibres due to the smaller cross section and thus need for a stronger coupling lens. Furthermore, the coupling to a ridge waveguide requires matching the polarisation to the TM mode which adds extra complexity, whereas this is not an issue for fibres due to their circular symmetry.

Even accounting for these extra sources of loss and assuming some efficiency improvement remains, beyond 4.25 µm the significant self-steepening produced by the wavelength-dependence of the fundamental modal area introduces a significant clamping effect which reduces the generation of longer wavelengths.

In order to mitigate this problem, a thicker silicon layer of 600 nm was considered, which has a reduced self-steepening barrier. However, with even this modest increase in the ridge waveguide thickness, the phase-matching conditions for transferring spectral power to these longer wavelengths are too spaced apart, so the conversion efficiency becomes negligible. Increasing the waveguide thickness further (to 800 nm) offers no improvement in the available phase-matching conditions. Still further increases in thickness also increase the effective area such that the nonlinear coefficient approaches that of a fibre.

Silicon fibres were shown in the previous chapter to have robust phase-matching profiles for the target wavelengths. This, in addition to the less stringent coupling conditions mentioned above, means that the tapered fibre platform remains the better choice for extending a SC into the mid-IR while boosting the average powers available on the long-wavelength edge.

Chapter 9

Conclusion

In this thesis I have studied supercontinuum (SC) generation in silicon-core fibres and silicon-on-insulator (SOI) ridge waveguides. I have used the generalised nonlinear Schrödinger equation to model the propagation of light, in both continuous wave and pulsed form, through these fibres and waveguides. I checked the validity of this model, which includes silicon-specific effects such as two- and three-photon absorption and free-carriers, against experiments. These comprised straight sections of fibre and waveguide as well as tapered fibres fabricated and tested by my colleagues at Southampton. These simulations showed good agreement between the model and the experimental outputs.

In the second half of the thesis, I look at ways in which silicon fibres can be tapered in order to improve nonlinear wavelength conversion and SC generation. I start with a very simple approach to wavelength conversion which uses two different fibre-diameters, the first of which is optimised to produce degenerate four-wave-mixing (FWM), which results in signal generation from a pump and idler seed. The second fibre section is optimised for non-degenerate FWM, which takes in the three wavelengths from the first section and converts them to a target wavelength. This design is shown to work and can be used to extend the wavelength-range that can be reached with any combination of pump and seed, providing the intermediate signal and target output wavelength lie in the transparency range of the material.

This approach of using a second diameter to change the phase-matching conditions (in this case using a larger second diameter to reach a longer wavelength range) is adapted for SC generation. The design is expanded into a full taper-shape, with a down-taper from a large input facet to a waist region, an up-taper, and a fixed-diameter end section. The down-taper and waist replaces the first fixed-diameter section in the wavelength-conversion design. In this case, several processes (self-phase modulation and soliton fission as well as degenerate FWM) produce initial spectral-broadening. The up-taper then introduces new phase-matching conditions for non-degenerate FWM-based conversion to progressively longer wavelengths. This process culminates in the fixed-diameter end facet, which is optimised to maximise the number of phase-matching conditions to a particular target wavelength range. The taper design is shown to work with a range of input powers, improving the efficiency of conversion to several output wavelength ranges out to 5.5 µm.

Finally, this taper design is adapted for SOI ridge waveguides. For a thickness of 500nm, it is found that the widths of the output sections lie very close to the width that matches the zero-dispersion wavelength (ZDW) to the input pump (2.1 µm), so the design is simplified to a down-taper and end-facet. This is also shown to work for the output wavelengths out to 4.25 µm, but beyond this the boosting effect is clamped due to the wavelength-dependence of the effective area of the fundamental mode.

Thus, for the purpose of generating longer wavelengths in the mid-IR, the silicon-core fibre platform is the better choice.

Appendix A

Appendix A: Cash-Karp method

My GNLSE solver uses the general symmetrised form Eq. 2.72. It then solves the nonlinear integral using the Cash-Karp method [43]:

$$k_1 = h\hat{N}A \tag{A.1}$$

$$k_2 = h\hat{N}(A + \frac{k_1}{5}) \tag{A.2}$$

$$k_3 = h\hat{N}(A + \frac{3k_1}{40} + \frac{9k_2}{40}) \tag{A.3}$$

$$k_4 = h\hat{N}(A + \frac{3k_1}{10} - \frac{9k_2}{10} + \frac{6k_3}{5}) \tag{A.4}$$

$$k_5 = h\hat{N}(A - \frac{11k_1}{54} + \frac{5k_2}{2} - \frac{70k_3}{27} + \frac{35k_4}{27}) \tag{A.5}$$

$$k_6 = h\hat{N}(A + \frac{1631k_1}{55296} + \frac{175k_2}{512} - \frac{575k_3}{13824} + \frac{44275k_4}{110592} + \frac{253k_5}{4096}) \tag{A.6}$$

$$\hat{N}_4 = \hat{N}(A + \frac{2825k_1}{27648} + \frac{18575k_3}{48384} + \frac{13525k_4}{55296} + \frac{277k_5}{14336} + \frac{k_6}{4}) \tag{A.7}$$

$$\hat{N}_5 = \hat{N}(A + \frac{37k_1}{378} + \frac{250k_3}{621} + \frac{125k_4}{594} + \frac{512k_6}{1771}). \tag{A.8}$$

This sequence of steps produces two new nonlinear operators $\hat{N}_4$ and $\hat{N}_5$ which are accurate to fourth and fifth order respectively. In order to check this, they should converge to within a specified tolerance δN i.e. $|\hat{N}_5 - \hat{N}_4| < \delta N$. Providing this condition is met, the $\hat{N}_5$ is passed into Eq. 2.72 i.e.

$$A(z+h,t) = \exp\left(\frac{h}{2}\hat{L}\right)\exp(h\hat{N}_5)\exp\left(\frac{h}{2}\hat{L}\right)A(z,t). \tag{A.9}$$

If the tolerance check fails, the process is repeated with the z-step reduced as follows:

$$h_{\text{new}} = 0.95h \times \left(\frac{\delta N}{|\hat{N}_5 - \hat{N}_4|}\right)^{0.25}. \tag{A.10}$$

In fact, this adjustment to the z-step size is performed regardless, so if $|\hat{N}_5 - \hat{N}_4| < \delta N$, it will be increased for the following propagation step (but the current propagation step is not repeated). This allows the algorithm to perform with more computational efficiency when the pulse propagates with little change, as the step size can keep growing and will only be reduced again when more complex pulse evolution requires it.

Appendix B

Appendix B: Tensor vector triple dot product

The shorthand for a triple dot product between a third-order tensor and a vector is:

$$\begin{aligned} T^{(3)} \vdots \mathbf{VVV} &\equiv T^{(3)} \cdot \mathbf{V} \cdot \mathbf{V} \cdot \mathbf{V} \\ &= \mathbf{V_2} \end{aligned}$$

where $\mathbf{V_2}$ is a new vector. This can be broken down into stages:

$$T^{(3)} \cdot \mathbf{V} = T^{(2)} \tag{B.1}$$

$$T^{(2)} \cdot \mathbf{V} = \mathbf{M} \tag{B.2}$$

$$\mathbb{M} \cdot \mathbf{V} = \mathbf{V_2} \tag{B.3}$$

For our purposes, we are looking at a third-order tensor, $\chi^{(3)}$ which has three indices per dimension, x, y and z, corresponding to spatial dimensions. As the tensor has four dimensions, it has $3^4 = 81$ elements, represented as $\chi^{(3)}_{xxxx}$, $\chi^{(3)}_{xyxx}$, $\chi^{(3)}_{xxzz}$ etc.

Let's start with Eq. (B.1), defining the elements of the resulting $T^{(2)}$:

$$
\begin{aligned}
T^{(2)}_{xxx} &= T^{(3)}_{xxxx}V_x + T^{(3)}_{xyxx}V_y + T^{(3)}_{xzxx}V_z \\
T^{(2)}_{xyx} &= T^{(3)}_{yxxx}V_x + T^{(3)}_{yyxx}V_y + T^{(3)}_{yzxx}V_z \\
T^{(2)}_{xzx} &= T^{(3)}_{zxxx}V_x + T^{(3)}_{zyxx}V_y + T^{(3)}_{zzxx}V_z \\
T^{(2)}_{yxx} &= T^{(3)}_{xxyx}V_x + T^{(3)}_{xyyx}V_y + T^{(3)}_{xzyx}V_z \\
T^{(2)}_{yyx} &= T^{(3)}_{yxyx}V_x + T^{(3)}_{yyyx}V_y + T^{(3)}_{yzyx}V_z \\
T^{(2)}_{yzx} &= T^{(3)}_{zxyx}V_x + T^{(3)}_{zyyx}V_y + T^{(3)}_{zzyx}V_z \\
T^{(2)}_{zxx} &= T^{(3)}_{yxzx}V_x + T^{(3)}_{yyzx}V_y + T^{(3)}_{yzzx}V_z \\
T^{(2)}_{zyx} &= T^{(3)}_{zxzx}V_x + T^{(3)}_{zyzx}V_y + T^{(3)}_{zzzx}V_z \\
T^{(2)}_{zzx} &= T^{(3)}_{zxzx}V_x + T^{(3)}_{zyzx}V_y + T^{(3)}_{zzzx}V_z
\end{aligned}
$$

$$
\begin{aligned}
T^{(2)}_{xxy} &= T^{(3)}_{xxxy}V_x + T^{(3)}_{xyxy}V_y + T^{(3)}_{xzxy}V_z \\
T^{(2)}_{xyy} &= T^{(3)}_{yxxy}V_x + T^{(3)}_{yyxy}V_y + T^{(3)}_{yzxy}V_z \\
T^{(2)}_{xzy} &= T^{(3)}_{zxxy}V_x + T^{(3)}_{zyxy}V_y + T^{(3)}_{zzxy}V_z \\
T^{(2)}_{yxy} &= T^{(3)}_{xxyy}V_x + T^{(3)}_{xyyy}V_y + T^{(3)}_{xzyy}V_z \\
T^{(2)}_{yyy} &= T^{(3)}_{yxyy}V_x + T^{(3)}_{yyyy}V_y + T^{(3)}_{yzyy}V_z \\
T^{(2)}_{yzy} &= T^{(3)}_{zxyy}V_x + T^{(3)}_{zyyy}V_y + T^{(3)}_{zzyy}V_z \\
T^{(2)}_{zxy} &= T^{(3)}_{xxzy}V_x + T^{(3)}_{xyzy}V_y + T^{(3)}_{xzzy}V_z \\
T^{(2)}_{zyy} &= T^{(3)}_{yxzy}V_x + T^{(3)}_{yyzy}V_y + T^{(3)}_{yzzy}V_z \\
T^{(2)}_{zzy} &= T^{(3)}_{zxzy}V_x + T^{(3)}_{zyzy}V_y + T^{(3)}_{zzzy}V_z
\end{aligned}
$$

$$
\begin{aligned}
T^{(2)}_{xxz} &= T^{(3)}_{xxxz}V_x + T^{(3)}_{xyxz}V_y + T^{(3)}_{xzxz}V_z \\
T^{(2)}_{xyz} &= T^{(3)}_{yxxz}V_x + T^{(3)}_{yyxz}V_y + T^{(3)}_{yzxz}V_z \\
T^{(2)}_{xzz} &= T^{(3)}_{zxxz}V_x + T^{(3)}_{zyxz}V_y + T^{(3)}_{zzxz}V_z \\
T^{(2)}_{yxz} &= T^{(3)}_{xxyz}V_x + T^{(3)}_{xyyz}V_y + T^{(3)}_{xzyz}V_z \\
T^{(2)}_{yyz} &= T^{(3)}_{yxyz}V_x + T^{(3)}_{yyyz}V_y + T^{(3)}_{yzyz}V_z \\
T^{(2)}_{yzz} &= T^{(3)}_{zxyz}V_x + T^{(3)}_{zyyz}V_y + T^{(3)}_{zzyz}V_z \\
T^{(2)}_{zxz} &= T^{(3)}_{xxzz}V_x + T^{(3)}_{xyzz}V_y + T^{(3)}_{xzzz}V_z \\
T^{(2)}_{zyz} &= T^{(3)}_{yxzz}V_x + T^{(3)}_{yyzz}V_y + T^{(3)}_{yzzz}V_z \\
T^{(2)}_{zzz} &= T^{(3)}_{zxzz}V_x + T^{(3)}_{zyzz}V_y + T^{(3)}_{zzzz}V_z
\end{aligned}
$$

Now, to perform Eq. (B.2) to get the elements of **M**:

$$\begin{aligned}
M_{xx} &= T^{(2)}_{xxx}V_x + T^{(2)}_{xyx}V_y + T^{(2)}_{xzx}V_z \\
M_{xy} &= T^{(2)}_{yxx}V_x + T^{(2)}_{yyx}V_y + T^{(2)}_{yzx}V_z \\
M_{xz} &= T^{(2)}_{zxx}V_x + T^{(2)}_{zyx}V_y + T^{(2)}_{zzx}V_z
\end{aligned}$$

$$\begin{aligned}
M_{yx} &= T^{(2)}_{xxy}V_x + T^{(2)}_{xyy}V_y + T^{(2)}_{xzy}V_z \\
M_{yy} &= T^{(2)}_{yxy}V_x + T^{(2)}_{yyy}V_y + T^{(2)}_{yzy}V_z \\
M_{yz} &= T^{(2)}_{zxy}V_x + T^{(2)}_{zyy}V_y + T^{(2)}_{zzy}V_z
\end{aligned}$$

$$\begin{aligned}
M_{zx} &= T^{(2)}_{xxz}V_x + T^{(2)}_{xyz}V_y + T^{(2)}_{xzz}V_z \\
M_{zy} &= T^{(2)}_{yxz}V_x + T^{(2)}_{yyz}V_y + T^{(2)}_{yzz}V_z \\
M_{zz} &= T^{(2)}_{zxz}V_x + T^{(2)}_{zyz}V_y + T^{(2)}_{zzz}V_z
\end{aligned}$$

Finally, we can perform Eq. (B.3) to get the elements of $\mathbf{V_2}$:

$$\begin{aligned}
V_{2x} &= M_{xx}V_x + M_{xy}V_y + M_{xx}V_z \\
V_{2y} &= M_{yx}V_x + M_{yy}V_y + M_{yx}V_z \\
V_{2z} &= M_{zx}V_x + M_{zy}V_y + M_{zx}V_z
\end{aligned}$$

Using the assumption that $V_y = V_z = 0$ gives:

$$\begin{aligned}
V_{2x} &= M_{xx}V_x = T^{(2)}_{xxx}V_x^2 = T^{(3)}_{xxxx}V_x^3 \\
V_{2y} &= M_{yx}V_x = T^{(2)}_{xxy}V_x^2 = T^{(3)}_{xxxy}V_x^3 \\
V_{2z} &= M_{zx}V_x = T^{(2)}_{xxz}V_x^2 = T^{(3)}_{xxxz}V_x^3
\end{aligned}$$

Now we can substitute $\mathbf{V} = \mathbf{E}(\mathbf{r}, t)$ and $T^{(3)} = \chi^{(3)}$:

$$\mathbf{P_{NL}}(\mathbf{r}, t) = \epsilon_0 \chi^{(3)} \vdots \mathbf{E}(\mathbf{r}, t)\mathbf{E}(\mathbf{r}, t)\mathbf{E}(\mathbf{r}, t) \tag{B.4}$$

Further subsituting Eqs. (2.28) and (2.30) into Eq. (2.33) leaves only x-components, such that:

$$\begin{aligned}
\mathbf{P_{NL}}_x(\mathbf{r}, t) &= \epsilon_0 \chi^{(3)} \vdots \mathbf{E}_x(\mathbf{r}, t)\mathbf{E}_x(\mathbf{r}, t)\mathbf{E}_x(\mathbf{r}, t) \\
&= \epsilon_0 \chi^{(3)}_{xxxx} \mathbf{E}_x^3(\mathbf{r}, t)
\end{aligned}$$

Thus,

$$\frac{1}{2}[P_{NL}(\mathbf{r}, t)\exp(-\mathrm{i}\omega_0 t) + \mathrm{c.c.}] = \epsilon_0 \chi^{(3)}_{xxxx} \left(\frac{1}{2}[E(\mathbf{r}, t)\exp(-\mathrm{i}\omega_0 t) + \mathrm{c.c.}] \right)^3 \tag{B.5}$$

To solve this, we'll use the general form:

$$
\begin{aligned}
(A+A^*)^3 &= (A+A^*)^2(A+A^*) \\
&= (A^2+2AA^*+A^{*2})(A+A^*) \\
&= (A^2+A^{*2}+2|A|^2)(A+A^*) \\
&= A^3+A^2A^*+A^{*2}A+A^{*3}+2|A|A^2+2|A|^2A^* \\
&= A^3+A^{*3}+3|A|^2(A+A^*)
\end{aligned}
$$

Now we can plug this back in:

$$
\begin{aligned}
\frac{1}{2}[P_{NL}(\mathbf{r},t)\exp(-\mathrm{i}\omega_0 t)+\text{c.c.}] &= \frac{1}{8}\epsilon_0\chi^{(3)}_{xxxx}([E^3(\mathbf{r},t)\exp(-3\mathrm{i}\omega_0 t)+\text{c.c.}] \\
&+ 3|E(\mathbf{r},t)|^2[E(\mathbf{r},t)\exp(-\mathrm{i}\omega_0 t)+\text{c.c.}])
\end{aligned}
$$

We make the assumption that third-harmonic frequency generation, involving the $3\omega_0$ term, is generally negligible in optical fibres as the phase-matching condition is difficult to fulfill, so the equation reduces to:

$$
\begin{aligned}
\frac{1}{2}[P_{NL}(\mathbf{r},t)\exp(-\mathrm{i}\omega_0 t)+\text{c.c.}] &= \frac{3}{8}\epsilon_0\chi^{(3)}_{xxxx}|E(\mathbf{r},t)|^2[E(\mathbf{r},t)\exp(-\mathrm{i}\omega_0 t)+\text{c.c.}] \\
\Longrightarrow P_{NL}(\mathbf{r},t) &= \frac{3}{4}\epsilon_0\chi^{(3)}_{xxxx}|E(\mathbf{r},t)|^2E(\mathbf{r},t) \\
&= \epsilon_0\epsilon_{NL}E(\mathbf{r},t) \qquad \text{(B.6)}
\end{aligned}
$$

where

$$
\epsilon_{NL} = \frac{3}{4}\chi^{(3)}_{xxxx}|E(\mathbf{r},t)|^2 \qquad \text{(B.7)}
$$

List of Publications

(1) **J. Campling**, P. Horak, A. C. Peacock, "*Designing silicon-core fiber tapers for efficient supercontinuum generation in the greenhouse gas absorption region*", in JOSAB 2020 (OSA).

(2) D. Wu, L. Shen, H. Ren, **J. Campling**, T. Hawkins, J. Ballato, U. J. Gibson, A. Peacock, "*Net optical parametric gain in a submicron silicon core fiber pumped in the telecom band*", in APL Photonics 2019.

(3) H. Ren, L. Shen, **J. Campling**, A. F. J. Runge, O. Aktas, T. Hawkins, P. Horak, J. Ballato, U. J. Gibson, A. Peacock, "*Octave-spanning supercontinuum generation in a dispersion managed crystalline silicon core fiber*", in CLEO: Science and Innovations 2018 (OSA).

(4) A. Peacock, **J. Campling**, A. F. J. Runge, H. Ren, L. Shen, O. Aktas, P. Horak, N. Healy, U. J. Gibson, J. Ballato, "*Wavelength conversion and supercontinuum generation in silicon optical fibers*", in JSTQE 2017 (IEEE).

(5) H. Ren, A. Runge, **J. Campling**, M. Jones, T. Hawkins, J. Ballato, P. Horak, U. J. Gibson, A. Peacock, "*Silicon fibre nano-spike for robust coupling to silica fibres*", in CLEO Europe Conference 2017 (IEEE).

List of Conferences

(1) **J. Campling**, P. Horak, A. C. Peacock, "*Silicon-core fiber tapers for efficient mid-IR supercontinuum generation*", Poster at Workshop on Specialty Optical Fibers 2019, South Carolina.

(2) **J. Campling**, P. Horak, A. C. Peacock, "*Silicon-core fiber tapers for efficient mid-IR supercontinuum generation*", Presentation uploaded to Photonics Europe 2020 online forum.

Bibliography

[1] C. J. Fecko et al. “Ultrafast Hydrogen-Bond Dynamics in the Infrared Spectroscopy of Water”. In: *Science* 301.5640 (2003), pp. 1698–1702. ISSN: 0036-8075. DOI: 10.1126/science.1087251.

[2] T. Töpfer et al. “Room-temperature mid-infrared laser sensor for trace gas detection”. In: *Appl. Opt.* 36.30 (1997), pp. 8042–8049. DOI: 10.1364/AO.36.008042. URL: http://ao.osa.org/abstract.cfm?URI=ao-36-30-8042.

[3] D. A. Rothery, P. W. Francis, and C. A. Wood. “Volcano monitoring using short wavelength infrared data from satellites”. In: *J. Geophys. Res. Solid Earth* 93.B7 (1988), pp. 7993–8008.

[4] M. Ferrari and V. Quaresima. “A brief review on the history of human functional near-infrared spectroscopy (fNIRS) development and fields of application”. In: *NeuroImage* 63.2 (2012), pp. 921 –935. ISSN: 1053-8119. DOI: https://doi.org/10.1016/j.neuroimage.2012.03.049.

[5] R. Soref. “Mid-infrared photonics in silicon and germanium”. In: *Nat. Photonics* 4.8 (2010), p. 495.

[6] W. Herrmann et al. “Short wavelength infrared (SWIR) spectral analysis of hydrothermal alteration zones associated with base metal sulfide deposits at Rosebery and Western Tharsis, Tasmania, and Highway-Reward, Queensland”. In: *Econ. Geol.* 96.5 (2001), pp. 939–955.

[7] J. M. Dudley, G. Genty, and S. Coen. “Supercontinuum generation in photonic crystal fibre”. In: *Rev. Mod. Phys.* 78.4 (2006), p. 1135.

[8] I. Hartl et al. “Ultrahigh-resolution optical coherence tomography using continuum generation in an air–silica microstructure optical fibre”. In: *Opt. Lett.* 26.9 (2001), pp. 608–610. DOI: 10.1364/OL.26.000608. URL: http://ol.osa.org/abstract.cfm?URI=ol-26-9-608.

[9] R. K. W. Lau et al. “Octave-spanning mid-infrared supercontinuum generation in silicon nanowaveguides”. In: *Opt. Lett.* 39.15 (2014), pp. 4518–4521. DOI: 10.1364/OL.39.004518.

[10] C. F. Kaminski et al. “Supercontinuum radiation for applications in chemical sensing and microscopy”. In: *Appl. Phys. B* 92.3 (2008), p. 367. ISSN: 1432-0649. DOI: 10.1007/s00340-008-3132-1.

[11] S. Ashfar V., M. Turner, and T. M. Monro. “Nonlinear optics in emerging waveguides”. In: *Supercontinuum Generation in Optical fibres*. Ed. by J. M. Dudley and J. R.Editors Taylor. Cambridge University Press, 2010, pp. 226–284. DOI: 10.1017/CBO9780511750465.004.

[12] S. Dai et al. “A review of mid-infrared supercontinuum generation in chalcogenide glass fibers”. In: *Applied Sciences* 8.5 (2018), p. 707.

[13] A. C. Peacock, U. J. Gibson, and J. Ballato. “Silicon optical fibres–past, present, and future”. In: *Adv. Phys. X* 1.1 (2016), pp. 114–127.

[14] F. Leo et al. “Generation of coherent supercontinuum in a-Si:H waveguides: experiment and modeling based on measured dispersion profile”. In: *Opt. Express* 22.23 (2014), pp. 28997–29007. DOI: `10.1364/OE.22.028997`.

[15] N. Singh et al. “Midinfrared supercontinuum generation from 2 to 6um in a silicon nanowire”. In: *Optica* 2.9 (2015), pp. 797–802.

[16] B. Kuyken et al. “An octave-spanning mid-infrared frequency comb generated in a silicon nanophotonic wire waveguide”. In: *Nat. Commun.* 6 (2015), p. 6310.

[17] L. Shen et al. “Four-wave mixing and octave-spanning supercontinuum generation in a small core hydrogenated amorphous silicon fibre pumped in the mid-infrared”. In: *Opt. Lett.* 39.19 (2014), pp. 5721–5724. DOI: `10.1364/OL.39.005721`.

[18] L. Yin and G. P. Agrawal. “Impact of two-photon absorption on self-phase modulation in silicon waveguides”. In: *Opt. Lett.* 32.14 (2007), pp. 2031–2033. DOI: `10.1364/OL.32.002031`.

[19] P. Koonath, D. R. Solli, and B. Jalali. “Limiting nature of continuum generation in silicon”. In: *App. Phys. Lett.* 93.9 (2008), p. 091114. DOI: `10.1063/1.2977872`.

[20] G. P. Agrawal. “Chapter 2 - Pulse Propagation in fibres”. In: *Nonlinear fibre Optics*. Fifth. Optics and Photonics. Boston: Academic Press, 2013, pp. 27 –56. DOI: `http://doi.org/10.1016/B978-0-12-397023-7.00002-4`.

[21] R. Deiterding et al. “A Reliable Split-Step Fourier Method for the Propagation Equation of Ultra-Fast Pulses in Single-Mode Optical fibres”. In: *J. Lightwave Technol.* 31.12 (2013), pp. 2008–2017. ISSN: 0733-8724.

[22] J. Leuthold, C. Koos, and W. Freude. “Nonlinear silicon photonics”. In: *Nat. Photonics* 4.8 (2010), p. 535.

[23] K. Narayanan, A. W. Elshaari, and S. F. Preble. “Broadband all-optical modulation in hydrogenated-amorphous silicon waveguides”. In: *Opt. Express* 18.10 (2010), pp. 9809–9814. DOI: `10.1364/OE.18.009809`.

[24] A. C. Peacock et al. “Wavelength Conversion and Supercontinuum Generation in Silicon Optical fibres”. In: *IEEE J. Sel. Top. Quantum Electron.* 24.3 (2018), pp. 1–9. ISSN: 1077-260X. DOI: `10.1109/JSTQE.2017.2762958`.

[25] L. Lagonigro et al. “Low loss silicon fibres for photonics applications”. In: *Appl. Phys. Lett.* 96.4 (2010), p. 041105. DOI: `10.1063/1.3294630`. eprint: `http://dx.doi.org/10.1063/1.3294630`. URL: `http://dx.doi.org/10.1063/1.3294630`.

[26] J. Ballato and A. C. Peacock. “Perspective: Molten core optical fiber fabrication—A route to new materials and applications”. In: *APL Photonics* 3.12 (2018), p. 120903. DOI: `10.1063/1.5067337`.

[27] J. Ballato et al. “Silicon optical fibre”. In: *Opt. Express* 16.23 (2008), pp. 18675–18683. DOI: `10.1364/OE.16.018675`.

[28] E. F. Nordstrand et al. “Alkaline oxide interface modifiers for silicon fibre production”. In: *Opt. Mater. Express* 3.5 (2013), pp. 651–657. DOI: `10.1364/OME.3.000651`.

[29] N. Healy et al. “Tapered silicon optical fibers”. In: *Opt. Express* 18.8 (2010), pp. 7596–7601. DOI: `10.1364/OE.18.007596`.

[30] H. Ren et al. “Tapered silicon core fibres with nano-spikes for optical coupling via spliced silica fibres”. In: *Optics Express* 25.20 (2017), pp. 24157–24163.

[31] G. K. Celler and S. Cristoloveanu. “Frontiers of silicon-on-insulator”. In: *Journal of Applied Physics* 93.9 (2003), pp. 4955–4978. DOI: `10.1063/1.1558223`.

[32] W. Bogaerts et al. “SOI nanophotonic waveguide structures fabricated with deep UV lithography”. In: *Photonics and Nanostructures - Fundamentals and Applications* 2.2 (2004), pp. 81–86. ISSN: 1569-4410. DOI: `https://doi.org/10.1016/j.photonics.2004.07.002`.

[33] I. H. Malitson. “Interspecimen comparison of the refractive index of fused silica”. In: *JOSA* 55.10 (1965), pp. 1205–1209.

[34] A. C. Peacock et al. “Nonlinear pulse dynamics in multimode silicon core optical fibres”. In: *Opt. Lett.* 37.16 (2012), pp. 3351–3353. DOI: `10.1364/OL.37.003351`.

[35] L. Tong, J. Lou, and E. Mazur. “Single-mode guiding properties of subwavelength-diameter silica and silicon wire waveguides”. In: *Opt. Express* 12.6 (2004), pp. 1025–1035. DOI: `10.1364/OPEX.12.001025`.

[36] K. Okamoto. “Chapter 3 - Optical fibres”. In: *Fundamentals of Optical Waveguides*. Second. Burlington: Academic Press, 2006, pp. 57 –158. ISBN: 978-0-12-525096-2. DOI: `https://doi.org/10.1016/B978-012525096-2/50004-0`.

[37] P. M. Morse and H. Feshbach. “Chapter 9”. In: *Methods of Theoretical Physics*. McGraw-Hill, 1953.

[38] Q. Lin, O. J. Painter, and G. P. Agrawal. “Nonlinear optical phenomena in silicon waveguides: Modeling and applications”. In: *Opt. Express* 15.25 (2007), pp. 16604–16644. DOI: `10.1364/OE.15.016604`.

[39] N. Singh et al. “Midinfrared supercontinuum generation from 2 to 6um in a silicon nanowire”. In: *Optica* 2.9 (2015), pp. 797–802. DOI: `10.1364/OPTICA.2.000797`.

[40] J. A. Fleck, J. R. Morris, and M. D. Feit. “Time-dependent propagation of high energy laser beams through the atmosphere”. In: *Appl. Phys.* 10.2 (1976), pp. 129–160. ISSN: 1432-0630. DOI: `10.1007/BF00896333`. URL: `http://dx.doi.org/10.1007/BF00896333`.

[41] M. Lax, J. H. Batteh, and G. P. Agrawal. “Channeling of intense electromagnetic beams”. In: *Journ. Appl. Phys.* 52 (1981), pp. 109–125. DOI: `10.1063/1.328442`.

[42] J. Hult. “A Fourth-Order Runge-Kutta in the Interaction Picture Method for Simulating Supercontinuum Generation in Optical fibres”. In: *J. Lightwave Technol.* 25.12 (2007), pp. 3770–3775. ISSN: 0733-8724. DOI: `10.1109/JLT.2007.909373`.

[43] J. R. Cash and A. H. Karp. “A variable order Runge-Kutta method for initial value problems with rapidly varying right-hand sides”. In: *ACM Transactions on Mathematical Software (TOMS)* 16.3 (1990), pp. 201–222.

[44] G. P. Agrawal. “Chapter 5 - Optical Solitons”. In: *Nonlinear fibre Optics*. Fifth. Boston: Academic Press, 2013, pp. 129 –191. DOI: `http://doi.org/10.1016/B978-0-12-397023-7.00005-X`.

[45] G. P. Agrawal. “Chapter 3 - Group-Velocity Dispersion”. In: *Nonlinear fibre Optics*. Fifth. Optics and Photonics. Boston: Academic Press, 2013, pp. 57 –85.

[46] N. K. Hon, R. Soref, and B. Jalali. “The third-order nonlinear optical coefficients of Si, Ge, and Si1-xGex in the midwave and longwave infrared”. In: *J. Appl. Phys.* 110.1 (2011), p. 011301. DOI: `10.1063/1.3592270`.

[47] G. P. Agrawal. "Chapter 10 - Four-Wave Mixing". In: *Nonlinear fibre Optics*. Fifth. Boston: Academic Press, 2013, pp. 397 –456. DOI: `http://doi.org/10.1016/B978-0-12-397023-7.00010-3`.

[48] R. R. Jones et al. "Raman techniques: Fundamentals and frontiers". In: *Nanoscale research letters* 14.1 (2019), pp. 1–34.

[49] K.J. Blow and D. Wood. "Theoretical description of transient stimulated Raman scattering in optical fibers". In: *IEEE Journal of Quantum Electronics* 25.12 (1989), pp. 2665–2673. DOI: `10.1109/3.40655`.

[50] Lianghong Yin, Qiang Lin, and Govind P Agrawal. "Soliton fission and supercontinuum generation in silicon waveguides". In: *Optics letters* 32.4 (2007), pp. 391–393.

[51] R. R. Alfano. *The Supercontinuum Laser Source: The Ultimate White Light*. Springer New York, 2016. ISBN: 9781493933266. URL: `https://books.google.co.uk/books?id=SYqRCwAAQBAJ`.

[52] J. C. Travers, M. H. Frosz, and J. M. Dudley. "Nonlinear fibre optics overview". In: *Supercontinuum Generation in Optical fibres*. Ed. by J. M. Dudley and J. R. Taylor. Cambridge University Press, 2010, 32–51. DOI: `10.1017/CBO9780511750465.004`.

[53] G. P. Agrawal. "Chapter 12 - Novel Nonlinear Phenomena". In: *Nonlinear fibre Optics*. Fifth. Boston: Academic Press, 2013, pp. 497 –552.

[54] G. Genty, S. Coen, and J. M. Dudley. "fibre supercontinuum sources (Invited)". In: *JOSA B* 24.8 (2007), pp. 1771–1785. DOI: `10.1364/JOSAB.24.001771`.

[55] C. Dorrer and I. Kang. "Simultaneous temporal characterization of telecommunication optical pulses and modulators by use of spectrograms". In: *Opt. Lett.* 27.15 (2002), pp. 1315–1317. DOI: `10.1364/OL.27.001315`. URL: `http://www.osapublishing.org/ol/abstract.cfm?URI=ol-27-15-1315`.

[56] G. P. Agrawal. "Chapter 1 - Introduction". In: *Nonlinear fibre Optics*. Fifth. Optics and Photonics. Boston: Academic Press, 2013, pp. 1 –25. DOI: `http://doi.org/10.1016/B978-0-12-397023-7.00002-4`.

[57] H. Ren et al. "Octave-spanning supercontinuum generation in a dispersion managed tapered crystalline silicon core fibre". In: *Conference on Lasers and Electro-Optics*. OSA, 2018, SM3D.5. DOI: `10.1364/CLEO_SI.2018.SM3D.5`.

[58] R. Kitamura, L. Pilon, and M. Jonasz. "Optical constants of silica glass from extreme ultraviolet to far infrared at near room temperature". In: *App. Optics* 46 (2007), pp. 8118–8133.

[59] S. Morris et al. "On loss in silicon core optical fibers". In: *Opt. Mater. Express* 2.11 (2012), pp. 1511–1519. DOI: `10.1364/OME.2.001511`.

[60] H. Ren et al. "Low-loss silicon core fibre platform for mid-infrared nonlinear photonics". In: *Light: Science & Applications* 8 (Nov. 2019), p. 105. DOI: `10.1038/s41377-019-0217-z`.

[61] T. Wang et al. "Multi-photon absorption and third-order nonlinearity in silicon at mid-infrared wavelengths". In: *Opt. Express* 21.26 (2013), pp. 32192–32198. DOI: `10.1364/OE.21.032192`.

[62] J. Campling, P. Horak, and A. C. Peacock. "Designing silicon-core fibre tapers for efficient supercontinuum generation in the greenhouse gas absorption region". In: *J. Opt. Soc. Am. B* 37.6 (2020), pp. 1698–1706. DOI: `10.1364/JOSAB.392346`.

[63] IPG Photonics. *CL and CLT Series Narrow-line Cr:ZnSe/S CW Lasers*. 2020. URL: `https://www.ipgphotonics.com/en/products/lasers/mid-ir-hybrid-lasers/1-8-3-4-micron/cl-and-clt-1-150-w` (visited on 11/08/2020).

[64] H. Saghaei and V. Van. "Broadband mid-infrared supercontinuum generation in dispersion-engineered silicon-on-insulator waveguide". In: *J. Opt. Soc. Am. B* 36.2 (2019), A193–A202. DOI: `10.1364/JOSAB.36.00A193`.

[65] D. Grassani et al. "Mid infrared gas spectroscopy using efficient fibre laser driven photonic chip-based supercontinuum". In: *Nature Commun.* 10.1 (2019), p. 1553.

[66] M. Vainio and L. Halonen. "Mid-infrared optical parametric oscillators and frequency combs for molecular spectroscopy". In: *Phys. Chem. Chem. Phys.* 18 (6 2016), pp. 4266–4294. DOI: `10.1039/C5CP07052J`.

[67] C. W. Rudy, M. J. F. Digonnet, and R. L. Byer. "Advances in 2-μm Tm-doped mode-locked fibre lasers". In: *Optical fibre Technol.* 20.6 (2014), pp. 642–649.

[68] D. D. Hickstein et al. "Ultrabroadband supercontinuum generation and frequency-comb stabilization using on-chip waveguides with both cubic and quadratic nonlinearities". In: *Physical Review Applied* 8.1 (2017), p. 014025.

[69] S. M. Lindecrantz and O. G. Hellesø. "Estimation of propagation losses for narrow strip and rib waveguides". In: *IEEE Photonics Technology Letters* 26.18 (2014), pp. 1836–1839.

[70] K. K. Lee et al. "Effect of size and roughness on light transmission in a Si/SiO2 waveguide: Experiments and model". In: *Applied Physics Letters* 77.11 (2000), pp. 1617–1619. DOI: `10.1063/1.1308532`.

[71] U. Y. et al. "Towards low-loss waveguides in SOI and Ge-on-SOI for mid-IR sensing". In: *J. Phys. Comm.* 2.4 (2018), p. 045029. DOI: `10.1088/2399-6528/aaba24`.

[72] "Silicon Photonic Waveguides and Devices for Near- and Mid-IR Applications". English. In: *IEEE J. Selected Topics in Quan. Electron.* 21.4 (Aug. 2015), pp. 1–12. ISSN: 1077-260X. DOI: `10.1109/JSTQE.2014.2381469`.